Effect of Flow and Fluid Structures on the Performance of Vertical River Hydrokinetic Turbines

By

AMIR HOSSEIN BIRJANDI

A thesis submitted to the Faculty of Graduate Studies of
the University of Manitoba
in partial fulfillment of the requirements
of the degree of

DOCTOR OF PHILOSOPHY

Department of Mechanical and Manufacturing Engineering
University of Manitoba
Winnipeg

Degree:	Doctor of Philosophy
University:	University of Manitoba
Department:	Mechanical and Manufacturing Engineering
Title:	Effect of flow and fluid structures on the performance of vertical river hydrokinetic turbines
Author:	Amir Hossein Birjandi
Supervisors:	Dr. E. L. Bibeau Dr. V. Chatoorgoon

Abstract

Field and laboratory measurements characterize the performance of vertical axis hydrokinetic turbines operating in uniform and non-uniform inflow conditions for river applications. High sampling frequency velocity measurements, taken at 200 Hz upstream of a stopped and operating 25-kW H-type vertical axis hydrokinetic turbine in the Winnipeg River, show the existence of large eddies with an order of magnitude of the turbine's diameter. Scaling laws allow modeling river conditions in the laboratory for more detailed investigations.

A small-scale, 30 cm diameter, squirrel-cage vertical turbine designed, manufactured and equipped with a torque and position sensors is investigated for the detail behavior of the turbine subjected to different inflow conditions in a laboratory setting to study the effect of flow and fluid structures. The adjustable design of the laboratory turbine enables operations with different solidities, 0.33 and 0.67, and preset pitch angles, 0°, ±2.5°, ±5° and ±10°. Tests are first performed with uniform inflow condition to measure the sensitivity of the turbine to solidity, preset pitch angle, free-surface, and Reynolds number to obtain the optimum operating conditions. During the free-surface testing a novel dimensionless coefficient, clearance coefficient, is introduced that relates the change in turbine efficiency with change in the free-surface height. High-speed imaging at 500 fps of semi-submerged blades visualizes the vortex-shedding pattern behind the blades and air entrainment. High-speed imaging results of large eddy pattern behind the vertical turbine are consistent with theory and measurements.

Subsequently, cylinders of different diameters create non-uniform inflow conditions in the water tunnel by placing them at different longitudinal and lateral locations upstream of the model turbine. Thus, the effects of non-uniform inflow generated under controlled settings shows the impact of eddies and wake on the turbine performance. High sampling frequency measurements of torque and position at 683 Hz enables investigating the impact of flow variations on turbine performance in the frequency domain. These results are also useful for fatigue analysis.

Finally, entrained air bubbles in the flow—in river and laboratory settings—affect turbulence quantities, as measured using an acoustic Doppler velocimeter, and successfully addressed by implementing a new hybrid filter developed for this application.

Acknowledgements

My first and earnest acknowledgement must go to my advisers: Dr. Eric Bibeau and Dr. Vijay Chatoorgoon. Dr. Bibeau and Dr. Chatoorgoon have been instrumental in ensuring my academic, professional, financial and moral well-being ever since I started to work with them. Many thanks also to committee members: Dr. Mark Tachie and Dr. Shawn Clark for their constructive advice.

Far too many people to mention individually have assisted in so many ways during my research work. They all have my sincere gratitude. In particular, I would like to thank Tom Molinski and John Woods for their role in setting up the Pointe du Bois test site, Shamez Kassam for field measurement assistance, Derek Neufeld for machining of the turbine blades.

This research was financially supported by the by the NSERC/Manitoba Hydro Chair in Alternative Energy and to them I am deeply grateful. In addition, I would like to thank Vince Gartner and Clayton Bear for their support and supplying the 5 and 25 kW vertical turbines tested at Pointe du Bois.

I wish to express my appreciation to Neda Kianmehr for her beautiful cover design. Finally, I owe my dearest thank to my family, for their encouragements, inspiration and supports.

Table of contents

List of tables

List of figures

List of copyrighted material for which permission was obtained

Nomenclature

A	cross sectional area
A_T	turbine cross sectional area
AR	aspect ratio
B	blockage ratio
c	blade chord length
C_D	drag coefficient
C_h	clearance coefficient
C_L	lift coefficient
C_N	normal force coefficient
C_p	power coefficient
C_T	tangential force coefficient
D	diameter of the turbine
d	diameter of the cylinder
f	focal length
f	frequency
F_D	drag force
F_L	lift force
F_N	normal force
F_T	tangential force
Fr	Froude number, $U\sqrt{//,,//\text{gh}}/\sqrt{gh}$
g	gravity
h	water depth

H	water height above the turbine
I	turbulence intensity
k	reduced frequency
L	blade length
M_b	bending moment
n	total number of data points
N	number of blades
n_i	number of data points in the i^{th} velocity range
P_{Ave}	average output power
P_{Hyd}	hydraulic power
r	radius of the turbine
Re	blade Reynolds number, $\frac{\rho U c}{\mu}$
Re_D	turbine Reynolds number, $\frac{\rho U D}{\mu}$
Re_{rel}	blade relative Reynolds number, $Re \times \lambda$
St	Strouhal number
t	thickness
T	torque
Tr	total thrust
Tr_t	turbine thrust
U	free stream velocity
u	fluctuating velocity in the flow direction
U_w	wake velocity
U_{ad}	flow velocity in the downstream actuator disk
U_{au}	flow velocity in the upstream actuator disk
U_{ave}	average velocity

U_b	bypass velocity
U_{rel}	blade relative velocity
U_t	flow velocity in the turbine disk
v	fluctuating velocity in the lateral direction
V	flow velocity in the lateral direction
w	fluctuating velocity in the vertical direction
W	flow velocity in the vertical direction
x	longitudinal distance
y	lateral direction
z	vertical direction

Greek Symbol

α	blade angle of attack
α_0	mean angle of attack
α_p	preset pitch angle
α_m	amplitude of the oscillating angle of attack
α_{max}	blade maximum angle of attack
β	ratio of the free stream speed to the flow speed in the actuating disk, U/U_t
ε	ratio of the far-wake speed to the free stream speed, U_w/U
θ	azimuth angle
$\theta_{\alpha_{max}}$	azimuth angle of the blade at maximum angle of attack location
Δh	free-surface drop height
λ	tip speed ratio, $\frac{\omega r}{U}$
μ	viscosity
ρ	density

ρ_{uv}	non-dimensional correlation coefficient
σ	solidity, $\frac{Nc}{r}$
τ	ratio of the bypass flow speed to the free stream speed, U_b/U
χ	thrust ratio
ω	turbine rotational speed

Abbreviation

ADCP	acoustic Doppler current profiler
ADV	acoustic Doppler velocimeter
DWT	discrete wavelet transform
HAHT	horizontal axis hydrokinetic turbine
HAT	horizontal axis turbine
PSD	power spectral density
rpm	revolutions per minute
STFT	short time Fourier transform
VAHT	vertical axis hydrokinetic turbine
VAT	vertical axis turbine

Chapter 1

Introduction

1.1 World energy demand

Energy demand is a function of the population, labor productivity, economic activity, technological change, energy prices, energy taxes, and tariffs [1]; however, among the mentioned parameters, population is a critical factor. According to the United Nations Secretariat [2], the world's population in 2030 will exceed 8.3 billion. During this time, the world's energy demand will increase from 138.5 TWh to 678 TWh [3], as shown in Figure 1.1. Thus, with the current rate of energy consumption in the world, the world may consume the majority of the remaining fossil energy during this century. Peak fossil fuel issues, global warming, and the need to derive a higher percentage of our primary energy from renewables are some of the reasons that make renewable energy technologies attractive. Fusion from the sun, fission from within the earth's crust and planetary motion provide renewable energy.

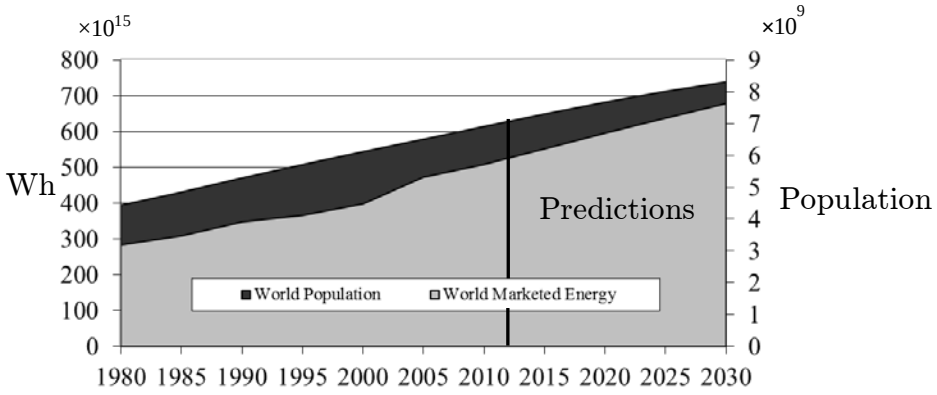

Figure 1.1: World energy demand and population predictions: 1980–2030, [2,3]

A portfolio of renewable energy solutions will be required to replace fossil fuels. This thesis investigates hydrokinetic energy generated by planetary motion and by the sun's radiation, which creates currents due to differential temperatures and water evaporation.

1.2 Hydrokinetic energy

Hydrokinetic turbines extract kinetic energy from water currents in oceans and rivers and work on similar operating principles as wind turbines. According to historians, Persians built the first machines utilizing wind kinetic energy in approximately 900 AD [4]. These wind turbines consisted of two or more vertical sails or paddles that took advantage of drag to turn the turbine shaft. Drag driven devices have low efficiency and cannot convert more than 20% of the available kinetic energy to mechanical energy. Kinetic turbines reach performances exceeding 35% when using lift to generate torque with respect to the axis of rotation. Although lift-driven wind turbines were introduced in the early decades of the twenty century, commercial models of wind turbines have

operated for three decades after the original invention [5]. More serious investigations of wind kinetic turbines started in the 1970's following the energy crisis. Wind energy concept was the focus of the researchers in this period with few studies focused on hydrokinetic turbines for extracting power from water currents in oceans and rivers. At the beginning of the twenty first century, global warming issues and environmental impact of fossil fuels brought renewed attention to hydrokinetic turbines. Hydrokinetic energy has a relatively high energy density, is a predictable resource, and can address base loads. Recent marine technological roadmaps by Canada and the US show a desire to commercialize this technology in the next few decades [6, 7].

Hydrokinetic energy from water currents can generally deliver predictable power to the grid as water currents are predominately driven by gravity rather than by weather. With extensive coastal and inland waters, Canada has the ideal environment for tapping the potential of hydrokinetic energy. The total estimated capacity of Canada's hydrokinetic energy is roughly 200,000 MW, or three times more than current electricity demand in Canada [8]. According to the vision defined in the marine renewable energy technology roadmap (MRE-TRM) developed by Ocean Renewable Energy Group (OREG), Canada will have a generating capacity of 2,000 MW marine renewable energy by 2030 [7].

The traditional hydro technology harnesses power of the water's potential energy by storing water behind dams, while hydrokinetic turbines harness kinetic energy of the flow at much reduced power densities. Dams and barriers have an ecological foot print by blocking the fish migration path and modifying the climate in their vicinities [9, 10] and are not always practical for smaller communities. Hydrokinetic turbines do not need dams or large constructions for

installation, so they are most suitable for remote power applications. However, they produce power at the community level.

There are two types of lift-driven hydrokinetic turbines used to harness the power of the water's kinetic energy: horizontal axis hydrokinetic turbine (HAHT) and vertical axis hydrokinetic turbine (VAHT), as shown in Figure 1.2. The VAHT is a type of hydrokinetic turbine in which the axis of rotation is normal to the flow direction. Georges Jean Marie Darrieus introduced the idea of the vertical turbines in 1923 and patented this idea in 1931 [11]. The vertical drive shaft allows the placement of the generator, gearbox, and bearings potentially above water level, which simplifies the installation and avoids the requirement for a waterproof sealed bearing. In addition, VAHTs harness kinetic energy independent of the flow direction: no yawing mechanism is needed to keep the axis aligned with the flow. VAHTs operate efficiently at lower heads compared to HAHTs [12], therefore they may be economical for a wide range of sites such as river current and tidal areas.

Despite the advantages of vertical axis turbines specifically in hydro applications, this design suffers from the dynamic complexity that causes this technology and its applications in wind and hydrokinetic energy extraction to remain more commercially undeveloped. In contrast with the horizontal turbine whose dynamic performance is symmetrical about the axis of rotation, the vertical turbine blades experience an unsteady condition through each rotation. Because of the angle of attack variation, blades experience a variable load with a chance of dynamic stall occurrence, specifically at low rotational speeds. The blade-wake interaction in the second half of the rotation adds to the complexity of the dynamic loading phenomena, which is still beyond the scope of current knowledge

for accurate predictions. When these turbines operate in an unsteady environment due to large-scale turbulence eddies, proper understanding of dynamic phenomena is even more limited.

(a) (b)

Figure 1.2: Hydrokinetic turbine configurations tested at Pointe du Bois on the Winnipeg River: (a) horizontal axis, and (b) vertical axis

1.3 Non-uniform inflow

Sutherland and Kelley [13] demonstrated that turbulent inflows with large-scale eddies can impose extreme loads on horizontal wind turbine blades and induce higher levels of fatigue. Unsteady inflow also affects the power production. The National Renewable Energy Laboratory is currently doing a comprehensive investigation for better understanding of the effects of unsteady inflow on horizontal wind turbines [13-16]. Yokosi [17] measurements in the Uji River and

the Sosui canal show that the depth and width of the river determine the order of magnitude of the largest eddies. Sources of large-scale eddy in rivers are:

- rapid changes in the profile of riverbeds and banks,
- presence of large boulders and ice floes,
- man-made obstructions like a bridge pier or upstream turbines, and
- rapid river level changes leading to hydraulic jumps.

Eddies carried along with the mean flow introduce a rapid change in the relative velocity locally over the turbine's blades. During these rapid changes in the flow and turbine's operation condition, the large river field cannot respond quickly enough to establish steady-state conditions and blades may experience dynamic stall. Dynamic stall may occur on the blade operating in this time-dependent inflow condition if the blade passes the static stall angle [18]. The dynamic stall applies fluctuating aerodynamic loads on blades. The amplitude of fluctuating aerodynamic loads depends on the intensity of the stall occurring on blades. High frequency measurements are required to distinguish dynamic loads due to the non-uniform inflow from the inherent dynamic behavior of VAHT.

To the author's knowledge, there is no literature about non-uniform inflow interaction with VAHT, either experimental or numerical that quantifies the impact of fluid structures. It would be beneficial to characterize the river flow upstream of a VAHT, and perform tests to quantify the effect of inflow non-uniformity on the performance characteristics of a VAHT. Moreover, certain aspects of how changing the free-surface and how turbine arrays will perform need improving—the same test facility used for non-uniform inflow can be used

to incorporate such investigations to add to our fundamental understanding of VAHT.

1.4 Objectives

The main objective of this research is to characterize the effect of non-uniform inflow on the performance of VAHTs by conducting comprehensive field measurement in a river and tests using a water tunnel. The field measurement quantifies the flow characteristics in the river upstream a hydrokinetic turbine. The detailed performance behavior of a small-scale VAHT in a non-uniform inflow condition is then investigated in the water tunnel to quantify the effect of fluid structures. The method employed to generate non-uniform inflow is by placing cylinders upstream of the turbine and measure the performance characteristics of the turbine. The average and instantaneous performance of the turbine are then analyzed at different non-uniform inflow conditions. The instantaneous performance data can describe the quality of the power output and improve the fatigue life estimation of the turbine. Additional objectives include (1) testing the small-scale turbine in a uniform inflow condition and extracting the performance characteristics for variations in free-surface height, pitch angle, solidity and Reynolds number, and (2) extrapolate the average performance data of a VAHT to improve the output power prediction for turbine arrays.

1.5 General approach

The following three experimental steps describe the approach employed to characterize the impact of flow and fluid structures on VAHT to achieve the research objectives.

1.5.1 Field measurement

The first stage of the research is a series of river velocity measurements taken one diameter upstream of a 25-kW vertical axis river kinetic turbine deployed in the Winnipeg River at Pointe du Bois, located 150 km northeast of Winnipeg. An acoustic Doppler velocimeter (ADV) measures velocity fluctuations at a sample rate of 200 Hz. Analysis of ADV velocity data measured upstream of the turbine quantifies the variation in the mean and fluctuating components of river flow velocity. By further analysis, the order of magnitude of large eddies is extracted from the autocorrelation function. Measurements are conducted upstream of stopped and operating turbine to quantify the interaction of the operating turbine on the upstream flow pattern. These measurements quantify the scale of eddies in rivers with respect to turbine blade chord length and they contribute to scale laboratory tests.

1.5.2 A small-scale turbine design, testing and performance characterization in uniform and non-uniform inflow

The second stage of the research focuses on the design, manufacturing and instrumentation of a small-scale vertical turbine. This small turbine has an adjustable design, which allows testing the turbine at various operating scenarios. The turbine is capable of securing 2 or 4 blades at preset pitch angles between ±10°. The Plexiglas endplates enable flow visualization testing inside the actuating disk of the turbine. Unlike the conventional generator and friction systems, the gear motor driving mechanism operates the turbine from very low tip speed ratios (TSR) to freewheeling. A torque transducer and encoder record the torque and azimuth angle at a frequency rate of 683 Hz.

The overall performance of the turbine in uniform inflow is investigated. To obtain the optimum arrangement for the non-uniform inflow testing, the turbine is tested at several configurations and operating conditions. The 2 and 4 bladed configurations are tested at preset pitch angles between -5° and +10°. The flow Reynolds number and the water level are two operating conditions at which the turbine is tested for sensitivity study. The Reynolds number of the flow is controlled by the free stream speed in the test section of the water tunnel.

Non-uniform inflows are imposed on the turbine. Upstream cylinders create wake and large eddies behind them that simulate the non-uniformity in the inflow. These cylinders of four different sizes model non-uniform inflow with different strengths. The damping effect is investigated by employing cylinders at five longitudinal locations. For one size of the cylinder, the effect of both longitudinal and lateral locations on the performance diagram of the turbine is investigated. The frequency analysis is conducted on the power coefficient data to quantify the effect of upstream eddies on the power of the turbine in the frequency domain. The frequency domain quantifies the quality of the power output signal and helps to improve the lifetime estimation by better understanding of applying dynamic loads that cause fatigue.

1.5.3 ADV filtering code

A new filter is critically required for this research to allow using the ADV data measured in field measurements and in laboratory settings because of entrained air bubbles in both these applications. A filtering method developed to remove abnormal data points from the velocity dataset allows subsequent post processing of the data to achieve desired objectives and research contributions.

1.6 Contributions to the state of knowledge

1.6.1 Investigation of turbine-river interaction

For the first time, series of river velocity measurements are conducted upstream of an operating hydrokinetic turbine in the field. Results consist of velocity measurements upstream of an operating and stopped New Energy Corporation's 25-kW vertical hydrokinetic turbine connected to a heater unit dissipating the energy (resistive load only). A Nortek Vectrino AS ADV results provide a better understanding of how an operating turbine changes the flow pattern of the river, including length scales, turbulence intensity and mean flow speed. They can be used to scale laboratory experiments. The turbine-river interaction study offers information for fatigue lifetime of the turbine.

1.6.2 Develop a filtering method for ADV measurements in rivers

A new hybrid despiking method is introduced which has advantages over conventional methods such as the acceleration thresholding method and the phase-space thresholding method when using ADV in bubbly flow. Spikes due to air bubbles not only increase the standard deviation of the velocity, but also corrupt the autocorrelation and power spectra. As some of these spikes appear like velocity fluctuations, developing accurate despiking procedures is an important requirement during post-processing of ADV velocity measurements in bubbly flow applications. This despiking method considerably improves the quality of the ADV velocity dataset. ADV river velocity measurements near kinetic turbines demonstrate the proposed method. This method is applicable to other bubbly flow applications to characterize the liquid phase using ADV. Milk

is also introduced in the method to address insufficient data scattering during winter conditions with no algae in rivers.

1.6.3 Develop methods to study aerodynamic loading on VAHT

Design and implementation of an accurate dynamic load measurement system is accomplished for the water tunnel. This system consists of a custom torque transducer, position encoder, as well as a gear motor with a controller to manage the rotational speed of the turbine to a set value. Having employed a gear motor to drive turbine, it is feasible to measure torque at low rotational speeds. The instrumentation system is able to capture data with a sampling rate of 683 Hz, which is much higher than the rotational frequency of the turbine. Therefore, the system not only measures the average torque of the turbine in rotation, but also it measures dynamics loads during rotation.

1.6.4 Study the free-surface effect

A comprehensive study of the free-surface effect on the power coefficient of the vertical hydrokinetic turbine is conducted. Vertical turbines in arrays of turbines experience a fixed blockage effect because of adjacent turbines and a variable free-surface effect due to water level changes above turbine blades if they are not secured to a floating device on the surface. For tidal applications, the water level above the turbine blades changes continuously throughout the day; for river applications, the water level changes on a seasonal basis. Due to the costly process of deployment of hydrokinetic turbines in deep waters, some turbines operate near free-surface areas. The small-scale model turbine is tested at various water levels to study the free-surface effect. To classify the free-surface effect, a non-dimensional clearance height parameter is introduced. To assess the

water separation during the time that a part of the blade operates above the water surface, a high-speed camera is used to capture the separation phases in detail. There is no experimental investigation reported in the literature on the free-surface effect and water separation on the blade in a semi-submerged condition.

1.6.5 Expand the experimental measurement database

Testing performed on a VAHT at various Reynolds numbers expands the current experimental measurement database for aerodynamic loading and wake behavior. Specifically, at very low blade speed ratios where dynamic stall effects are predominant. The effect of the solidity and preset pitch angle on the prevalence of dynamic stall is also investigated by testing several different blade settings.

1.6.6 Improve the fundamental understanding of VAHT farms

Testing performed on a small-scale VAHT provides a better understanding of the fundamental operational behavior of VAHT in a hydrokinetic farm since during the testing in a water tunnel VAHT is subjected to both blockage and free-surface effects. Operational behavior of the turbine measured at a rate of 683 Hz improves the resolution of the dynamic loads applied on a VAHT through one rotation. In particular, the effects of the following aspects on turbine performance are investigated at high-resolution measurement:

- Reynolds number
- Solidity
- Free-surface effect
- Preset pitch angle

- Non-uniform inflow

1.6.7 Assessment of non-uniform inflow condition

The VAHT scale model is tested in several non-uniform inflow conditions and performance results are summarized based on the size and intensity of the upstream vortices in both longitudinal and lateral directions. The operating condition in rivers or channels can be corresponded by a proper size of the cylinder at a relevant distance from the VAHT. High frequency measurements enable the investigation of average and instantaneous power output for various eddy sizes. The average power represents the efficiency of the turbine while the instantaneous power indicates the quality of the power output.

1.7 Thesis outline

This thesis consists of seven chapters: introduction, literature review and theory, field measurements, experimental test facility and instrumentation, sensitivity study, non-uniform flow measurements, and conclusions and recommendations. Chapter 2 covers literature review and theory, which includes the theory of VAHTs, static and dynamic stall definitions, numerical approaches toward VAHT aerodynamics and their weaknesses, previous reports and studies on non-uniform inflow condition. Chapter 3 reports new in-situ measurement results of the velocity upstream of an operating VAHT. This chapter also presents the measurement and data reduction methods employed for these tests. Chapter 4 outlines the scale VAHT model, test facility, and instrumentation employed in this part of the research. The focus in Chapter 5 is on the sensitivity analysis including preset pitch angle, solidity, free-surface effect, Reynolds number and

how they influence the operating behavior of the VAHT in a uniform flow. Chapter 6 describes the experimental results of the VAHT operating in a non-uniform inflow. The final chapter concludes the achievements of the research and provides recommendations for future research.

1.8 Publications

Published materials from this research are shown below. In addition, two journal papers are near completion.

Peered reviewed journal papers

[1]. Birjandi A. H., Bibeau E. L., Chatoorgoon V., Kumar A., "Power measurement of hydrokinetic turbines with free-surface and blockage effects," Applied Energy (under review).

[2]. Birjandi A. H., Woods J., Bibeau E. L., "Investigation of macro-turbulent flow structures interaction with a vertical hydrokinetic," Renewable Energy, vol. 48, pp. 183-192, 2012.

[3]. Birjandi A. H., Bibeau E. L., "Improvement of acoustic Doppler velocimetry in bubbly flow measurements as applied to river characterization for kinetic turbines," International Journal of Multiphase Flow, vol. 36(8), pp. 919-929, 2011.

Peered reviewed technical reports

[1]. Birjandi A. H., Gaden D., Shahsavarifard M., Bibeau E., "Scaling-up, hydrodynamic similarity laws, and guidelines to design hydrokinetic turbines for vertical hydrokinetic turbines," NRCan, Ottawa, Technical Report, 2012.

[2]. Birjandi, A.H., "Vertical kinetic turbines operation at low tip speed ratios," New Energy Company, Calgary, Technical Report, 2009.

Peered reviewed conference papers

[1]. Birjandi A. H., Bibeau E. L., Huang J., "On the scaling-up, hydrodynamic similarity laws of designing vertical hydrokinetic," Asian Wave and Tidal Energy Conference, 2012.

[2]. Birjandi A. H., Bibeau E. L., Chatoorgoon V., "How turbulence large-scales affect the power output quality of vertical hydrokinetic turbines," Asian Wave and Tidal Energy Conference, 2012.

[3]. Birjandi A. H., Bibeau E. L., Chatoorgoon V., "Impact of preset pitch angle on the power coefficient for conditions representative of vertical hydrokinetic turbine arrays," Proceedings of The Canadian Society for Mechanical Engineering (CSME) International Congress, 2012.

[4]. Birjandi A. H., Woods J., Bibeau E. L., "High frequency velocity measurement upstream of a 25 kw vertical river kinetic turbine," International Conference Energy and Meteorology (ICEM), Gold Coast, Australia, 2011.

[5]. Birjandi A. H., Bibeau E. L., "Reynolds effects on the freewheeling behavior of a high solidity vertical river kinetic turbine," ASME International Mechanical Engineering Congress and Exposition, Vancouver, British Colombia, Canada, 2010.

[6]. Birjandi A. H., Bibeau E. L., "Bubble effects on the acoustic Doppler velocimeter (ADV) measurements," Proceedings of the ASME Fluids Engineering Division Summer Conference, Vail, Colorado, United States, vol. 2, pp. 27-32, 2009.

[7]. Saremi A., Birjandi A. H., Wang G. G., Elmekkawiy T., Bibeau E. L., "Enhanced multiagent normal sampling technique for global optimization," Proceedings of the ASME International Design Engineering Technical Conferences and Computers and Information in Engineering Conference, New York City, NY, United states, vol. 1, pp. 532-542, 2009.

Posters

[1]. Birjandi A. H., Bibeau E. L., Chatoorgoon V., "The efficiency of a vertical kinetic turbine at variable tide levels," International Conference Energy and Meteorology (ICEM), Gold Coast, Australia, 2011.

[2]. Birjandi A. H.,Woods J., Shahsavarifard M., Bibeau E. L., Molinski, T., "Kinetic turbine research, demonstration and development in Manitoba rivers," CSBE /SCGAB Annual General Meeting and Technical Conference, Winnipeg, Canada, 2011.

[3]. Birjandi, A. H., "The double stall phenomenon on contaminated wind turbines," PHEV Conference, Winnipeg, Canada, 2007.

Chapter 2

Literature review and theory

The theory and previous experimental studies reported in the literature are reviewed in this chapter. Understanding the theory helps to explain the physical phenomena occurring in the field and in laboratory tests. Theory may not explain the behavior of the VAT in some areas due to the high level of complexity. Therefore, the experimental studies from the literature attempt to fill many of gaps in those areas. The focus of the wide range of previous experimental studies is on vertical wind turbines; hydrokinetic VAHT literature remains limited to review. However, due to the similarity laws, results obtained for wind turbines are valid for comparison with the behavior of a turbine in water. Moreover, literature documenting the impact of non-uniform flow on any vertical turbines remains limited for all applications.

The unsteady aerodynamics and dynamic stall are the main theoretical concepts involved in the study of VATs. Due to the nature of the VAT, blades operate in an unsteady condition and experience dynamic loads during their rotation. The relative speed and angle of attack of the blade oscillate continuously with the rotational frequency of the turbine. Additionally, while the angle of attack of the blade exceeds the static stall angle of attack, which occurs at low tip speed ratios, dynamic stall is a common phenomenon for the blade. Blades on the downstream

pass interact with the wake generated on upstream pass; therefore, the level of unsteady forces is higher on the downstream pass. The non-uniformity in the incoming flow changes the relative velocity pattern of the blades in the upstream pass at a frequency higher than the rotational frequency of the blades. The unsteady incoming flow condition for the upstream pass directly affects the quality of the output power of the turbine, as the majority of the net torque is created in this pass.

The literature review presents the basic dynamic and aerodynamic theory of vertical turbines in Section 2.1. Parameters that may have influence on the performance of a VAT are discussed in Section 2.2 based on original work performed for NRCAN recently completed. Section 2.3 explores strength and weakness of the available numerical models developed to study VATs. A comprehensive literature review on effects of turbulent and non-uniform incoming flow conditions on the behavior of VATs, including wind turbines, is conducted in Section 2.4. Finally, in Section 2.5 the scaling similarity laws for the performance of VATs are discussed to expand the laboratory test results for the real size turbine in the field.

2.1 Dynamics and aerodynamics of the VAT

Unlike horizontal turbines, whose blades operate in a steady condition, the dynamic nature of vertical turbines subjects the blades to unsteady aerodynamics. The steady aerodynamic condition is unable to describe the dynamic forces acting on the VAT's blades. In this section, the dynamics and aerodynamics of vertical turbines are discussed.

2.1.1 Blade angle of attack and relative velocity

The angle between the relative velocity, U_{rel} , and the blade chord line is defined as the blade angle of attack, α, as shown in Figure 2.1. Blades in rotating vertical turbines are subject to an oscillating angle of attack. Assuming there is no loss in fluid momentum through the actuating disk of the turbine, the local angle of attack of the airfoil can be defined as:

$$\alpha = \tan^{-1}\left[\frac{\sin(\theta)}{\lambda + \cos(\theta)}\right] - \alpha_p \,, \qquad 2.1$$

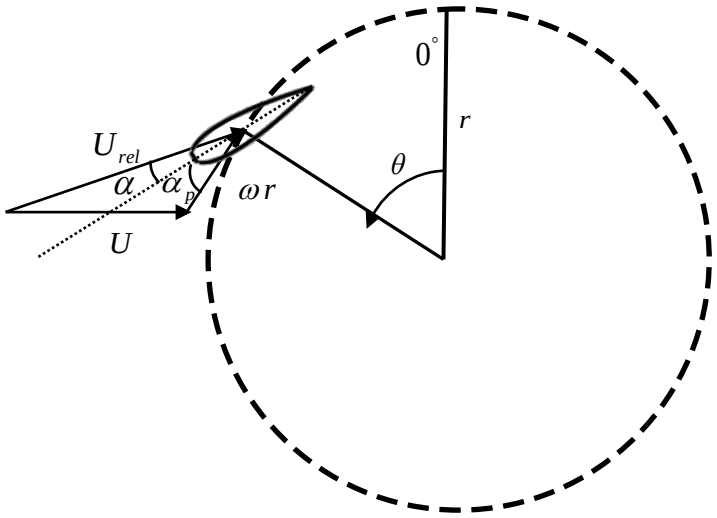

Figure 2.1: Schematic view of the angle of attack for a vertical turbine

where $\lambda = \omega r / U$, and is known as the blade speed ratio or tip speed ratio, θ is the azimuth angle of the blade, and α_p is the preset pitch angle of the blade. A positive value of α_p is defined to cause the airfoil to toe-out, as seen in Figure 2.1. Blades on the upstream pass extract the momentum and decelerate the flow. On the downstream portion of the rotation ($180° < \theta < 360°$) λ is much higher than the tip speed ratio for upstream blades. Therefore, Equation 2.1 gives a fair

estimate of the blade angle of attack only on the upstream portion of the rotation. By setting the derivative of Equation 2.1 to zero, the maximum angle of attack in a rotation is found to be:

$$\alpha_{\max} = \tan^{-1}\left(\frac{1}{\sqrt{\lambda^2 - 1}}\right). \qquad 2.2$$

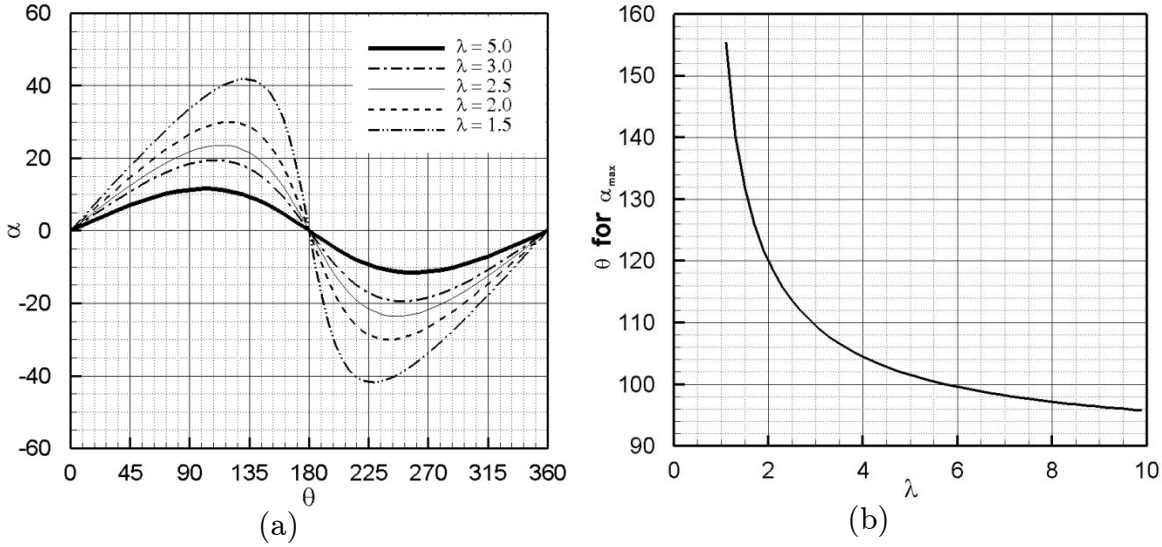

Figure 2.2: For a vertical turbine blade (a) angle of attack as a function of the tip speed ratio and azimuth angle, and (b) azimuth angle at which the maximum angle of attack occurs for a given tip speed ratio

The maximum angle of attack in a rotation occurs when the azimuth angle of the blade is:

$$\theta_{\alpha_{\max}} = \cos^{-1}(-\frac{1}{\lambda}). \quad 2.3$$

Figure 2.2 (a) shows the variation of the angle of attack as a function of the tip speed ratio and Figure 2.2 (b) shows the azimuth angle at which the maximum angle of attack occurs. Although the rotational speed and the mean flow speed are constant, the relative speed varies through one rotation due to the changing angle between the tangential speed of the blade and the flow velocity vector. Figure 2.3 shows the relative velocity of the blade, U_{rel}, after a rotation of θ°. According to the law of cosines U_{rel} is:

$$U_{rel} = \sqrt{U^2 + \omega^2 r^2 + 2U\omega r\cos(\theta)}, \quad 2.4$$

where U is the free stream velocity, ω is the rotational velocity of the turbine, and r is the radius of the turbine. By employing the definitions of λ, blade relative Reynolds number, $\mathrm{Re}_{rel} = \rho U_{rel} c/\mu$, and the free stream Reynolds number, $\mathrm{Re} = \rho Uc/\mu$, the dimensionless form of Equation 2.4 is:

$$\mathrm{Re}_{rel} = \mathrm{Re}\sqrt{1 + 2\lambda\cos(\theta) + \lambda^2}. \quad 2.5$$

In these definitions ρ represents the density of the fluid, c is the chord length of the blade, and μ is the dynamic viscosity of the fluid. Figure 2.4 shows the blade relative Reynolds number normalized by the free stream Reynolds number for various tip speed ratios, once again based on the assumption that there is no loss in fluid momentum through the turbine. The difference between the normalized maximum relative Reynolds number and minimum relative Reynolds number is always two units; however, the ratio between the minimum and maximum normalized relative Reynolds number drops from 0.67 at $\lambda = 5$ to 0.20 for $\lambda = 1.5$. The relative Reynolds number deviation about the mean value at high tip speed ratios ($\lambda > 5$), is limited to approximately ±20%. At low tip speed ratios ($\lambda \leq 1.5$), relative Reynolds number deviation increases to more than ±0.67%. This large fluctuation has an impact on both the nature and magnitude of the loading on the blades, and thus the overall performance and output of the turbine. The next section provides more detail on the relation between the forces acting on the vertical turbine blades and aerodynamic parameters of the blade, profile shape, α and Re_{rel}.

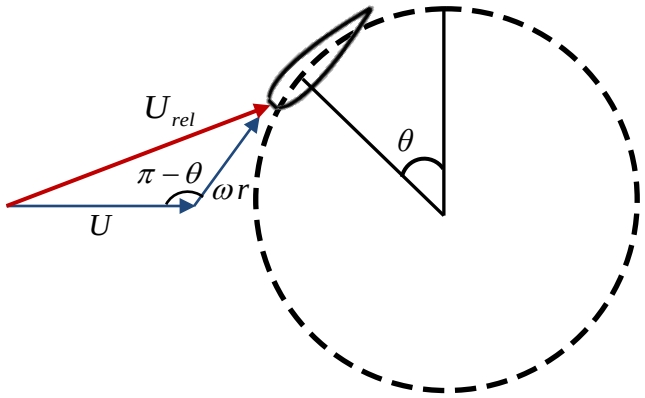

Figure 2.3: Relative angle between the rotational speed and the flow speed after θ° rotation

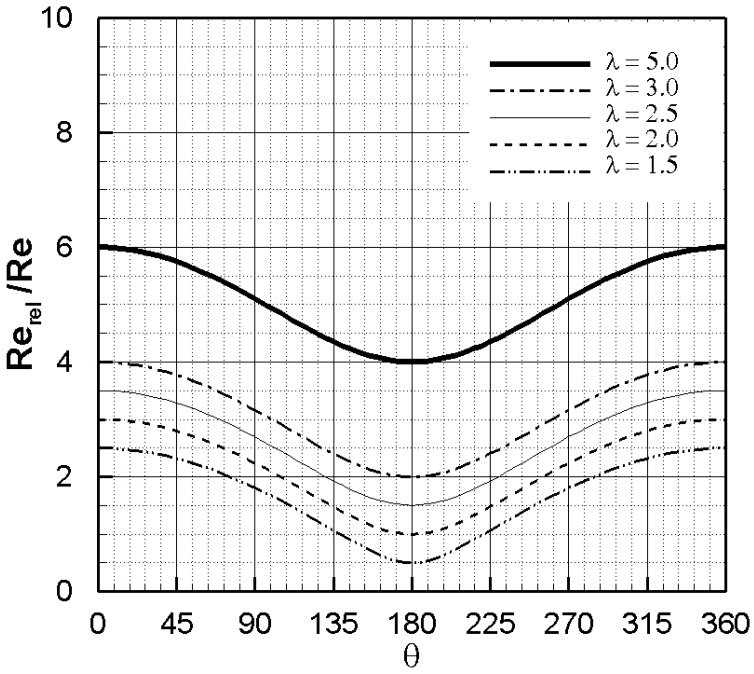

Figure 2.4: Normalized relative Reynolds number

2.1.2 Acting forces

In the blade reference coordinate system, the net force acting on the blades can be divided into two main components: the drag force, F_D, acting in the U_{rel} direction and the lift force, F_L, acting perpendicular to the U_{rel}, as shown in Figure 2.5. The dimensionless lift and drag coefficients per unit span of a blade with the chord length of c are defined as:

$$C_L = \frac{F_L}{0.5\rho U^2 c}, \tag{2.6}$$

$$C_D = \frac{F_D}{0.5\rho U^2 c}. \tag{2.7}$$

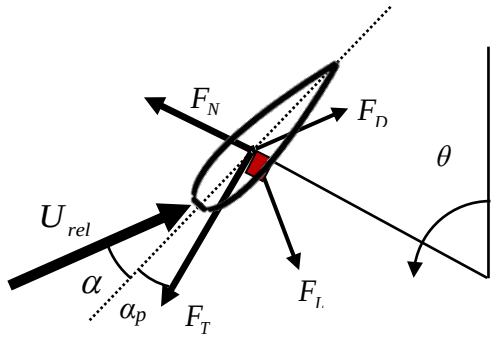

Figure 2.5: Schematic view of forces acting on a blade at the aerodynamic centre of the blade

The lift and drag coefficients are functions of the blade angle of attack, profile shape, and the relative Reynolds number. For a symmetric airfoil, like NACA-0021, the lift coefficient is zero at $\alpha = 0$; however, the drag coefficient has a non-zero value. The lift coefficient increases almost linearly with the angle of attack before the stall, at which point the flow separates from the low pressure surface, or suction surface, of the airfoil. The separation of the flow increases the pressure on the suction surface of the airfoil while the pressure distribution on the high pressure surface is relatively unaffected, resulting in a significant drop in the lift coefficient, accompanied by a sharp rise in the drag coefficient, as shown in Figure 2.6. Compared to low Reynolds number flows, high Reynolds number flows postpone the stall due to their high energy content, which delays separation and increases the maximum lift coefficient, as shown in Figure 2.7. The lift coefficient drop in the post stall region is smoother in the high Reynolds number flows.

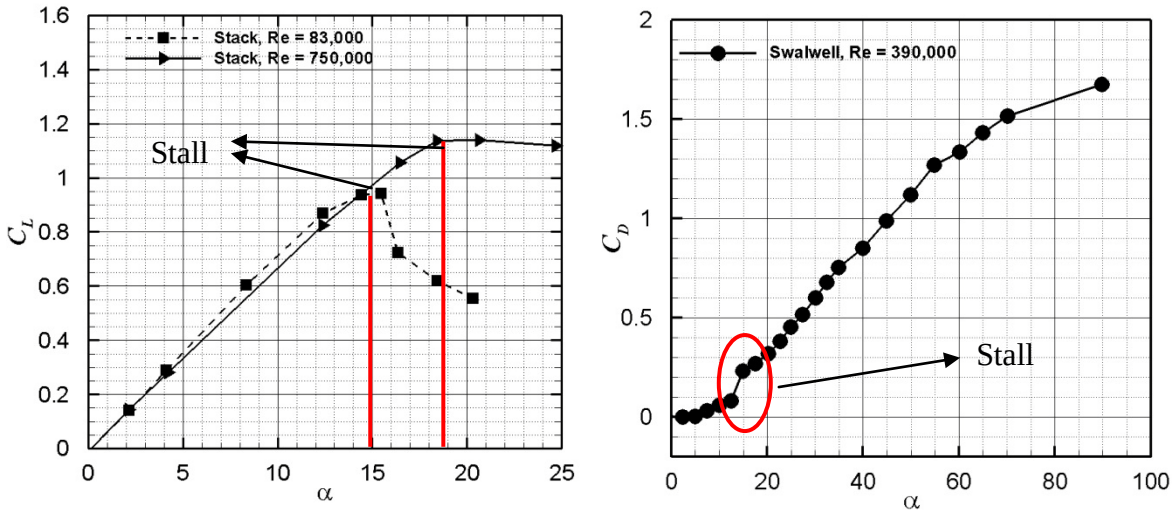

(a) (b)

Figure 2.6: Effect of stall on (a) NACA-0021 lift coefficient, adapted from [19], and (b) NACA-0021 pressure drag coefficient, adapted from [20]

In the turbine coordinate system the force tangent to the rotational path, F_T, generates torque about the rotational center of the turbine and consequently it is the primarily force in power production. The normal force, F_N, however, generates no power; instead this force stimulates the vibration modes of the turbine. The dimensionless tangential and normal forces of individual blade acting on a vertical turbine can be defined as functions of blade lift and drag coefficients as follow:

$$C_T = \frac{F_T}{0.5\rho U^2 c} = C_L \sin(\alpha + \alpha_p) - C_D \cos(\alpha + \alpha_p), \quad 2.8$$

$$C_N = \frac{F_N}{0.5\rho U^2 c} = -C_D \sin(\alpha + \alpha_p) - C_L \cos(\alpha + \alpha_p). \quad 2.9$$

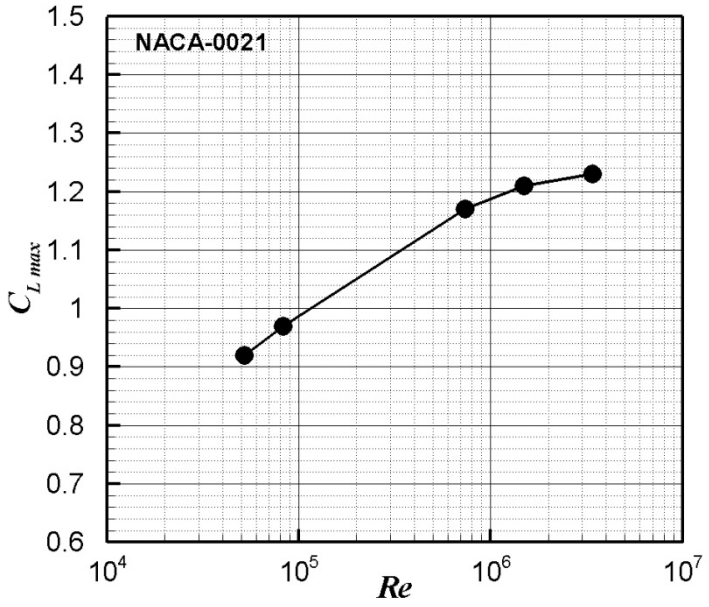

Figure 2.7: Effect of Reynolds number on maximum lift coefficient, adapted from [21]

To obtain the mechanical net torque, T, of a vertical turbine, the tangential forces of all blades is multiplied by the radius of the turbine, Equation 2.10. The power output, P, is equal to the net torque multiplied by the rotational speed of the turbine, Equation 2.11. The dimensionless power coefficient is defined as the ratio of the power output to the available power in the free stream passing through the area equivalent to the cross sectional area of the turbine, A_T, Equation 2.12. The power coefficient of a turbine represents the efficiency of the turbine as well.

$$T = r \times \sum F_T \,, \tag{2.10}$$

$$P = T \times \omega \,, \tag{2.11}$$

$$C_p = \frac{P}{0.5 \rho U^3 A_T} \,. \tag{2.12}$$

2.1.3 Dynamic blade

In a VAT, blades are subjected to a time-dependent angle of attack during a rotation.

$$\alpha(t) = \alpha_0 + \alpha_m \sin(\omega t), \tag{2.13}$$

where α_0 is the mean angle of attack, α_m is the amplitude of the oscillating angle of attack, and ω is the oscillation frequency. This dynamic motion is called pitch oscillation. The lift and the drag coefficients of the oscillating blade not only are affected by the Reynolds number but also they are a function of the mean angle of attack, amplitude of the oscillating angle of attack and the reduced frequency. The reduced frequency is a dimensionless parameter used to characterize the degree of unsteadiness of the blade. The reduced frequency, k, for a blade of chord c oscillating at angular frequency ω in a flow of velocity U is defined as:

$$k = \frac{c\omega}{2U}. \tag{2.14}$$

For $k = 0$, the flow is steady. The flow is considered quasi-steady for $0 < k < 0.05$ and for reduced frequencies higher than 0.05 the flow is considered unsteady.

The dynamic blade has two motions: upstroke and downstroke motions. The blade angle of attack increases with time during the upstroke motion. In this motion the blade experiences a downward induced velocity causing an effective angle of attack smaller than the geometric angle of attack, Figure 2.8 (a). The

induced velocity is upward in the downstroke motion which results an effective angle of attack greater than the geometric angle of attack, Figure 2.8 (b).

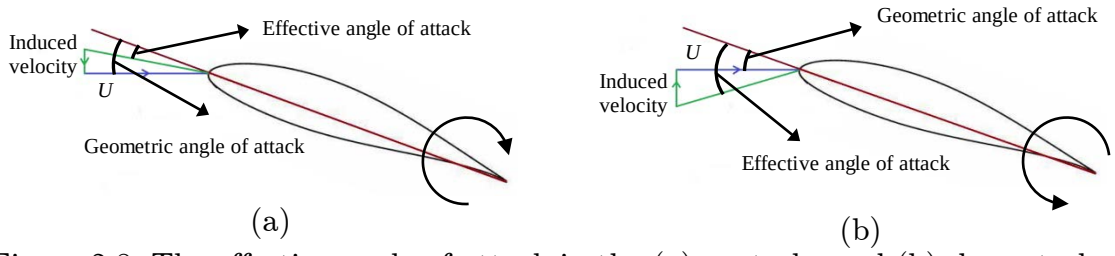

Figure 2.8: The effective angle of attack in the (a) upstroke and (b) downstroke motions

Figure 2.9 shows the dynamic and static lift coefficient of the blade with the profile section of NACA-63-617. The dynamic lift coefficient has a counterclockwise loop before the stall. The lift coefficient decreases in the downstroke motion as the angle of attack decreases and in the upstroke motion, the angle of attack increases. Hence, the lift coefficient increases also. For a specific angle of attack, the lift coefficient of the blade in the upstroke motion is less than the static lift coefficient while in the downstroke motion the lift coefficient is higher than the static lift coefficient. When the blade pitches down, the blade experiences an upward induced velocity in addition to the free stream velocity; therefore the effective angle of attack increases and consequently the lift coefficient increases too. In the upstroke motion, the blade experiences a downward induced velocity causing a reduction in the effective angle of attack. The effective angle of attack of the static blade is smaller than the downstroke effective angle of attack and higher that the upstroke angle of attack. Therefore, the static lift coefficient before the stall always passes through the dynamic lift coefficient loop.

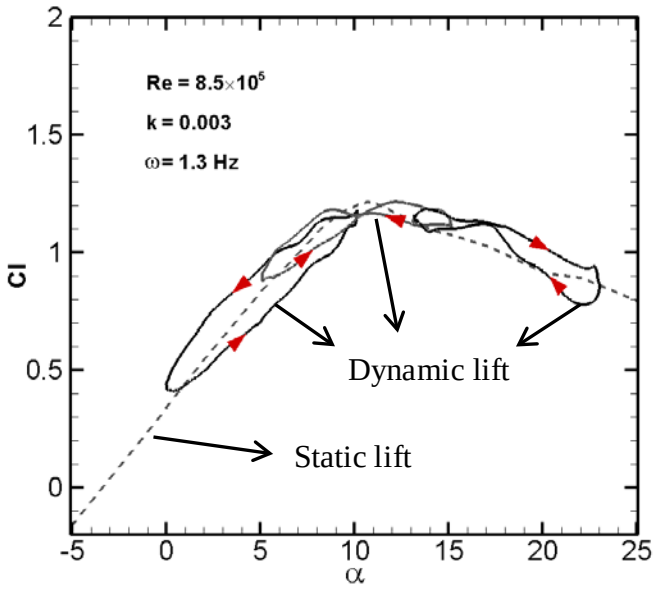

Figure 2.9: Dynamic and static lift coefficient of NACA-63-617

In the post stall region, the dynamic lift coefficient has a clockwise loop. The clockwise loop means that at a specific geometrical angle of attack, the upstroke lift coefficient is more than the downstroke one. In the post stall region, the upstroke motion creates a downward induced velocity and causes a reduction in the effective angle of attack. Therefore, the effective angle of attack is smaller than the geometric angle of attack. In the post stall region, the reduction in angle of attack causes the lift coefficient to rise. For the downstroke motion the situation is inverse. The effective angle of attack is greater than the geometric angle of attack; therefore, the lift coefficient decreases.

The width of the hysteresis in the dynamic lift coefficient loop is a function of the reduced frequency. Figure 2.10 shows the lift coefficient loop of the NACA-63-617 in the pre-stall region at various reduced frequencies. The behavior of the dynamic blade with small reduced frequency is close to the behavior of the static blade and the width of the hysteresis loop is small. At high reduced frequencies

the magnitude of the induced velocity increases; therefore the difference between the effective angle of attack in the upstroke and downstroke motions increases. The hysteresis loop expands as the induced velocity increases.

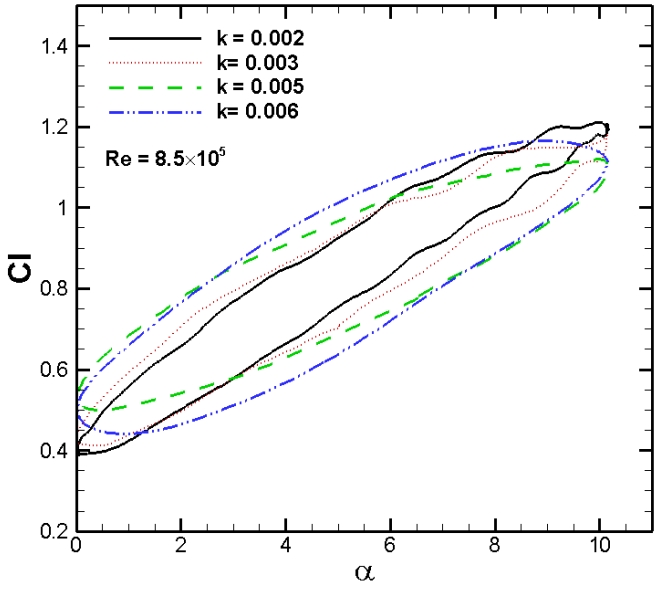

Figure 2.10: The effect of reduced frequency on the lift coefficient of NACA-63-617

2.1.3.1 Dynamic stall

The dynamic stall occurs on the blade if the angle of attack in a rotation exceeds the static stall angle [22]. Figure 2.11 shows the various stages of the dynamic stall process. First due to the reduction in adverse pressure gradients as the result of the kinematics of dynamic pitch motion, the onset of the separation is postponed and the blade exceeds the static stall angle. In stage 2 of the dynamic stall process, the flow separates and a vortex is formed near the leading edge area of the blade. The vortex convects downstream of the blade with a speed between

one third and one half of the free stream velocity [24,25], stage 3. The convection of the leading edge vortex on the suction surface adds to the lift coefficient of the blade. When the vortex leaves the trailing edge of the blade, the flow separates from the suction surface of the blade and it is accompanied by a sudden loss of lift, stage 4 [22,26].

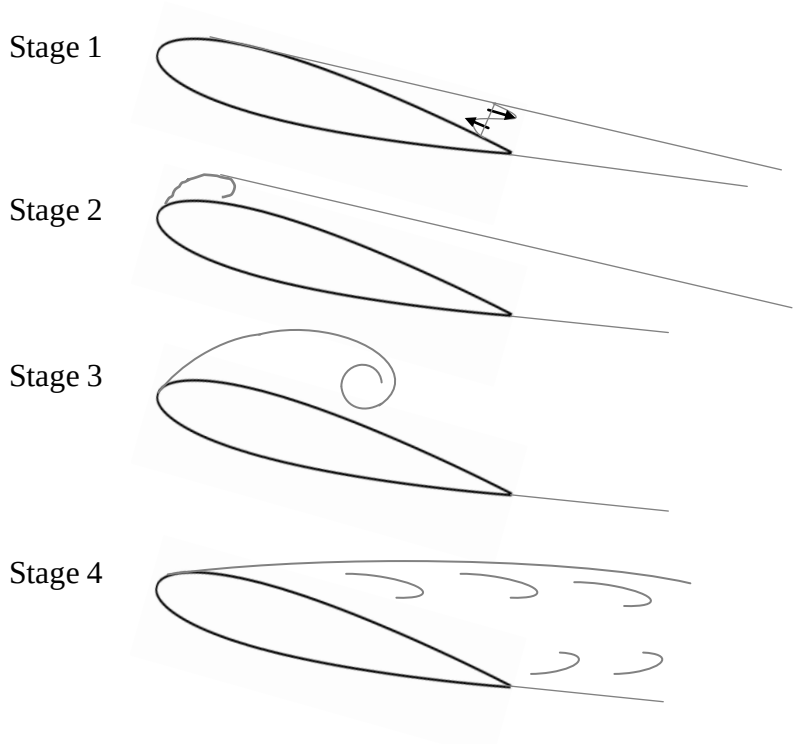

Figure 2.11: Dynamic stall stages

The lift and moment coefficient curves have a cross over point in the dynamic stall condition, which looks like a figure eight. The cross over point divides the curve into two loops. The left loop, small angles of attack, is counter-clockwise; while the right loop is clockwise. The right loop then grows in size when blade enters the deep stall regime. The clockwise moment loop reduces the torsional aerodynamic damping of the blade. If the clockwise loop grows larger than the counter-clockwise loop there is a possibility of aeroelastic problems including stall flutter [27].

2.2 Performance parameters of a VAT

This work was developed as part of an NRCAN study recently published [28]. The performance of a VAT is affected by design parameters and operating conditions. Table 2.1 and Table 2.2 summarize the design and operating parameters respectively. The research proposes six design parameters and six operating conditions that directly influence the performance of a VAT for hydro applications. Some of these parameters are dimensionless while the rest have dimensions. Dimensionless parameters are introduced to describe the performance of the VAT irrespective to the size of the turbine.

Table 2.1: Design parameters

#	Parameter name	Symbol	Dimension
1	Chord length	c	m
2	Radius of the turbine	r	m
3	Span of the blades	L	m
4	Number of blades	N	-
5	Preset pitch angle	α_p	-
6	Profile shape	-	-

Table 2.2: Operating conditions

#	Parameter name	Symbol	Dimension
1	Free stream speed	U	m/s
2	Rotational speed	ω	read/s
3	Fluid viscosity	`	kg/m.s
4	Fluid density	ρ	kg/m^3
5	Turbulence	-	-
6	Clearance coefficient	C_h	-

2.2.1 Dimensionless parameters

Dimensional analysis reduces the number of experimental variables by introducing dimensionless parameters. It also can be used to find universal similarity laws between the small-scale VAT turbine designs and large, utility-scale, turbine designs. Table 2.3 has listed possible dimensionless parameters affecting the performance of the VAT. The number of dimensionless parameters is equal to the number of performance parameters; however, a closer inspection of Table 2.3 shows that some dimensionless parameters are a combination of other dimensionless parameters; such as the blade Reynolds number, which is a combination of the free stream Reynolds number and the solidity. Some of the dimensionless parameters are design parameters, such as solidity and aspect ratio, some represent the operating conditions, such as turbulence and Reynolds number, and the rest are dependent parameters, which are functions of other parameters.

Table 2.3: Dimensionless parameters for scaling similarity law

#	Parameter name	Symbol	Definition	Type
1	Solidity	σ	$\frac{Nc}{2r}$	Design
2	Aspect ratio	AR	$\frac{L}{2r}$	Design
3	Tip speed ratio	λ	$\frac{\omega r}{U}$	Design
4	Preset pitch angle	α_p	-	Design
5	Profile shape	-	-	Design
6	Supporting arms profile shape	-	-	Design
7	Blade Reynolds number	Re	$\frac{\rho cU}{\mu}$	Operating
8	Clearance coefficient	C_h	$\frac{H^*}{L}$	Operating
9	Turbulence	-	-	Operating
10	Reduced frequency	k	$\frac{\pi c \omega}{U} = \frac{\pi}{N} \times \sigma \times \lambda$	Dependent
11	Turbine Reynolds number	$\mathrm{Re_D}$	$\frac{2\rho rU}{\mu} = 2N \times \frac{\mathrm{Re}}{\sigma}$	Dependent
12	Blade relative Reynolds number	Re_{rel}	$\mathrm{Re} \times \lambda$	Dependent

***** H is the height of the water above the turbine

2.3 Numerical models

2.3.1 Blade element momentum model

This model simulates the blades with their cross sectional airfoils and expresses the torque acting on the airfoils as a function of the lift coefficient, drag coefficient and angle of attack. The first application of momentum theory to model VATs is attributed to Templin [29]. He used Bernoulli's equation to obtain the velocity within a single stream tube encompassing the entire turbine. Wilson and Lissaman [30] and after them Strickland [31] extended Templin's single stream tube into multiple stream tubes. In this model, the actuator disk of the turbine is divided into a series of adjacent and independent parallel stream tubes with different inflow velocities. Bernoulli's equation is carried out separately for each stream tube.

Because of the momentum extraction on the upstream pass, the flow velocity reduces for the downstream pass. Paraschivoiu in 1981 [32] introduced the double multiple stream tube model. In this model, the upstream and downstream-induced velocities are different as well, Figure 2.12. Upstream and downstream calculations are decoupled. The induced velocity in the upstream half of the rotation is obtained from Bernoulli's equation using the free stream velocity. For the second half of the rotation, downstream, the upstream-induced velocity is considered the free stream velocity in induced velocity calculations.

The blade element momentum model assumes homogenous, incompressible, and steady-state free stream conditions. The frictional drag, rotating wake and wake vortices are neglected. This model is invalid for high tip speed ratios and high

rotor solidities due to the simplifying assumptions applied to the momentum equations. Despite these disadvantages, the blade-element-momentum method is the fastest numerical method to obtain an estimate of the power output for VATs.

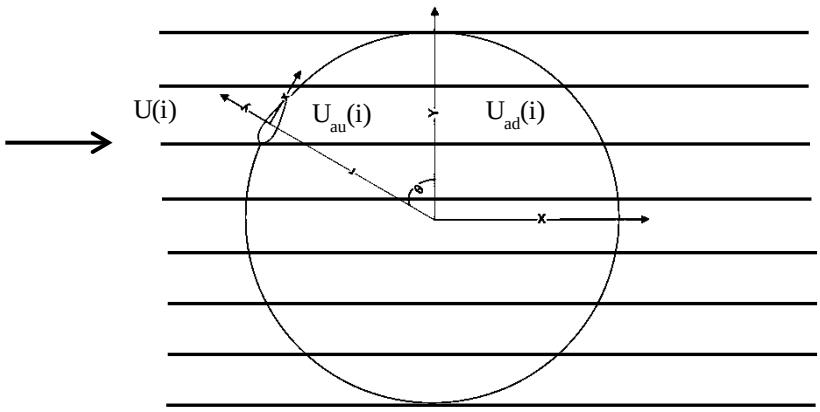

Figure 2.12: Double multiple stream tube model

2.3.2 Vortex model

Fanucci and Walter [33] developed a two-dimensional vortex method for straight bladed vertical turbine applications in 1976. Strickland [34] extended the method to a three-dimensional vortex method in 1981 to predict the performance and aerodynamic loads of the Troposkein turbines, and implemented it in the vortex method for Darrieus turbine (VDART) program. This model considers the stall effects and later Strickland included dynamic effects as well.

The vortex method uses the potential flow assumption to solve the velocity field around the turbine influenced by the vortices in the wake of the blades. The blade is modeled as a bound vortex or lifting-line along the span, with its associated trailing vortices. The strength of the vortex is calculated from experimental or numerical databases available for the airfoil. The vortex method

not only calculates the lift and drag forces of the blade during a rotation but also solves the velocity flow field around the turbine. Therefore, the effect of upstream wakes in the downstream path is considered. However, this method requires more computational time compared to the blade-element-momentum model, and furthermore, this method suffers from significant assumptions and simplifications such as small angle of attack, thin lifting surfaces and incompressible flow. The viscosity and dynamic behavior of the blade are neglected in this method as well as the rotational nature of the wake and turbulence effects.

2.3.3 Numerical solution of Navier-Stokes equations

Time-dependent solutions of the Navier-Stokes equations for high Reynolds-number turbulent flows in complex geometries, e.g., near VAT blades, are not feasible due to the high computational time. The Reynolds averaged Navier-Stokes (RANS) and large eddy simulation (LES) are two alternative methods improving the computational time by not simulating the small-scale turbulent fluctuations. Both methods introduce new unknown variables and turbulence models are needed to model these unknowns in order to achieve a closure for the unknowns. The accuracy of the turbulence model depends on the geometry and the operating conditions of the problem. Compared to RANS models, LES is more accurate; however, this model requires a significant amount of computational time. The most widely used turbulence RANS models are: Spalart-Allmaras, k-ε [35] and k-ω [36] models. The k-ε and k-ω are two-equation models that use two partial differential equations to model turbulence quantities. The k-ε model has proven to perform well for simple flow cases; it is well known to have poor behavior for complex swirling flows. Some of the situations where

the standard k-ε model fails are: bluff-body flows, 2-D separation, streamline curvature, swirl, buoyancy, adverse pressure gradients, turbulence-driven secondary motions, etc [37]. The accuracy of the k-ω model is higher compared to that of the k-ε model for swirling and separated flow.

Spalart-Allmaras is a simple one-equation model designed specifically for aerospace applications involving wall-bounded flows and adverse pressure gradients, such as those on the suction surface of the VAT blades.

2.4 Non-uniform inflow

2.4.1 Homogeneous turbulence for static blades

In laboratory testing, the turbulence intensity of the flow is increased by employing a screen upstream of the model. When the flow passes through the screen, small vortices generated by the screen increase the turbulence intensity of the flow. The size of the generated vortices is in the order of magnitude of the screen wires' diameter. This technique increases the turbulence intensity homogeneously in the entire flow. Compared to the low turbulence intensity flow, a high turbulence intensity flow postpones the stall phenomenon to higher angle of attacks and increases the maximum lift coefficient of the blade. This statement is true as long as the sizes of the vortices in the turbulent flow are much smaller than the chord length of the blade. Turbulence increases the energy content of the flow; therefore, the flow delays the separation in the adverse pressure gradient region of the blade. Figure 2.13 shows the wind tunnel testing results of the lift coefficient versus the angle of attack of the NACA-0021

airfoil with and without the upstream screen at the blade Reynolds numbers of 7.30×10^5 and 1.60×10^6 [38]. Results show an increase in the stall angle of attack and the maximum lift coefficient of the blade with the upstream screen.

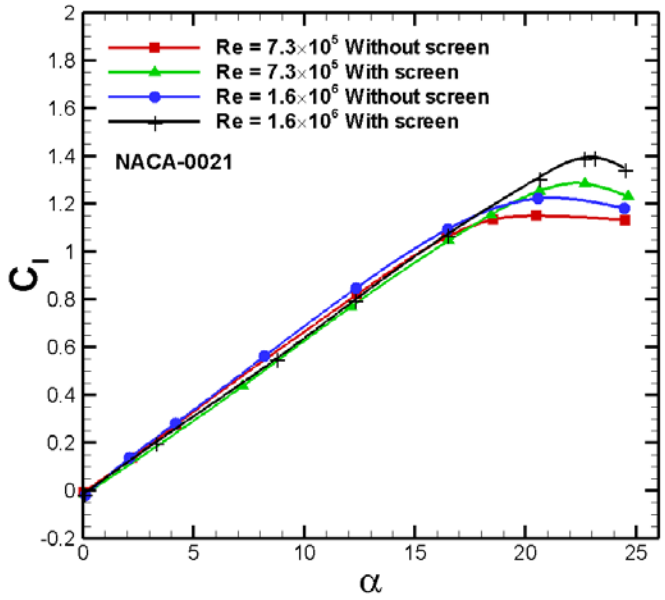

Figure 2.13: Effect of increased turbulence intensity on the lift diagram of the NACA-0021 airfoil [38]

As mentioned in the previous section, blades experience an oscillating angle of attack during a rotation in a VAT. The dynamic behavior of the blade is different from that of the static one and it is a function of the oscillation frequency, mean angle of attack and the amplitude of the oscillating angle of attack. The uniform turbulence in the upstream flow not only improves the static lift coefficient of the blade but also enhances the lift coefficient of the dynamic blade. The dynamic performance of a contaminated section of a horizontal wind turbine blade with the profile shape of NACA-63-617 is tested in the wind tunnel with and without the upstream screen. The geometry of the blade section and the experimental apparatus are described in Reference [39]. The upstream screen increases the turbulence intensity of the wind tunnel test

section from 0.1% to about 3%. Results show that the higher turbulence intensity increases the lift coefficient value at a specific angle of attack and postpones the dynamic stall. Figure 2.14 shows the dynamic lift coefficients of the contaminated blade section with and without the upstream screen at the blade Reynolds number of 8.5×10^5, oscillation frequency of 1.3 Hz, reduced frequency of 0.017, mean angle of attack of 10°, and 5° amplitude of the oscillating angle of attack.

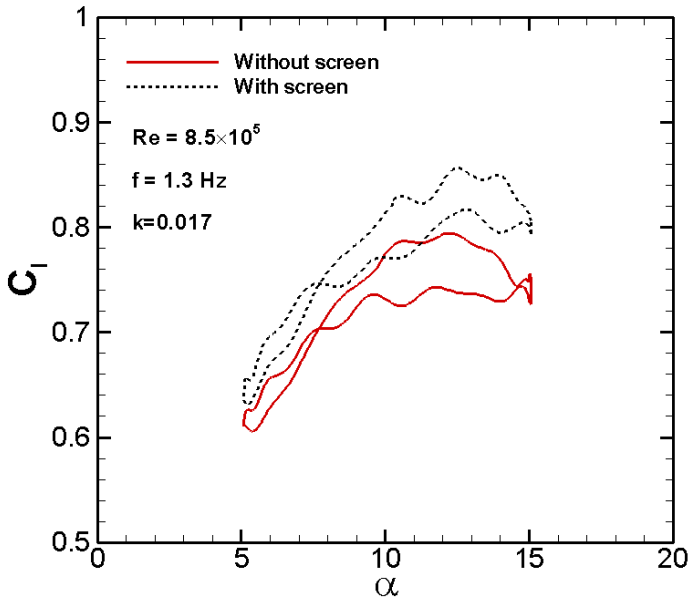

Figure 2.14: Effect of the turbulence intensity on the dynamic lift

2.4.2 Background

In February 1977 Sheldahl and Blackwell [40] tested a 5-meter diameter Troposkein Darrieus turbine in the free air condition at the Sandia Laboratories Wind Turbine Site. When they repeated the test for the 150 rpm at the same operating conditions in late July and August, they found that the maximum power coefficient decreases from 0.28 to 0.24, as shown in Figure 2.15. They investigated the quality of the wind for these two tests. The wind speed frequency distribution shows that for the first test, Test a, the distribution is much smoother than that of the second test, Test b, Figure 2.16. They concluded that the reduction in the power coefficient for the Test b is the result of the high wind speed fluctuations.

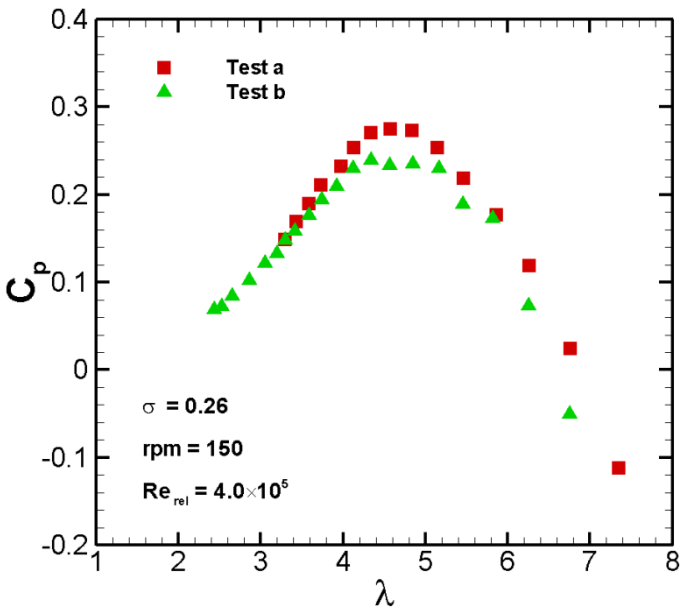

Figure 2.15: Power coefficient data of the 5-meter Troposkein turbine at 150 rpm for Test a and Test b [40]

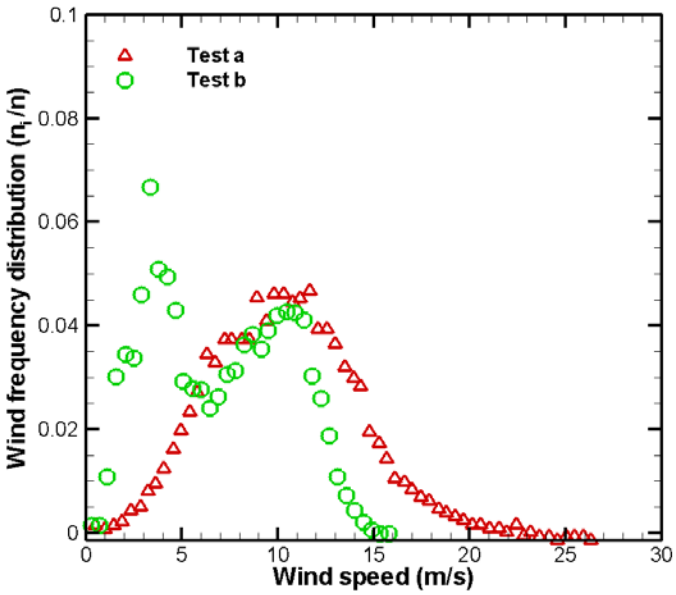

Figure 2.16: Wind frequency distribution for the Test a and Test b [40]

Sheldahl et al. [41] tested a 5-m diameter, 3-bladed Troposkein wind turbine with a NACA-0015 profile section in the field. They recorded the wind speed and the turbine torque simultaneously, Figure 2.17. They found that due to the nonlinear relationship between the wind speed and torque of the turbine it is impossible to assign a wind speed corresponding to a given torque measurement. The torque measurement not only is affected by the wind speed values but also by the wind speed fluctuations. Parts of the wind speed fluctuations are damped in the torque diagram due to the inertia of the turbine. However, due to the low frequency measurement method, this study suffers from a lack of information on the high frequency fluctuating loads acting on the blades.

In 1981, Sheldahl [42] compared the field and wind tunnel power coefficient results of a 2-m diameter Troposkein Darrieus turbine. He found that due to differences in test conditions between the wind tunnel and field, the rotational

speed of the turbine should be higher in the wind tunnel testing to obtain the same blade relative Reynolds number for wind tunnel and field-testing. He also tested the turbine in the field with the same rotational speed of the wind tunnel testing. With the same rotational speed, the blade relative Reynolds number at the field-testing is lower than that of the wind tunnel testing. For tip speed ratios greater than 5, field data shows improved performance over the wind tunnel data, Figure 2.18. During the tests, both wind tunnel and field, the rotational speed of the turbine was fixed at 400 rpm and 460 rpm respectively. Therefore, the higher tip speed ratios represent a low speed wind. Barthelmie et al. [43] measurements at Middelgrunden offshore wind farm show that the minimum turbulence intensity occurs at wind speeds between 8 and 12 m/s, at lower wind speeds turbulence intensity is higher. It can be concluded that the improved performance of the turbine operating in field at tip speed ratios greater than 5 is due to the higher turbulence intensity of the low speed wind.

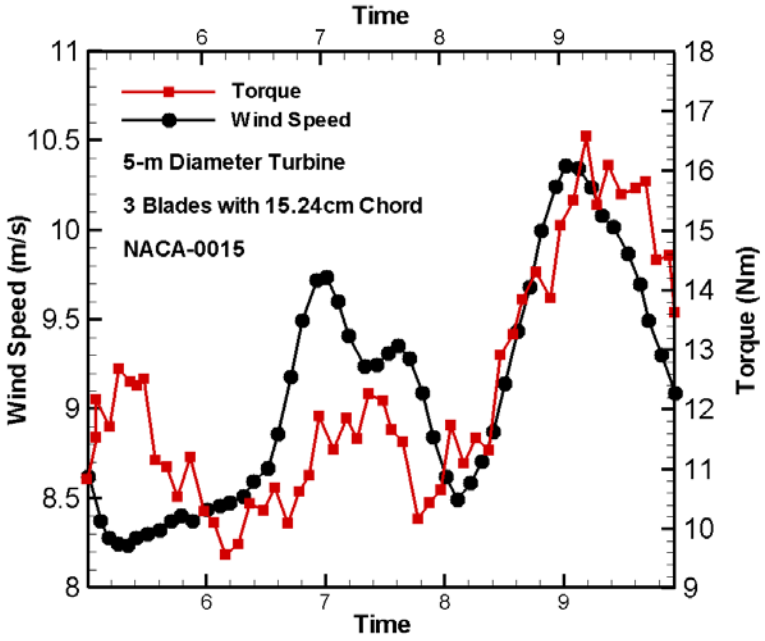

Figure 2.17: Site wind speed and the turbine torque [41]

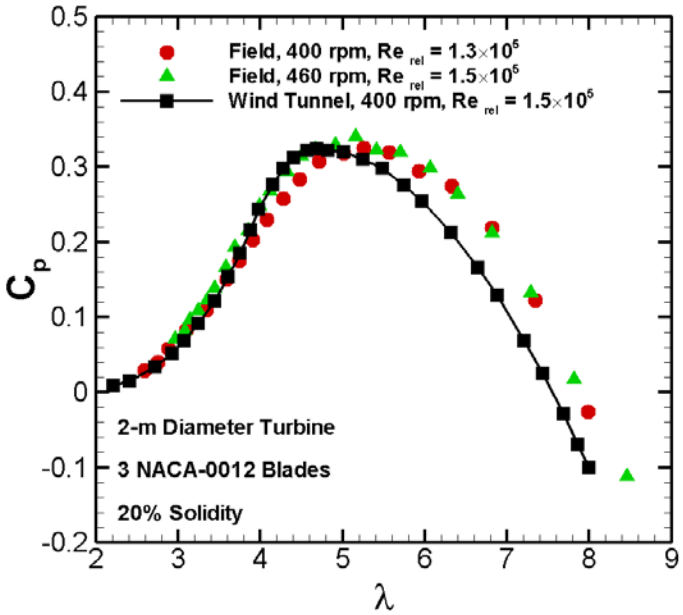

Figure 2.18: Power coefficient of a turbine tested in the field and wind tunnel [42]

2.4.3 Numerical models

The blade forces repeat exactly for each rotor revolution when a uniform flow is assumed. Therefore in the power spectral density diagram, the dominant frequencies are limited to integer multiplies of the turbine rotational speed. However, the aerodynamic loads due to a turbulent flow contain all frequencies, not only the per revolution frequencies. The power spectral density is a proper way to describe the stochastic loads on the blade while the relation between the incident flow and the blade forces is nonlinear. In 1984, Veers [44] employed the stochastic atmospheric turbulence model suggested by Frost et al. [45] to improve the results of the numerical model developed by Strickland, multiple streamtubes [46]. This method assumes a Gaussian random velocity distribution with the specified turbulence power spectral density at the upstream of the VAT. The results of this study show that the turbulent upstream conditions shift the blade loads to higher frequencies in the power spectral density diagram. The

high frequency loads are the results of the variation in blade angle of attack due to the upstream turbulence. Although turbulence slightly varies the blade angle of attack, the nonlinear relationship between angle of attack and blade load magnifies this effect, especially when the turbine operates at low tip speed ratio where dynamic stall is occurring. Mann [47,48] introduced an algorithm to simulate the homogeneous, neutrally stratified atmospheric boundary-layer turbulence for wind turbine applications. This method is a spectral tensor model and is capable of simulating two or three-dimensional flow fields. Compared to the Veers method, this algorithm simulates the atmospheric turbulence more accurately and is simple to work with, as fewer parameters are involved in the algorithm. The Mann method is widely employed in aero-elastic calculations.

2.4.4 Operation in wake

In kinetic turbine farms, not only is the quality of the free stream flow important, but also the quality of the flow in the wakes of upstream turbines plays a critical role for the power output of downstream turbines. Increasing the turbulence intensity of the free stream is the common method used by industry for compensating the wake effect. However, this method is unable to capture the effect of wake deficit and large shed eddies from upstream turbines.

Several investigations have been conducted on the shape, properties and the propagation of wakes downstream of kinetic turbines [43, 49-53]. Most of these investigations are limited to horizontal wind turbines. Barthelmie et al. [43] investigated the power loss due to the wakes in the Middelgrunden offshore wind farm. They found that on average the overall performance of the wind farm is 10% less than the efficiency of the individual turbine due to wakes. The

efficiency of the second turbine in a row of 20 turbines with 2.4 diameter spacing is only 20% of the efficiency of the first turbine while the row of turbines is aligned with the wind direction. The efficiency increases from the third and subsequent turbines. The wind speed in the wake is about 80% of the free stream speed and remains constant in the array.

Troldborg et al. [53] simulated the wake of a horizontal turbine operating in atmospheric turbulence and compared the results with the wake of the turbine in uniform inflow. They coupled the large eddy simulation solver developed by Michelsen [54,55] and Sorensen [56] with the actuator line method developed by Sorensen and Shen [57]. The turbulence was added to the simulation by Mann algorithm [47,48]. They found that the turbine operating in a uniform inflow has a stable wake approximately 5 rotor diameters downstream of the turbine. While in a turbulent inflow the wake of the turbine becomes unstable one rotor diameter downstream of the turbine. Therefore, the wake of the turbine has a smaller tail in a turbulent inflow and the wake recovers faster. It means that by considering a non-uniform inflow, the spacing between the turbines in a wind farm is much smaller than that obtained from a uniform inflow simulation.

Several numerical methods have been developed to simulate the wake effects. Followings are some of the popular methods: Riso National Laboratory [58,59], Uppsala University [60], Hassan [61], University of Oldenburg [62], Netherlands Research Foundation [63]. Rados et al. [51] compared the results of these methods against the wake data collected from the Vindeby turbine and found that almost all methods overestimate the wake effects behind the turbine. Close to the turbine, the results of the methods have the most inconsistency.

2.4.5 Flow around a VAT

Fujisawa and Shibuya [64] used the PIV measurement and dye injection technique in a wind tunnel testing to visualize the flow around a vertical axis wind turbine. They observed two pairs of counter-rotating vortices, developing in the wake of the blade in the upstream path. The first pair of the vortices forms between the azimuth angle of 45° and 90°; and the second pair forms between the azimuth angle of 90° and 135°. In the pair of counter-rotating vortices, the first vortex is the result of the flow separation from the leading edge of the blade due to the high angles of attack. The roll-up flow motion from the pressure side of the blade to the suction side through the trailing edge creates the second vortex pair. The second vortex pair rolls up and re-attaches the flow. These two vortex pairs are similar to vortices in the Von Karman vortex street.

Ferreira [65-69] conducted a comprehensive investigation on the dynamic stall and the wake pattern of vertical axis turbines. He investigated several turbulence models for the vertical axis wind turbine application and he found that the unsteady Reynolds-averaged Navier-Stokes (UNRANS) k-ε model is able to detect the single large leading edge vortex at $\theta = 90°$ to $\theta = 110°$; however, in the detached eddy simulation (DES) model, a hybrid method of URANS and large eddy simulation (LES), the vorticity is a distribution of smaller vortices [67]. By employing the DES model, Ferreira found that both normal and tangential forces contain frequencies higher than the frequency of rotation of the turbine, Figure 2.19. These high frequency loads are the result of the separation and re-attachment vortices convected over the blade suction side, Figure 2.20.

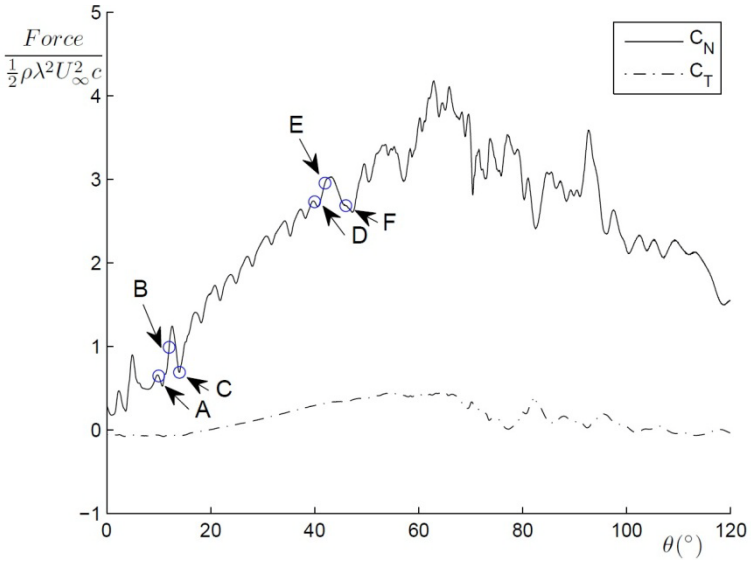

Figure 2.19: Non-dimensional forces acting on the blade between the azimuth angles of 0° and 120°. The azimuth angle is 10°, 12°, 14°, 40°, 42° and 46° for points A, B, C, D, E and F respectively [66]

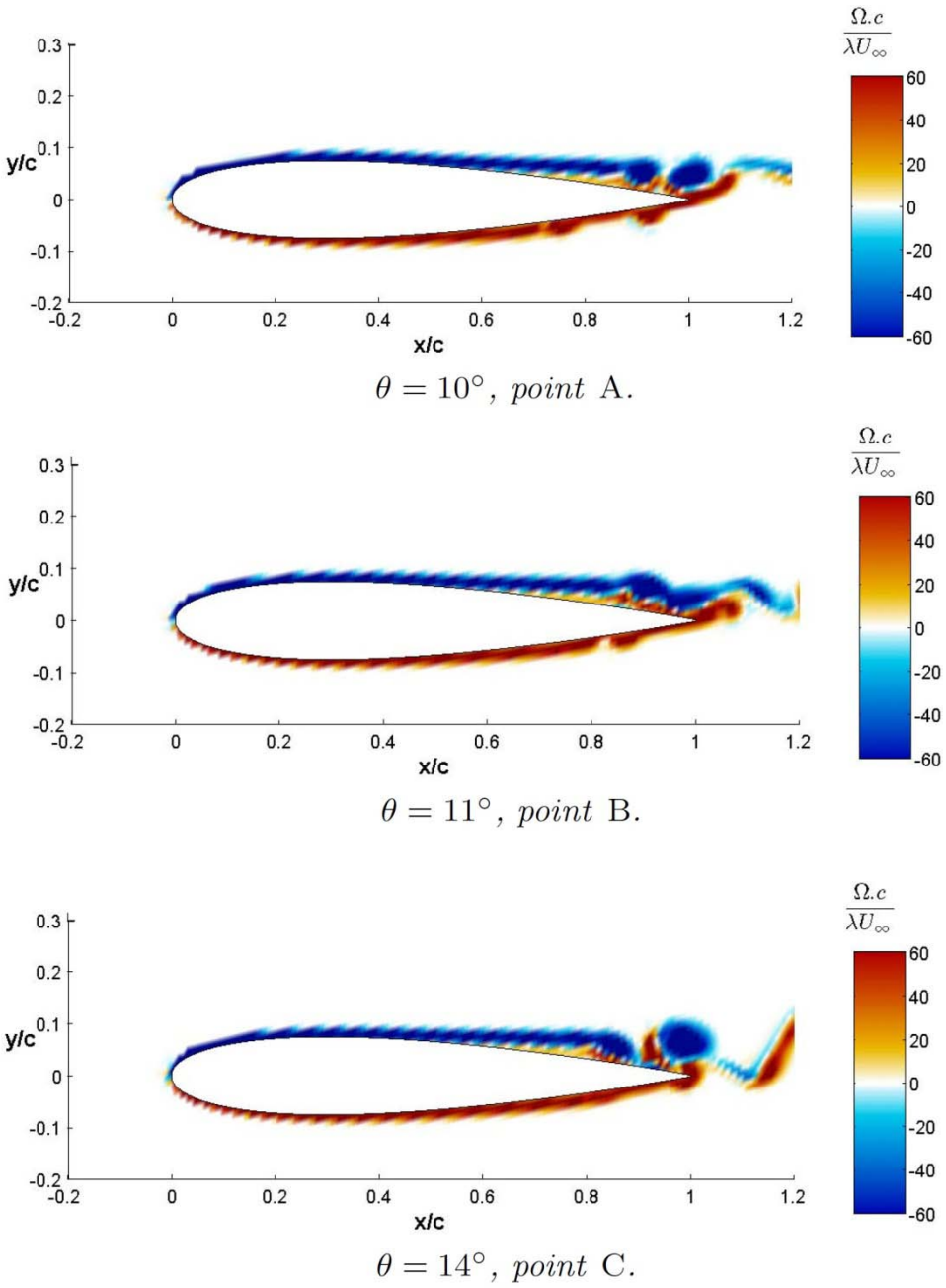

Figure 2.20: Non-dimensional vorticity around the blade section relative to Figure 2.19. The top side of the airfoil represents the suction/ inner side of the blade [66]

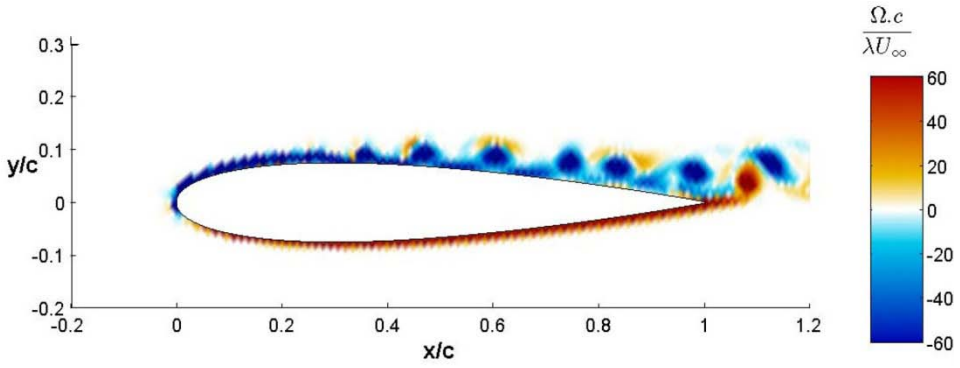

$\theta = 40°$, *point* D.

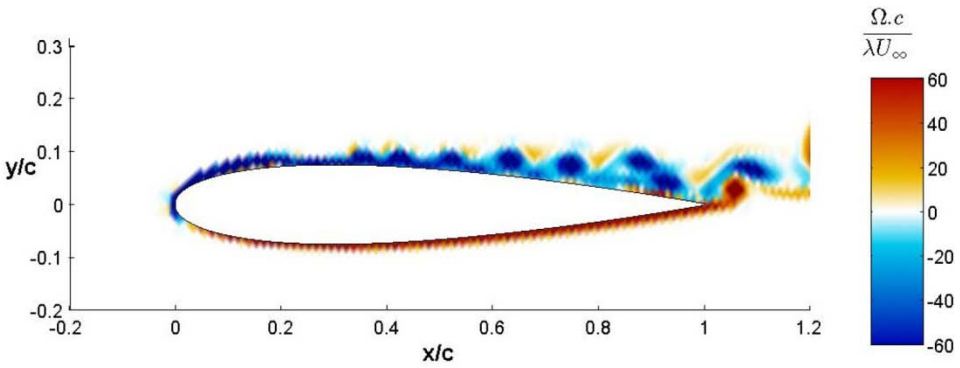

$\theta = 42°$, *point* E.

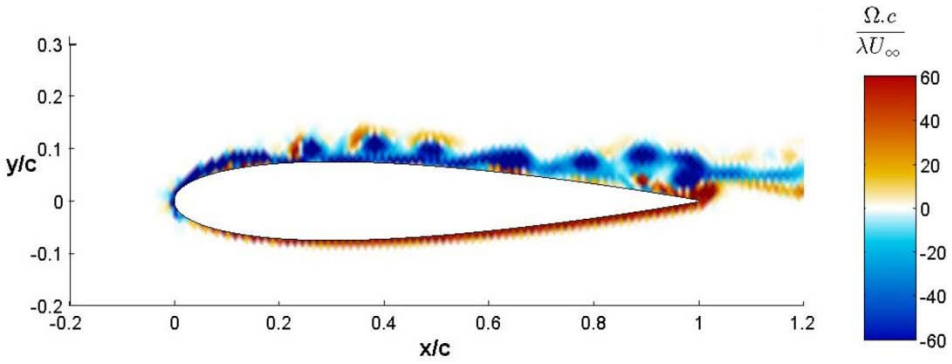

$\theta = 46°$, *point* F.

Figure 2.20 (cont.): Non-dimensional vorticity around the blade section relative to Figure 2.19. The top side of the airfoil represents the suction/ inner side of the blade [66]

2.4.6 River measurements

Measurements conducted by Birjandi et al. in the Winnipeg River at Pointe du Bois [70] show that the river flow contains large eddies with the order of

magnitude of the turbine's diameter. The operating turbine breaks these large eddies to smaller ones. However, the size of the small eddies are still comparable with the chord length of the blade. The comprehensive results of this study are presented in Chapter 3 of this thesis. Yokosi [71] measurements in the Uji River and the Sosui canal also show that the depth and width of the river determine the order of magnitude of the largest eddies. Sources of large-scale eddies in rivers are:

- rapid changes in the profile of riverbeds and banks,
- presence of large boulders and ice floes,
- man-made obstructions like a bridge pier or upstream turbines, and
- rapid river level changes leading to hydraulic jumps.

Areas around bridges are potential opportunities to install hydrokinetic turbines. There are several advantages to place kinetic turbines close to a bridge. Bridges are usually constructed in the narrowest part of a river, which has the maximum current velocity; therefore, the available kinetic power density increases, since the power is proportional to the cubic of the current velocity. In addition, the funneling effect imposed by the bridge piers increases the flow velocity near the bridges even more. Bridges are convenient for maintenance of the kinetic turbine and the power unit. Riverbed should be smooth and solid near the bridge piers to secure the piers from sliding. Solid riverbed is a proper place for anchoring the kinetic turbine unit while the smooth bed offers fairly uniform flow with a low velocity gradient in the current direction. Furthermore, the initial cost of the infrastructure needed for the river kinetic power unit installation is reduced considerably.

There is little information available in the literature about large-scale turbulence eddies interaction with vertical hydrokinetic turbines. These few literatures are limited to horizontal wind turbines. The National Renewable Energy Laboratory is currently doing a comprehensive investigation for better understanding of the effects of unsteady inflow on horizontal wind turbines [73-75,13].

The large eddies impose a non-uniform inflow on the turbine which may cause a power reduction and higher fatigue loads. The non-uniform inflow also affects the power production by altering aerodynamic/hydrodynamic loads on blades.

2.4.7 Fatigue

Periodic fluctuating blade loads due to the passing of the blades through the non-symmetric velocity profiles generated by the large eddies, can cause significant fatigue damage to the turbine and affect blade loads and power quality. For horizontal axis turbines, the most severe loadings may occur when the wind direction is a few degrees off the rotational axis of the turbine, since blades pass through a non-symmetric mean velocity field [76]. Sutherland and Kelley [13] demonstrated that turbulent inflows with large-scale eddies impose extreme loads on horizontal wind turbine blades and induce higher levels of fatigue.

During a VAHT's design life of 20 or 30 years, it may well perform 5×10^8 rotations. VAHTs are subjected to natural excitation from the flow to which they respond. The loads on a VAHT blade are due to both deterministic and stochastic sources. In order to evaluate the fatigue damage; both sources must therefore be included. The VAHT blade is subjected to forces resulting from centrifugal, gravitational and aerodynamic loads. Of these loads, only the

aerodynamic loads produce fatigue-inducing vibratory blade stresses. These are caused by changes in the effective aerodynamic blade angle of attack that occur during the turbine rotation. The non-uniform inflow adds extra unsteady aerodynamic loads on the blades by changing the blade angle of attack at frequencies higher than the rotational frequency of the turbine. The standard deviation of the inflow speed is proportional to the fatigue loads on the turbine [77]. Jorgenson et al. [78] introduced a relationship between the standard deviation of power output and the standard deviation of the inflow speed. Therefore, to measure the fatigue loads on a turbine one can measure either the turbulence of the inflow speed or the fluctuations of the power output.

2.4.8 Modeling the non-uniform inflow

It is impossible to model the real incoming flow conditions in the field for lab testing. The upstream screen increases the turbulence intensity of the flow; however, it is unable to simulate the wake deficit and meandering. Medici and Alfredsson [79] measured the velocity field behind a two-bladed horizontal wind turbine model with 18 cm diameter in a wind tunnel test. They measured all three-velocity components using a two-component hot wire. In the frequency domain, they found that the velocity signal shows velocity peaks at frequencies much lower than that of the rotational frequency. The Strouhal ($St = \omega D/U$) number of these low frequency peaks decreases with increasing tip sped ratio, and when it exceeds a specific tip speed ratio it levels out. This Strouhal number is similar to the Strouhal number of a solid disk with the same diameter as the turbine. Therefore, the vortex shedding behind the horizontal turbine has the same characteristics as the vortex shedding behind a bluff body.

The VAT has a cylindrical shape; consequently, the vortex shedding behind a VAT may be modeled by the vortex shedding behind a cylinder. The vortex shedding behind a two-dimensional cylinder is known as Von Karman vortex street. Fujisawa and Shibuya [64] showed that the vortex shedding behind the VAT blades have similar pattern as vortices in the Von Karman vortex street.

2.5 Scaling similarity laws

Measurements in the field are expensive and, due to the uncontrollable operating conditions, it is impractical to conduct a comprehensive testing on the performance of the turbine. The laboratory testing is a convenient method to extract the performance characteristics of a turbine and assess the effects of operating conditions on the behavior of the turbine. However, dimensional restrictions of the laboratory facilities require testing models smaller than the real size turbines. To extend the laboratory results for the real scale turbine, similarity laws are applied. Similarity laws for VAHTs are presented in a report prepared for NRCAN [28]. In this study the performance characteristics of the turbine is described as a function of the dimensionless design and operating parameters. Then the effect of each parameter in the scaling procedure is assessed. It should be noticed that for number of dimensionless parameters, like Reynolds number, it is unfeasible to achieve the same number for the laboratory and field. For these parameters, the performance trend of the turbine in the laboratory test is extrapolated to predict the field performance of large turbines. The following is the conclusion of the NRCAN report [28] on how dimensionless parameters affect the scaling process.

The *solidity* and *aspect ratio* are two design parameters and, in a simple scaling by definition, these remain constant. However, due to the structural issues they may be changed when designing larger turbines. This may be required to change the aspect ratio and the solidity to reduce bending loads on the bearing. A lower aspect ratio and lower solidity may be selected to achieve structural objectives to reduce costs, but aerodynamics or scaling laws do not dictate this.

The *tip speed ratio* is mainly a function of the solidity. If the solidity remains constant, a straight scaling will preserve the tip speed ratio in theory. However, using a smaller solidity for structural reasons for large turbines implies a higher tip speed ratio for the large turbines. This will impact, for example, marine life as the rotational speed needs to increase for a given free stream velocity. This may also increase fatigue loads and slightly change the generator characteristics.

In general, the *toe-out preset pitch angle* improves the efficiency of the turbine. A typical toe-out preset pitch angle is between 2° and 7°, however, large-scale turbines require a smaller toe-out pitch angle if the solidity is reduced for structural reasons.

The *clearance coefficient* is smaller for large turbines. Therefore, scale-up improves the efficiency of larger turbines operating near the surface, providing a slight advantage.

At lower *Reynolds numbers*, the performance of turbines is improved when increasing the Reynolds number. During operation, this implies better efficiency at higher free stream velocities. However, when the blade Reynolds number exceeds a specific value, the operating behavior of the turbine becomes

independent of the Reynolds number. The scale-up of VAHT implies a higher Reynolds, and therefore, larger turbines will experience less change in their efficiency due to Reynolds number.

Thick airfoils with a better performance in the post-stall region are recommended for small turbines having high solidities. If the solidity is reduced for large-scale turbines for structural reasons, a thinner airfoil with a lower drag coefficient is recommended.

Aerodynamic *support arms* add resistance load on the turbine. The contribution of this load is not linear with scaling. For each design, this requires a structural analysis, as many parameters are involved. For example, increasing the turbine diameter increases the bending moment on the arms requiring more arm stiffness. However, this can be mitigated partially by increasing the buoyancy of the horizontal arms. The higher aspect ratio design could potentially require more arms along the blade to address possible blade buckling.

The *turbulence large scales* impact on scaling is two-fold. (1) Turbine efficiency decreases less for larger scale turbines for given turbulence length scales, and (2) for VAT farm applications, larger-scale turbines generate larger eddies in their wake. Larger eddies apply a stronger dynamic load on the blade and reduce the lifetime of the turbine by increasing the fatigue on the blades and impact efficiency.

It is concluded that the performance characteristics of the turbine remain unaffected during the scaling process as long as the dimensionless performance parameters remain constant. Therefore, it is practical to test a small-scale

turbine in a water tunnel with high flow velocity and predict the performance characteristics of the large unity-scale turbine.

2.6 Summary

The principal dynamics and aerodynamics of the VAT were reviewed in this chapter. It was shown that the unsteady aerodynamics is the dominant phenomenon in the VAT operation. The unsteady aerodynamics is a complex area and there is no general analytical solution available for the flow motion equations for this type of flow. The unsteady aerodynamics of the VAT becomes even more complicated when it operates in a non-uniform inflow condition. The non-uniform flow is the result of the geometry, boundary conditions and upstream objects. In the lab testing, the screen in the upstream flow only increases the turbulence intensity of the flow and is unable to model the wake deficit and meandering. Studies show that the vortex shedding in the wake behind the horizontal and vertical kinetic turbine is similar to the vortex shedding behind a bluff body. A cylinder is able to simulate the effect of an upstream turbine and other vortex shedding phenomena in a river.

Chapter 3

Field measurements

Time-dependent river velocity measurement obtained one diameter upstream of an operational 25-kW vertical kinetic turbine is considered in this chapter. In June 2008, New Energy Corporation, University of Manitoba, and Manitoba Hydro deployed a 25-kW vertical axis hydrokinetic turbine (VAHT) in the Winnipeg River at Pointe du Bois and connected it to the Manitoba Hydro grid. It was an opportunity to measure the flow characteristics near a VAHT operating in a river at flow velocities between 2.1 to 2.5 m/s. The high frequency time-dependent velocity measurement reveals the size of large eddies interacting with the turbine in the river. An operating turbine changes the flow patterns upstream of the turbine, including the size of the large eddies. This chapter helps to provide a better understanding of the flow characteristics in a river and sizes of these large eddies causing non-uniform flow velocity distribution on the VAHT disk. It also includes the interaction between the turbine and river flow upstream of the turbine. There are few deep river measurements reported in the literature.

For these in-situ experiments, first an acoustic Doppler velocimeter (ADV) measures the flow velocity one diameter upstream of the turbine with the turbine brake activated. Due to a low solidity of the turbine, $\sigma = 0.3$, the assumption is that these measurements can provide the flow characteristics of the undisturbed

river flow. This particular assumption is justified by measurements conducted upstream of a $1/11^{th}$-scale model of the turbine at the University of Manitoba water tunnel. The results of the water tunnel measurements show that the difference in statistical properties of the flow, such as average flow speed, turbulence intensity, skewness and kurtosis, at one diameter upstream of the turbine is less than 3% when the brake is activated. After disengaging the brake, the turbine starts operating and the ADV measures the upstream flow characteristics and interaction with the turbine. During these experiments, a resistive load is applied to simplify the signal analysis from the generator, operating at a power factor of unity.

The results aim to characterize flow in rivers to improve our understanding of the impact of non-uniform inflow on hydrokinetic power generation, and to contribute to the optimization of vertical axis hydrokinetic turbines. Furthermore, power spectrum measurements and standard deviation of the river velocity provide data to improve the fatigue lifetime estimation of hydrokinetic turbines. In addition, it is required to improve ADV filtering analysis for these types of experiments—for river and for water tunnel measurements—as bubble entrainment occurs in both situations.

3.1 Pointe du Bois test site

Pointe du Bois located on the Winnipeg River 150 km northeast of Winnipeg is selected as the site for testing hydrokinetic turbines due to its flat riverbed formation, accessibility, opportunities for cold weather testing, and relatively steady flow rate above 2 m/s. Located near the border between Manitoba and Ontario, Pointe du Bois offers a granite riverbed ideal for installation of river

bottom anchors. Unlike many rivers in the Red River Valley, the water is relatively free of suspended particles, which have proven to be abrasive to the rotors of hydrokinetic turbines [80]. Anchors located 90 m upstream of the test site cemented in place 2 m into the bedrock secure a 3.2 cm diameter cable used to attach the pontoon test facility that holds the turbine below a footway bridge. Figure 3.1 shows the anchoring system. A Manitoba Hydro dam downstream of the site and a spillway upstream of the test site controls the flow rate where the turbine is located. Figure 3.2 shows the aerial view of the site. The walkway bridge provides an easy access to the turbine and systems.

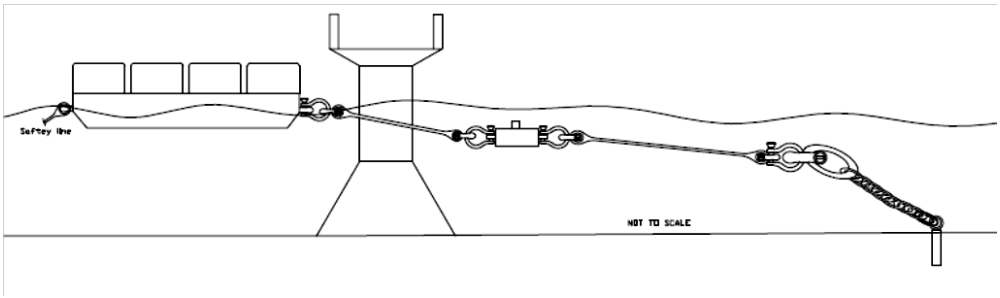

Figure 3.1: Schematic anchoring system used for stabilizing the turbine in the river

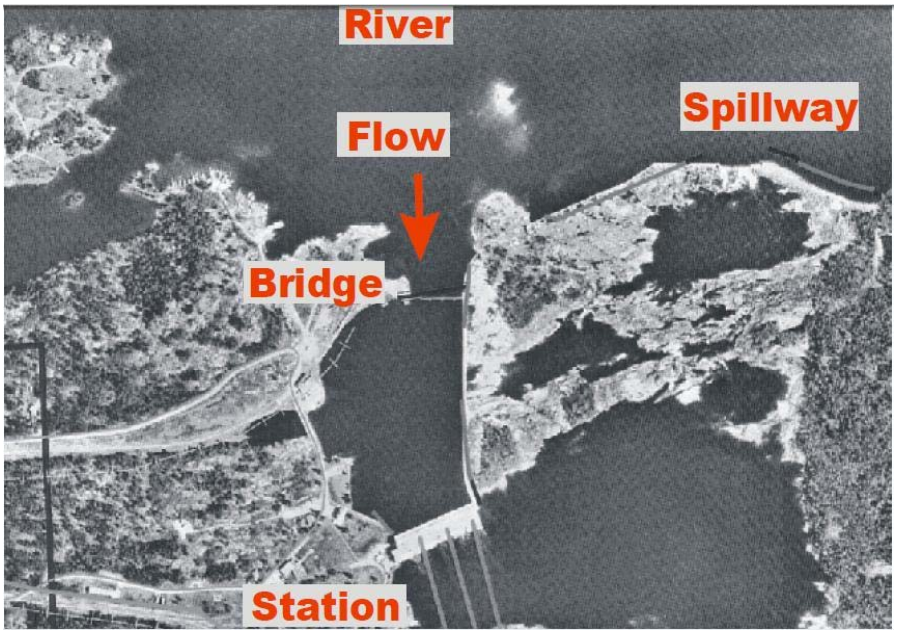

Figure 3.2: Aerial view of the Point du Bois kinetic turbine test site

Near the bridge, the river narrows and provides a higher velocity current. An acoustic Doppler current profiler (ADCP) is used to measure water current velocities for a range of depths [81]. The typical depth of the river at the site near the bridge was about 7 to 10 meters. The resulting river velocity contours, shown in Figure 3.3, indicate that the maximum velocity occurs immediately downstream of the walkway bridge that connects the shoreline to the sidewall of the dam. The bridge has three piers with the third pier close to a retaining wall. The flow velocity is less than 2 m/s between the shoreline and the first pier due to the low depth and high shear forces near the shoreline. Wall friction drops the current velocity between the dam and the third pier. The flow between the second and third pier offers a large high velocity area. In this area, the average velocity is above 2 m/s and it was chosen for the test location.

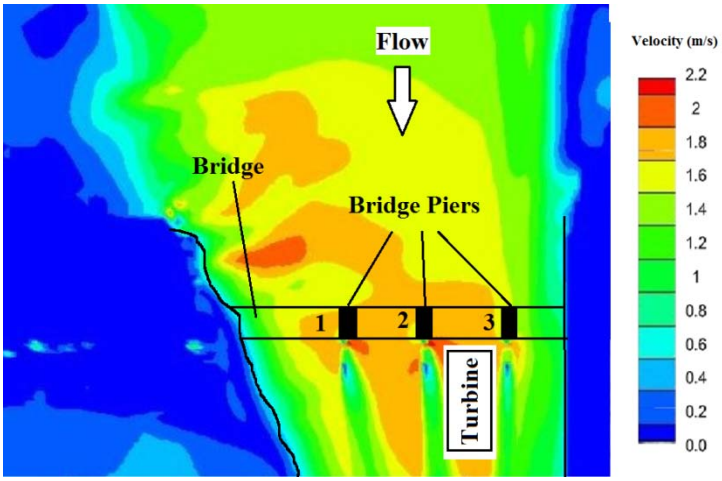

Figure 3.3: Velocity contours of the Winnipeg River in the Pointe du Bois area as measured using ADCP by Manitoba Hydro

The location near a bridge offers several logistical advantages as well. Bridges are often constructed in the narrowest part of a river, which has the maximum local flow velocity; therefore, the available kinetic power is highest in that area. Bridges are convenient for maintenance of the kinetic turbines and the power units. Using a bridge-way can reduce the testing costs and infrastructure needed for the river kinetic turbines. However, as for this application, the turbine cannot be secured directly to the bridge due to increased static and dynamic loads.

3.2 25-kW vertical kinetic river turbine

New Energy Corporation designed and manufactured a 25-kW vertical river kinetic turbine unit to operate in flow velocities of 1.5 to 3.0 m/s with the first demonstration tests conducted at Pointe du Bois in 2008 with a 5-kW unit.

The 25-kW turbine consists of four 4.24 m length straight blades connected to the central shaft using two support profiled-arms per blade. Blades travel on a

3.40 m diameter circle. The gearbox and generator stand above the water level and the turbine operates beneath them in the water. A pontoon boat supports the turbine, gearbox, and generator using a novel support pipe rotating on two supports that minimizes pontoon buoyancy requirements. An anchoring system attaches the pontoon boat to the riverbed and holds it 5.8 m downstream of the walkway bridge between the second and third piers. The centerline of the turbine is 4.6 m in the left side of the third pier and 15.4 m in the right side of the second pier. Figure 3.4 shows the turbine on the pontoon boat before placing in the operation site for the 25-kW unit.

(a) (b)

Figure 3.4: The 25-kW vertical river kinetic turbine unit manufactured by New Energy Corp (a) in transit to test site and, (b) being lowered into the flow using balancing arm resting on two pillars

Rated for 25-kW at a water velocity of 3 m/s, the rotor rotates at approximately 40 rpm. With a gearbox ratio of 30.7:1, the maximum generator output voltage is 307 V. At lower river velocities, the turbine generates less power. Figure 3.5 shows the maximum output power of the turbine verses the current velocity upstream of the turbine. The average water velocity at the chosen site is 2.2 m/s. At this velocity, the output power is 9 kW due to the relationship between power output and the cube of the average velocity. As is the case with wind-power applications, the tip speed ratio for a turbine defines the maximum

power output for a given turbine in a given flow. The tip speed ratio is the ratio between the rotational speed of the blade and the current velocity. A maximum power point tracking (MPPT) algorithm used also for a 5-kW vertical axis turbine is described by Ginter in [82].

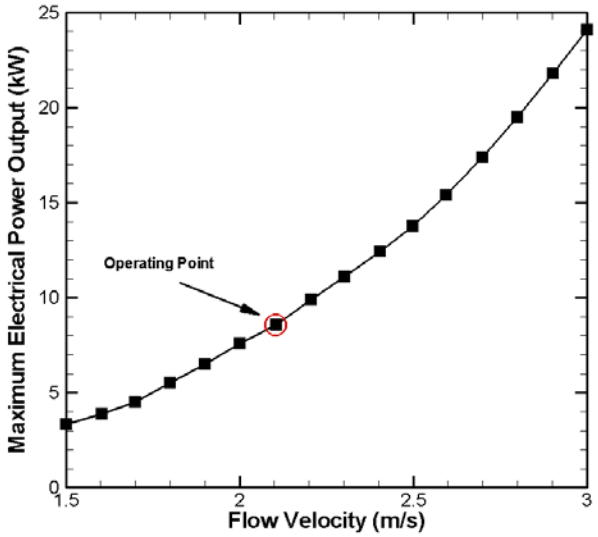

Figure 3.5: Performance chart of the 25-kW hydrokinetic turbine by New Energy Corporation

Brake pads are used to stop the turbine shaft and to prevent the turbine from freewheeling during deployment. A stopped turbine generates no electricity, has no voltage at the terminals and, due to the low solidity of the vertical turbine, upstream flow is assumed to remain relatively undisturbed. Because the ADV sampling volume is below the bottom of the pontoons and near the front, we further assume the pontoons have negligible impact on the flow measurements upstream. When the brake is released, the flow will ideally self-start the turbine. In some cases, the shaft is rotated manually to initiate rotation, mainly due to viscosity of the gearbox oil. With no load on the generator, the rotational speed increases until freewheeling conditions are attained. Then electrical load on the generator is increased to the maximum power point for a given rotational speed beyond which the rotor will begin to stall or become otherwise unstable. As in

most small-scale wind power generation, MPPT systems control the electrical output of the system based on a table of rotational speed versus power output [82]. The system output is varied by means of a power converter which converts alternating current (in this case 400 Hz from the permanent magnet generator connected to the rotor) to direct current, then converts it back to grid-suitable, 60 Hz, electric power. The converter has non-linear and frequency dependent characteristics, and is built to be autonomous: the power electronics changes its characteristics to suit changes in the rotational speed. Therefore, for purposes of isolating the turbulence effects in the water flow from the interaction of the power converter, purely resistive loads are applied in these tests.

3.3 High frequency velocity measurement method

A Nortek Vectrino AS ADV located upstream of the turbine measures the velocity fluctuations in the river. The detailed description of the ADV employed in these measurement are discussed in the next chapter as a new filtering system had to be developed. ADV is a common tool to measure velocity in three directions with frequency variation of up to 200 Hz in laboratory and field settings. Measurement techniques such as laser Doppler anemometers are impractical outside laboratory settings [83] and others like propeller gauges and pitot tubes are inaccurate [84] for turbulence measurements. Compared to optical and laser techniques, ADV is simple and compact, as the acoustic emitter and receivers are installed within a common device. Additionally, acoustic waves penetrate deeper in water when compared to light or laser beams [85]. Because of these advantages, ADV is widely used by researchers for flow velocity measurements in laboratory and field applications [84,86-89].

ADV operates on the principle of Doppler shift. When the transducer of the ADV transmits periodic short acoustic pulses, suspended particles in the sampling volume reflect a small fraction of the energy of the transmitted acoustic pulses. The Doppler shift between the transmitted and reflected signal is a function of particle velocity in the sampling volume representing the actual flow velocity. The sampling volume for the ADV instrument used in this testing is a 0.6 cm diameter cylinder with 0.9 cm in height, located 10 cm away from the ADV transmitter. Although measuring velocity with ADV has advantages over other velocity measurement methods, this technique is sensitive to operating conditions, particularly in field settings such as rivers. The raw ADV velocity data set requires further processing before analysis can proceed. The size and the number of suspended particles in the ADV sampling volume are the two main parameters directly affecting the quality of the velocity data set. For in-situ river flow studies operating near the water surface at relatively high velocities, the entrainment of air bubbles significantly complicates measurements. This phenomenon also occurs in the lab tests so the filtering algorithm is applied for both measurement series.

3.3.1 Low particle density during cold seasons

The intensity of the backscatter of the reflecting acoustic signal relates directly to the number of particles in the flow. The number of particles in normal tap water is insufficient for the ADV measurement. Small spherical polyamide seeding particles of order of 50 μm diameter added to the water in the water laboratory flume create required targets for the acoustic signals. These polyamide-seeding particles at a density of 1.03 g/cm^3 emulsify and suspend themselves in water. However, in river field measurements, seeding particles consist of sediment

particles, organic particles, and entrained air bubbles, none of which can be controlled. Moreover, entrained air bubbles are detrimental to the measurements.

At the turbine location, the depth of the river is approximately 10 m so sediment particles have a low chance to reach to the surface area where the measurements occur. Furthermore, it was found that in the winter and in early spring, there are insufficient naturally occurring particles in the water. The ADV probe check displays the strength of the signal being acquired in terms of signal amplitude. Figure 3.6 shows a sample probe check signal for the Winnipeg River when particles in the river are low. The 198 mm^3 control volume of the ADV, located 10 cm away from the transmitting signal at the stem of the probe, receives a signal ranged between 50 and 60 counts per second. During the winter months, the signal count is low as there are not enough particles in the water to obtain a proper return signal. The snow and ice cover during the winter months inhibit various naturally occurring particles from seeding the river, and plant growth in the water is stopped. In the spring, rainwater run-off introduces enough suspended particles into the river and the warm summer months encourage the growth of small plants and other organisms, which increase the particle count.

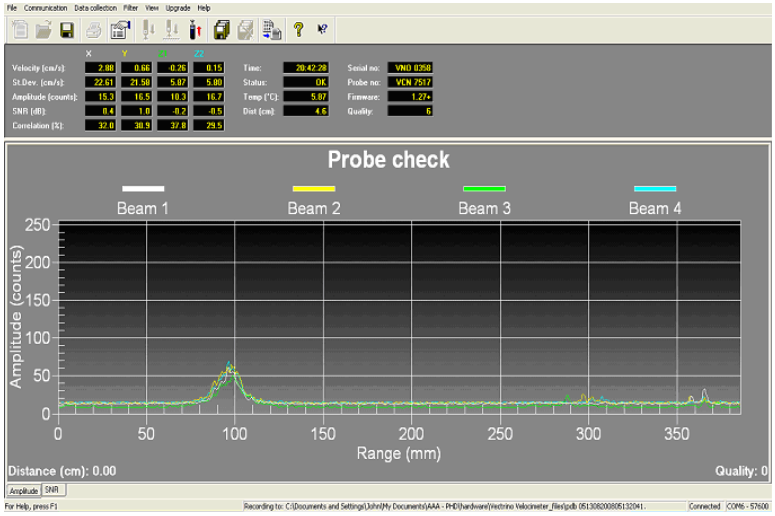

Figure 3.6: ADV probe check signal required before performing measurements

The ADV requires over 40 counts of particles per second, as this is the threshold for noise; 80 counts and higher provide a proper ADV measurement condition [90]. For reliable and accurate flow measurements during cold months, our research group had to develop a method for seeding the river flow. Introducing particulates to the environment must be accomplished with a minimal ecological footprint. Milk is an organic substance with approximately the same density as water. Unlike other synthetic particles, milk is not toxic and biodegraded. Milk is injected into the flow upstream of the ADV and directly into the ADV sampling volume. Figure 3.7 shows the stream of milk as it enters the flow. Milk particles improve the amplitude of the back scattered signal and consequently the signal-to-noise ratio and the auto-correlation.

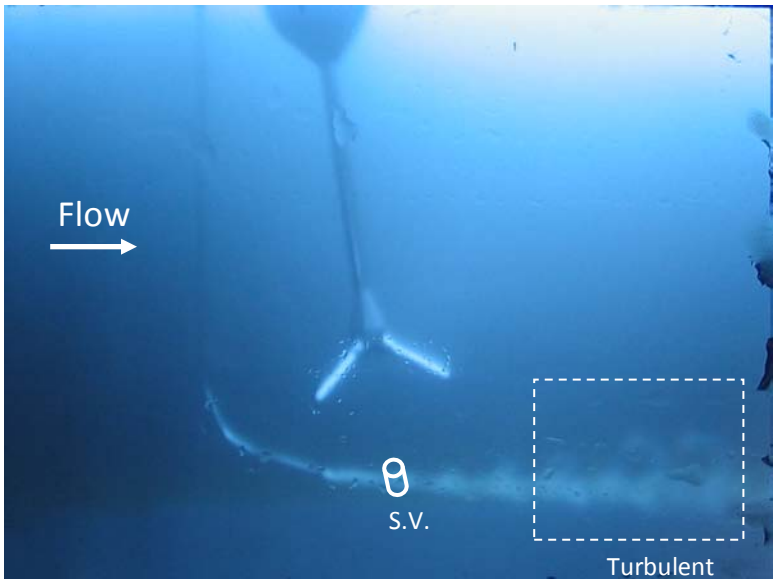

Figure 3.7: Milk injected into the sampling volume of the ADV in the river measurement helping the camera to visualize the turbulence occurring throughout the flow. Actual video shows many air bubbles streaming by

A twelve liter pressurized tank injects the milk into a series of tubes to introduce the milk upstream and in line with the sampling volume of the ADV. This volume of milk proves sufficient to operate the ADV for 8.3 minutes, or 100,000

samples with 200 Hz sampling frequency. The natural turbulence within the flow disperses the milk as the plume of milk gets visibly sparse as it travels downstream. We tested the ADV using different milk to water ratios to obtain an adequate signal with minimal injection of milk. The amplitude is not consistent throughout the sampling period as turbulence breaks up the steady stream of milk. There are times when the flow led the milk away from the sampling volume and/or the turbulence disperses the milk, leading to a temporarily lower amplitude signal. A breakdown of the maximum and average amplitudes for the different milk to water ratios is presented in Table 3.1.

Table 3.1: ADV tests using milk to seed the flow in the river

Test #	Milk to Water Ratio	Sample Size	Max Amplitude	Mean Amplitude
1	1:0	30,000	173	87
2	1:1	50,000	171	149
3	2:1	50,000	170	96
4	3:2	3,404	150	65
5	3:1	1,173	158	72

The 1:1 ratio produces the largest amplitude counts and maintains it for most of the samples. The 2:1 ratio is also adequate with lower mean amplitude indicating that there are pockets of lower counts caused by the water mixture. It is difficult to pinpoint a single reason for lower amplitudes. Turbulence disperses the milk within the flow. Flow deviations that push the milk away from the sampling volume, or larger than acceptable particles within the milk, all contribute to an undesirable signal.

3.3.2 Spikes in the velocity data set

The measured ADV data sets may contain Doppler noise due to aliasing of the return signal above the Nyquist frequency. This happens if the velocity of the flow velocity rises above or below the velocity range of the instrument [83]. Velocity shear in the sampling volume generates a large velocity gradient in the direction of the acoustic beam, which causes Doppler noise in the ADV velocity data sets [91]. In addition to noise, the data set can contain large amplitude spikes, which are not simple to isolate. There can be ambiguity for the root cause of these spikes. However, most studies that report spike issues are related to the measurements of high turbulent flows [92,93], surf-zones [91,94,95], bed areas [96], and downstream of flow steps [97]. In these studies bubbly flow occurs: the flow contains air bubbles except in the bed area where the existence of air bubbles has a much lower probability.

The size of seeding particles used for ADV measurement has to be small enough in comparison with the acoustic wavelength to have an accurate and spikeless data set. The Nortek Vectrino AS ADV has a 10 MHz acoustic transmitter generating acoustic waves with a 0.01 cm wavelength. Large sound scattering particles result in non-isotropic scattering and introduce velocity spikes. Large particles not only generate spikes in the velocity data set of the ADV, but also due to their high moment of inertia, they are unable to respond as quickly to velocity fluctuations. The water samples from the Winnipeg River show that the suspended particles are smaller than the acoustic wavelength of the ADV; however, the velocity data set in the field measurement contains numerous spikes. These spikes vary in number and strength in each measurement. An underwater camera can reveal the flow conditions in the river. The underwater

video camera shows air bubbles entrained in the flow upstream the turbine. The camera detects numerous air bubbles larger than the sampling volume size.

Quality improvement methods for the ADV signal specifically for surf-zone applications could be applied to this dataset [98,99]. However, Birjandi and Bibeau [100] conducted series of experiments in the University of Manitoba's water-tunnel facility to assess the effects of air bubbles on the quality of the ADV velocity data set and developed a filtering algorithm. They showed that while the mean velocity remains almost unaffected by spikes, moment of higher orders deviate significantly. In spectral analysis, spikes increase the noise energy [100, 101] and disrupt the spatial correlations [100]. Birjandi and Bibeau [102] introduced a new hybrid method to remove spikes from the ADV velocity data set. The advantage of this method over conventional methods is its accuracy in dealing with high spike density data sets, such as river velocity data sets. The detailed description of the hybrid despiking method is discussed in [102]. Before any further analysis on the river velocity data set, the hybrid method is used to filter spikes. The spectral analysis was shown to be insensitive to the removal of data points due to spikes. However, the correlation function depends on the time interval between two velocity data points hence, the removed spikes have to be replaced. The hybrid method uses linear interpolation to replace removed spikes. Figure 3.8 shows a sample velocity data set in the Winnipeg River before and after despiking with the hybrid method. The ADV data set for the river flow data and the filtering algorithm code are available in Reference [103] and performance of the 5-kW and 25-kW turbines is quantified during winter and spring tests [104]. The hybrid method is also used for the water tunnel tests to study the impact of turbulence on power as air bubbles are entrained into the water tunnel behind cylinders.

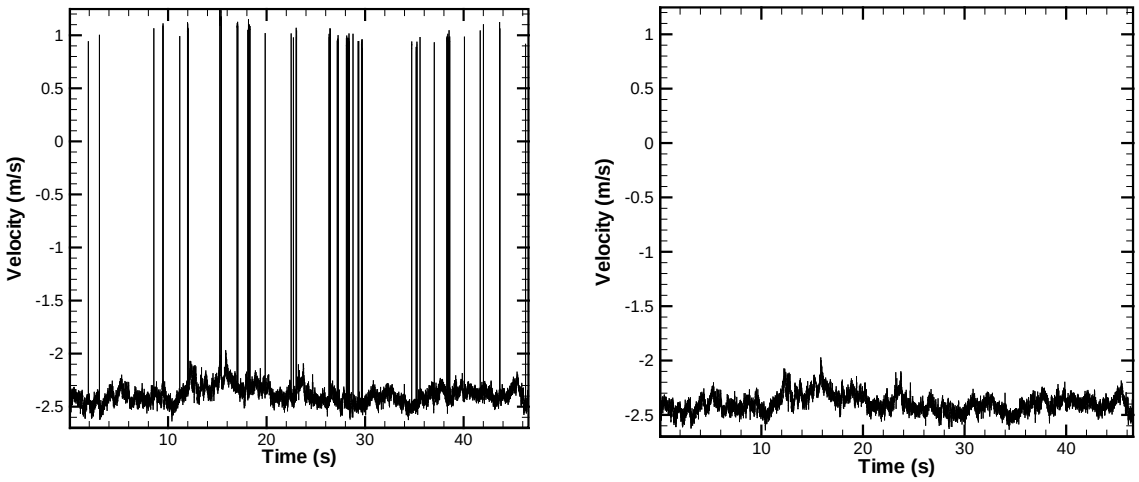

(a) (b)

Figure 3.8: The ADV measurement in the Winnipeg River: (a) a sample raw velocity data set, and (b) a despiked velocity data set by the hybrid filtering method developed for this project

3.4 Experimental overview

River flow characteristics are a function of time and location. In this study we locate the 25-kW turbine 5.8 m downstream of the walkway bridge and 4.6 m away from the third pier. The ADV measurements are conducted at $x/D = 1$ upstream of the turbine, where D is the diameter of the turbine and x is the longitudinal distance between the measurement location and the turbine centerline. The lateral distance between the turbine axis of rotation and the ADV is zero. Figure 3.9 shows the experimental setup at Pointe du Bois.

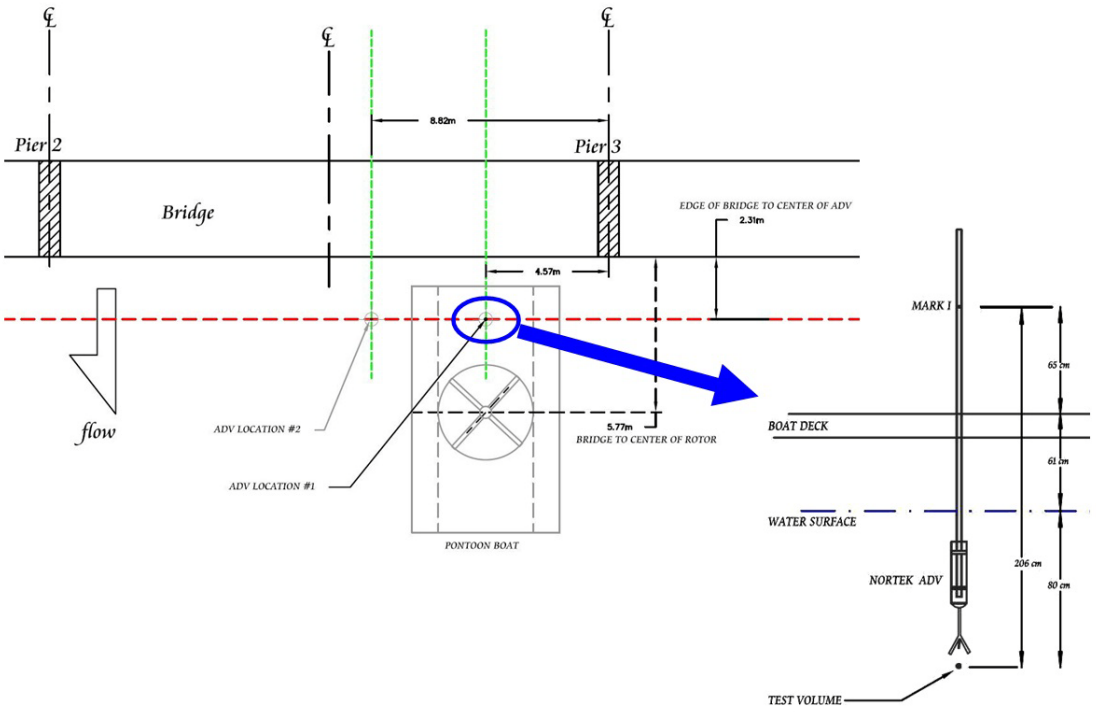

Figure 3.9: Experimental setup at Point du Bois for ADV in-situ measurements

The initial location of the turbine is close to the third pier. At this location, the wake of the third pier may affect the river velocity measurement, adding turbulence to the flow due to the wake of this manmade structure. To remove the possible influence of the third pier, the pontoon boat with the turbine is relocated away from the third pier, with new velocity measurements repeated at a location that is 8.82 m away from the third pier, as shown in Figure 3.9. Further measurements reveal no evidence of the bridge wake interference at both measurement locations. In these two locations, the velocity is measured for 250 s. For the first 30 s the turbine brake is applied. The stopped turbine has a low blockage ratio, due to the low solidity of the turbine, $\sigma = 0.3$; therefore it is assumed the flow remains undisturbed at the location of the ADV. The velocity measurement upstream of the stopped turbine therefore approximately represents the river natural fluctuations. The turbine starts after 30 s upon releasing the

brake and adding a small torque with a hand wrench to initiate the rotation. The turbine is connected to a heater unit to dissipate the energy. Velocity measurements continue for 220 s after the turbine started. Table 3.2 shows the two river tests conditions. During these tests, power output from the generator is recorded simultaneously using a digital oscilloscope.

Table 3.2: The ADV measurements conditions

Test #	Distance from the third pier (m)	Sampling volume depth (m)	Stopped turbine period (s)	Measurement period (s)
Test-1	4.57	0.8	30	250
Tes-2	8.82	0.8	30	250

3.5 Average velocity

During the first 30 s of the test the characteristics of the flow approximate the undisturbed river. The average velocity of the river measured in Test-1 (near pier 3) and Test-2 (away from pier 3) is 2.45 and 2.46 m/s, respectively. Measurements show no evidence of the bridge wake at both measurement locations. When the turbine starts rotating, the average velocity upstream of the turbine drops. The river flow requires about 10 s to become statistically steady due to the turbine ramp up. After this 10 s time period the average measured velocity reduces to 1.96 and 1.98 m/s in Test-1 and Test-2, respectively. Agreement between the Test-1 and Test-2 shows a 20% reduction in the mean river velocity at a location $x/D = 1$ upstream of the operating turbine. The reduction in the mean velocity is apparent in Figure 3.10 with velocity fluctuations increasing considerably when the turbine is producing power.

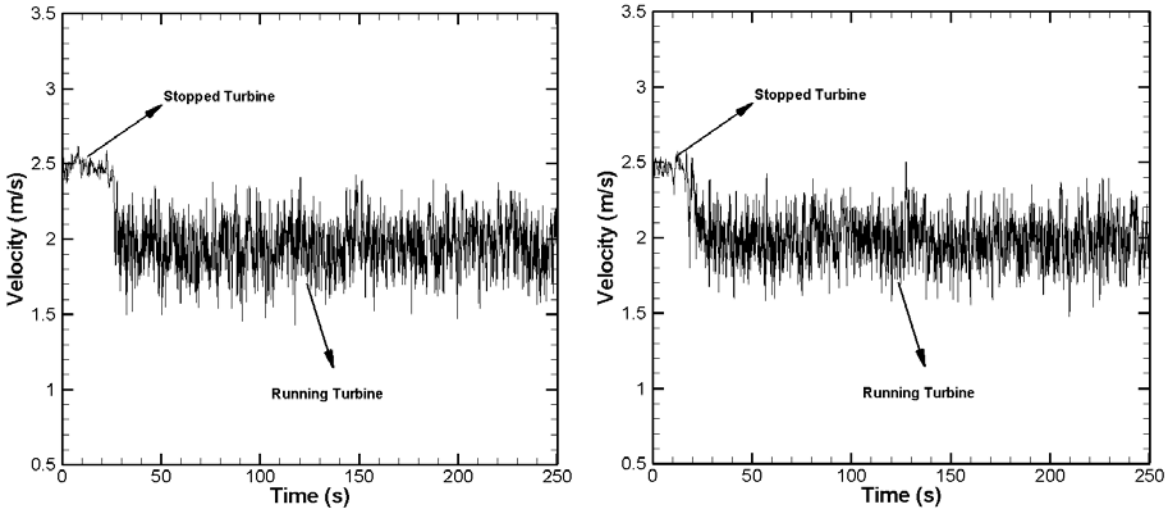

(a) (b)

Figure 3.10: Velocity data set upstream of the turbine, (a) Test-1 (near pier 3), and (b) Test-2 (away from pier 3)

3.6 Turbulence intensity

Each velocity data set, U, consists of an average, U_{ave}, and a fluctuation or turbulence part, u, defined as:

$$U = U_{ave} + u. \tag{3.1}$$

Turbulence intensity, I, represents the level of turbulence in the flow:

$$I = \frac{std(U)}{U_{ave}}. \tag{3.2}$$

Typically, a turbulence intensity lower than 1% is considered a low-turbulence case occurring at controlled lab facilities [105,106]. Between 1% and 5%, it is a medium-turbulence case; like downstream of the turbulence generating grids, flow

in deep-wide rivers or low velocity shallow rivers [107,108]. Between 5% and 20%, it is a high-turbulence case; like surf-zone, step-pool and near gravel-beds [109-111]. Table 3.3 shows the turbulence level upstream of the turbine. The river has a medium-turbulence level when the turbine brake is activated. When the turbine produces power, it disturbs the upstream flow at $x/D = 1$ and increases the turbulence intensity to a high-turbulence case. Figure 3.10 shows that although the average velocity upstream of the operating turbine is lower, the velocity fluctuations are larger.

Table 3.3: Turbulence intensity upstream of the turbine

	Test-1		Test-2	
	Stopped	Operating	Stopped	Operating
Turbulence Intensity	2.5%	15.6%	2.4%	15.4%

3.7 Turbulence kinetic energy

Turbulent flow can be considered as a superposition of a spectrum of velocity fluctuations over a mean flow. Turbulence consists of eddies of different lengths scales. Large eddies carry a higher energy level compared to small eddies [112]. In rivers where the mean flow provides the energy required for the turbulence, turbulence kinetic energy is always lower than the mean flow kinetic energy. Shear forces or velocity gradients in rivers, such as wakes of submerged bodies and rapid changes in the river bed, create large-scale eddies. Large-scale eddies obtain energy from the mean flow and also from each other. However, the operating turbine changes the velocity pattern in the river. A low velocity area near the turbine imposes a negative velocity gradient upstream of the turbine.

This local negative velocity gradient in the uniform river flow creates a large shear force which causes energy cascade from the mean flow and large eddies to the smaller size eddies. Table 3.4 shows the kinetic energy of the mean and the turbulent part of the flow upstream of the turbine. Due to the medium level of the turbulence in the river most of the kinetic energy is carried by the mean flow. An operating turbine introduces a velocity gradient upstream of the turbine and reduces the mean flow velocity. Although the mean velocity kinetic energy drops upstream of the operating turbine, turbulence kinetic energy increases considerably due to the energy cascade from the mean flow to small eddies.

Table 3.4: Kinetic energy of the mean and turbulent parts of the flow per unit mass

	Test-1		Test-2	
	Stopped	Operating	Stopped	Operating
Turbulence Kinetic Energy (m^2/s^2)	0.01	0.12	0.01	0.13
Mean Velocity Kinetic Energy (m^2/s^2)	3.11	1.91	3.09	1.98

3.8 Shear stresses

Reynolds stress tensor is an important concept in the theory of turbulence representing the average momentum flux due to turbulence velocity fluctuations. The diagonal components of the Reynolds stress are the normal stresses while the off-diagonal components are the shear stresses. Reynolds shear stress being a symmetric tensor has only three components: uv, uw, vw, where u, v, and w are stream-wise, normal and vertical velocity fluctuation components, respectively. Table 3.5 shows the average shear stresses for Test-1 and Test-2. The operating

turbine increases the <uw> considerably due to the high velocity gradient in both axial flow direction and the vertical direction. However, the order of magnitude of other shear stresses, <uv> and <vw>, remains almost the same. In Test-2 <uv> and <vw> show a rise in their magnitude for the operating turbine condition; but much lower increase than for <uw>. The reason can be the measurement location of the ADV, which is at the centerline of the turbine but close to the top of the turbine. Therefore, there is a negative velocity gradient in the axial flow direction, a positive velocity gradient in the vertical direction.

Table 3.5: Average shear stresses

	Test-1		Test-2	
	Stopped	Operating	Stopped	Operating
<uv> (m^2/s^2)	-3.57e-4	-1.78e-4	-2.56e-4	-42.21e-4
<uw> (m^2/s^2)	0.07e-4	132.87e-4	-1.2020e-4	127.31e-4
<vw> (m^2/s^2)	-5.52e-4	-2.66e-4	2.16e-4	8.60e-4

Figure 3.11 shows the shear stresses in the flow upstream of the turbine. Shear stresses upstream of the operating turbine are more symmetric in their shape but have a larger deviation from their mean value.

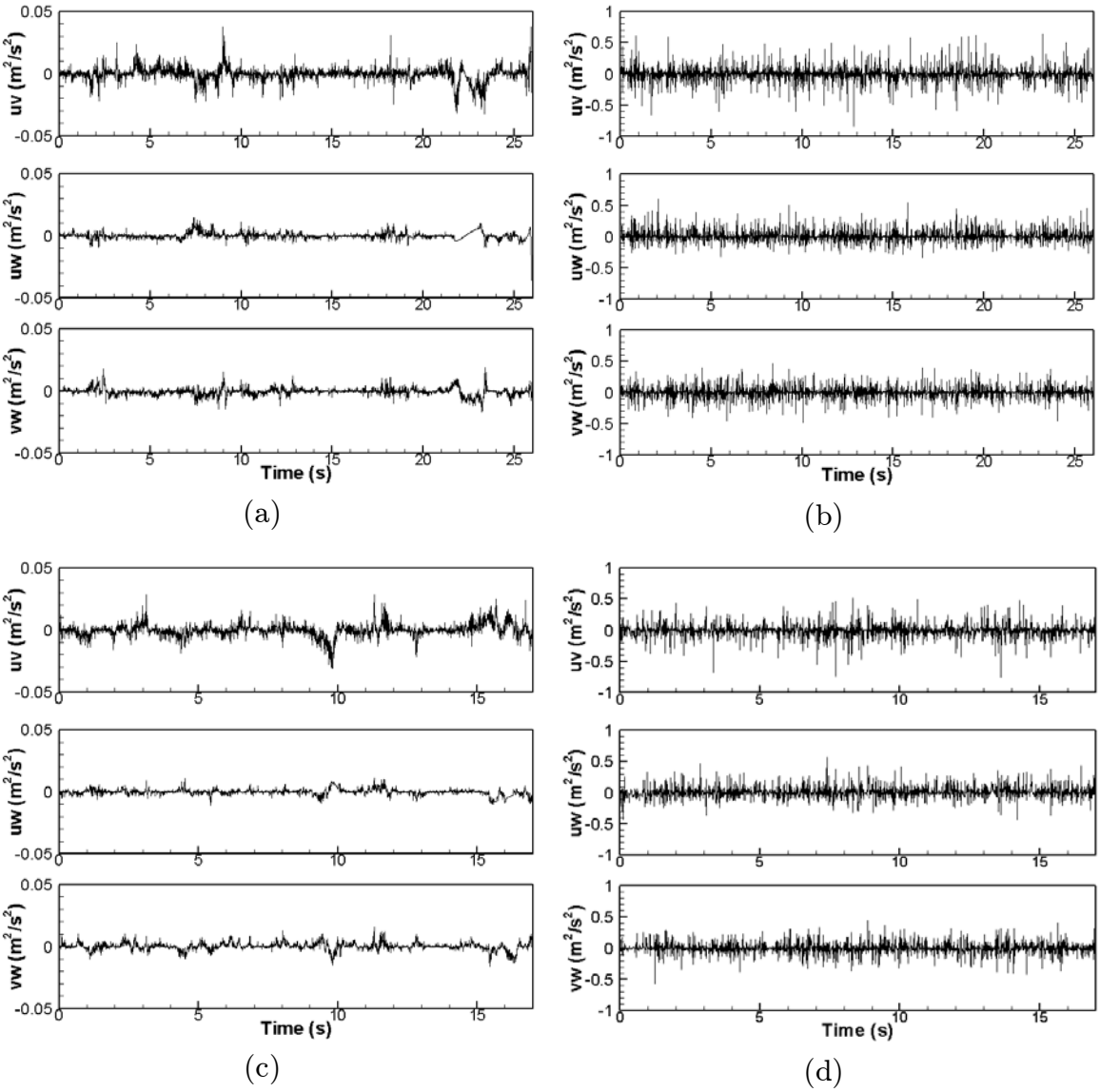

Figure 3.11: Shear stresses upstream of the turbine (a) Test-1 stopped turbine, (b) Test-1 operating turbine, (c) Test-2 stopped turbine, and (d) Test-2 operating turbine

3.9 Length scales and power spectrums

The autocorrelation coefficient can be used to define the length scales in the flow.

The non-dimensional correlation coefficient is written as:

$$\rho_{uv} = \frac{\overline{uv}}{\left[\left\langle u^2 \right\rangle \left\langle v^2 \right\rangle\right]^{1/2}}, \qquad 3.3$$

which lies between -1 and 1, due to the Cauchy-Schwartz inequality. If the correlation coefficient is zero, variables are statistically independent and if the absolute value of the correlation coefficient is unity, variables are deterministically related. The temporal autocorrelation is the correlation of any signal with itself at different time lags, where:

$$\rho_{uu} = \frac{\overline{u_t u_{t+\tau}}}{\left\langle u^2 \right\rangle}. \qquad 3.4$$

The autocorrelation coefficient is unity at a time lag of zero. As the time lag increases the correlation decays to zero. In the turbulence application, the multiplication of the temporal autocorrelation integral by the mean velocity defines the order of magnitude of macro length scales in the flow. Figure 3.12 shows the autocorrelation function for the stopped and operating turbine conditions during the Test-1 and Test-2. Results show that the operating turbine reduces the correlation in the velocity data set. In the Winnipeg River the autocorrelation coefficient of the velocity signal with the stopped turbine gradually approaches zero after about 0.6 s time lag. The operating turbine reduces the correlation in the velocity signal and autocorrelation coefficient is near zero after about 0.05 s time lag.

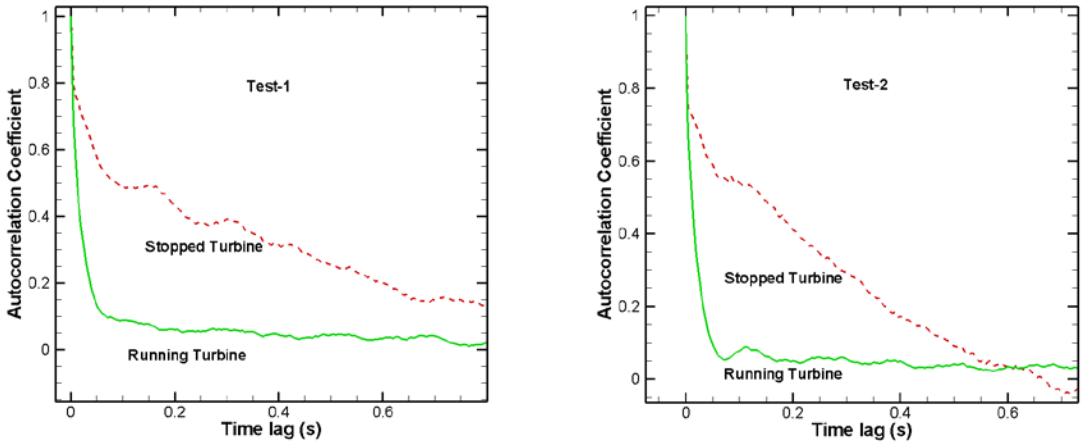

(a) (b)

Figure 3.12: Autocorrelation coefficient for (a) Test-1, and (b) Test-2

The integral of the autocorrelation coefficient from zero time lag to the first zero crossing is a measure of the average time over which velocity fluctuations correlate with each other. This value is the integral time scale. Integral time scale is a function of the site and size of eddies in the current. Eddies are relatively coherent, well correlated, and have characteristic times on the same order as the integral time scale. Multiplying the integral time scale by the mean velocity gives the integral length scale. The integral length scale tends to be more constant over a range of river velocities than the integral time scale and, thus, is somewhat more representative of a river or site. Table 3.6 shows measurement results for the integral time scales and length scales in the river and upstream of the operating turbine. Results show that the larger eddies contained in the undisturbed river flow are broken into small eddies when the flow approaches the operating turbine. Although the operating turbine breaks the large eddies into smaller eddies, the length scales are still comparable with the chord size of the blades, 0.1 m. At these sizes of length scales, eddies may apply

a sudden velocity change on the blades surface and cause a local separation, or stall, due to an adverse pressure gradient.

Table 3.6: Time and length scales upstream of the turbine

	Test-1		Test-2	
	Stopped	Operating	Stopped	Operating
Integral time scale (s)	0.441	0.057	0.191	0.053
Integral length scale (m)	1.01	0.11	0.47	0.11

Figure 3.13 shows the power spectral density obtained for Test-1 and Test-2. The spectra show the expected -5/3 slope for inertial range, as Kolmogorov predicts [113]. Inertial range starts at lower frequencies for the stopped turbine, which represents large size eddies. Velocity fluctuations upstream of the operating turbine have more power compared to velocity fluctuations of the river. The higher turbulence energy upstream of the operating turbine shows energy cascading from the mean flow velocity to the turbulent part of the flow. Among the inflow parameters, the mean flow velocity, turbulence intensity, mean Reynolds stresses, and turbulence kinetic energy are the most widely recognized as having the main influence on fatigue loads. These velocity fluctuation rises measured upstream of an operating turbine adds to dynamic loads, contributes to turbine component fatigue and influences capital, maintenance, and operating costs.

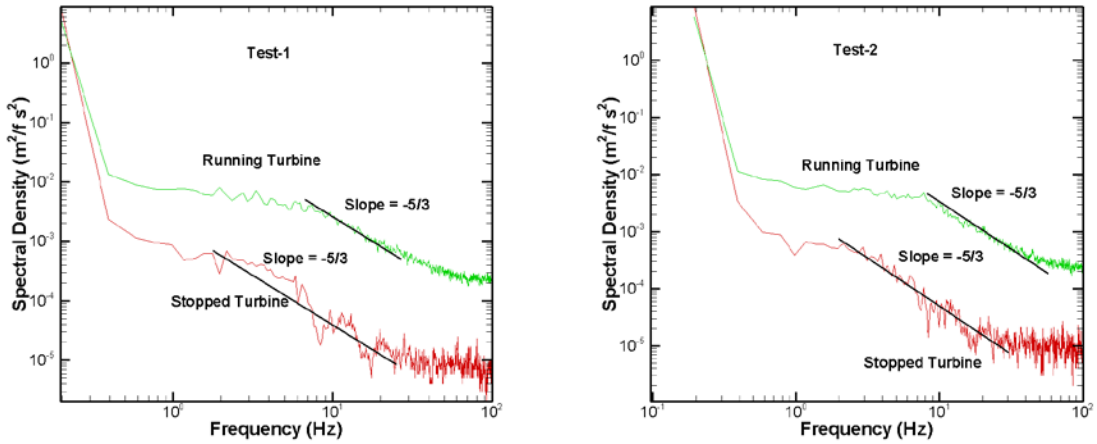

(a) (b)

Figure 3.13: Spectra of the stream wise velocity component estimated from 2000-sample series using a Hamming window with 50% overlap for (a) Test-1, and (b) Test-2

3.10 Summary

Field measurements show that the river flow contains large-scale eddies with couple of meters in diameter. These eddies provide a non-uniform inflow condition for vertical turbines. The operating turbine changes the flow pattern and imposes a negative velocity gradient to the upstream flow by reducing the flow velocity in the actuating disk of the turbine. Measurements show that the mean velocity drops 20% at $x/D = 1$ upstream of the 25-kW kinetic vertical turbine while the turbulence kinetic energy of the flow increases. It indicates that the intensity of small eddies increases in the flow. The negative velocity gradient upstream the operating turbine increases shear forces in the flow. Shear forces convert large-scale eddies into smaller eddies. This phenomenon is observable in the autocorrelation function results while the running turbine decreases the integral time scale value. The power spectrum of the measurement upstream of the running and stopped turbine shows a power increase at all ranges of frequencies. Although the size of eddies decreases due to the rotation of the

turbine, length scales are still comparable with the chord length of the turbine. This may cause a local separation over the blades or their stall. Further testing and investigations on the effect of upstream eddies on the performance characteristics of the VAHTs are conducted on a small-scale VAHT model in the water tunnel. The next chapters present the experimental setup and results of the small-scale VAHT model in the water tunnel to study various aspects under a more controlled and safer environment.

Chapter 4

Laboratory test facility and instrumentation

This chapter presents the facilities and instrumentations used for the laboratory experiment. A small-scale squirrel cage VAHT is designed and manufactured for testing in the University of Manitoba's water tunnel. The model is equipped with the appropriate sensors to monitor the behaviour of the turbine. This chapter first describes the facilities used for the tests, then presents the geometric characteristics of the turbine, and finally introduces sensors and equipments used for measurements.

4.1 Water tunnel

The water tunnel facility of the University of Manitoba is a recirculating design with the flow loop arranged in a vertical configuration. The interior dimensions of the test section are 61 cm wide by 60 cm high by 183 cm long. Flow around the models can be observed and video recorded from the bottom, front and back sides of the test section through Plexiglas windows. A single stage, axial flow, propeller pump drives the water in the water tunnel. The pump delivers a maximum flow rate of 362 l/s that creates 1 m/s flow speed in the test section when the height of the water is 60 cm at a full condition. The pump is belt

driven by a 30 HP, 1800 rpm, 460 VAC 3Ø 60 Hz Toshiba induction motor, Figure 4.1.

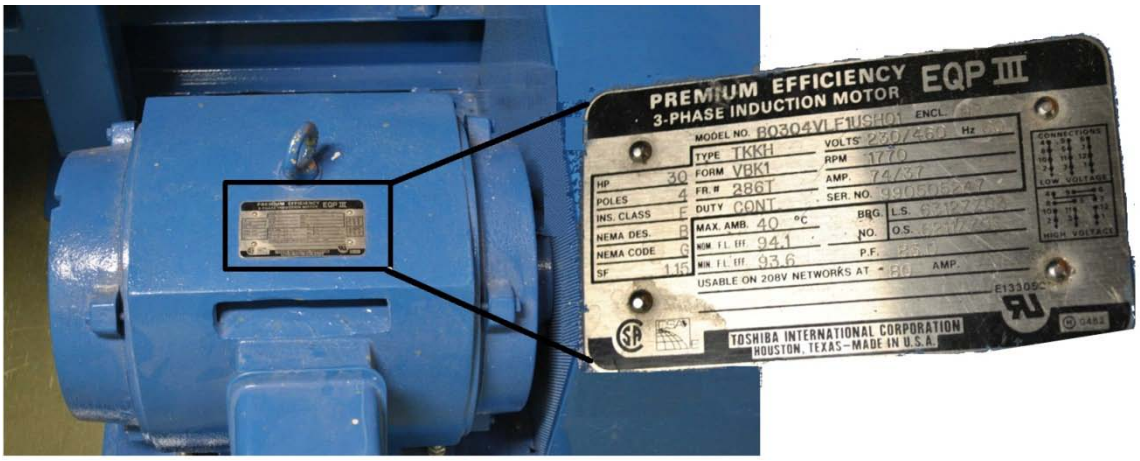

Figure 4.1: Driving motor of the water tunnel

A transistor inverter type, variable speed motor control regulates the pump flow rate adjusting the motor rpm, Figure 4.2 (a). The inverter is graded from 0 to 60 Hz. At 0 Hz the motor is stopped and it works at full power while the frequency is 60 Hz. Figure 4.2 (b) shows the relation between the current speed in the test section and the frequency of the inverter for the full test section, water height of 60 cm. The velocity uncertainty in the test section is less than 2.5 %. A series of honeycombs located before the test section break large eddies generated in the pump and reduce the turbulence intensity in the test section to less than 3% for the 1 m/s velocity. At lower speeds the turbulence intensity in the test section drops below 3%. A drain system enables the water tunnel to operate at any water height up to 60 cm.

(a)

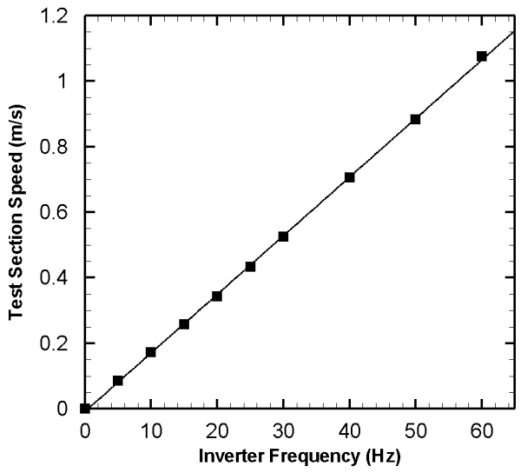

(b)

Figure 4.2: (a) Speed control inverter, and (b) current speed in the test section versus the inverter frequency

4.2 Model turbine

A scaled vertical turbine is designed for testing in the University of Manitoba's water tunnel. The design is a squirrel-cage vertical turbine with adjustable preset pitch angle system. The turbine is 30 cm in diameter and 30 cm in height. Blades are attached to two solid disks at both ends to approximate two-dimensional flow conditions for blades, eliminating tip vortexes and span-wise flow. The central shaft and support arms are eliminated in this design to reduce the blockage effect of the turbine and increase the power output. The turbine is capable of operating with two-bladed and four-bladed configurations, $\sigma = 0.33$ and $\sigma = 0.66$ respectively. Figure 4.3 shows the configurations of the scaled squirrel-cage turbine tested in the University of Manitoba's water tunnel. The turbine consists of three main sections: blades, endplates and supporting structure.

(a) (b)

Figure 4.3: Scaled turbine (a) four-bladed, and (b) two-bladed configurations

4.2.1 Blades

The blades are straight with no twist and taper, 30 cm in span and 5 cm in chord length. The blades are machined from T6082-T6 aluminum alloy on a computer numerical control (CNC) machine at the University of Manitoba with the accuracy of 0.05 mm. The blades are screwed at two points, $x/c = 0.25$ and $x/c = 0.5$, to solid disks at both ends. Figure 4.4 shows the blade of the turbine.

(a) (b)

Figure 4.4: The geometry of the blade (a) side view, and (b) profile section

The blades consisting of NACA-0021 airfoil profile sections, Figure 4.5. The first two digits of the NACA number describe, respectively, the maximum camber as

percentage of the chord and distance of maximum camber from the airfoil leading edge in tens of percent of the chord. For a symmetric airfoil, these two digits are zero. The last two digits describe the maximum thickness of the airfoil as percent of the chord. Therefore, NACA-0021 has no camber with a maximum thickness of 21% of the chord. The shape of a symmetric four-digit NACA airfoil is obtained from the Equation 4.1 where c is the chord length, x is the position along the chord, and y is the half thickness at a given value of x.

$$y_t = \frac{0.21}{0.2} c \left[0.2969\sqrt{\frac{x}{c}} - 0.1260\left(\frac{x}{c}\right) - 0.3516\left(\frac{x}{c}\right)^2 + 0.2843\left(\frac{x}{c}\right)^3 - 0.1015\left(\frac{x}{c}\right)^4 \right]. \qquad 4.1$$

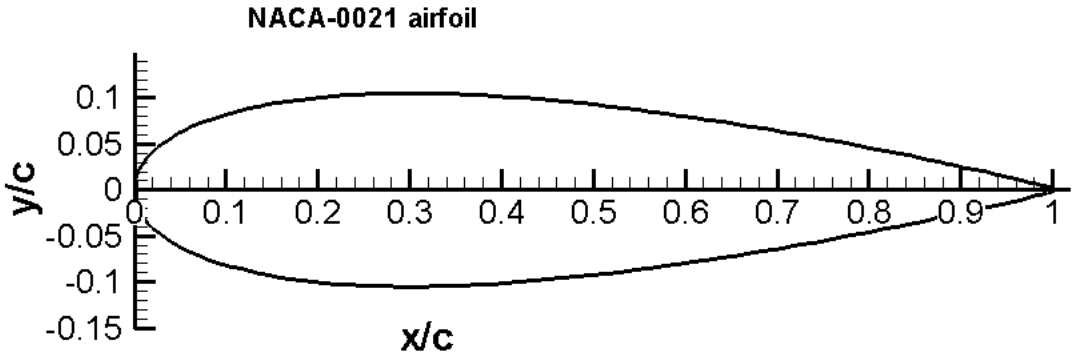

Figure 4.5: NACA-0021 profile

4.2.2 Endplates

The blades are attached to two solid disks at both ends to approximate two-dimensional flow conditions for the blades, eliminating tip vortexes and span-wise flow. Endplates are attached to each blade by two screws. A first screw fastens the turbine blades to the endplates at both ends allowing each blade to pivot ±10° around the aerodynamic center at $x/c = 0.25$; at $x/c = 0.5$, a second screw

in a sliding slot arrangement adds stiffness. The zero angle of attack is defined as the angle at which the position vector from the axis of rotation to any blade span wise position perpendicularly intersects the blade chord at $x/c = 0.25$. Angles between +10° and -10° are marked with 2.5° increments on the endplates at the trailing edge of the blades. In order to adjust the preset pitch angle, the second screw located at $x/c = 0.5$ is untightened, then the blade pivots freely around the $x/c = 0.25$. The trailing edge is adjusted in front of a marked point on the endplate that represents the right preset pitch angle and the screw at $x/c = 0.5$ is retightened. Figure 4.6 shows the blade preset pitch angle adjustment on endplates.

Aluminum and Plexiglas endplates are employed in this research, Figure 4.7 shows the two types of endplates. The aluminum endplates can operate at high-tension condition; therefore, they are used for general testing. The Plexiglas endplates are utilized in short periods for flow visualization inside the operating disk of the turbine specifically around the blades. Aluminum endplates have four sets of attachment holes and the Plexiglas endplates have 12 sets, every 30 degrees. The central hole allows the endplates to be attached to the holding shaft. Figure 4.8 shows the attachment holes on the endplates.

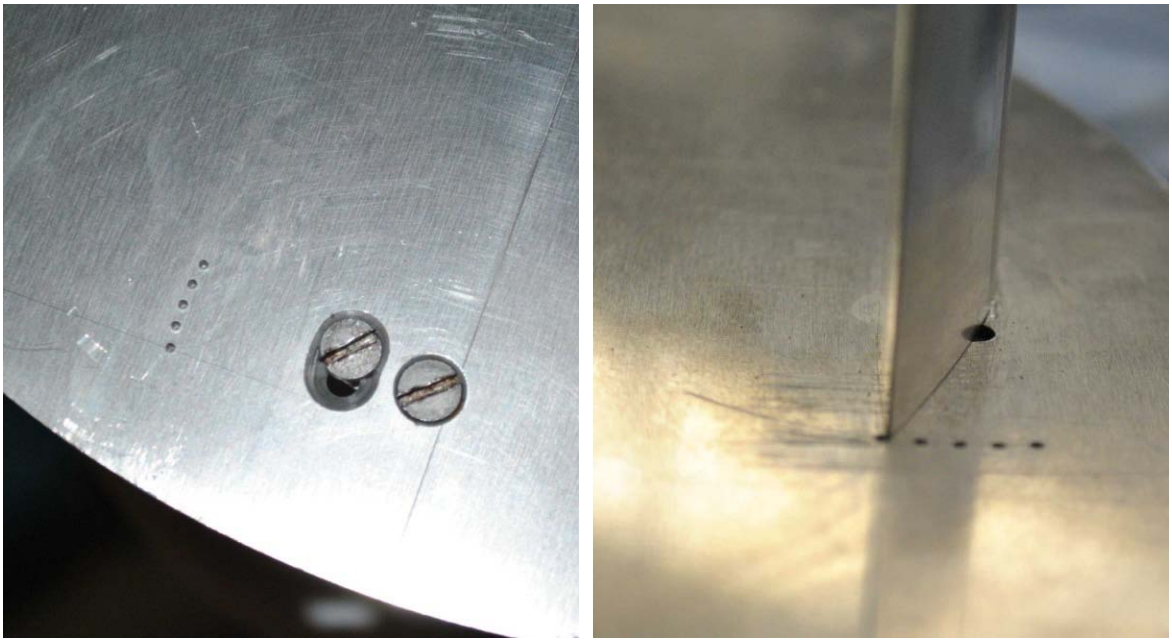

(a) (b)

Figure 4.6: Preset pitch angle adjustment on endplates (a) adjustment screws, and (b) preset pitch angle marks

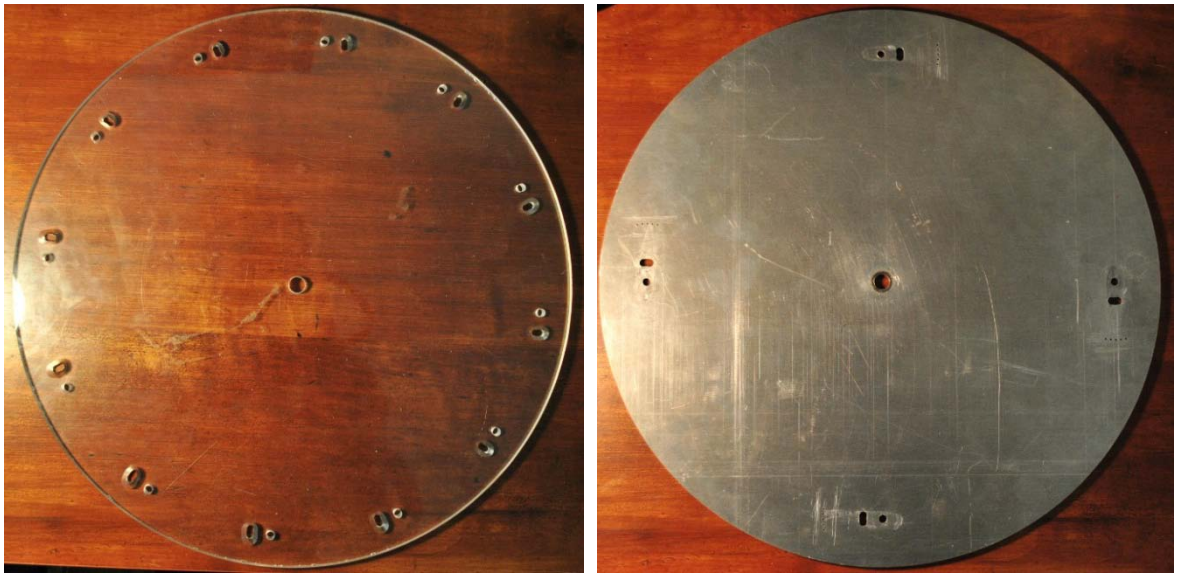

(a) (b)

Figure 4.7: Endplates (a) the Plexiglas model and (b) the aluminum model

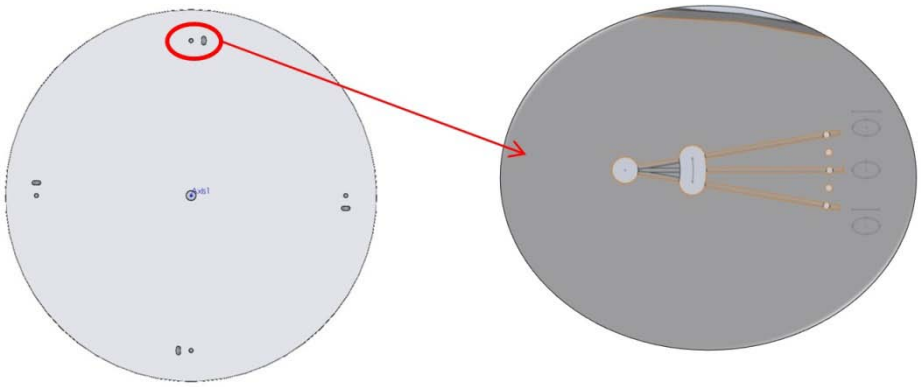

Figure 4.8: Blade attachment holes on the endplates

Figure 4.9: Vertical turbine and its supporting frame

4.2.3 Supporting structure

The supporting structure consists of two parts: frame and shafts. A cubic frame holds the turbine in the water tunnel. The width of the frame is equal to the internal width of the water tunnel, 60 cm, and the height of the frame is 65 cm. Sidebars of the frame are in the boundary layer of the water tunnel walls; therefore, they have a negligible effect on the flow pattern. However, to

eliminate the effect of the frame on the flow, the upstream bars are removed and are brought backwards, and are aligned with the center of the turbine. Figure 4.9 shows the turbine position in the frame. The frame is clamped to the water tunnel edge during testing, to increase the moment of inertia in order to reduce the structural vibrations.

The turbine is connected to the frame by two shafts: top shaft and bottom shaft. The bottom shaft connects the turbine to the frame, supporting the axial and radial forces resulting from the drag force and the weight of the turbine. A NTN 4T-LM11949 tapered roller bearing links the bottom shaft to the frame as they can take axial forces as well as being able to sustain radial forces. The top shaft passes through a NTN R16RS radial ball bearing embedded in the top steel bar of the frame. The radial ball bearing cancels the remained drag force of the turbine. The tapered roller bearing and radial ball bearing employed in the supporting structure are shown in Figure 4.10; Figure 4.11 shows the assembly of the turbine on the supporting frame.

(a) (b)

Figure 4.10: Connecting bearings: (a) tapered roller bearing, and (b) ball bearing

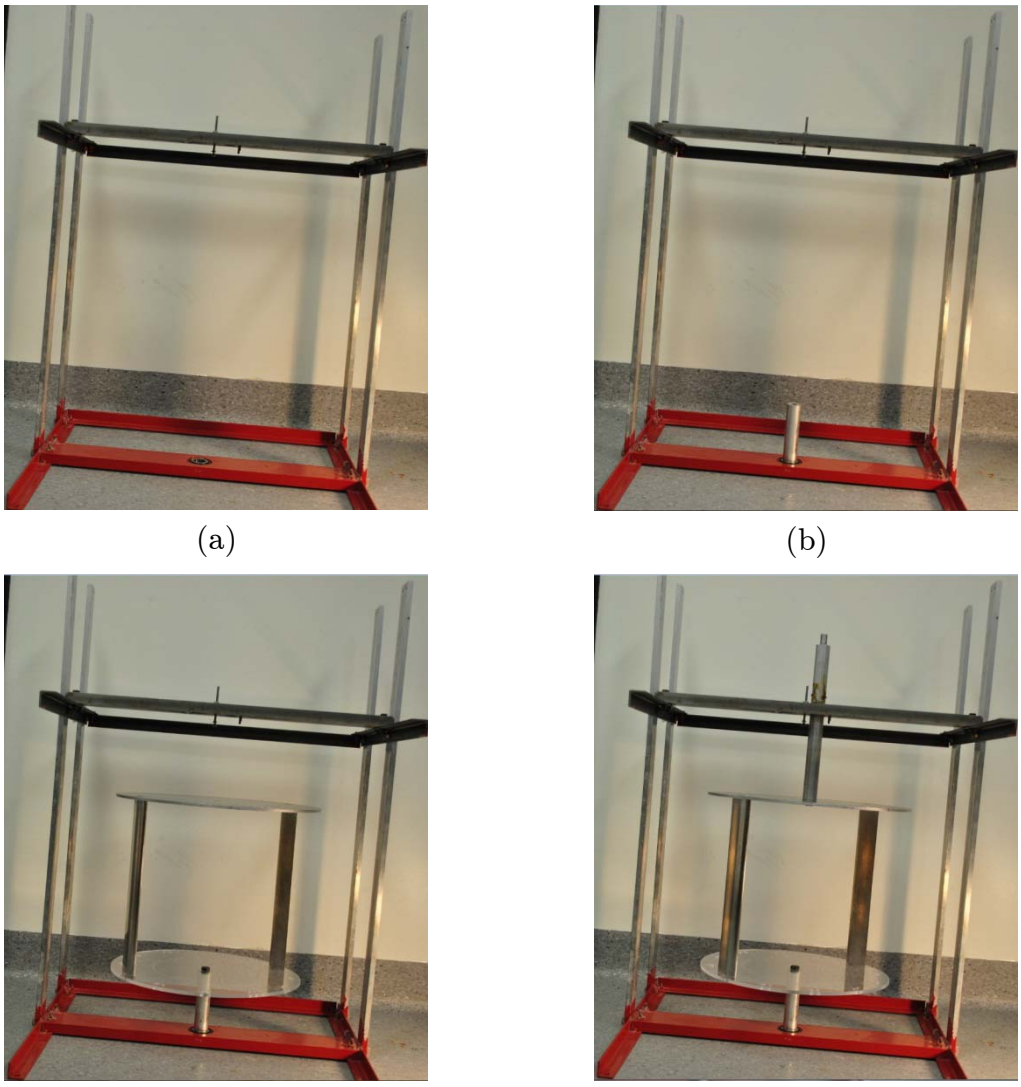

(a) (b)

(c) (d)

Figure 4.11: The turbine assembly on the supporting frame (a) supporting frame, (b) bottom shaft placement, (c) turbine placement in the bottom shaft, and (d) top shaft placement

4.3 Motor and controller

The power coefficient of the turbine varies with tip speed ratio. With no load on the generator, the rotational speed increases until freewheeling conditions are attained. The output power at freewheeling is equivalent to the frictional losses in the bearings and the rotational speed reaches the maximum value. To extract power from the turbine the rotational speed is decreased from the freewheeling

condition. The friction brake [114] or generator arrangement [115] are conventional methods to extract the output power and reduce the rotational speed of the turbine in laboratory settings. However, these methods are unable to cover the entire low rotational speed range due to the turbine stall at low tip speed ratios. The power coefficient measurement at low tip speed ratios is essential for understanding the behavior and performance of the turbine at starting stages while the inadequate torque at low tip speed ratios causes the self-starting a major issue for vertical turbines [116].

To address this issue, a driving motor assembly is adopted, where the motor operates the turbine at a constant tip speed ratio. The nominal torque of the driving motor has to be greater than the maximum torque of the turbine to be able to control the rotational speed of the turbine on the entire range of the tip speed ratio. Conventional AC and DC motors have a high nominal speed, about 1800 rpm. Therefore, their nominal torque is small. Electric motors operate with the nominal torque at rotational speeds lower than the nominal rotational speed, as shown in Figure 4.12. Based on the preliminary calculations a motor with the minimum torque of 5 Nm is required to operate the turbine for the range of tip speed ratios investigated. Using a motor with a typical nominal speed of 1800 rpm requires a motor with the minimum power of 1.25 HP. Motors at this size are relatively large and heavy for this application.

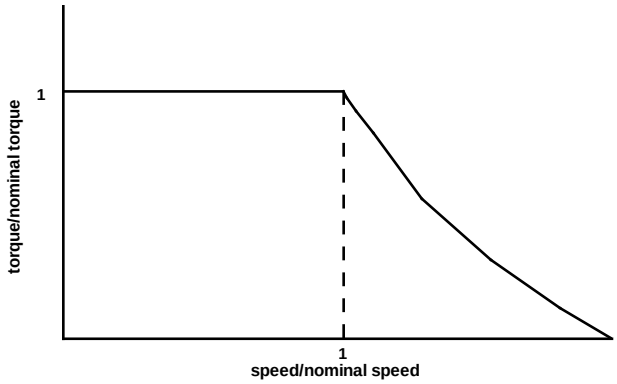

Figure 4.12: Schematic torque-speed diagram of an electric motor

Gear motors provide a high torque at low rotational speeds due to their low nominal rotational speeds. A 0.25 HP, 10:1 gear ratio Baldor GPP7451 DC gear motor is employed along with a Baldor DC controller to cover the entire range of the tip speed ratio, as shown in Figure 4.13. The output torque of this motor is 5.5 Nm with the maximum rotational speed of 250 rpm. For a typical flow speed of 0.7 m/s in the water tunnel, the driving motor is capable of running the turbine up to a tip speed ratio of 5.5. According to the field measurement and preliminary simulations, the maximum power coefficient of the turbine happens at a tip speed ratio between 2.5 and 3.2. A tip speed ratio of 5.5 is high enough to cover the entire power coefficient diagram.

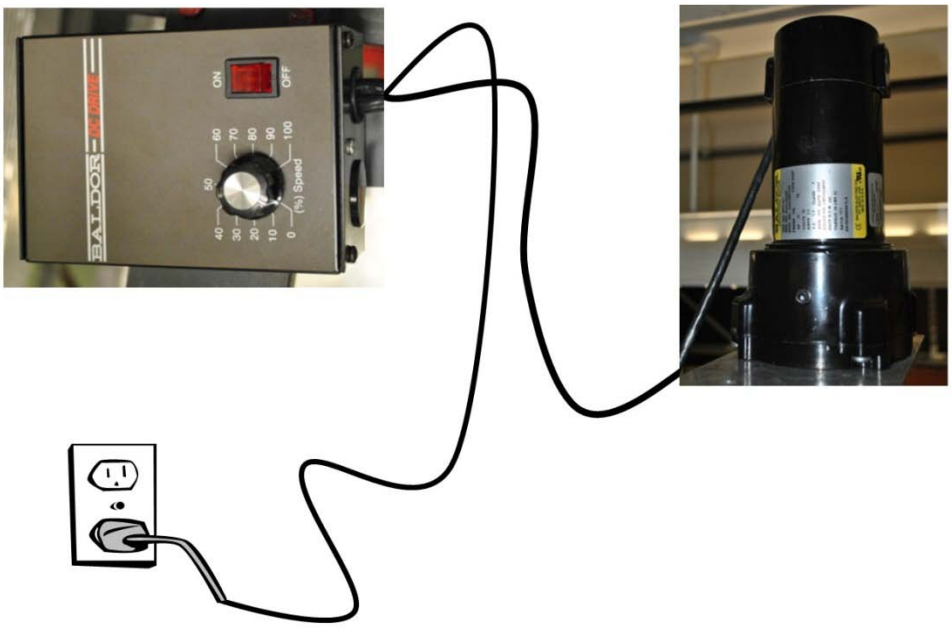

Figure 4.13: Driving system consist of a gear motor and a DC speed controller

4.4 Torque transducer

A TORQSENSE Rayleigh wave rotary torque transducer measures the bi-directional rotary torque in the shaft between the turbine and the gear motor, Figure 4.14. The transducer is a RWT-311-DB-KB model with the maximum torque range of 5 Nm and the maximum speed of 300 rpm. It also has a rotational speed sensor enabling direct measurements of transmitted power. The accuracy of the torque transducer is ±0.25% with a respond frequency of 100 Hz. A positive torque means the turbine tends to turn the motor faster but the motor resists and the torque transducer measures the motor resistance. At low tip speed ratios when the turbine stalls, the motor drives the turbine; therefore, the torque transducer measures a negative torque.

The outputs of the system are both analog and digital. However, the analog output is used. The analog DC voltages vary linearly with the torque and

rotational speed. The connection cable of the torque transducer is connected to the backside of the panel box described later. The maximum output voltage of the torque sensor is 5 V corresponding to 5 Nm torque, and the maximum output voltage of the rotational speed sensor is 10 V corresponding to 300 rpm.

The torque transducer is electrically connected and operational during the installation process to avoid damaging due to any torque overload. To avoid any axial loads or bending moments, the body of the transducer is restrained from rotation using a flexible strap and couplings for transducer shaft ends connections.

Figure 4.14: Torque transducer

4.5 Encoder

A Lika ROTAPULS C80 incremental optical encoder measures the azimuth angle of the turbine during the tests, Figure 4.15. The encoder is placed above the torque transducer before the gear motor; therefore, the measured torque remains unaffected by the resistance of the encoder. The connecting shaft goes through the central hole of the encoder and three side grub screws fix the encoder to the

shaft. In one rotation, the encoder sends 360 pulses through the connection cable to the backside of the panel box, described later. The output voltage increases linearly from 0 to 10 v while the azimuth angle increases from zero to 360°. The accuracy of the encoder is ±0.1 degrees.

Figure 4.15: Encoder

4.6 Panel box

The panel box contains a 12-volt adapter and a panel meter. The cables of the torque transducer and encoder are connected to the back side of the panel box. The panel box supplies the adequate operating voltage for the sensors and gathers the output ports of the sensors in a serial port. On the backside of the box there is an on/off switch for supplying power for the sensors and the display, Figure 4.16 (a). Two ports, a M23 port for encoder and a 15-pin serial port for torque transducer connect the box to the sensors. A 9-pin serial port links the box to the data acquisition system. On the front side of the panel, a display indicates the instantaneous azimuth angle Figure 4.16 (b). The setting of the panel meter is not accumulative. Therefore the azimuth angle is set to zero whenever it passes the 360° mark. There are three buttons on the front side of

the box. From top to bottom, they zero the azimuth angle, torque and peak torque.

(a) (b)

Figure 4.16: Panel box (a) back view and (b) front view

4.7 Data acquisition system

The data acquisition system consists of an instrument and software. The WINDAQ DI-158U is a portable data acquisition system that communicates with the recording computer through the USB port, Figure 4.17 (a). Power is derived from the PC through the USB interface so no external power is required. The DI-158U offers four fixed differential analog inputs as well as four bi-directional, I/O, digital ports. The 12-bit measurement resolution provides a responsive instrument capable of registering changes as small as one part in 2,048 ±0.05% of the full scale measurement range. Throughout ranges from sub-Hertz to up to 14,400 Hertz, allowing the DI-158 to connect to both static and dynamic signals. The data transfer rate of 14,400 samples per second is divided equally between the three channels engaged in measurement. The DI-158 provides gain ranges per channel of 1, 2, 4, and 8 with a full scale range of ±10 volts.

The data acquisition software, WINDAQ/Lite, offers real-time display and disk streaming Figure 4.17 (b). The real-time display can operate in a smooth scroll or triggered sweep mode with a scalable unit of measure. The error calculations for the power coefficient are provided in Appendix A.

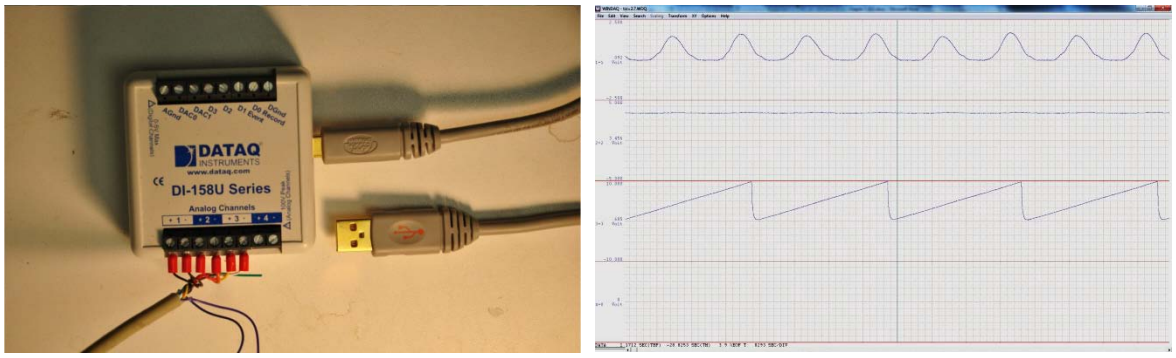

(a) (b)

Figure 4.17: Data acquisition system (a) hardware, and (b) software display

4.8 Assembly and calibration

The turbine is assembled on the supporting structure. A ceiling crane places the unit in the test section of the water tunnel. The front bar of the frame aligned with the center of the turbine is clamped to the water tunnel to reduce structural vibrations. The turbine shaft connects to the torque transducer using a jaw coupling to eliminate tension due to misalignment, as shown in Figure 4.18. Another jaw coupling attached to the gear motor connects the other side of the torque transducer shaft. The encoder is located between the transducer and the motor. Sensors are connected to the panel box and their outputs are connected to the analog ports of the data acquisition system and then displayed by the data acquisition software. Figure 4.19 shows the setup used during the water tunnel testing.

Calibration is required before testing at zero velocity flow. To calibrate the azimuth angle, first the motor turns the turbine to align the leading screw at $x/c = 0.25$ with the center of the front bar. At this position, the azimuth angle is zero; therefore, by holding the top button on the panel box the azimuth angle is set zero. The torque signal is set to zero by holding the two red buttons on the panel box bellow the position button. The real-time signals have offset from zero even after calibration. To reduce the error, the offset signal is measured before and after testing and average offset is calculated and removed from the signal of the operating turbine.

(a)

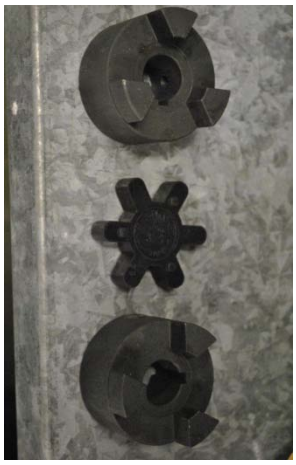

(b)

Figure 4.18: (a) The connection of the torque transducer and (b) jaw coupling

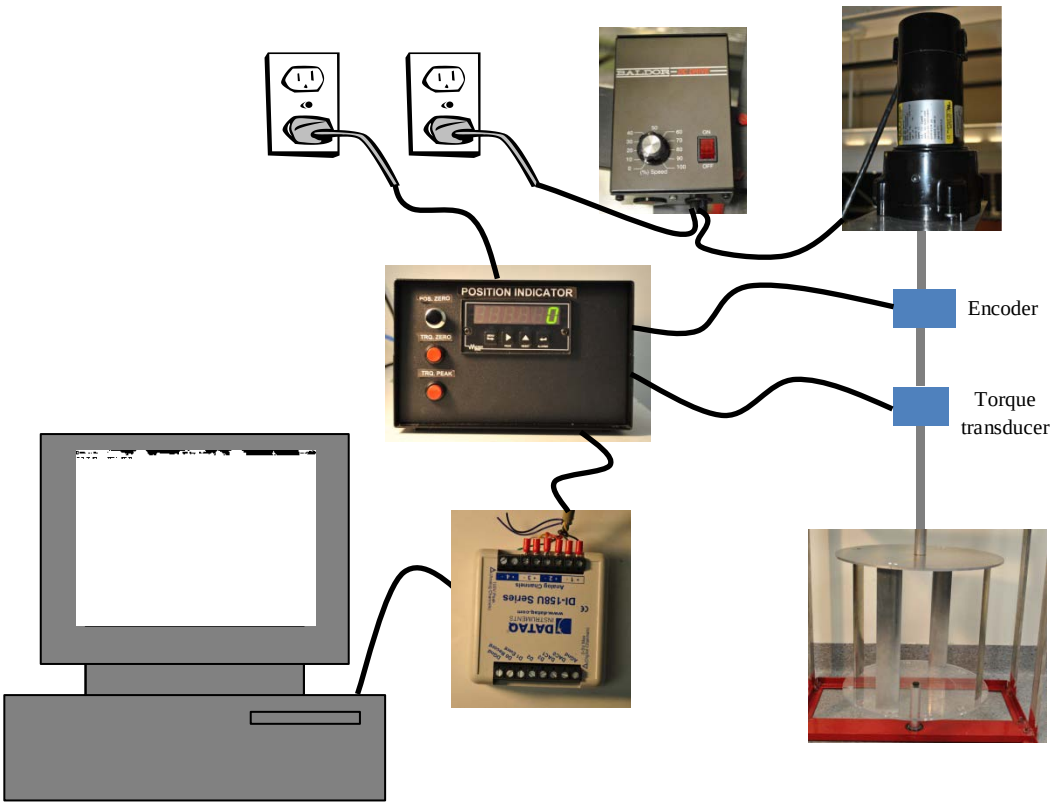

Figure 4.19: Test setup for the water tunnel experiment

4.9 ADV

The ADV measures local flow velocity in three directions. This technique uses the Doppler frequency shift between the emitted and reflected acoustic waves from scattering particles in the sampling volume to calculate the instantaneous velocity of the flow. During this research a Vectrino Nortek AS ADV measures the water velocity in both field and lab facility. This model of ADV has one transmit transducer and four receivers in parallel and allows data collection rates of up to 200 Hz. Figure 4.20 shows the ADV instrument and two sampling probes: a small size for the laboratory applications and a large size for the field measurements. The sampling volume of the laboratory probe is 5 cm away from the probe while for the field probe this distance is 10 cm. The sampling volume has a cylinder shape with 0.6 cm in diameter. The height of the sampling volume

is user adjustable and varies between 0.31 and 0.91 cm, as shown in Figure 4.21. Increasing the sampling volume size improves the precision of the measured velocity as a result of the higher number of samples used for the velocity calculation. However, the size of the sampling volume indirectly increases the signal-to-noise-ratio (SNR). According to the recommendations given by the manufacturer, the recording is valid as long as the SNR is above 10; however, for an accurate turbulence measurement the SNR should be above 19. Increasing the number of suspended particles in the flow helps to improve SNR. Table 4.1 contains the other specifications of the ADV.

Table 4.1: Vectrino Nortek AS ADV specifications

Velocity range	±0.01, 0.1, 0.3, 1, 2, 4 m/s (software selectable)
Accuracy	±0.5% of measured value ±1 mm/s
Sampling rate	1–200 Hz
Internal sampling rate	200–5000 Hz
Acoustic frequency	10 MHz
Uncertainty	1% of velocity range

The Vectorino measures the velocity components in XYZ coordinates. The receiver arm with the red marking represents the positive X-direction. The positive Z-direction is towards the ADV instrument and therefore the positive Y-direction is the cross product of the positive Z and X vectors, Figure 4.22.

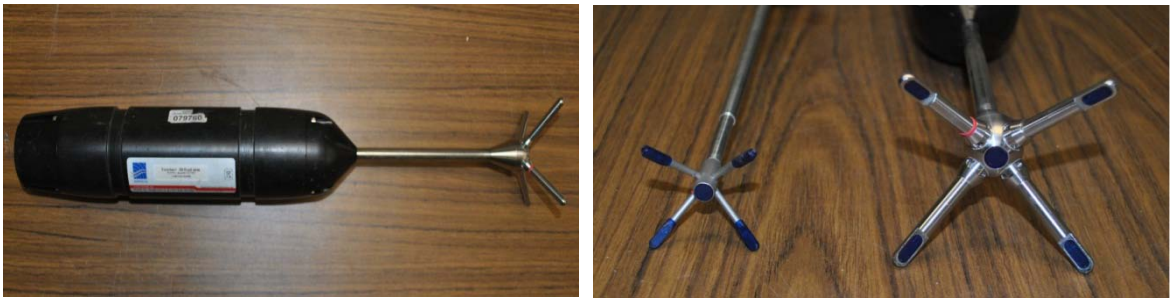

(a) (b)

Figure 4.20: Vectrino Nortek AS ADV (a) the instrument, and (b) laboratory (left) and field (right) probes

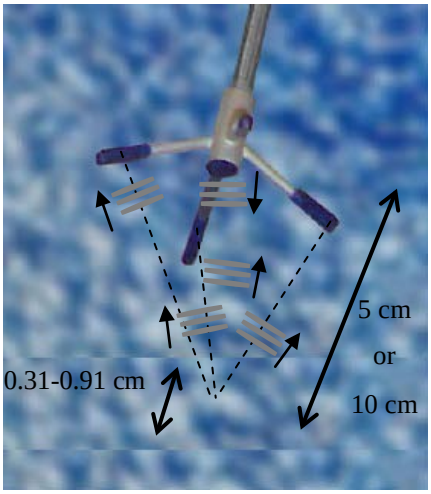

Figure 4.21: ADV probe and the sampling volume

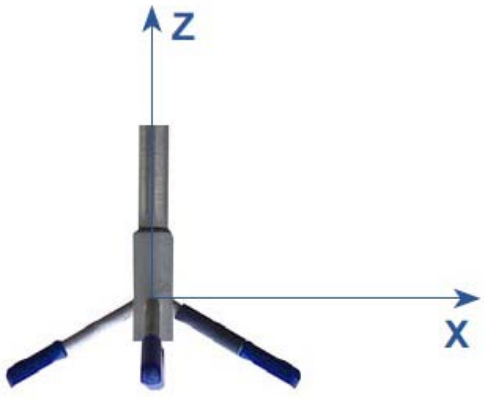

Figure 4.22: XYZ coordinate system for Vectorino

For laboratory application, DANTEC Polyamide seeding particles with 20 and 50 μm in diameter seed the flow, Figure 4.23. The density of these particles is close to that of the water, therefore, they follow the velocity pattern and remain suspended for a long period, about 3 to 4 hours with no flow. The size of seeding particles used for ADV measurement has to be small enough in comparison with the acoustic wavelength to have an accurate and spikeless data set. The Nortek Vectrino AS ADV has a 10 MHz acoustic transmitter, which generates acoustic waves with a 0.01 cm wavelength. The ADV requires over 40 counts per second of particles, as this is the threshold for noise; 80 counts and higher provide a proper ADV measurement condition [117]. The ADV probe-check displays the strength of the signal acquired in terms of signal amplitude.

(a) (b)

Figure 4.23: Seeding particles (a) in their packages and (b) suspended in the water passing in front of the ADV probe

Chapter 5

Sensitivity assessment

The primary goal of this research is to characterize the effects of the non-uniform inflow on the power output behavior of a vertical turbine in an array of turbines. To achieve this goal, the behavior of the turbine in the uniform inflow has to be characterized as a benchmark for comparisons process. As mentioned in the theory section, Chapter 2, nine dimensionless operating and design parameters define the performance characteristics of the turbine. The profile shape, aspect ratio, and the support arm are defined based on the geometry of the turbine, discussed in Chapter 4, and are unchangeable during the experiment. Other parameters like solidity, Reynolds number, preset pitch angle, and clearance coefficient are variable during the tests. The performance of the turbine is affected by these parameters. This chapter evaluates the effects of variable parameters on the performance of the turbine. Then the optimum operating domain of the turbine is obtained and the non-uniform inflow assessment is conducted through this domain.

5.1 Solidity

As defined in the theory section, solidity is the ratio of the total blade area to the turbine swept area. For H-type VATs it can be simplified as the ratio of the summation of chord lengths to the turbine diameter. The solidity change is accomplished by a change in the blade chord length and / or the number of

blades while the overall dimensions of the turbine are fixed. In this research, the number of blades controls the solidity of the turbine.

The efficiency of the vertical turbine increases with increasing solidity. When the turbine exceeds the optimum solidity, the efficiency of the turbine remains almost unaffected for a range of solidities. Eventually when the solidity exceeds this range the efficiency of the turbine decreases, as a high solidity turbine blocks the flow.

5.1.1 Background

Some of the earliest works on vertical axis wind turbines were published in the 1970s and early 1980s by National Research Council Canada and Sandia National Laboratories. These studies focused on Troposkein Darrieus vertical axis wind turbines. The objective of the program was to develop technology that results in economic, industry produced, and commercially marketable wind energy systems. To achieve the optimum design, several configurations, including rotors with different solidities, were tested in fields and wind tunnels. Blackwell et al. [118] tested a 2-meter diameter Troposkein turbine with variety of solidities ranging from $\sigma = 0.13$ to $\sigma = 0.3$ in the LTV Aerospace Corporation low speed wind tunnel. They employed two different test methods: constant turbine rotational speed with variable wind speed and constant wind speed with variable turbine rotational speed. The effect of solidity on the power coefficient is shown in Figure 5.1 for $\mathrm{Re}_{rel} = 1.5\times10^5$, at constant rotational speed, and $\mathrm{Re}_D = 1.15\times10^5$, at constant wind speed. Re_D is the Reynolds number defined based on the diameter of the turbine and the free stream speed. The most noticeable influence of solidity is that the freewheeling tip speed ratio increases with decreasing

solidity. For a synchronous application, this implies that power can be produced over a greater wind speed variation for a given turbine rotational speed. The tip speed ratio at maximum power coefficient increases with decreasing solidity. To obtain the maximize power coefficient, a solidity in the range from 0.2 to 0.25 should be chosen.

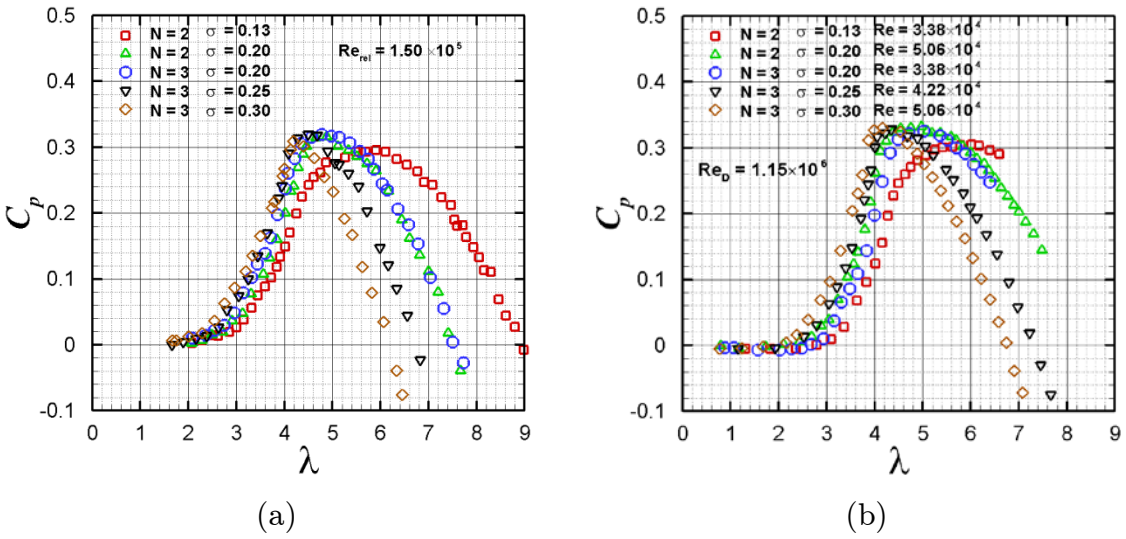

Figure 5.1: Power coefficient data for the Sandia 2-meter diameter Darrieus turbine as function of tip speed ratio at different solidities σ from 0.13 to 0.30 at (a) constant rotational speed, and (b) constant wind speed [118]

5.1.2 Water tunnel testing

In order to investigate the effect of solidity on the performance of the turbine, four- and two-bladed configurations are tested at four different Reynolds numbers. The four-bladed configuration has a rotor solidity of 0.67 while the two-bladed configuration has half of that, 0.33. For solidity experiments, the preset pitch angle is set to zero, as measured to the quarter-chord position on the airfoil. The turbine efficiency can exceed the Betz's limit, due to the high blockage ratio to simulate an operating turbine in an array of turbines.

Constant flow speed and variable turbine rotational speed are the testing conditions. Both configurations are tested at constant flow speeds of 0.4 , 0.5, 0.6 and 0.7 m/s corresponding to turbine Reynolds numbers, Re_D, of 1.35×10^5, 1.65×10^5, 2.00×10^5, and 2.35×10^5, respectively.

The performance characteristics of both turbine configurations are evaluated for constant flow speeds. Figure 5.2 shows the solidity effect on the power coefficient data for each of the four flow speeds. Solidity has two noticeable effects on the power coefficient diagram. First, higher solidity shifts the power coefficient diagram to the left side, with lower tip speed ratios. Second, for this turbine design, increasing solidity increases the maximum C_p.

Tip speed ratios at optimum C_p and freewheeling occur at lower values while the solidity increases from 0.33 to 0.67. The optimum C_p occurs at a tip speed ratio of 3 for a solidity of 0.33; whereas a solidity of 0.67 has an optimum power coefficient at a tip speed ratio of 2.5. At a constant flow speed, a lower tip speed ratio represents a lower rotational speed. For hydrokinetic applications, a low rotational speed decreases the probability of fish strikes and any impact with suspended objects in water.

The frequency of the dynamic loads on blades decreases with decreasing rotational speed. Conversely, the frequency of the dynamic loads on the turbine shaft increases by a factor of 1.67 (2×2.5/3) as the higher solidity is achieved by doubling the number of blades. The maximum angle of attack increases from ±19.5° to ±23.6° while the solidity increases from 0.33 to 0.67. Therefore, during the low solidity configuration tests, blades experience a light dynamic stall where

large vortex generation typically does not occur. At a low tip speed ratio of 2.5, high solidity, the maximum angle of attack exceeds approximately 5° above the static stall angle, resulting in a deep stall regime. As described in the theory section, during deep stall the blade will stall for a significant portion of the time, resulting in a negative damping loop, causing stall flutter.

The high solidity turbine, four-bladed configuration, improves the maximum power coefficient of the turbine between 15% and 30% for the Reynolds numbers higher than 1.35×10^5. At the turbine Reynolds number of 1.35×10^5, this improvement is more than 200%.

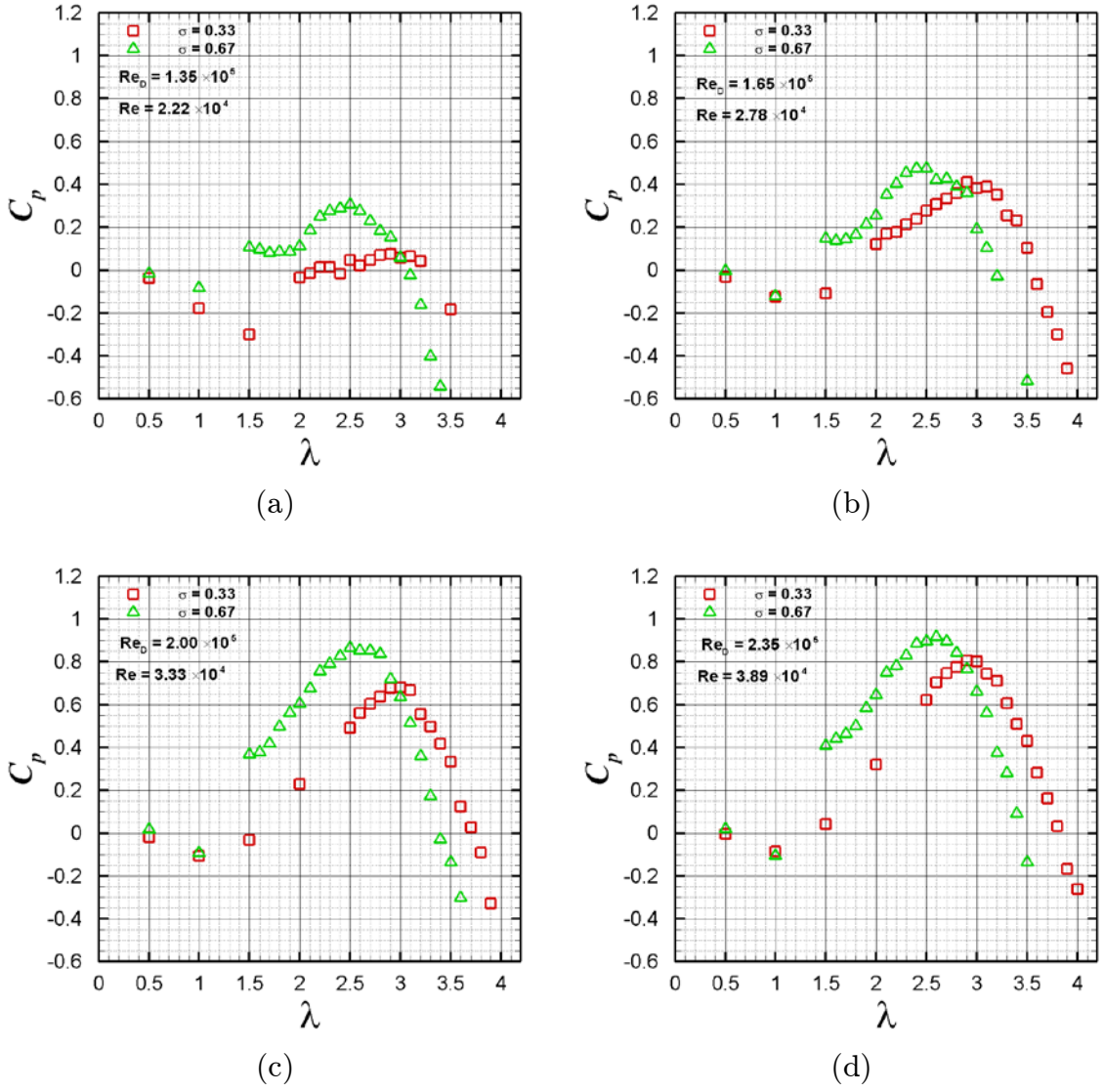

Figure 5.2: Power coefficient variation with rotor solidity at the turbine Reynolds number of (a) 1.35×10^5, (b) 1.65×10^5, (c) 2.00×10^5, and (d) 2.35×10^5

Figure 5.3 shows the effect of solidity on the tip speed ratio at the maximum power coefficient where a number of optimum tip speed ratios are plotted against their solidity. The data is adapted from tests conducted by Sandia Laboratories reported in SAND76-0130 [118], SAND77-1063 [40] and SAND80-0179 [41], National Research Council Canada (NRC) reported in NRC-LTR-LA-105 [119], Shawn Armstrong [120] and tests performed by the author. Both Sandia and

NRC turbines are the Troposkein Darrieus type, while the Armstrong and Birjandi tests were performed on straight-bladed turbines. For a Troposkein turbine, the tip speed ratio is reported at the point of largest diameter, located at the equator of the turbine where the radius is largest. Most of the blade is traveling at lower speeds than the equator on a Troposkein turbine whereas the entire straight blade travels at the same speed for H-type and squirrel cage turbines. Furthermore, since solidity is the ratio of the total blade area to the area swept by the turbine, for a Troposkein turbine, a large fraction of the blade does not contribute to the power output.

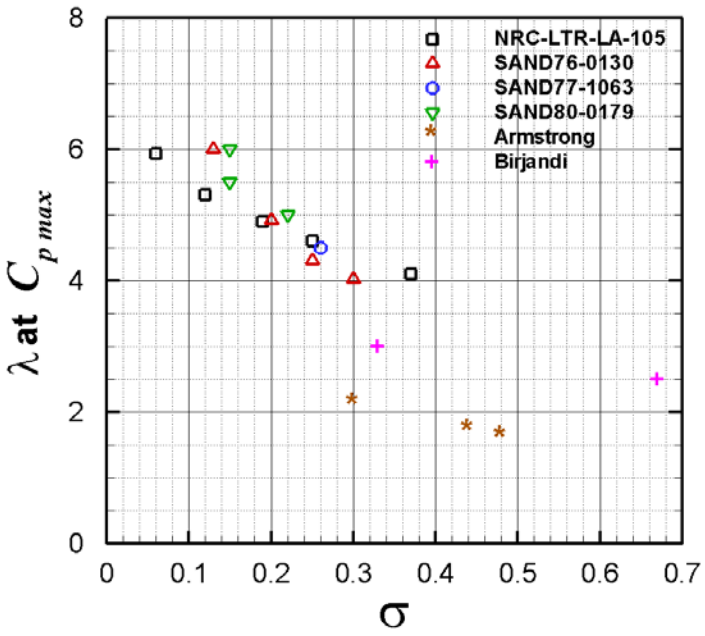

Figure 5.3: Tip speed ration at maximum power coefficient of vertical turbines for a number of solidities

In general, the tip speed ratio at the peak power decreases as the turbine solidity increases, which is in agreement with the water tunnel testing results. At low solidities, the optimal tip speed ratio appears to be roughly inversely proportional to the solidity while at higher solidities the curve is flattened out.

5.1.3 Summary

These tests and investigations show that VAT with a solidity less than 0.2 operates at a lower efficiency compare to a VAT with a solidity higher than 0.2. The performance of a VAT with low blockage ratio, like a single turbine operates in a wide channel or river, remains almost the same while the solidity increases above 0.2. However, for a turbine with high blockage ratio, like a turbine in an array of turbines or in a narrow waterway, even solidities higher than 0.6 still improve the performance of the turbine. At higher solidities, the maximum power coefficient occurs at lower tip speed ratios. The performance sensitivity of the turbine to the solidity is pronounced at low Reynolds numbers.

5.2 Preset pitch angle

There are two ways to control the blade angle of attack (AOA), α: by adjusting the tip speed ratio, λ, or by adjusting the preset pitch angle, α_p. Decreasing the tip speed ratio of the turbine causes the absolute value of α to increase in both upstream and downstream passes, and vice-versa. However, a positive preset pitch angle reduces α in the upstream pass and increases the absolute value of α in the downstream pass. Due to the energy extraction through the upstream pass, the flow speed decreases for the second half of the rotation; therefore α is smaller than the theoretical values for the downstream pass. Increasing the preset pitch angle increases α for downstream pass enables the turbine to extract more energy in the second half of the rotation. It also reduces the extent of dynamic stall by reducing α on the upstream pass.

5.2.1 Background

The first report into the effect of the preset pitch angle on the performance of vertical turbines was a result of blade manufacturing process errors, reported by South and Rangi in 1972 [119]. They tested a two-bladed, 4.27 m diameter Darrieus turbine with a solidity $\sigma = 0.07$ at the NRC 9 m wind tunnel. The turbine blades used in their investigation were symmetrical NACA-0012 profile blades. They accidentally used a preset pitch angle of $\alpha_p = 0°$ instead of the intended pitch angle of $\alpha_p = 4°$. Their results showed that the neutral pitch angle increases C_p approximately 11% more than the value obtained with a 4° toe-out. It also can be seen from Figure 5.4 that the maximum C_p occurs at a lower λ when $\alpha_p = 0°$.

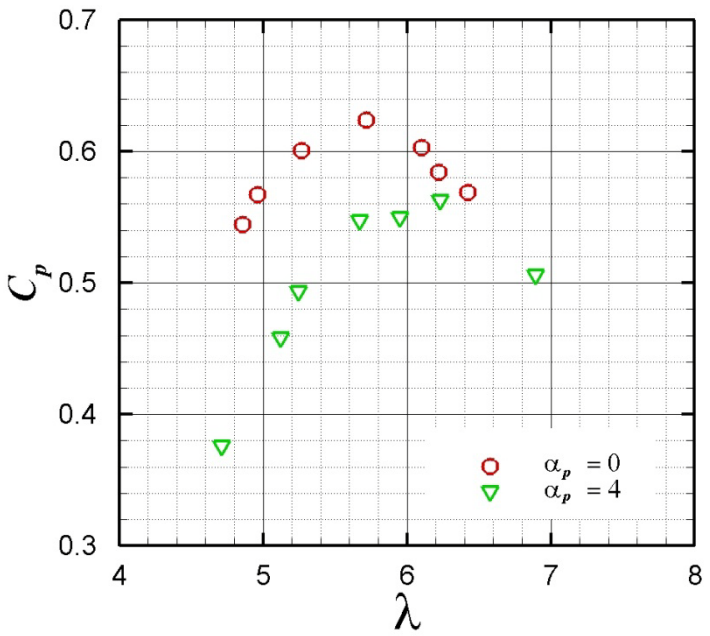

Figure 5.4: South and Rangi power coefficient diagrams during the accidental preset pitch angle offset [119]

Klimas and Worstell [121] conducted the first systematic investigations on preset pitch angle effects by adjusting the tower-blade attachment offset. In the tower-

blade attachment offset method the preset pitch angle is adjusted by offsetting the perpendicular intersection of the blade chord line and the blade position vector from the axis of rotation. They tested a two-bladed, 5.0 m diameter Darrieus turbine with a solidity $\sigma = 0.15$ and symmetrical NACA-0015 profile blades. They showed that, while the leading edge of the blade is attached to the central shaft, the leading edge of the blade experiences a zero incident angle to the flow. However, due to the farther distance of other parts of the blade from the center of the rotation, Figure 5.5, they experience a local non-zero toe-out angle. Using this concept, Klimas and Worstell translated the tower-blade attachment offset into the effective preset pitch angle. The equivalent preset angle of the blade with a tower-blade attachment offset of x can be determined by:

$$\alpha_p = \arctan\left(\frac{x}{r}\right). \qquad 5.1$$

In this investigation they tested the turbine at various tower-blade attachment offset equivalent preset pitch angles between $\alpha_p = 7°$ and $\alpha_p = -3°$. They found that for the preset pitch angles tested, the power coefficient varies from a maximum of 0.36 at $\alpha_p = 2°$ to a minimum of 0.24 at $\alpha_p = -3°$. Figure 5.6 shows the results for the power coefficient versus tip speed ratio at various pitch angles. The maximum power coefficient occurs at tip speed ratios between 5.4, at $\alpha_p = 2°$, 7°, and 6.5, at $\alpha_p = -1°$, 0.5°. The preset pitch angle not only changes the maximum power coefficient characteristics of vertical turbines, but it also changes the freewheeling tip speed ratios. The highest tip speed ratio value for freewheeling, $\lambda = 10.5$, occurs at $\alpha_p = 0.5°$ and the lowest one, $\lambda = 7.9$, occurs at

$\alpha_p = 7°$. At the end of the study, Klimas and Worstell concluded that vertical turbines are sensitive to the preset pitch angle, as they observed a 50% variation in the turbine efficiency throughout their experimental range of preset pitch angles.

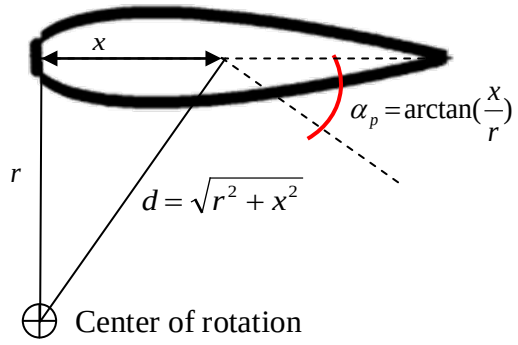

Figure 5.5: Blade distance from the central shaft as a function of chord location

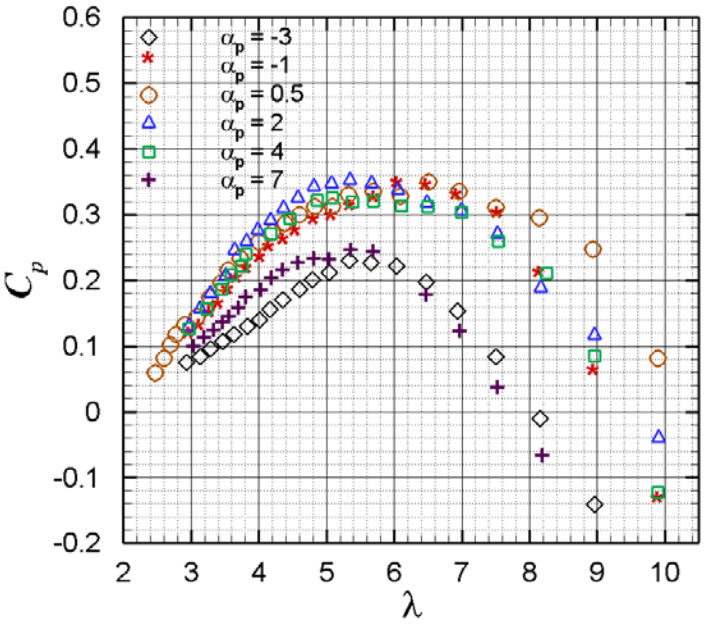

Figure 5.6: Klimas and Worstell power coefficient diagrams during the accidental preset pitch angle offset [121]

5.2.2 Test procedure

In this study, the squirrel-cage vertical hydrokinetic turbine is tested in the water tunnel to assess the influence of the preset pitch angle on the power coefficient of vertical turbines. The turbine blades are fastened at two points to the endplates and can pivot ±10° around the position $x/c = 0.25$, while the attachment at position $x/c = 0.5$ is a sliding slot. The angle of attack is defined as the angle between the blade chord line and a line tangent to the blade motion from the quarter chord position, with toe-out having a positive value. Angles between +10° and -10° with 2.5° increments are marked on the endplates at the trailing edge of the blades. In order to adjust the preset pitch angle, the fastener located at $x/c = 0.5$ is loosened, allowing the blade to freely pivot around the position $x/c = 0.25$. The trailing edge is adjusted in front of a marked point on the endplate that represents the correct preset pitch angle and the fastener at position $x/c = 0.5$ is tightened.

Tests are performed at four turbine Reynolds numbers, 1.35×10^5, 1.65×10^5, 2.00×10^5, 2.35×10^5 and 2.40×10^5, on the turbine with two solidities, $\sigma = 0.67$ and $\sigma = 0.33$. The Reynolds number is modified by changing the free stream speed. First, four blades are mounted on the turbine, $\sigma = 0.67$, and the turbine is tested at series of preset pitch angles from -5° to +10° by increments of 5°. Then two of the blades are removed and the turbine is tested at the same preset angles except the turbine is tested at the preset pitch angle of 2.5° at turbine Reynolds numbers of 2.00×10^5 and 2.35×10^5.

5.2.3 Test results

Results for the four-bladed turbine, $\sigma = 0.67$, show that the power coefficient is significantly sensitive to the preset pitch angle, as shown in Figure 5.7. The power coefficient on the entire range of tip speed ratios is negative while the preset pitch angle is -5°, toe-in. At a preset pitch angle of zero, the turbine generates positive power through all tip speed ratios. The maximum power coefficient occurs at a tip speed ratio of 2.5 except for the turbine Reynolds number of 2.40×10^5 that occurs at 2.6. Increasing the preset pitch angle to 5° increases the maximum power coefficient considerably and causes it to occur at a smaller tip speed ratio. For the 5° preset pitch angle, the power coefficients increase 74%, 75%, 21% and 59% at turbine Reynolds numbers of 1.35×10^5, 1.65×10^5, 2.00×10^5, 2.35×10^5 respectively. The 5° toe-out preset pitch angle also reduces the freewheeling tip speed ratios of the four-bladed turbine. The power coefficient of the turbine rapidly drops as the preset pitch angle increases to 10°, as shown in Figure 5.7. Although the power coefficient decreases for 10° toe-out preset pitch angle, the tip speed ratios at maximum power coefficient and freewheeling show reductions in their values.

Two blades are removed from the turbine and the tests are performed on the two-bladed turbine, $\sigma = 0.33$. Results show that the low solidity turbine in Figure 5.8 follows the same pattern. The maximum power coefficient increases while the preset pitch angle increases from zero to 5°; and it decreases when the pitch angle increases from 5° to 10°. In order to find an optimum preset pitch angle, the two-bladed turbine is tested with 2.5° preset pitch angle at two

Reynolds numbers of $Re_D = 2.00\times10^5$ and $Re_D = 2.35\times10^5$. Results show that the turbine with a preset pitch angle of 2.5° outperforms the turbine with a preset pitch angle of 5°. The maximum power coefficient increases 33% and 26% at the turbine Reynolds numbers of 2.00×10^5 and 2.35×10^5 respectively while the preset pitch angle decreases from 5° to 2.5°. For the rest of the experiments the 2.5° preset pitch angle is used.

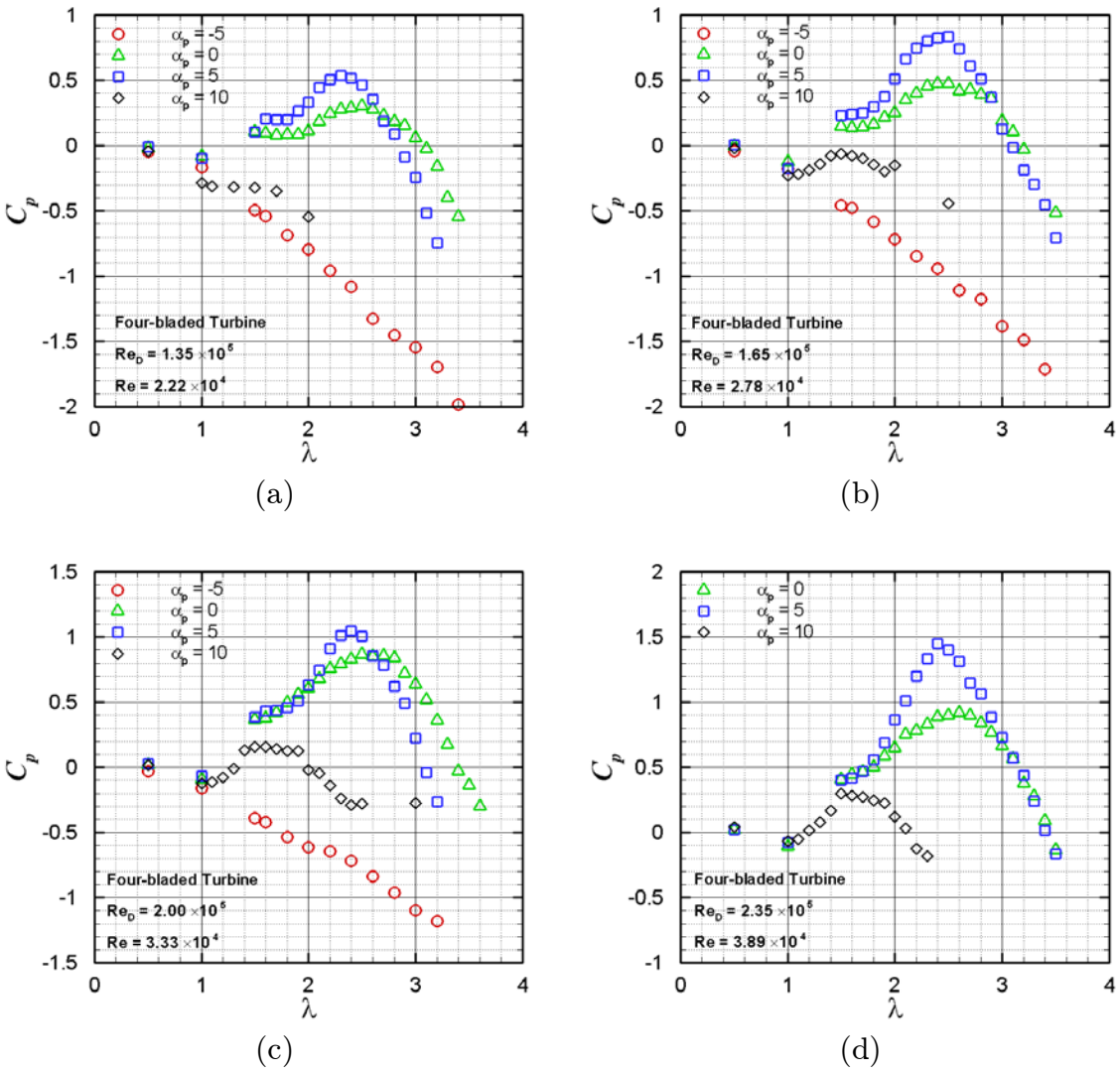

Figure 5.7: Preset pitch angle effects on the performance of the four-bladed turbine at turbine Reynolds numbers of (a) 1.35×10^5, (b) 1.65×10^5, (c) 2.00×10^5, and (d) 2.35×10^5

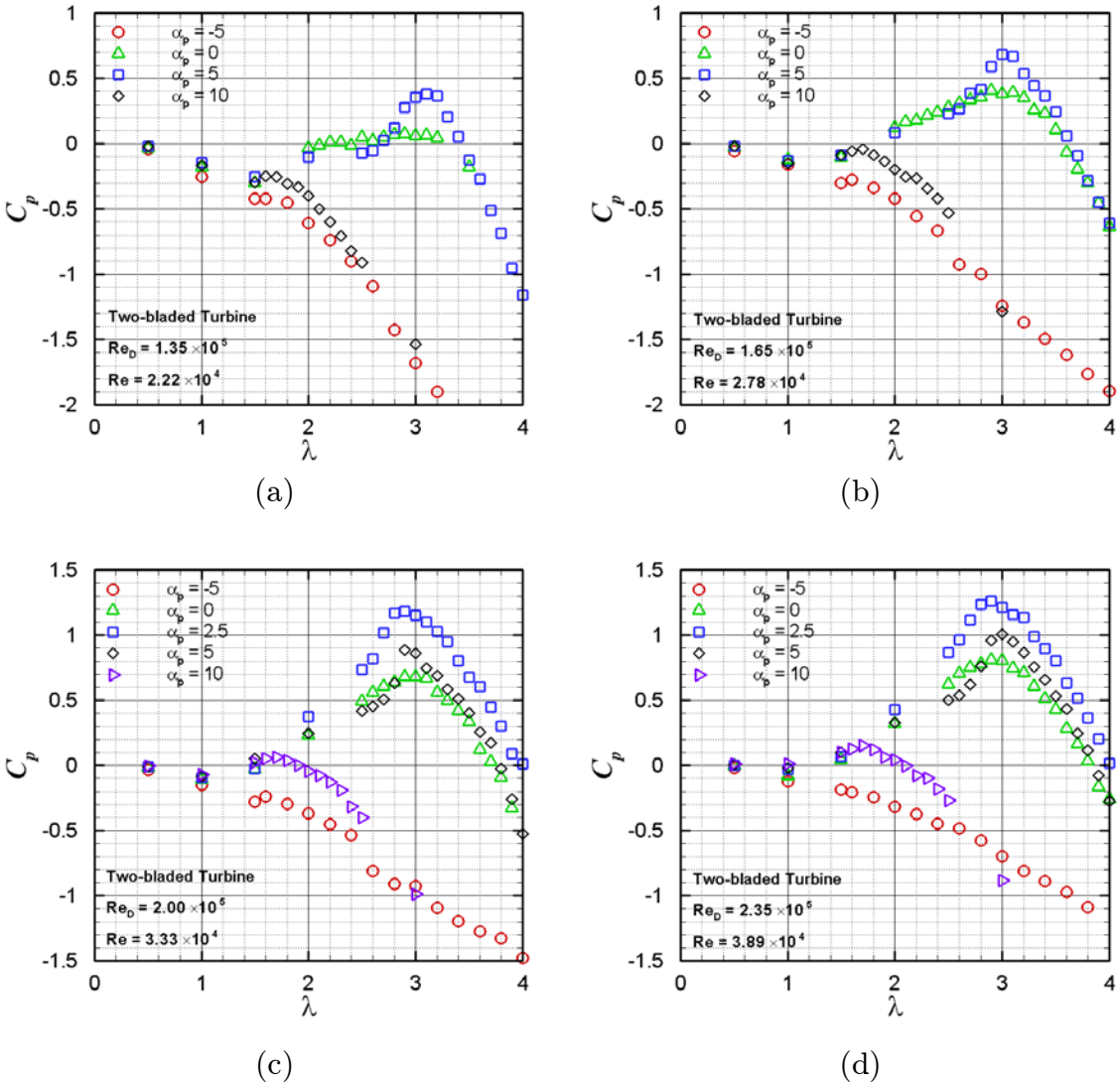

Figure 5.8: Preset pitch angle effects on the performance of the two-bladed turbine at turbine Reynolds numbers of (a) 1.35×10^5, (b) 1.65×10^5, (c) 2.00×10^5, and (d) 2.35×10^5

5.2.4 Summary

The performance of VATs is sensitive to the preset pitch angle. Toe-in angle has a negative effect on the efficiency of the turbine while toe-out angles between 2° and 7° can help to improve the efficiency of the turbine. The toe-out angle reduces the angle of attack in the upstream pass and increases the absolute value

of the blade angle of attack in the downstream pass. Therefore, the toe-out preset pitch angle reduces the intensity of the dynamic stall in the upstream pass and increases the power extraction in the downstream pass of the turbine. By considering results at the solidity section, one can conclude that the toe-out preset pitch angle is an essential rule for high solidity turbines. High solidity turbines operate at low tip speed ratios; therefore, the maximum angle of attack in the upstream pass is high above the stall angle of attack. In this condition, the turbine loses efficiency due to the deep dynamic stall conditions. The toe-out preset pitch angle reduces the maximum angle of attack in the upstream pass and moderates the dynamic stall intensity. At the same time, the toe-out angle enables the turbine to extract more power in the downstream pass. Thus, a toe-out preset pitch angle between 2 and 7 is highly recommended for VATs, particularly for high solidity models.

5.3 Free-surface effect

The installation and maintenance of hydrokinetic turbines in deep waters are challenging; therefore, many turbines operate near free-surface areas, especially VAHT models. Deep waters limit accessibility and increase installation and maintenance costs. There are various installation methods for hydrokinetic turbines: installation on the riverbed or seabed, use of a vertical mast, installation beneath a floating platform, and kiting the turbine with a cable. The riverbed or seabed installation is practical when the bed is smooth. The floating platform installation is a convenient method as it offers an easy access to the turbine. However, it is limited by cold weather and floating debris [122]. Irrespective of installation methods, turbines can be influenced by the free-surface, as the water level changes on a daily and seasonal basis in tidal and river

applications. Blades may be above the free-surface during low tide or low river level conditions. The proximity of the free-surface and the fact that the blades themselves are partially submerged affects the hydrodynamics and thus the power coefficient of these turbines.

The water level in the test section of the water tunnel is adjustable from zero to 60 cm. In this section, the turbine is tested at various water levels to investigate the free-surface effect on the performance of the turbine. Based on the results obtained in this section, an appropriate water height is chosen for the rest of the rest of the experiment.

5.3.1 Hydrokinetic clearance coefficient

There are few operational tidal and river kinetic turbines tested in the field. Some of the hydrokinetic turbines are subjected to free-surface blockage. To classify the free-surface blockage effects, a non-dimensional clearance coefficient, C_h, is defined as:

$$C_h = \frac{H}{L}, \tag{5.2}$$

where H is the water height above the turbine and L is the rotor diameter for horizontal turbines and blade height for vertical turbines. The positive clearance coefficient means the water level is above the turbine blades; when the water level is below the top of the turbine blades, C_h is negative. We now classify the clearance coefficient, C_h, for recent hydrokinetic turbine demonstrations.

Seaflow: In May 2003, 3 km north east of Lynmouth on the North Devon Coast, England, in the Bristol Channel with a tide range of 10 m, the prototype SeaFlow was installed [123]. SeaFlow has a 2-bladed horizontal axis rotor, 11 m in diameter, and a rated power of 300 kW. Test results show that the efficiency of the single turbine is between 40% and 50% which is larger than the expected design efficiency. For almost four years, SeaFlow was the world's largest offshore tidal generator. Having an average depth of 25 m at Bristol Channel, the clearance coefficient C_h of SeaFlow varies between 0.18 and 0.64.

SeaGen: SeaGen is the world's first commercial-scale grid-connected tidal turbine developed by Marine Current Turbines. The nominal output power of SeaGen is approximately 1.2 MW. Turbine consists of twin 16 m diameter axial flow rotors mounted on a crossbeam on either side of a steel vertical tower. Each rotor generates 600 kW power [124]. The first SeaGen generator was installed in Strangford Narrows between Strangford and Portaferry in Northern Ireland in April 2008 and was connected to the grid in July 2008. The Strangford Narrows has an average depth of 26.2 m at the test site. At the lowest tide the water level drops to 24 m and it rises to 28.3 m at the highest point. Based on the dimensions of the turbine and the depth of the sea, the estimated clearance coefficient C_h varies between 0.25 and 0.38.

HS300: HS300 is a 300 kW prototype tested in Kvalsund, Norway and became operational in November 2003. The turbine has proven to be both efficient and reliable through deployment, operation, retrieval, maintenance and, redeployment cycle. HS300 is a three-bladed horizontal axis hydrokinetic turbine developed by Hammerest Storm [125]. The water depth is about 50 m at Kvasund test site giving a C_h of 0.75.

AK-1000: In August 2010 the Atlantis Resources Corporation's AK-1000 turbine was unveiled at Invergordon, Ross and Cromarty, Highland, Scotland. It is claimed to be the largest tidal turbine ever built. AK-1000 has twin rotor sets with fixed blades and is rated at 1 MW at a flow speed of 2.6 m/s. AK-1000 was deployed during the summer of 2011 at the European Marine Energy Centre (EMEC) facility in Orkney. EMEC's tidal test site in the Fall of Warness has a 50 m depth [126]. In this depth of water, AK-1000 has a clearance coefficient of 1.02 at that location which is larger than that of the other tidal turbine demonstration projects.

Verdant Power: Verdant Power developed the world's first array of grid-connected tidal turbines in the Manhattan East River in the New York City between 2006 and 2008. Three-bladed, horizontal axis turbines with 5 m in diameter generate approximately 35 kW each at the tidal currents of 2 m/s. The water level in the East River fluctuates between 7.5 and 9 m. The bottom of the rotors are 2 m above the riverbed, therefore rotors have a clearance coefficient between 0.1 and 0.4 [127].

New Energy: New Energy develops vertical hydrokinetic turbines with 5, 10, 25, 125 and 250 kW power generation systems. A 5 kW system was installed in December of 2007 at Pointe du Bois, Manitoba, Canada at a site operated by the University of Manitoba upstream of a Manitoba Hydro generating facility. The system operated through the winter and was removed prior to spring breakup. In June of 2008, a 25 kW unit was installed and connected to the Manitoba Hydro grid [122]. Both turbines were deployed under a pontoon vessel so that the gear box, generator and brake are mounted above the water surface. This

deployment method provides a convenient turbine installation and removal; water depth imposes no restriction on this method. Distance between the turbine and the free-surface is always fixed and water level fluctuation has no influence. However, the shaft length, which determines the clearance coefficient, is a design parameter and the designer has the option to modify this length. The 5, 10 and 25 kW turbines are 1.52, 1.52 and 4.83 m in diameter with the blade heights of 0.76, 1.52 and 2.41 m respectively. The distances from the top of rotors to the free-surface are 0.65, 0.75 and 1.05 m correspondingly for 5, 10 and 25 kW turbines. The clearance coefficients for vertical turbines are calculated based on their rotor height and it is almost a fixed number for the installation beneath a floating platform. New Energy's vertical turbines' clearance coefficients are 0.87, 0.49 and 0.44 correspondingly for 5, 10 and 25 kW turbines.

Water tunnel tests of the University of Manitoba's scaled turbine: In this present study, a squirrel-cage vertical hydrokinetic turbine is tested in the University of Manitoba's water tunnel facility to assess the influence of the water level on the power coefficient of vertical turbines. The scaled turbine is constrained between the water tunnel walls and the free-surface, which represents realistic operating conditions for turbine arrays in shallow waters. As a result, the power coefficient of the model turbine increases due to the blockage and free-surface effect. The experiment starts with the water level above the turbine. Then the free-surface is lowered in 2 cm increments, the power coefficient measured at each water level, and water level is reduced until one third of the blade height is above the free-surface. During the experiment, the air suction and water separation phenomena were observed on the low-pressure side of the blades for negative clearance

coefficients. A high-speed camera was employed to capture these phenomena. The clearance coefficient in these tests is between 0.57 to -0.37.

5.3.2 Free-surface blockage theory

The one-dimensional actuator disk flow theory, attributed to Betz, limits the maximum power coefficient to 16/27 or 59%. The maximum power coefficient occurs when the turbine reduces the current speed to 2/3 of the value far upstream [128]. This analysis uses the following assumptions:

- Homogeneous, incompressible, steady state inflow,
- no frictional drag,
- an infinite number of blades,
- uniform thrust over the rotor area,
- a non-rotating wake,
- no blockage effect, and
- no surface effect.

Garrett and Cummins [129] extended the theory to predict the power of constrained turbines between two rigid walls. This occurs when a single turbine is deployed in a narrow channel or arrays of turbines block the waterway. Garrett and Cummins method neglects the drop in the free-surface behind the turbine. Whelan et al. [130] expanded the Betz one-dimensional analysis for shallow water applications. This theory considers the free-surface drop behind a constrained turbine operating in shallow waters and the associated increase in the bypass flow speed, as shown in Figure 5.9.

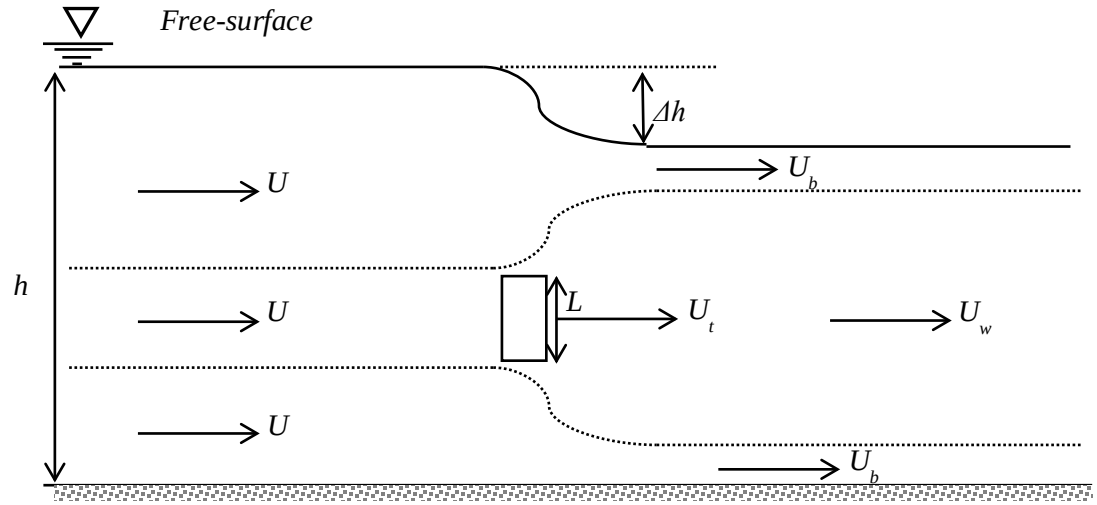

Figure 5.9: Schematic view of the one-dimensional control volume

Applying continuity and Bernoulli's equation, Whelan et al. developed a quartic polynomial solution for a turbine with the height L situated in a water depth h:

$$Fr^2\tau^4 + 4\varepsilon Fr^2\tau^3 + (4B - 4 - 2Fr^2)\tau^2 + (8 - 8\varepsilon - 4Fr^2\varepsilon)\tau + (8\varepsilon - 4 + Fr^2 - 4\varepsilon^2 B) = 0, \qquad 5.3$$

where $Fr = U/\sqrt{gh}$ is the upstream Froude number, g, is gravity, ε is the ratio of the far-wake speed, U_w, to the free stream speed, τ is the ratio of the bypass flow speed, U_b, to the free stream speed, and B is the blockage ratio and is given by:

$$B = \frac{L}{h}. \qquad 5.4$$

Equation 5.3 is an implicit function and the value of τ is obtained in terms of ε. Real solutions for τ are obtained for some specific range of ε. Beyond that

range, τ is imaginary. The power coefficient, C_p, as a function of τ and ε, is given by:

$$C_p = \beta(\tau^2 - \varepsilon^2), \tag{5.5}$$

where β is the ratio between the free stream speed, U, and the flow speed in the turbine actuating disk, U_t, and is given by:

$$\beta = \frac{\varepsilon}{B(\tau - \varepsilon)}\left[\tau\left(1 - \frac{\Delta h}{h}\right) - 1\right], \tag{5.6}$$

where Δh is the free-surface drop behind the turbine. Using the Bernoulli's equation along the free-surface gives:

$$\frac{\Delta h}{h} = \frac{Fr^2}{2}(\tau^2 - 1). \tag{5.7}$$

Substituting $\Delta h / h$ from Equation 5.7 and β from Equation 5.6 into Equation 5.5 and using Equation 5.3, we can find the power coefficient as a function of ε. This theory considers the free-surface drop and the increase in the bypass flow speed, however the following simplifications are involved:

- uniform inflow,
- uniform speed in the wake,
- uniform thrust over the rotor area, and
- symmetry between upper and lower bypass flows.

5.3.3 Test Procedure

Two-bladed vertical turbine tests start with the water tunnel at a 60 cm water depth and flow speeds of 0.5, 0.6 and 0.7 m/s, corresponding to turbine Reynolds numbers of 1.65×10^5, 2.00×10^5, and 2.35×10^5, respectively. At these speeds, the turbulence intensity of the test section measured using an ADV is between 3.21% and 3.95%.

Initially, the water tunnel is filled to its maximum water level, 60 cm, and the profile curve of the power coefficient versus tip speed ratio is measured at each Reynolds number. Once completed, the water level is lowered by 2 cm in declining steps and tests are repeated. The testing continues until the water level reaches 70% of the blade height providing a clearance coefficient of -0.3. Negative clearance coefficients introduce water separation phenomenon on the blades. This separation happens in the first half of the blade rotation path. A high-speed camera with a rate of 500 fps captures the flow separation phenomenon. The camera records the separation from the bottom and side views: the side view shows the separation propagation along the blade span, and the bottom view shows the 2-D details of the separation on a section of the blade. Two lenses with focal lengths of $f = 6$ mm and $f = 60$ mm are used to record details of the flow separation.

5.3.4 Test results

The high positive clearance coefficient represents a negligible free-surface effect situation, which follows closely the Betz's law with a maximum power coefficient limit of 16/27. Betz's law becomes invalid for low clearance coefficients wherein

the maximum power coefficient limit rises. Figure 5.10 shows the results for the power coefficient versus the tip speed ratio at various clearance coefficients. The general trend in all three Reynolds numbers is an increase in the power coefficient with positive clearance coefficient reduction, and a relatively sharp decrease in the power coefficient for negative clearance coefficients. The slope of the power coefficient decay in the negative side of the clearance coefficient axis is considerably steeper than the slope of the power gain in the positive side of the axis. When the water level is slightly above the blades, the highest power coefficient is achieved, which is more than Betz's limit and is close to unity. In these experiments, the maximum power coefficient occurs at a tip speed ratio between 2.7 and 2.9.

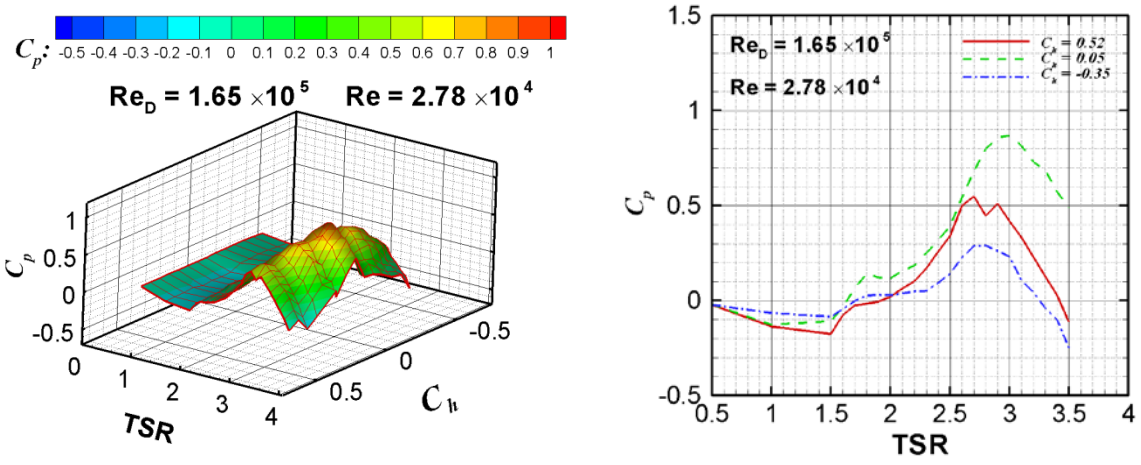

(a)

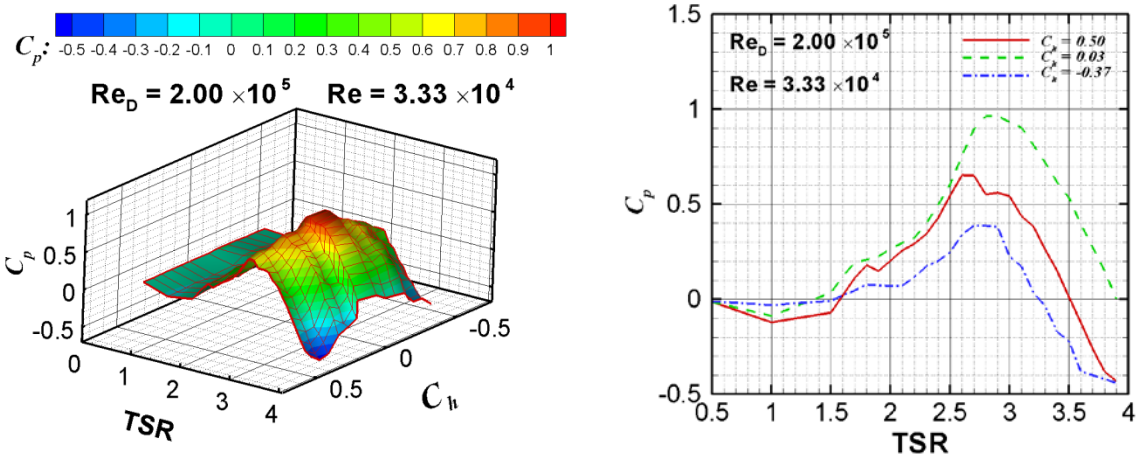

(b)

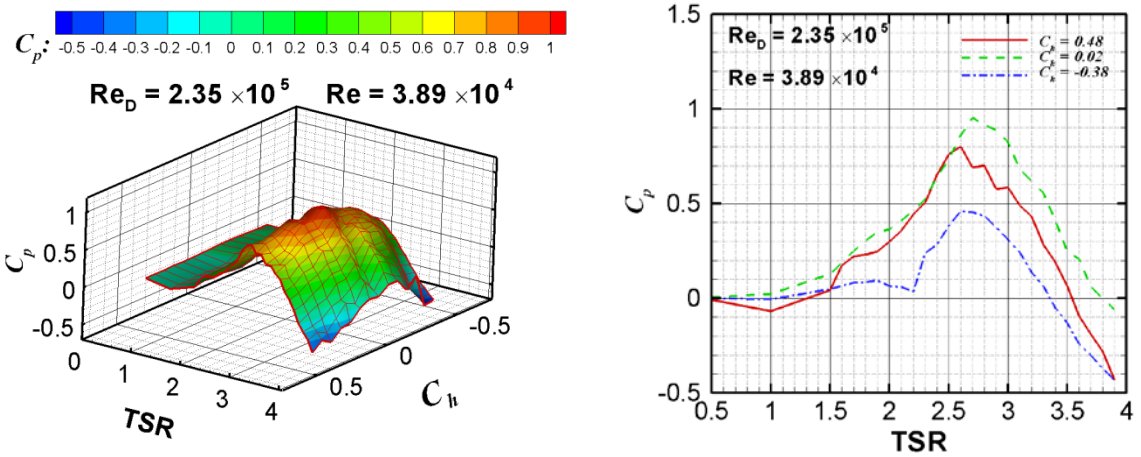

(c)

Figure 5.10: Power coefficient variation with clearance coefficient at the turbine Reynolds number of (a) 1.65×10^5, (b) 2.00×10^5, and (c) 2.35×10^5

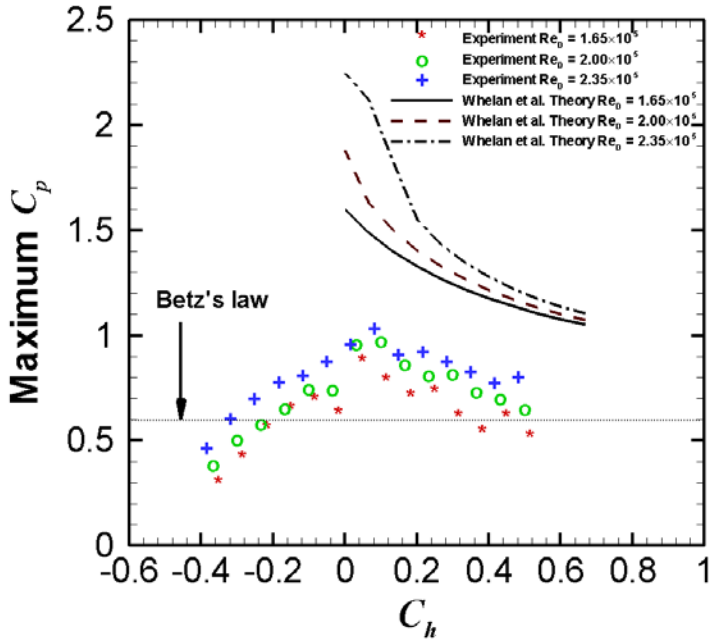

Figure 5.11: Comparison of experimental results and Whelan et al. model predictions

5.3.5 Positive clearance coefficient

The Whelan et al. theory for predicting the power coefficient is valid for positive clearance coefficients [130]. This theory is unable to predict the power coefficient behavior at negative clearance coefficients. Figure 5.11 compares the Whelan et al. theory to the experimental results for the maximum power coefficient versus the clearance coefficient at three Reynolds numbers. The theory predicts a maximum power coefficient that is approximately 100% higher than experimental results. Whelan et al. mentioned a 60% deviation of their theory from the experiment in their measurements [130]. Both theory and experiment show a rise in the power coefficient; however, the rise in power coefficient predicted by the theory extends up to the zero clearance coefficient. In the experiments, the power coefficient rise ends before the zero clearance coefficient is reached. At a clearance coefficient of zero the water level is slightly lower than the top plate of

the turbine due to the surface drop effect. When the water level is lower than the top plate, the blades are exposed to the air and the power coefficient of the turbine drops.

For the experimental data, the best-fit line shows that for a positive clearance coefficient the slope is the same for all three Reynolds numbers, being approximately -1. Bounding the clearance coefficient between 0.5 and 0.1 for the theory, the slope of the best fit line is -0.7, -0.9 and -1.5 for turbine Reynolds numbers of 1.65×10^5, 2.00×10^5 and 2.35×10^5, respectively. Although theory and experiment show the power coefficient reduction at higher clearance coefficients, the Bahaj et al. experiment [131] in a towing tank for a horizontal turbine shows a reverse behavior. In their study, they attribute a 10% to 15% power coefficient reduction in a low clearance coefficient condition with $C_h = 0.19$ due to the fact that the free-surface behaves like a reflection plane. They believe that this reflection plane nature of the free-surface in a low clearance coefficient condition prevents the full expansion of the wake, thereby reducing the power coefficient. Bahaj et al. corrected data for blockage effects and compared them after the correction. However, having different power coefficient levels for the same turbine after blockage correction indicates the inaccuracy of the blockage correction method used. A hydrokinetic turbine in free flow has a unique power coefficient diagram as long as the Reynolds number is constant.

5.3.6 Negative clearance coefficient

Negative clearance coefficient occurs when the water level is below the top plate of the turbine. In this condition, part of the blade is above the free-surface and exposed to air. The effective area of the turbine is not the total cross sectional

area of the turbine but it is the part of the cross sectional area that is in water. According to the Whelan et al. [130], theory, this situation is similar to a hydrokinetic turbine operating in a zero clearance coefficient condition with a smaller effective area. Therefore, the theory predicts a constant power coefficient and a lower power output due to the smaller effective area. Our experimental results contradict the theory and show a sudden power coefficient drop, as shown in Figure 5.11. Theoretically, the operating condition of a semi-submerged turbine is similar to that of the turbine with zero clearance coefficient. However, when the water level is below the top plate, blades are now partially exposed to air, and this situation has to be taken into account. High-speed photography shows evidence that the suction side, low-pressure side, of blades entrains air into the water causing flow separation from the blade surface. Therefore, the effective height of blades is less than the cross sectional area of the turbine in the water. The lift force contributes to the net torque of the turbine and water separation reduces the lift force considerably. Figure 5.12 shows the partial water separation phenomenon happening on the vertical turbine blades. The separation starts around the leading edge area of the blade where the flow accelerates on the blade and the pressure drops. When the water pressure drops below the atmospheric pressure, air pushes the water down and separates it from the blade surface. On the adverse pressure gradient part of the blade, the water speed drops and the pressure rises again. Therefore, the partial water separation has a conical shape, a narrow tail, and a wide top. The water pressure is equal to the atmospheric pressure on the free-surface but at deeper water levels the pressure rises and consequently the water separation may happen in a limited part of the blade around the maximum blade thickness.

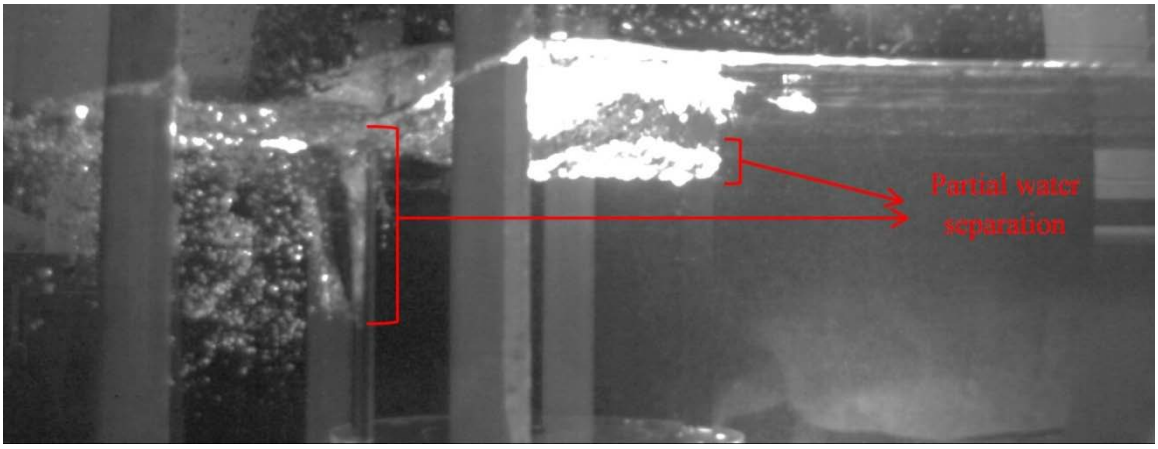

Figure 5.12: Partial water separation on the blades

For a negative clearance coefficient, partial water separation is consistent. In some experimental conditions, the separation expands through the entire length of the blade. Full water separation typically happens at a tip speed ratio close to 3. Figure 5.13 shows the power coefficient variation of the turbine at a tip speed ratio of 3.1 and the clearance coefficient of -0.1. The water separation starts around the blade position of 820° equivalent to 100° of the third rotation. The minimum power coefficient happens at 90° after the separation starting point, 910° or 190° of the third rotation. After 910° the water reattaches to the blade surface and the power coefficient rises. An overshoot in the power coefficient occurs after water reattachment. The turbine requires two full rotations after the separation to get back to the normal operational conditions.

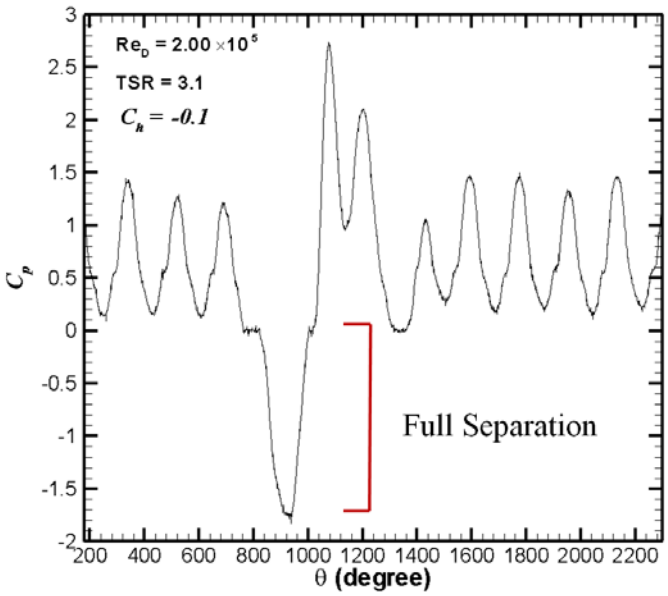

Figure 5.13: Power coefficient of a typical water separation on the turbine

For a typical tip speed ratio of 3.1 and the pitch angle of 2.5°, the maximum angle of attack of the blade is 16.3° and it occurs at approximately 108.8° azimuth angle. Comparison between the theory and experiment shows that the water separation starts while the blade is near the maximum angle of attack position. Fujisawa and Shibuya [64] reported the formation of two pairs of stall vortices behind the turbine blades: one forms at the azimuth angle between 45° and 90° and the second one between 90° and 135°. In the current experiment, the first pair of vortices is not strong enough to fully separate the flow from the blade. The second pair of stall vortices occurring at 100° azimuth angle is stronger than the first pair of vortices and is able to separate the water from the entire blade surface.

Water separation reduces the lift coefficient and consequently the torque and power coefficients drop. To compensate for the lower torque coefficient, the turbine tends to reduce the tip speed ratio; however, the driving motor resists

keeping the tip speed ratio constant. The motor resistance induces a negative torque on the torque transducer. After reattachment, the recovered lift raises the torque and power coefficients. From water reattachment to steady conditions, there is a transient state in which a starting vortex convects on the blade surface and leaves the trailing edge [132]. The vortex convection speed is between one third and one half of the relative speed of the blade [133, 134]. The starting vortex increases the lift coefficient on the blade and causes the power coefficient to overshoot.

Figure 5.14 shows the water separation propagation from the side view. The low-pressure side of the blade draws the air causing separation. The partial separation starts from the top of the blade when the azimuth angle of the blade is lower than 90°, as shown in Figure 5.15 (a) and Figure 5.15 (b). Near a 90° rotation, air covers the full span of the blade but with water still attached, as shown in Figure 5.15 (c) and Figure 5.15 (d). Figure 5.15 (e) and Figure 5.15 (f) show that at position angles greater than 100°, an air vortex forms on the leading edge of the blade and separates the water.

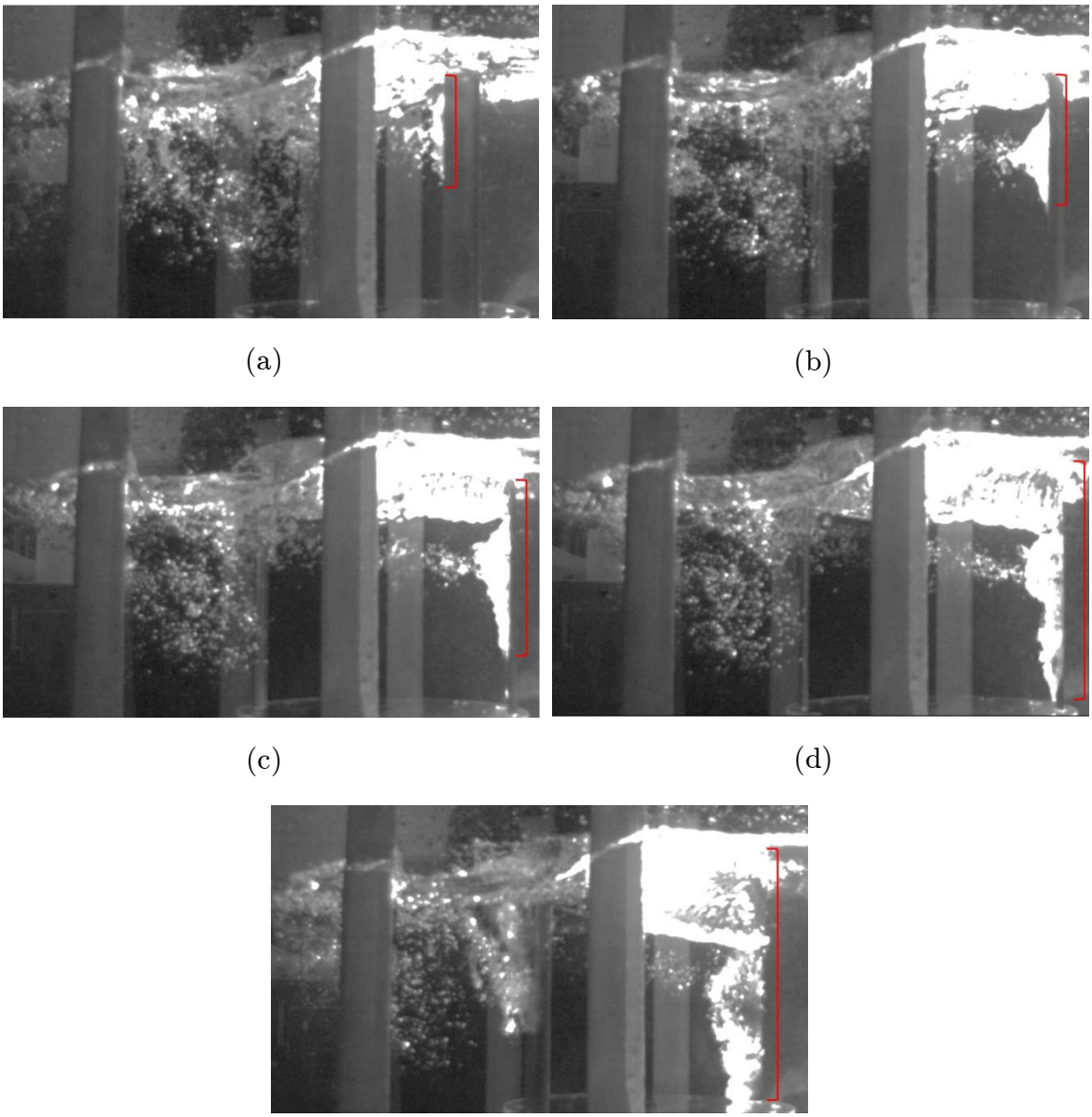

(a) (b)

(c) (d)

(e)

Figure 5.14: Full water separation process from the side view with the f = 6 mm lens. (a) and (b) are starting stages, (c) and (d) are propagation stages, and (d) is the full separation

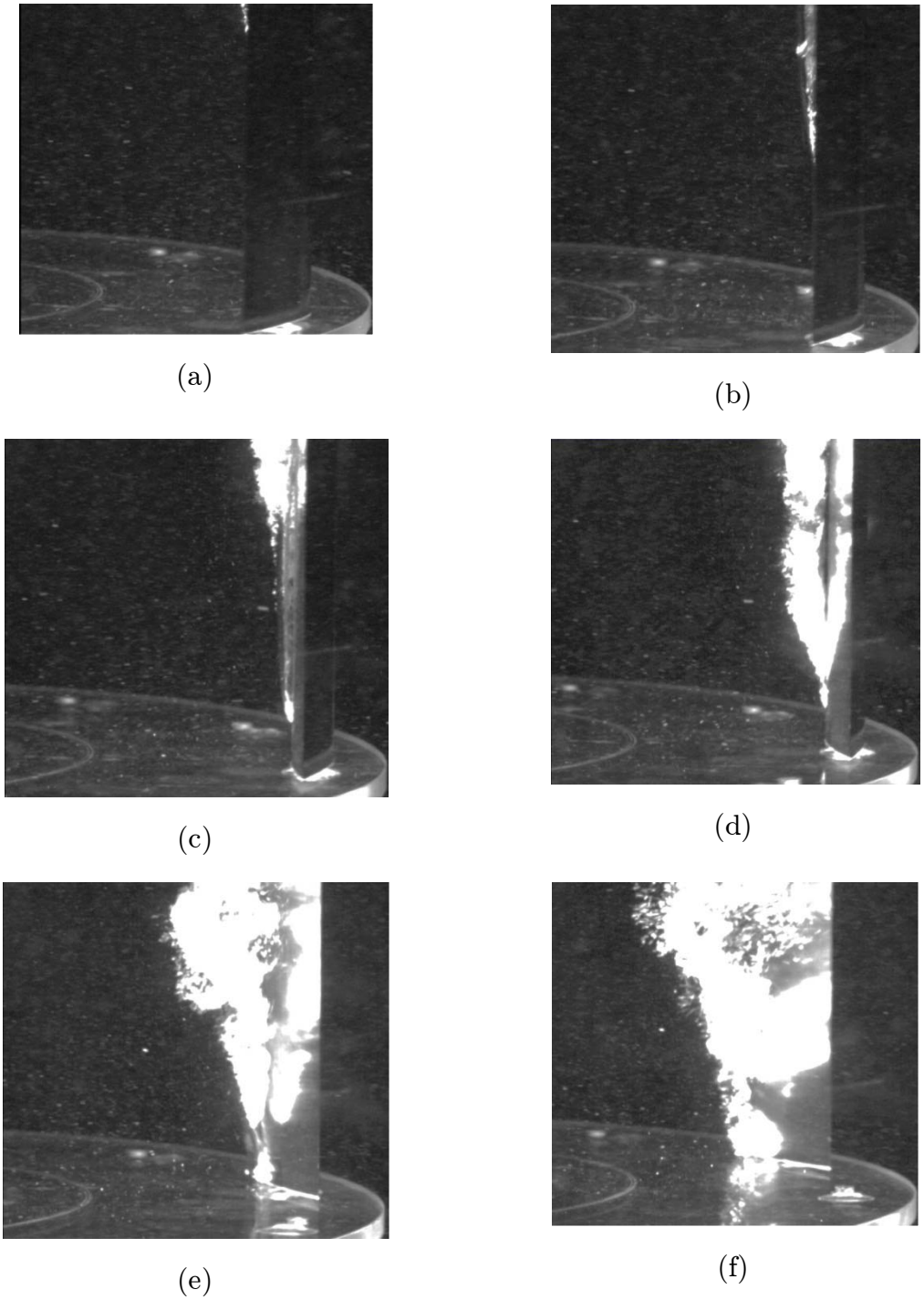

(a) (b) (c) (d) (e) (f)

Figure 5.15: Water separation from the blade during the full separation phenomenon with the f = 60 mm lens. (a) 60 degrees, (b) 75 degrees, (c) 85 degrees, (d) 90 degrees, (e) 105 degrees, and (f) 120 degrees

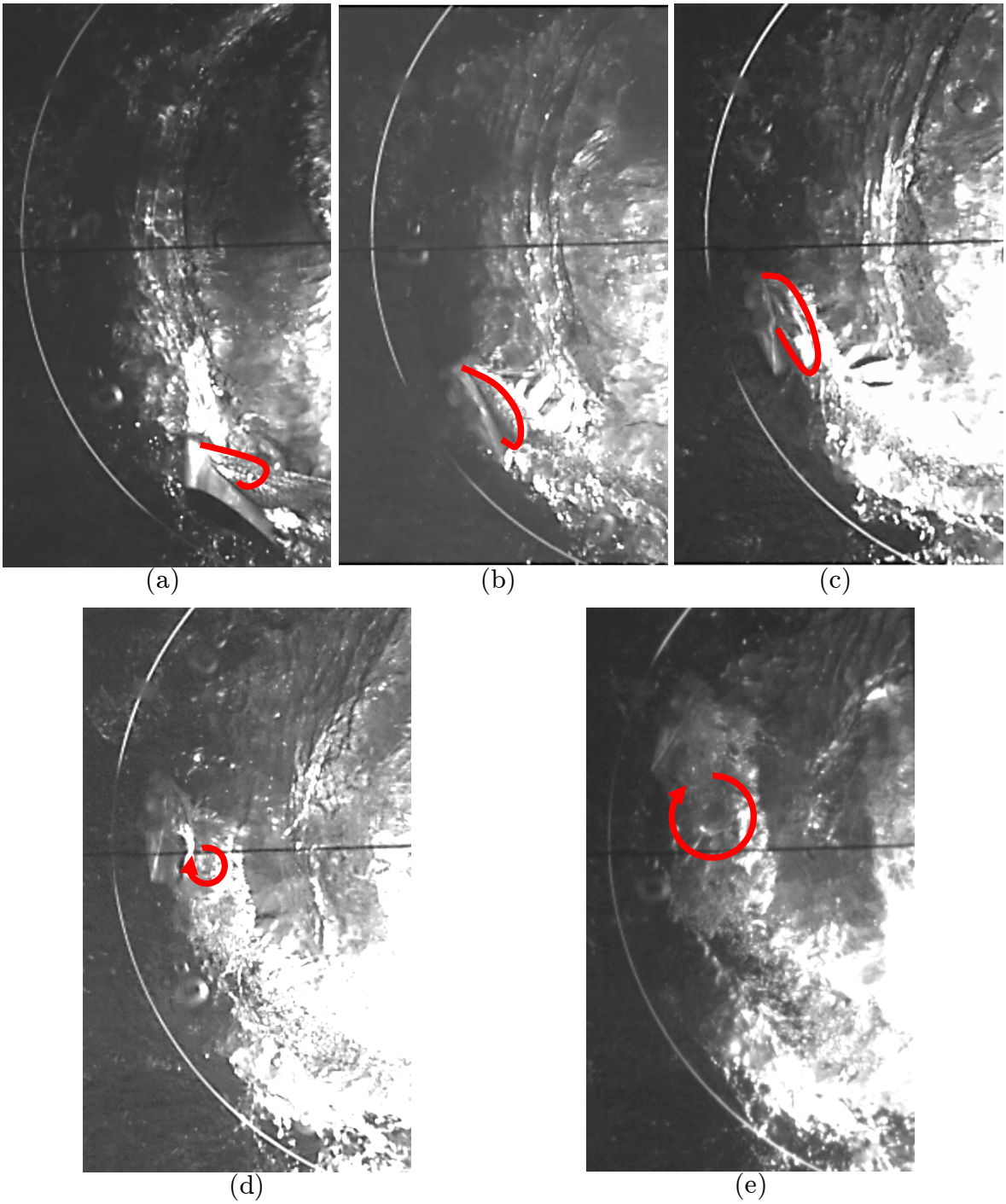

Figure 5.16: Air vortex formation and convection during the full separation, bottom view, f = 6 mm. The blade position of (a) 35 degrees, (b) 60 degrees, (c) 85 degrees, (d) 95 degrees, (e) 120 degrees

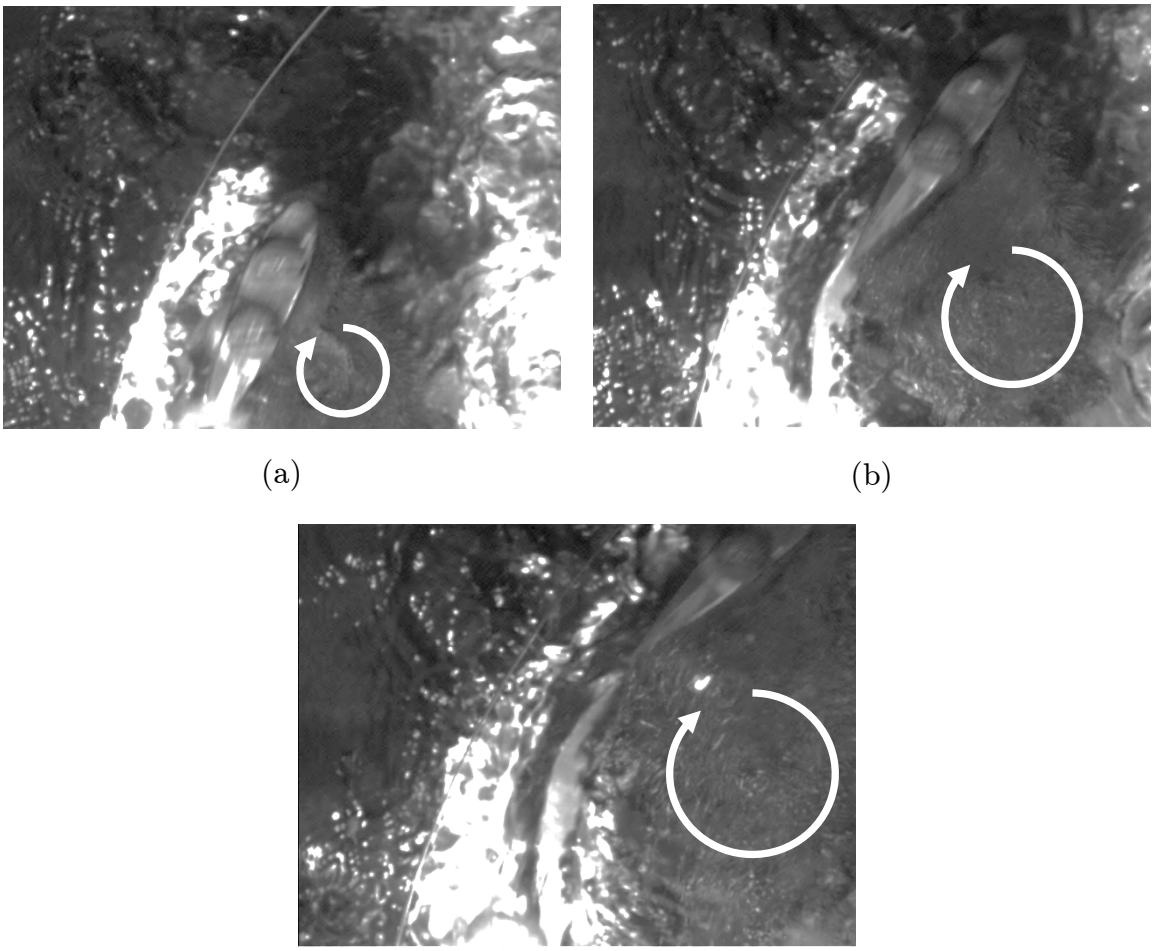

(a) (b)

(c)

Figure 5.17: Close up view of the air vortex formation on the blade, bottom view, f = 60 mm. The blade position of (a) 95 degrees, (b) 105 degrees, and (c) 110 degrees

When the camera is positioned underneath the test section, it captures the air vortex formation on the blade. Two lenses were used: one wide lens with a focal length of 6 mm and another lens with a focal length of 60 mm for close up pictures. Figure 5.16 shows the results of the f = 6 mm lens. At first the air vortex is an attached air bubble. The air bubble forms around the maximum thickness of the blade, as shown in Figure 5.16 (a). As the azimuth angle of the blade approaches 90°, this air bubble expands both towards the leading edge and

the trailing edge of the blade, as shown in Figure 5.16 (b) and Figure 5.16 (c). When the blade passes 90°, the air bubble rolls up and forms an air vortex, as shown in Figure 5.16 (d). This air vortex leaves the leading edge of the blade and convects downstream. Full separation occurs after the air vortex leaves the blade, as shown in Figure 5.16 (e). Figure 5.17 shows the close up view of the air vortex convection on the blade.

5.3.7 Summary

The free-surface blockage increases the power coefficient of the vertical kinetic turbine. In this condition, the maximum power coefficient can be higher than the Betz's limit. Results show that the power coefficient decreases with the positive clearance coefficient. The Whelan et al. one-dimensional theory predicts the negative slope of the power coefficient in the positive clearance coefficient section; however, the values are about 100% higher than the experimental results. The maximum power coefficient occurs around the clearance coefficient of zero. Negative clearance coefficient decreases the power coefficient considerably. The negative clearance coefficient means the turbine is semi-submerged and part of the blade is exposed to air. The suction side of the blade draws air into the water and separates the water from the blade, causing stall. This separation sometimes expands and covers the whole blade length and results in a negative torque and power coefficient. High-speed camera images show that the full water separation starts with an air bubble formation on the blade. This air bubble eventually bursts and forms an air vortex. The air vortex convects on the blade and after it leaves the trailing edge of the blade and the full water separation occurs.

The water level in the test section of the water tunnel is set 50 cm for the rest of experiments. Due to the dimensions of the turbine, the clearance coefficient of the turbine at this level of water is 0.23. This height of water provides sufficient amounts of water above the turbine that retain the blades fully submerged in the water even in the surface drop region. According to the results obtained in this section, the performance characteristics of the turbine exceed the Betz's limit for the clearance coefficient of 0.23.

5.4 Reynolds number

The Reynolds number influences the lift and drag coefficients of the blades. Two types of Reynolds numbers are defined in the literature for VAT studies: the free stream Reynolds numbers, Re and Re_D, and the blade relative Reynolds number, Re_{rel}. The free stream Reynolds numbers are defined based on the free stream velocity and the diameter of the turbine, $\mathrm{Re}_D = \rho UD/\mu$, or the blade chord length, $\mathrm{Re} = \rho Uc/\mu$. The blade relative Reynolds number is defined based on the blade chord length and the rotational speed of the blade, $\mathrm{Re}_{rel} = \rho U_{rel}\ c/\mu$. The blade relative Reynolds number Re_{rel} is a dependent parameter and is obtained from the blade Reynolds number Re and tip speed ratio of the turbine, λ. For a turbine with fixed dimensions, higher Reynolds numbers represent higher free stream flow speed, and for a site with a constant flow speed, higher Reynolds numbers occur with a larger turbine or blade. This section only investigates the effects of the free stream Reynolds number Re_D on the performance of the VAT.

5.4.1 Background

The free stream velocity changes the blade and turbine Reynolds numbers. In Blackwell et al. investigations [118] the effect of the free stream Reynolds number on the maximum power coefficient is evident. The main trend is the increase in the maximum power coefficient due to the increase in the free stream Reynolds number. Bravo et al. [135] tested a high solidity H-shaped Darrieus turbine in the NRC low speed wind tunnel at various wind speeds. Their results show that the power coefficient is sensitive to the free stream Reynolds number while the turbine operates at low wind speeds and low Reynolds numbers. Above a threshold wind speed, 8 m/s in this case, the power coefficient becomes independent of free stream Reynolds number. The 8 m/s wind speed is equivalent to the turbine Reynolds number of 1.25×10^{6} or blade Reynolds number of 2.00×10^{5} for their turbine.

5.4.2 Effect of Reynolds number on the freewheeling

The four-bladed squirrel-cage turbine was tested for the freewheeling condition at various free stream Reynolds numbers at the University of Manitoba water tunnel. Results show that there are three distinct regions characterized by behavioral differences in the turbine, as is evident by the tip-speed-ratio curve shown in Figure 5.18. These three regions each have an associated range of free stream Reynolds numbers. At blade Reynolds numbers less than 1.94×10^{4} the turbine operates at a tip speed ratio lower than unity. Therefore, during a rotation, blades pass the stall angle of attack and reach 180° angle of attack at which point the flow sweeps across the blades from the trailing edge toward the leading edge. Although in this region blades spend most of their rotation in the

post-stall condition, the turbine continues to rotate and the tip speed ratio increases somewhat linearly with the Reynolds number.

When the blade Reynolds number increases beyond 1.94×10^4, but does not exceed 2.34×10^5, the tip speed ratio suddenly jumps from 0.30 to 2.93. Here the turbine exhibits an unstable and transient form of operation. At low Reynolds numbers, the turbine is unable to pass the high negative power coefficient zone near the tip speed ratio of one. As the Reynolds number increases, the absolute value of the negative power coefficient near the tip speed ratio of one decreases. Therefore, the turbine can pass the unstable zone near the tip speed ratio of one. In the second region starting at 2.93, the tip speed ratio increases with the free stream Reynolds number similar to the first region. In the last region, during freewheeling, the tip speed ratio becomes independent of the free stream Reynolds number.

The angular velocity is divided into two main regions based on the free stream Reynolds number. In both regions, the variations are linear. There are two slopes corresponding to stall and pre-stall conditions. In the stall condition, the angular velocity varies slightly with Reynolds number. Just before stall, the slope increases, as shown in Figure 5.19. When the tip speed ratio is in the third region, a higher Reynolds number increases the angular velocity linearly even if the tip speed ratio remains almost constant.

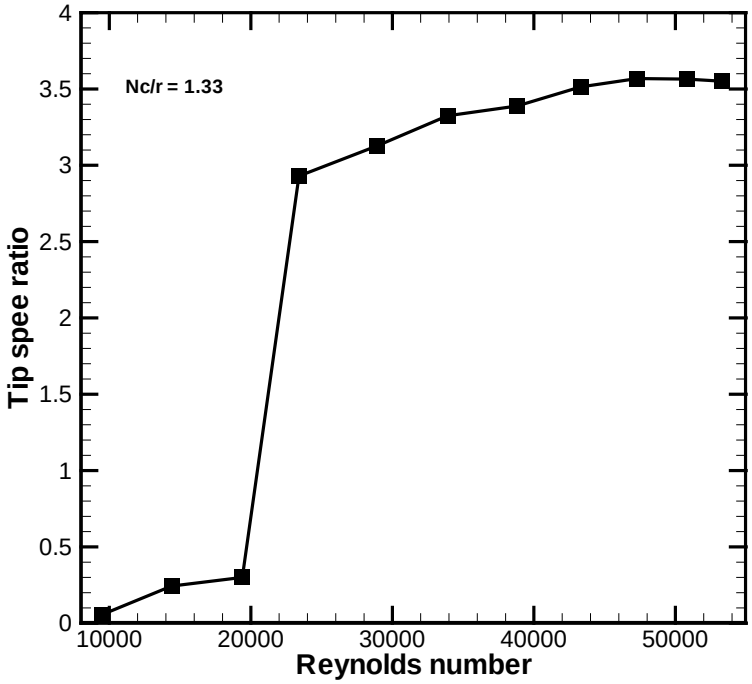

Figure 5.18: Tip speed ratio at various Reynolds numbers during freewheeling conditions

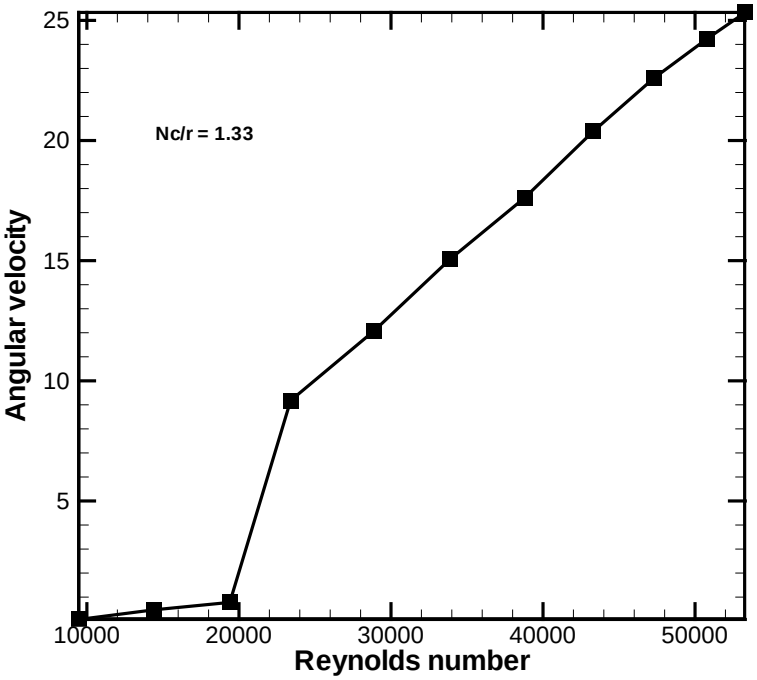

Figure 5.19: Angular velocity variation versus Reynolds number during freewheeling conditions

While the blade Reynolds number varies between 9.46×10^3 and 5.33×10^4, the maximum relative Reynolds number, $Re_{rel\ max}$, varies between 9.99×10^3 and 2.43×10^5 and the minimum relative Reynolds number, $Re_{rel\ min}$, varies between 8.94×10^3 and 1.36×10^5, as shown in Table 5.1. The maximum relative Reynolds number happens at an azimuth angle of zero when the blade goes opposite to the flow direction. At an azimuth angle of 180°, the blade travels in the flow direction, thus the blade experiences the minimum relative velocity corresponding to the minimum relative Reynolds number.

Table 5.1: Variations of tip speed ratio, rotational speed and maximum angle of attack by Reynolds number

V_∞(m/s)	ω (rad/s)	λ	Re	Re_D	$Re_{rel\ max}$	$Re_{rel\ min}$	α_{max} (deg)
1.07	25.33	3.55	5.33e4	3.20e5	2.43e5	1.36e5	16.4
1.02	24.24	3.56	5.08e4	3.05e5	2.32e5	1.30e5	16.3
0.95	22.6	3.57	4.73e4	2.84e5	2.16e5	1.22e5	16.3
0.87	20.38	3.51	4.33e4	2.60e5	1.96e5	1.09e5	16.5
0.78	17.62	3.39	3.88e4	2.33e5	1.70e5	9.28e4	17.2
0.68	15.07	3.32	3.39e4	2.03e5	1.46e5	7.87e4	17.5
0.58	12.09	3.13	2.89e4	1.73e5	1.19e5	6.14e4	18.7
0.47	9.18	2.93	2.34e4	1.40e5	9.20e4	4.52e4	20.0
0.39	0.78	0.30	1.94e4	1.16e5	2.52e4	1.36e4	180.0
0.29	0.47	0.24	1.44e4	8.64e4	1.80e4	1.09e4	180.0
0.19	0.07	0.06	9.46e3	5.68e4	9.99e3	8.94e3	180.0

In the stall condition, the tip speed ratio is less than unity; therefore, the maximum angle of attack is 180°. In the second region the tip speed ratio is above unity so the maximum angle of attack is less than 90°. At the beginning of the second region where the blade Reynolds number is 2.34×10^4, the maximum

angle of attack during freewheeling is 20°. Increase in the Reynolds number, leads to increases in the tip speed ratio, and the maximum angle of attack decreases. At a Reynolds number of 5.33×10^4, the maximum angle of attack that blades experience in a rotation is 16.4°. Based on the static wind tunnel results, at this relative Reynolds number, the stall angle of attack is approximately 12°. Upstream velocity measurements taken with an acoustic Doppler velocimeter probe shows that the free stream velocity is reduced by approximately 10% near the vertical turbine-actuating disk. Therefore, the local tip speed ratio is higher than the theory and, thus, the maximum angle of attack is lower than the theory.

5.4.3 Maximum power coefficient

The effect of the Reynolds number on the performance of the two-bladed and four-bladed squirrel cage turbines were investigated in University of Manitoba's water tunnel. Tests were conducted at four free stream velocities, 0.4, 0.5, 0.6 and 0.7 m/s, and two preset pitch angles, 0° and 5°. Figure 5.20 shows the effect of the free stream Reynolds number on the power coefficient of the turbine. The maximum power coefficient of the turbine increases with the free stream Reynolds number as expected, the four-bladed configuration with 5° pitch shows the largest increase in C_p with Re.

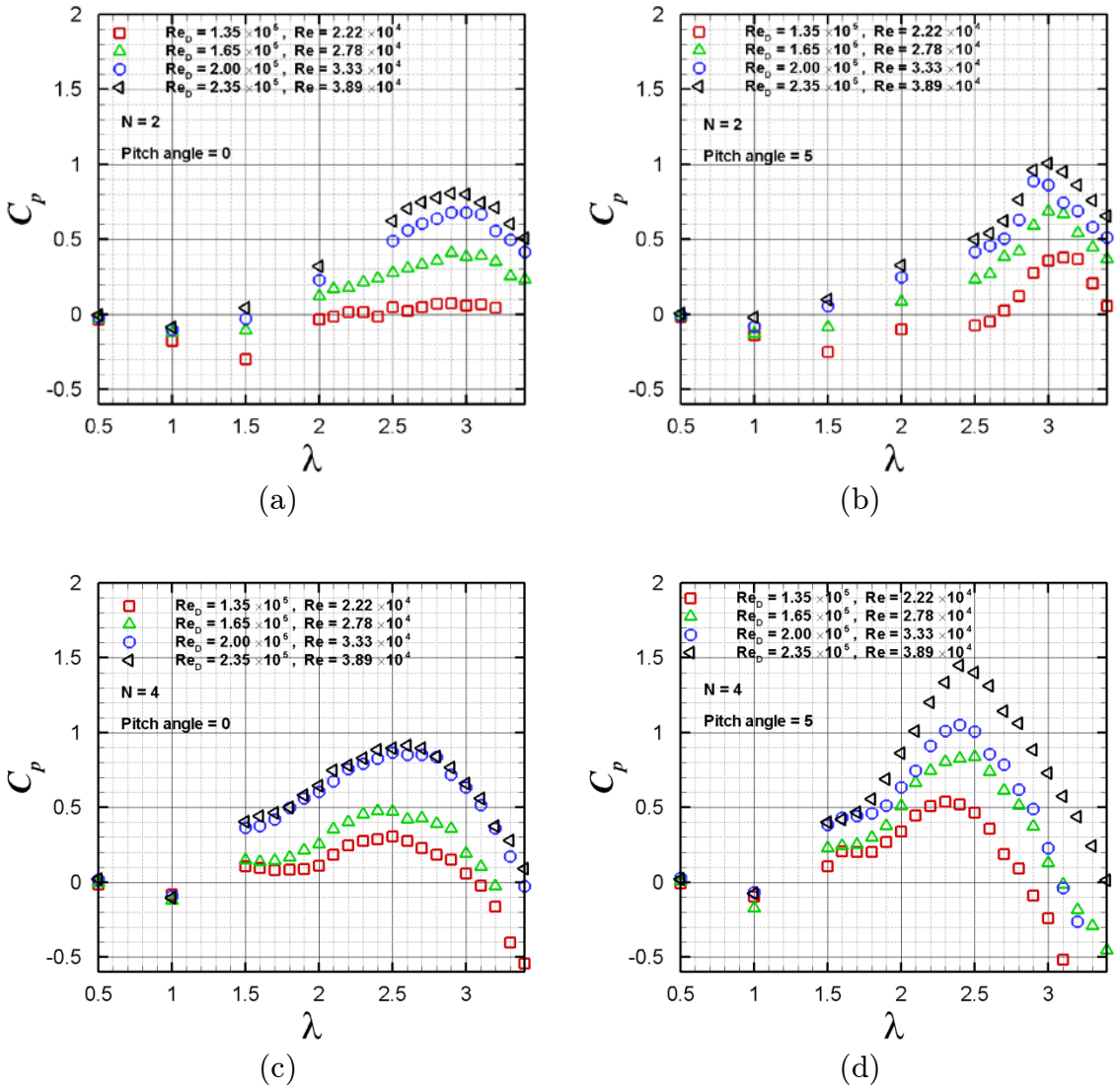

Figure 5.20: The power coefficient of the two-bladed squirrel-cage turbine at preset pitch angles of (a) zero and (b) 5° and the four-bladed turbine at preset pitch angles of (c) zero and (d) 5°

5.4.4 Summary

At low free stream Reynolds numbers, the power coefficient of the VAT is highly sensitive to the Reynolds number. The power coefficient becomes independent of the Reynolds number at high Reynolds numbers. The high Reynolds number region is defined based on the turbine geometry and other operating parameters;

however, typically when the blade Reynolds number exceeds 10^6, the operating behavior of the turbine becomes almost independent of the Reynolds number.

Freewheeling vertical turbines have three operating zones based on the free stream Reynolds number. At low Reynolds numbers, the tip speed ratio is lower than unity and the turbine operates in a stall condition. At a threshold value of the Reynolds number, the tip speed ratio increases above unity. Due to the unstable condition of the blades near a tip speed ratio of one, a vertical turbine is unable to operate with stability near this tip speed ratio. When the freewheeling tip speed ratio is less than unity, operating the turbine at these Reynolds numbers is not practical. When the turbine passes the tip speed ratio of unity, the variation of the tip speed ratio versus the Reynolds number is linear until the maximum angle of attack approaches the stall angle of attack of the blade. Then the tip speed ratio during freewheeling becomes independent of the Reynolds number.

Most of the experiments in this research are conducted at the turbine Reynolds number of 2.00×10^5, during the non-uniform inflow experiment. However to assess the Reynolds number effect, some limited experiments are performed at 1.35×10^5 and 2.35×10^5 as well. At the turbine Reynolds number of 2.00×10^5 the water speed in the test section is about 0.6 m/s and the free-surface is almost level with negligible fluctuations, less than ±0.02 cm. At higher speeds, about 0.8 m/s, a wave is formed on the free-surface of the test section. The fluctuating wave destabilises the testing condition and consequently affects the turbine performance.

5.5 Conclusion

The sensitivity of performance characteristics of the turbine is investigated in the uniform inflow before conducting non-uniform inflow tests. As mentioned in the theory section, Chapter 2, the performance of a VAT is a function of nine design and operating dimensionless parameters. However, among these parameters, some have greater impact on the performance characteristics. Based on the design flexibility and the test facility limitations, four key parameters, solidity, preset pitch angle, Reynolds number and free-surface, were assessed in this chapter. The sensitivity of the turbine to each of these parameters was quantified and the optimum values were selected for the non-uniform inflow tests.

Chapter 6

Non-uniform inflow

Unlike the uniform and low turbulence conditions of flow in water tunnels and towing tanks, flow in rivers, channels and oceans is highly turbulent and non-uniform due to the eddies with size that exceeds the diameter of the turbine. This condition accentuates in hydrokinetic farm applications where multiple turbines operate in eddies shed behind the upstream turbines. This chapter investigates the effect of non-uniform inflow and upstream vortices on the quality of the output power and the performance of vertical turbines. The non-uniform flow condition is generated by placing cylinders with different sizes upstream of the turbine, based on the studies of Medici and Alfredsson [79] and Fujisawa and Shibuya [64]. First, the cylinders are deployed in the water tunnel and the flow characteristics are measured. Then, measurement results are compared with the theory. The performance characteristics of the turbine operating behind cylinders are compared to that of the turbine operating in uniform inflow. Cylinders with different sizes are placed upstream of the scaled model turbine at various longitudinal and lateral locations. The effect of non-uniform inflow on the average output power and the instantaneous power fluctuations are discussed in this chapter.

This chapter first describes the flow pattern around and behind a cylinder, Section 6.1. In Section 6.2 the experimental setup and testing conditions are presented. The Reynolds number sensitivity of the turbine operating in a non-uniform inflow is discussed in Section 6.3. Section 6.4 investigates the effect of longitudinal distance of the cylinder from the turbine on the performance diagram of the turbine. The lateral distance of the cylinder is discussed in Section 6.5. In Section 6.6 a frequency analysis is conducted on the power data of the turbine to assess the power output quality of the turbine operating in a non-uniform inflow.

6.1 Flow pattern behind a cylinder

For a certain range of Reynolds number, bluff bodies in a fluid stream create vortices with an alternating double-row pattern known as Karman's vortex street. The size and the strength of the shed eddies are adjusted by regulating the size of the bluff body and the longitudinal distance of the bluff body to the measuring point. Cylinder is a simple bluff body with many practical applications. There are numerous experimental and numerical data available on the Karman's vortex street behind a cylinder [136-138]. The flow pattern behind a cylinder is classified by the Reynolds number.

For low Reynolds numbers, $0 < Re < 4$, inertial forces are small compared to viscous forces. This regime of flow is called Stokes flow or creeping flow. For this type of flow, the inertia forces are assumed negligible and friction forces balance pressure forces. Streamlines around a cylinder are almost symmetrical and the flow is attached to the surface of the cylinder, as shown in Figure 6.1 (a). At $4 < Re < 40$, two stable vortices are formed on the back of the cylinder as the

result of the flow separation, as shown in Figure 6.1 (b). As the Reynolds number exceeds 40, the two stable vortices are separated and alternately shed from the cylinder body. This repeating pattern of swirling vortices caused by the unsteady separation of flow is called Karman vortex street, as shown in Figure 6.1 (c). Figure 6.2, taken by NASA, shows the Karman vortex street in the clouds off the Chilean coast near the Juan Fernandez Islands on September 15, 1999. For $10^3 < \mathrm{Re} < 3\times10^5$ the laminar boundary layer separates from the cylinder on the upstream face, at about 80° from the stagnation point, and the Karman vortex street becomes turbulent and the wake forms behind the cylinder, Figure 6.1 (d). For $3\times10^5 < \mathrm{Re} < 3\times10^6$ the laminar separation on the upstream face is transformed to turbulent flow and reattaches to the surface of the cylinder. The turbulent flow separates again on the downstream face of the cylinder at about 120°. For turbulent separation, the width of the wake is thinner than the laminar separation. At higher Reynolds numbers, $\mathrm{Re} > 3\times10^6$, the boundary layer transition to turbulent occurs before the laminar separation; therefore the laminar separation disappears and the flow remains attached over the surface until the turbulent separation at an angle less than 120°, as shown in Figure 6.1 (e).

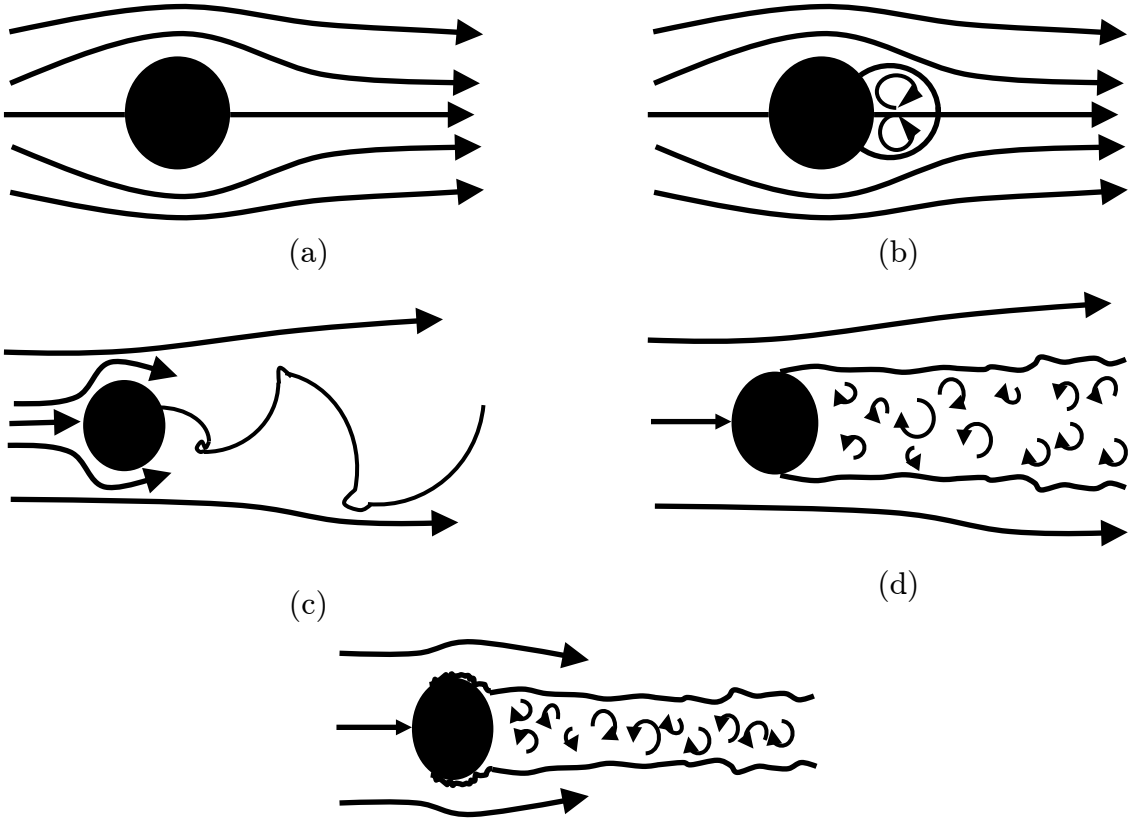

Figure 6.1: Flow over a cylinder at various typed of flow

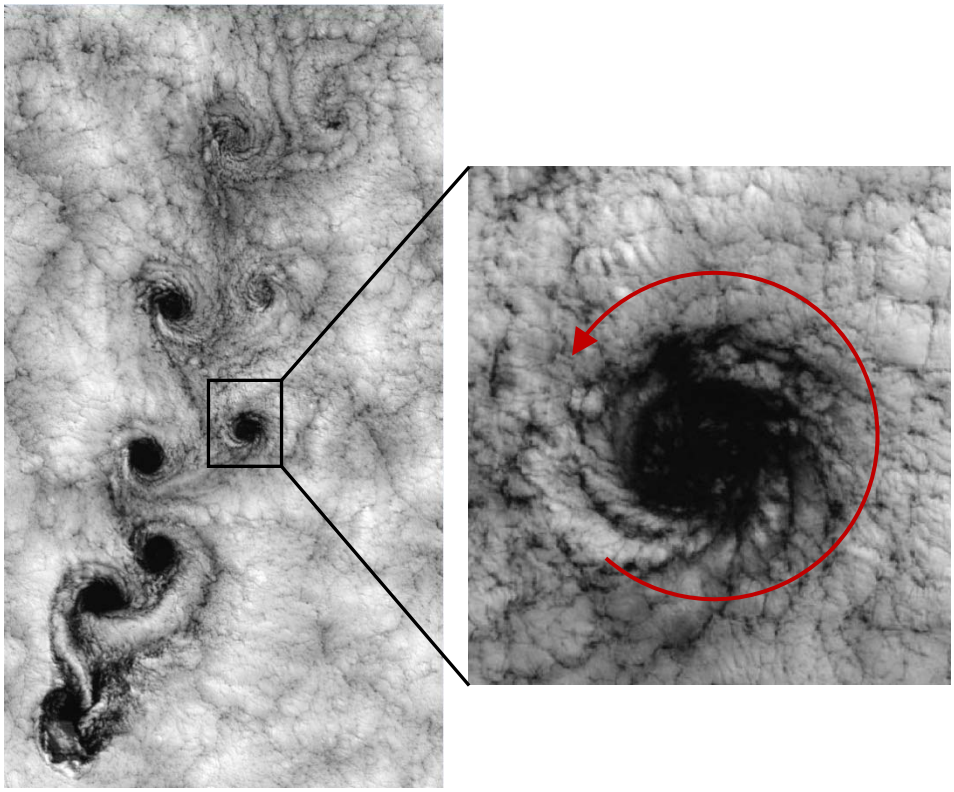

Figure 6.2: Karman vortex in the clouds near Juan Fernandez Islands

The frequency of vortex shedding for a long cylinder with a Reynolds number greater than 40 is given by the following empirical formula:

$$\frac{fd}{U} = 0.198\left(1 - \frac{19.7}{\mathrm{Re}}\right), \qquad 6.1$$

where f is the vortex shedding frequency, d is the diameter of the cylinder, and U is the free stream speed. The dimensionless parameter on the left hand side of Equation 6.1 is known as the Strouhal number. This formula is more accurate for Reynolds number between 250 and 250,000.

6.1.1 Measurements behind cylinders

During the non-uniform flow experiment, the turbine is tested behind cylinders with 2.54 (1.0), 5.08 (2.0), 7.62 (3.0), and 10.16 cm (4.0 in) diameters. The turbine is tested at free stream speeds of 0.4, 0.5, 0.6 and 0.7 m/s; therefore the Reynolds number of cylinders remain in the range of $10^3 < Re < 3\times10^5$ which represents a turbulent Karman vortex street. Figure 6.3 shows the flow pattern around the 7.62 cm diameter cylinder at a flow speed of 0.6 m/s. The turbulent wake and Karman vortex street are noticeable in this figure. The laminar separation occurs at the first half of the cylinder, then the transition to turbulent flow reattaches the flow and finally the turbulent separation occurs at the second half of the cylinder near 120°.

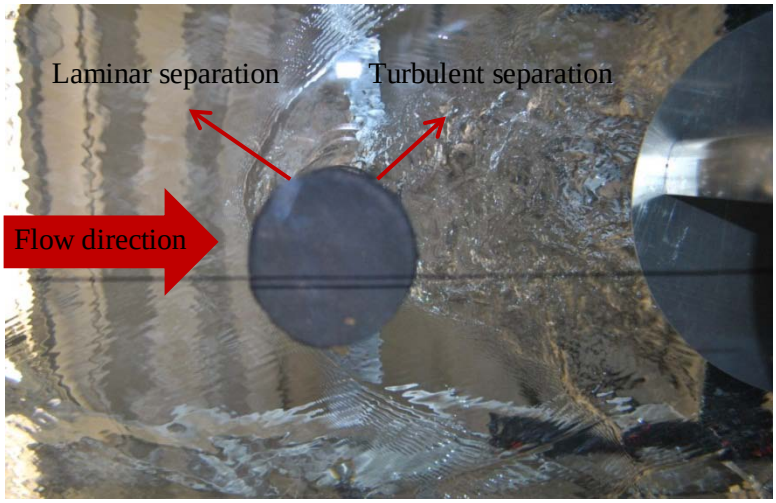

Figure 6.3: Flow pattern behind the upstream cylinder

ADV measurements are conducted downstream the 2.54 and 10.16 cm cylinders at two longitudinal distances to investigate the high frequency properties of the wake. The ADV measures the velocity fluctuations with a 200 Hz sampling frequency. The vortex shedding frequency of the cylinders is obtained from the

power spectral density (PSD) diagram—Fourier transformation of the auto-covariance function of the velocity dataset. This function describes power distribution in the frequency domain. In the frequency domain, the dominant frequency represents the vortex shedding frequency. Figure 6.4 shows the velocity signal in the frequency domain collected 81 cm downstream of the 10.16 cm diameter cylinder at the free stream speed of 0.2 m/s. The frequency peak of the diagram occurs around 0.36 Hz while from the theory for vortex shedding frequency of this cylinder is approximately 0.39 Hz. Table 6.1 summarizes the ADV measurement results and compares them with those obtained from the theory. The vortex shedding frequencies obtained from the ADV measurements closely follow the theory. The integral time scales are obtained from the autocorrelation of the measured velocity dataset. The integral length scales are non-dimensionalized with respect to the chord length of the blades cross section of 5 cm. The size of the length scales is comparable with the chord length of the blades. The vortices grow in size as they get farther away from the cylinder. The free stream speed also enlarges the size of vortices.

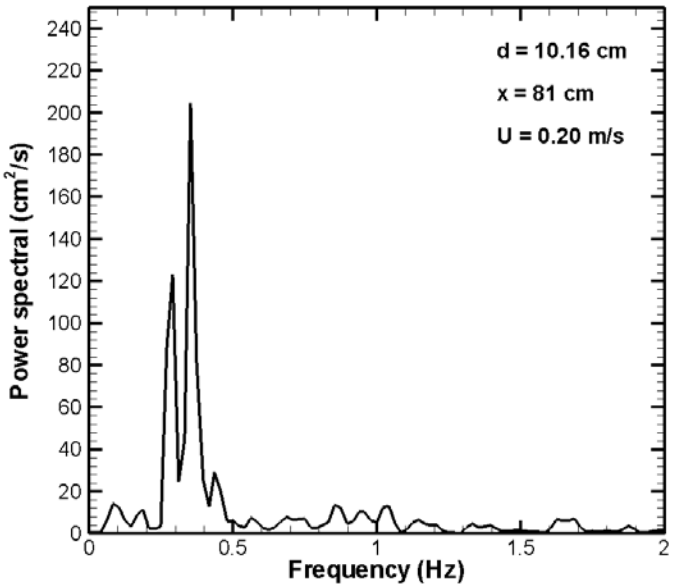

Figure 6.4: PSD of the velocity datasets recorded downstream of the 10.16 cm diameter cylinder at the free stream speed of 0.2 m/s

Table 6.1: Flow properties downstream of the cylinders

Diameter of the cylinder (d, cm)	10.16	10.16	10.16	2.54	2.54	2.54
Measurement distance from cylinder (x, cm)	40	81	81	40	81	81
Dimensionless distance (x/d)	3.94	7.97	7.97	15.75	31.89	31.89
Free stream velocity (U, m/s)	0.20	0.20	0.35	0.35	0.35	0.92
Reynolds number	2.03e4	2.03e4	3.56e4	8.89e3	8.89e3	2.34e4
Strouhal number	0.20	0.20	0.20	0.20	0.20	0.20
Vortex shedding frequency, theory (Hz)	0.39	0.39	0.69	2.76	2.76	7.24
Vortex shedding frequency, ADV (Hz)	0.37	0.36	0.65	2.79	2.75	7.25
Integral time scale (s)	0.13	0.36	0.54	0.04	0.06	0.10
Dimensionless length scale (l/c)	0.52	1.44	3.78	0.28	0.42	1.84

6.2 Experimental setup

The two-bladed configuration of the turbine is used for these tests. At a known tip speed ratio and rotational speed, the power coefficient of the four-bladed configuration has a first harmonic with twice the frequency as that of the two-bladed configuration, as shown in Figure 6.5. For measurements with a fixed sampling rate, harmonics with higher frequencies reduce the resolution of the measurement. During the non-uniform inflow testing, the sampling rate of the data acquisition system is set at 2049.1 Hz, to measure torque, rotational speed and position. The data acquisition system records for a 30 s period to allow statistically steady data.

In non-uniform inflow study, the focus is on the high frequency components while the upstream vortices in the non-uniform inflow impose high frequency fluctuations on the power diagram. Due to the higher number of blades in the four-bladed configuration, the interaction between the downstream blades and vortices shed behind the upstream blades cause considerable amount of high frequency fluctuations in the power coefficient signal. It is more challenging to distinguish the effect of non-uniform inflow from the high frequency fluctuations of the four-bladed turbine. High frequency fluctuations are reduced in the power coefficient diagram of the two-bladed configuration, Figure 6.5. Therefore, this configuration is more convenient to use for non-uniform inflow studies.

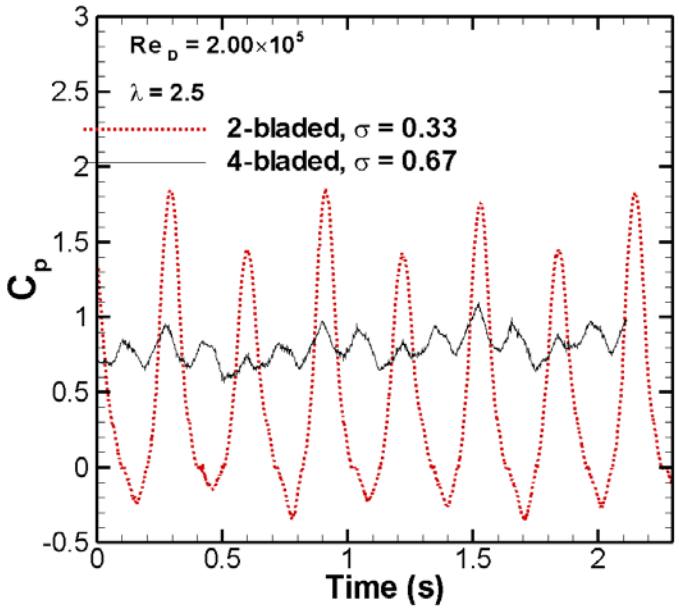

Figure 6.5: Solidity effect on the power coefficient signal

During the tests, the pitch angle is set to the optimum angle, 2.5°, and it has a counterclockwise rotation from the top view. The test section of the water tunnel is filled with water to 50 cm. The bottom of the turbine is 13 cm above the water tunnel floor and the height of the turbine is 30 cm. Having 50 cm water depth in the test section of the water tunnel, the clearance coefficient of the turbine is 0.23. First, the turbine is tested in a uniform inflow condition and the power diagram of the turbine is extracted. This test is referred the clean test from now on. The non-uniform inflow is simulated by four sizes of cylinder, 2.54 (1), 5.08 (2), 7.62 (3), and 10.16 cm (4 in) diameter. The dimensionless diameters of cylinders with respect to the diameter of the turbine are 0.08, 0.17, 0.25 and 0.34 respectively for the cylinder diameters of 2.54, 5.08, 7.06, and 10.16 cm. The height of the cylinders is 63 cm. The bottom of the cylinders sits on the test section floor and the top of them is screwed to an aluminum bar above the water surface. This aluminum bar is clamped to the sidewalls of the

water tunnel to place the cylinders in their position and cancel the undesirable vibrations of the cylinders due to the asymmetric vortex shedding.

The longitudinal and lateral distance of the cylinders are measured from the center of the turbine. Figure 6.6 shows the schematic top view of the experimental setup and demonstrates the positive directions of the longitudinal and lateral distances. Table 6.2 summarizes the test conditions conducted to investigate the effect of non-uniform inflow on the performance of the VAHT. In this naming method, the number following d represents the diameter of the upstream cylinder in inches, following x is the dimensionless longitudinal distance with respect to the diameter of the turbine, x/D, following y is the dimensionless lateral distance of the cylinder, y/D, and following u is the free stream speed in m/s. For example the d3x1y0.33u0.6 represents a test at the free stream velocity of 0.6 m/s while the 3-inch diameter cylinder is located at $x/D = 1$ and $y/D = 0.33$.

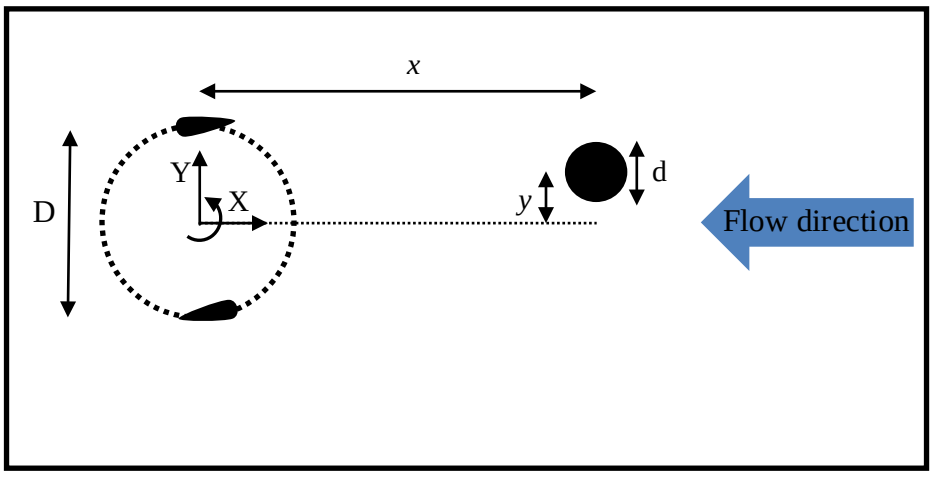

Figure 6.6: Schematic top view of the experimental setup

Table 6.2: Experimental testing conditions

Test	Cylinder diameter (in)	longitudinal distance (x/D)	lateral distance (y/D)	Free stream speed (m/s)
Clean	0	0	0	0.6
d1x1y0u0.6	1	1	0	0.6
d1x1.5y0u0.6	1	1.5	0	0.6
d1x2y0u0.6	1	2	0	0.6
d1x3y0u0.6	1	3	0	0.6
d1x4y0u0.6	1	4	0	0.6
d2x1y0u0.6	2	1	0	0.6
d2x1.5y0u0.6	2	1.5	0	0.6
d2x2y0u0.6	2	2	0	0.6
d2x3y0u0.6	2	3	0	0.6
d2x4y0u0.6	2	4	0	0.6
d3x1y-0.67u0.6	3	1	-0.67	0.6
d3x1y-0.5u0.6	3	1	-0.5	0.6
d3x1y-0.33u0.6	3	1	-0.33	0.6
d3x1y-0.17u0.6	3	1	-0.17	0.6
d3x1y0u0.5	3	1	0	0.5
d3x1y0u0.6	3	1	0	0.6
d3x1y0u0.7	3	1	0	0.7
d3x1y0.17u0.6	3	1	0.17	0.6
d3x1y0.33u0.6	3	1	0.33	0.6

Test	Cylinder diameter (in)	longitudinal distance (x/D)	lateral distance (y/D)	Free stream speed (m/s)
d3x1y0.5u0.6	3	1	0.5	0.6
d3x1y0.67u0.6	3	1	0.67	0.6
d3x1.5y-0.67u0.6	3	1.5	-0.67	0.6
d3x1.5y-0.5u0.6	3	1.5	-0.5	0.6
d3x1.5y-0.33u0.6	3	1.5	-0.33	0.6
d3x1.5y-0.17u0.6	3	1.5	-0.17	0.6
d3x1.5y0u0.6	3	1.5	0	0.6
d3x1.5y0.17u0.6	3	1.5	0.17	0.6
d3x1.5y0.33u0.6	3	1.5	0.33	0.6
d3x1.5y0.5u0.6	3	1.5	0.5	0.6
d3x1.5y0.67u0.6	3	1.5	0.67	0.6
d3x2y-0.67u0.6	3	2	-0.67	0.6
d3x2y-0.5u0.6	3	2	-0.5	0.6
d3x2y-0.33u0.6	3	2	-0.33	0.6
d3x2y-0.17u0.6	3	2	-0.17	0.6
d3x2y0u0.6	3	2	0	0.6
d3x2y0.17u0.6	3	2	0.17	0.6
d3x2y0.33u0.6	3	2	0.33	0.6
d3x2y0.5u0.6	3	2	0.5	0.6
d3x2y0.67u0.6	3	2	0.67	0.6
d3x3y-0.67u0.6	3	3	-0.67	0.6
d3x3y-0.5u0.6	3	3	-0.5	0.6
d3x3y-0.33u0.6	3	3	-0.33	0.6
d3x3y-0.17u0.6	3	3	-0.17	0.6
d3x3y0u0.6	3	3	0	0.6

Test	Cylinder diameter (in)	longitudinal distance (x/D)	lateral distance (y/D)	Free stream speed (m/s)
d3x3y0.17u0.6	3	3	0.17	0.6
d3x3y0.33u0.6	3	3	0.33	0.6
d3x3y0.5u0.6	3	3	0.5	0.6
d3x3y0.67u0.6	3	3	0.67	0.6
d3x4y-0.67u0.6	3	4	-0.67	0.6
d3x4y-0.5u0.6	3	4	-0.5	0.6
d3x4y-0.33u0.6	3	4	-0.33	0.6
d3x4y-0.17u0.6	3	4	-0.17	0.6
d3x4y0u0.6	3	4	0	0.6
d3x4y0.17u0.6	3	4	0.17	0.6
d3x4y0.33u0.6	3	4	0.33	0.6
d3x4y0.5u0.6	3	4	0.5	0.6
d3x4y0.67u0.6	3	4	0.67	0.6
d4x1y0u0.6	4	1	0	0.6
d4x1.5y0u0.6	4	1.5	0	0.6
d4x2y0u0.6	4	2	0	0.6
d4x3y0u0.6	4	3	0	0.6
d4x4y0u0.6	4	4	0	0.6

6.3 Reynolds number effects

6.3.1 Test procedure

The turbine model is tested at the $x/D = 1$ downstream of the 7.62 cm diameter cylinder for the Reynolds number sensitivity analysis. The lateral position of the

cylinder is aligned with the turbine's center of rotation in these tests. The Reynolds number of the turbine is controlled by the speed of the flow in the test section of the water tunnel. Tests are conducted at the flow speeds of 0.5, 0.6 and 0.7 m/s, corresponding to turbine Reynolds numbers of 1.65×10^5, 2.00×10^5, and 2.35×10^5, respectively. The power coefficient results of the turbine operating downstream of the cylinder are compared with the results of the operating turbine in a uniform flow for flow speeds of 0.6 and 0.7 m/s.

Although the maximum speed of the flow in the test section reaches up to 1.2 m/s, the free-surface of the test section is not level anymore and waves affect the height of the water when the speed exceeds 0.8 m/s. Flow speeds between 0.4 and 0.7 m/s are optimum speeds at which the free-surface is still level.

6.3.2 Results

The Reynolds effect on the performance of the turbine in a uniform inflow is discussed in the previous chapter. Those results showed that the maximum power coefficient of the turbine increases with the Reynolds number. The maximum power coefficient increases from 0.93 for the Reynolds number of 2.00×10^5 to 1.26 while the Reynolds number increases to 2.35×10^5, which is a 35% increase in value. The increasing trend persists in the non-uniform inflow. The maximum power increases 28%, from 0.95 to 1.22, while the Reynolds number increases from 2.00×10^5 to 2.35×10^5, as shown in Figure 6.7.

The general trend in the power coefficient diagram remains unaffected by changing the Reynolds number; therefore, the rest of the non-uniform inflow tests are conducted at a fixed Reynolds number, velocity of 0.6 m/s or $Re_D = 2.00\times10^5$.

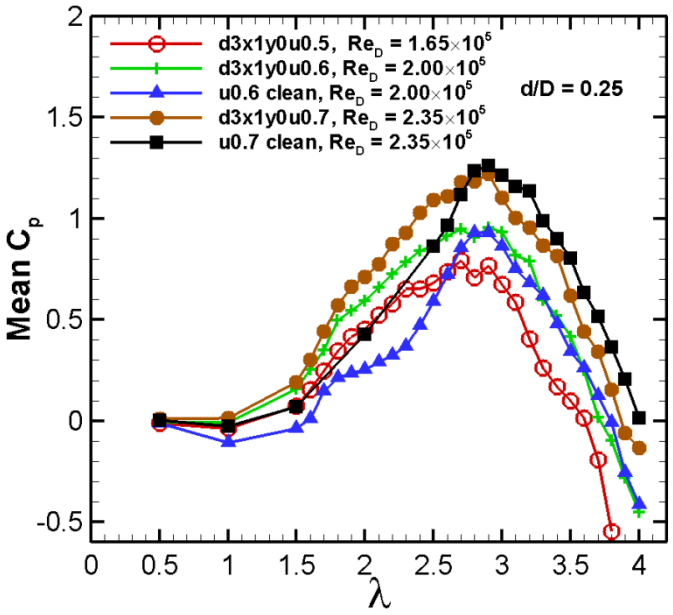

Figure 6.7: Reynolds number effect on the performance of the VAHT operating in a non-uniform inflow at 0.5, 0.6 and 0.7 m/s using one 3 in diameter cylinder compared to uniform flow ("clean") inlet condition at 0.6 and 0.7 m/s

6.4 Longitudinal distance

6.4.1 Test procedure

The longitudinal distance between the cylinder and the turbine affects the size and the strength of vortices interacting with the turbine. Cylinders are tested at five longitudinal distances from the center of the turbine, $x/D = 1$, 1.5, 2, 3 and 4. During the longitudinal tests, cylinders are aligned with the center of the turbine thus having zero lateral distance. At each longitudinal distance, the power coefficient of the turbine is measured, from a tip speed ratio of 0.5 to the freewheeling tip speed ratio. At low tip speed ratios, from 0.5 to 1.5, the turbine is tested at tip speed ratio steps of 0.5. Between the tip speed ratio of 1.5 and to the freewheeling tip speed ratio, the power measurement test is conducted at every 0.1 tip speed ratio steps.

6.4.2 Results

The power coefficient data at each tip speed ratio is averaged over the 30 s measurement period. The results of the averaging for the entire range of the tip speed ratio represent the power coefficient diagram of the turbine for a specific operating condition. This information is useful for the power output estimation; however, power oscillations and quality of the output power is discarded during the averaging.

Figure 6.8 (a) shows the average power diagram of the turbine operating downstream the $d/D = 0.08$ cylinder at different longitudinal distances. Results show that the upstream cylinder improves the overall performance of the turbine at the tip speed ratios lower than the optimum tip speed ratio. The maximum

power coefficient occurs at a higher tip speed ratio when the turbine operates in a uniform inflow. When the turbine passes the optimum tip speed ratio, the slope of the power coefficient diagram is identical for the uniform and non-uniform tests; however, the power coefficient of the turbine operating in a uniform inflow is higher as the optimum tip speed ratio is delayed for the clean test. Therefore, the freewheeling tip speed ratio is postponed for the uniform inflow test condition. The maximum power coefficient occurs at the tip speed ratio of 2.9, for the uniform inflow, while the upstream $d/D = 0.08$ cylinder causes the maximum power coefficient to occurs at lower tip speed ratio of 2.7.

Figure 6.8 (b) shows the longitudinal distance effect of the $d/D = 0.08$ cylinder on the maximum power coefficient of the turbine. The maximum power coefficient of the turbine increases with the longitudinal distance. However, at $x/D = 4$, the maximum power coefficient of the turbine experiences a slight drop.

Figure 6.9 (a) to Figure 6.11 (a) show the same pattern for $d/D = 0.17$, 0.25 and 0.34. Improvement in the power coefficient at tip speed ratios lower than the optimum tip speed ratio and deterioration at higher tip speed ratios. The maximum power coefficient occurs earlier and its value drops due to the upstream cylinder. However, Figure 6.9 (b) to Figure 6.11 (b) show a slight difference with Figure 6.8 (b) and that is the minimum power coefficient at $x/D = 1.5$, instead of $x/D = 1$, and an increasing power coefficient rate from $x/D = 3$ to $x/D = 4$, instead of a decreasing rate. The maximum power coefficient of the turbine operating downstream of a cylinder in line with the turbine is always less than the maximum power coefficient of the turbine

operating in uniform inflow. This difference is reduced with the longitudinal distance for x/D longer than 1.5.

At low tip speed ratios, or at tip speed ratios less than the optimum tip speed ratio, blades experience a deep dynamic stall condition. The upstream cylinder increases the turbulence intensity of the inflow for the blades; therefore, the stall angle of attack is enhanced and the intensity of the dynamic stall is scaled down. This explains the higher performance of the turbine in the non-uniform flow. The second effect of the upstream cylinder is the local velocity deficit due to the wake. The velocity deficit reduces the maximum power coefficient of the turbine and shifts the power diagram towards the lower tip speed ratios.

Figure 6.12 shows the variation of the maximum power coefficient of the turbine versus the longitudinal location of the upstream cylinder with various sizes. Except for $d/D = 0.08$, the maximum power coefficient is minimum while the longitudinal distance of the upstream cylinder is $x/D = 1.5$. In this particular case, the maximum power coefficient is even less than that of the case $x/D = 1$. When the upstream cylinder is located close to the turbine, $x/D = 1$, the vortices impacting the turbine are stronger. Due to the short distance, these strong vortices only cover a smaller part of the turbine. Increasing the longitudinal distance damps the strength of vortices, yet the wake deficit envelope containing vortices is wider. At $x/D = 1.5$ the combination of vortex strength and the width of the wake have the strongest adverse contribution on the power coefficient. The maximum power coefficient approaches the value of the uniform inflow test, as the longitudinal distance increases. Among the cylinders tested, $d/D = 0.25$ has the fastest recovery rate. At $x/D = 3$, the turbine exposed to a $d/D = 0.25$ upstream cylinder has a maximum power coefficient greater than

that of $d/D = 0.16$ and at $x/D = 4$, even exceeding that of the $d/D = 0.16$ cylinder.

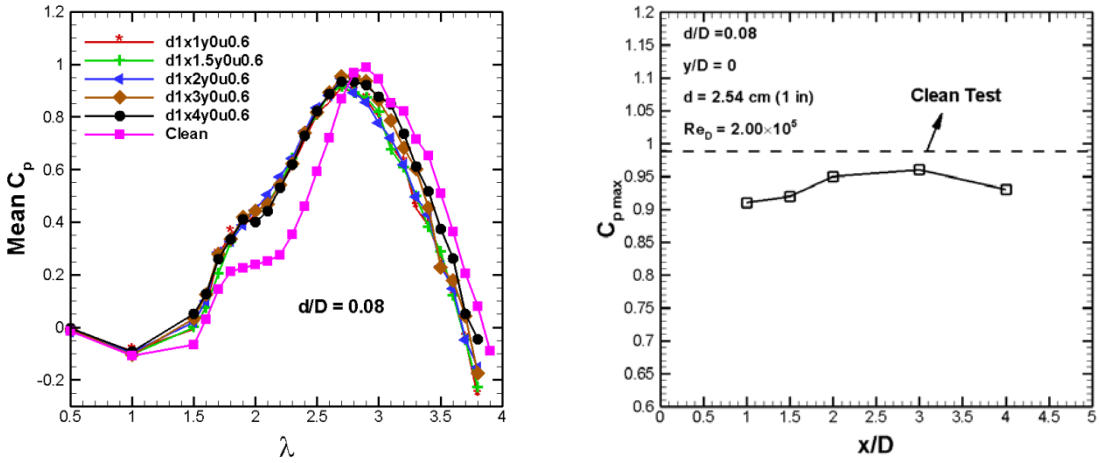

(a) (b)

Figure 6.8: The effect of the longitudinal position of a d/D = 0.08 cylinder at a velocity of 0.6 m/s for x/D spanning 1 to 4 as compared to uniform inlet clean tests: (a) power coefficient diagram, and (b) maximum power coefficient of the turbine

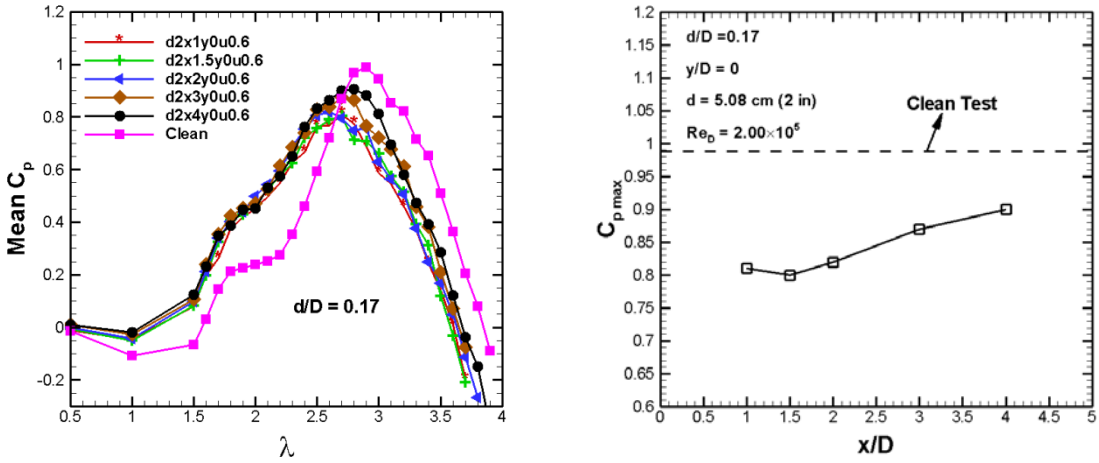

(a) (b)

Figure 6.9: The effect of the longitudinal position of a d/D = 0.17 cylinder at a velocity of 0.6 m/s for x/D spanning 1 to 4 as compared to uniform inlet clean tests: (a) power coefficient diagram, and (b) maximum power coefficient of the turbine

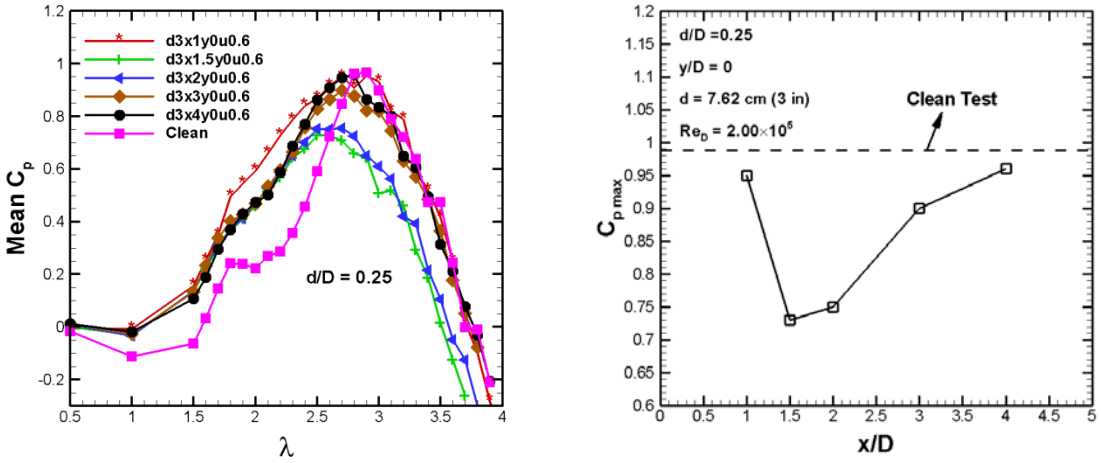

(a) (b)

Figure 6.10: The effect of the longitudinal position of a d/D = 0.25 cylinder at a velocity of 0.6 m/s for x/D spanning 1 to 4 as compared to uniform inlet clean tests: (a) power coefficient diagram, and (b) maximum power coefficient of the turbine

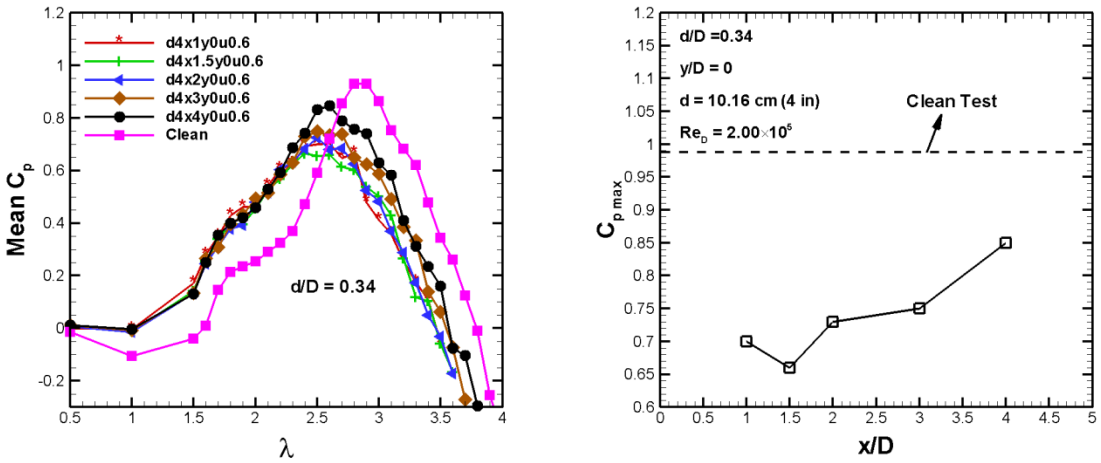

(a) (b)

Figure 6.11: The effect of the longitudinal position of a d/D = 0.34 cylinder at a velocity of 0.6 m/s for x/D spanning 1 to 4 as compared to uniform inlet clean tests: (a) power coefficient diagram, and (b) maximum power coefficient of the turbine

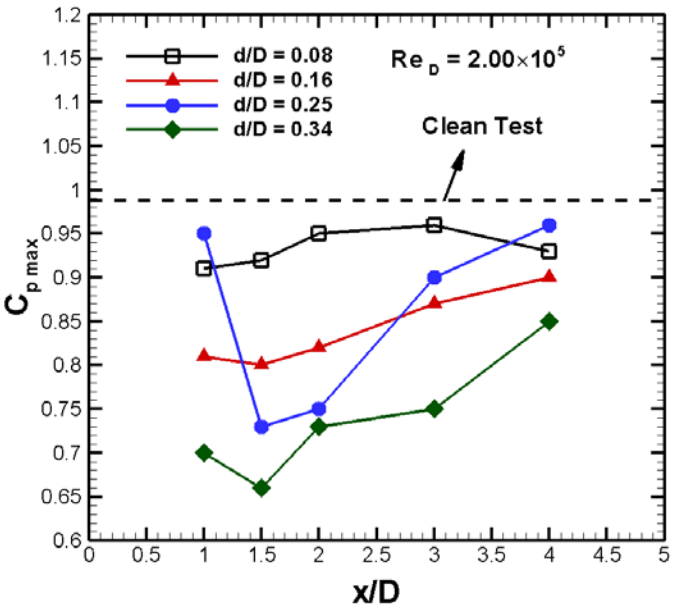

Figure 6.12: Maximum power coefficient of the turbine versus the longitudinal distance of cylinders with various sizes and compared to the clean uniform test

6.5 Lateral distance

For the longitudinal distance test, cylinders are aligned with the rotational center of the turbine. Therefore, the wake and the vortices shed behind the cylinders are symmetrically distributed around the center of the turbine and they hit the blades at $90°\pm\theta°$, where θ is a function of the longitudinal distance of the cylinder from the turbine. The non-symmetric wake around the turbine's center of rotation is generated by displacement of cylinders in the lateral direction. In this section, the effect of the lateral displacement of cylinders from the turbine centerline is assessed.

6.5.1 Test procedure

The power coefficient of the turbine is measured downstream of the d/D = 0.25 cylinder while the longitudinal positions of the cylinder varies from y/D = -0.67 to y/D = +0.67 in steps of y/D = 0.17. The positive longitudinal distance is where the blade turns in the direction of the flow and the negative longitudinal distance is where the blade turns in the opposite direction of the flow, as shown in Figure 6.6. The effect of the lateral distance of cylinders is tested at five longitudinal distances, x/D = 1, 1.5, 2, 3 and 4. During this test, the flow speed is set to 0.6 m/s representing a turbine Reynolds number of 2.00×10^5. The 50 cm flow height in the test section imposes a clearance coefficient of 0.24 on the turbine. The power coefficient of the turbine is measured for a 30 s period at each tip speed ratio starting from 0.5 and continues to the freewheeling tip speed ratio.

6.5.2 Results

Figure 6.13 to Figure 6.17 show the lateral position effect of the d/D = 0.25 cylinder at various longitudinal distances on the power coefficient of the turbine. For better presentation, the negative and positive lateral distances are shown in separate figures. Part (a) of the figures shows the effect of negative lateral distances and part (b) shows the effect of positive lateral distances. Except for x/D = 1, the power coefficient of the turbine increases with increase of the absolute value of the lateral distance. For x/D = 1, the power coefficient decreases as the cylinder moves from y/D = 0 to $|y/D|$ = 0.17; however, after that the power coefficient has an increasing rate as the absolute value of the lateral distance of the cylinder increases. Compared to the turbine in a

symmetric wake around the center of rotation, $y/D = 0$, non-centerline wakes diminish the power coefficient diagram at low tip speed ratios. The difference between the power coefficient of the turbine operating behind the cylinder centerline, $y/D = 0$, and non-centerline cylinders is more pronounced when the tip speed ratio exceeds the $\lambda = 2$. A step in the power diagram of the turbine operating behind the non-centerline cylinder specifically for negative lateral positions is noticeable.

The maximum power coefficient occurs at a higher tip speed ratio when the upstream cylinder has an offset from the turbine's centerline. The tip speed ratio of the maximum power coefficient increases as the lateral offset between the cylinder and the turbine's centerline increases. The cylinder offset improves the power coefficient of the turbine at tip speed ratios greater than the tip speed ratio of the maximum power coefficient.

According to the theory, the maximum blade angle of attack occurs at $\cos^{-1}(-1/\lambda)$. The tip speed ratio of the maximum power coefficient is 2.7 when the turbine operates behind the cylinder centerline. Therefore, the maximum angle of attack of the blade at this tip speed ratio occurs around the azimuth angle of 110° or the lateral location of $y/D = 0.17$. When the longitudinal distance of the cylinder from the turbine is more than $x/D = 1$, the maximum angle of attack of the blade happens in the wake of the cylinder. The flow speed decreases in the wake; therefore, the local tip speed ratio of the blade increases in the wake and causes a reduction in the blade maximum angle of attack and consequently the power output of the turbine is diminished. Turbine improves its blade angle of attack by slowing down the rotational speed.

The off-center cylinder affects the turbine in a different way. The flow speed increases outside the wake zone to satisfy the conservation of mass. The maximum blade angle of attack occurs outside of the wake zone for the off-center cylinder. Therefore, the flow speed increases for the blade outside of the wake zone and causes a higher angle of attack for the blade. For a turbine operating in a uniform inflow, the maximum blade angle of attack is near the stall angle of attack, or slightly above it. Moreover, the rise in the blade angle of attack due to the off-center upstream cylinder intensifies the dynamic stall condition of the blades and alters the turbine from the optimum operating condition. The self-adjustment nature of the turbine increases the blade rotational speed to reduce the blade angle of attack. Thus, the maximum power coefficient occurs at a higher tip speed ratio while the upstream cylinder is off-center.

Figure 6.18 shows the maximum power coefficient of the turbine operating behind the $d/D = 0.25$ cylinder at various longitudinal and lateral locations. The turbine experiences an increasing rate in the maximum power coefficient as the absolute value of the lateral distance of the cylinder is increased, except from $y/D = 0$ to $y/D = -0.17$ at longitudinal distances of $x/D = 1$ and 4. This increasing trend resumes to the lateral distances beyond the $y/D = \pm 0.5$. The longitudinal distance damps the increase rate in the maximum power coefficient due to the lateral displacement. Results show that the turbine is able to generate more power while the upstream cylinder is located in a positive lateral distance compare to the turbine operating behind the cylinder in a negative lateral distance. The cylinder with positive lateral distance increases the relative velocity over the blade due to the negative lateral velocity component of its wake. The higher relative velocity increases the aerodynamic loads and

consequently the torque of the blade. The cylinder with negative lateral distance has a reverse effect and reduces the relative velocity over the blade. The maximum power coefficient exceeds the maximum power coefficient of the uniform inflow test while the absolute value of the lateral distance passes 0.33.

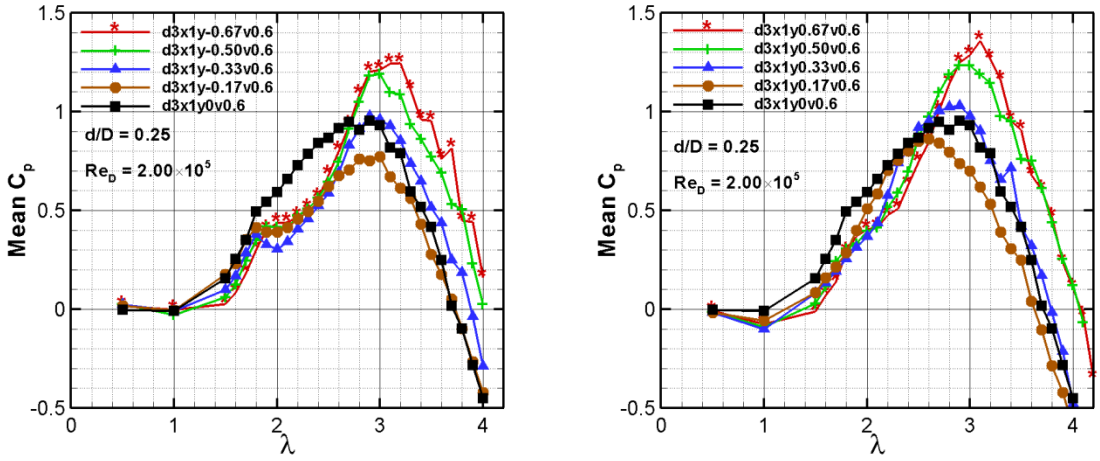

(a) (b)

Figure 6.13: The effect on the power coefficient of the turbine by changing the lateral position for a $d/D = 0.25$ cylinder placed at $x/D = 1$ at 0.6 m/s: (a) negative lateral positions, and (b) positive lateral positions

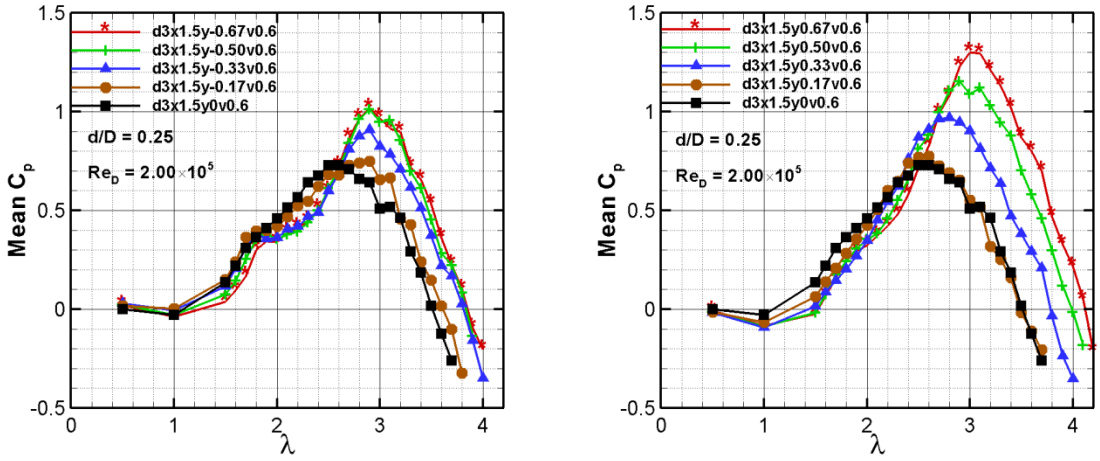

(a) (b)

Figure 6.14: The effect on the power coefficient of the turbine by changing the lateral position for a $d/D = 0.25$ cylinder placed at $x/D = 1.5$ at 0.6 m/s: (a) negative lateral positions, and (b) positive lateral positions

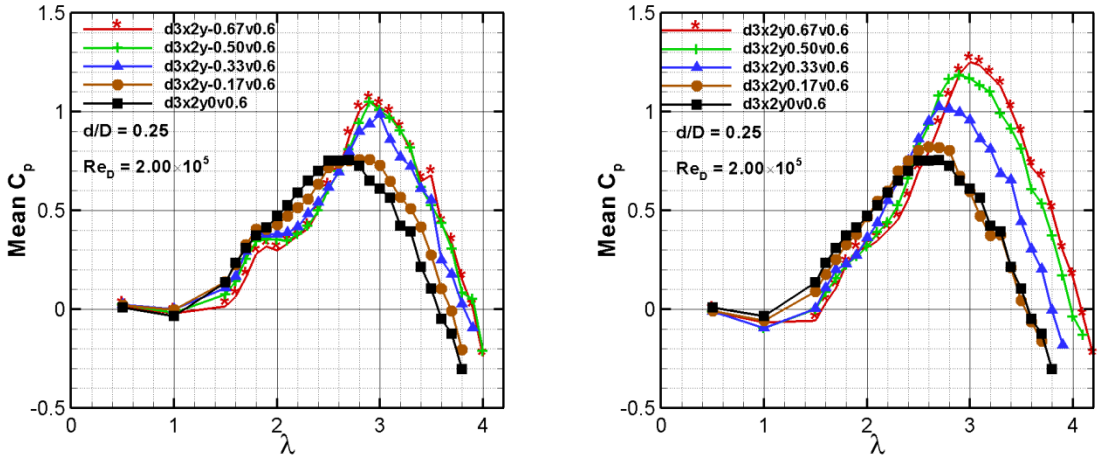

(a) (b)

Figure 6.15: The effect on the power coefficient of the turbine by changing the lateral position for a $d/D = 0.25$ cylinder placed at $x/D = 2$ at 0.6 m/s: (a) negative lateral positions, and (b) positive lateral positions

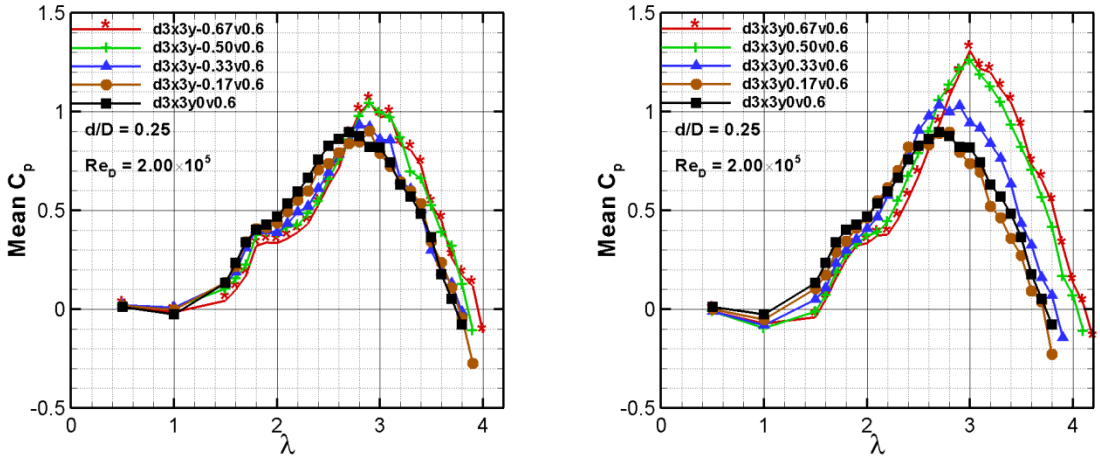

(a) (b)

Figure 6.16: The effect on the power coefficient of the turbine by changing the lateral position for a $d/D = 0.25$ cylinder placed at $x/D = 3$ at 0.6 m/s: (a) negative lateral positions, and (b) positive lateral positions

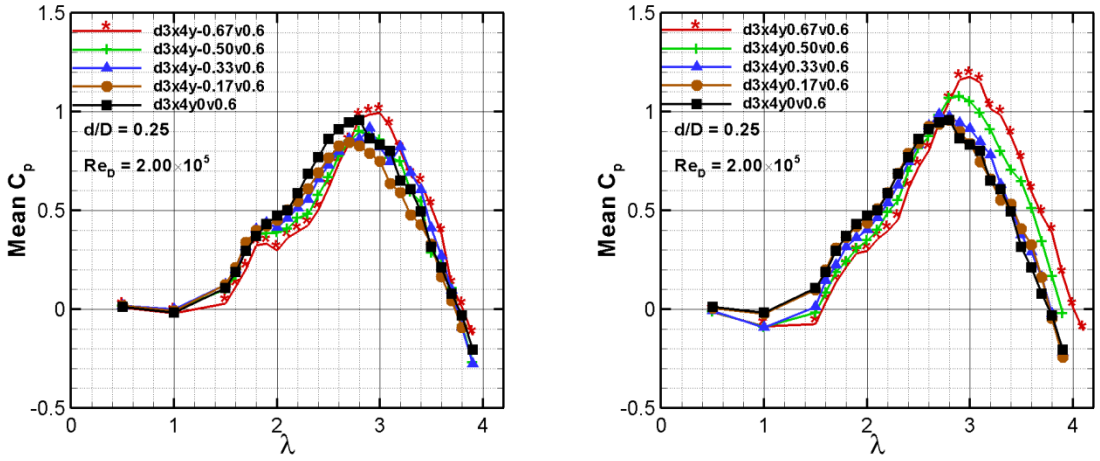

(a) (b)

Figure 6.17: The effect on the power coefficient of the turbine by changing the lateral position for a $d/D = 0.25$ cylinder placed at $x/D = 4$ at 0.6 m/s: (a) negative lateral positions, and (b) positive lateral positions

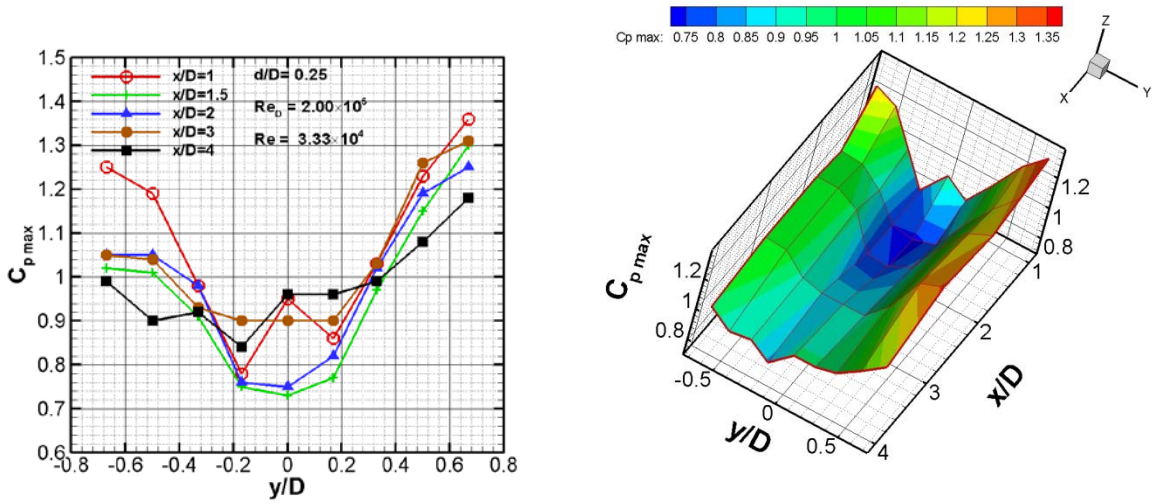

Figure 6.18: The maximum power coefficient of the turbine for various lateral and longitudinal distances for a $d/D = 0.25$ cylinder placed at x/D varying from 1 to 4 for lateral displacement -0.67 < y/D < 0.67

6.6 Frequency analysis

The average power is the key element to predict the output power of an array of turbines. However, it contains no information about the quality of the output power. The high fluctuating power not only can influence power systems, but also can reduce the lifetime of the turbine due to higher fatigue loads. The harmonics of the output power for a turbine operating in a uniform inflow are a factor of the rotational frequency of the turbine multiplied by the number of blades. Upstream cylinders change the inflow pattern and cause local high-speed and low-speed areas. These local velocity gradient areas add more fluctuations to the power output diagram due to the local fluctuations of the blade angle of attack.

From the average power diagram, the maximum power coefficient of the turbine occurs around the tip speed ratio of 2.7. Therefore, in this section, the frequency analysis is conducted on the power coefficient signal of the turbine at the tip peed ratio of 2.7. Figure 6.19 shows the power coefficient variations of the turbine for several rotational cycles with the upstream cylinders at various locations. Results show that the power coefficient does not follow a unique pattern in different cycles even in the absence of the upstream cylinder, when it is subjected to a uniform inflow. Although for uniform inflow, the turbine theoretically generates an identical output power in each rotation due to the blades identical angle of attack and Reynolds number. In reality however, the power output at a known azimuth angle fluctuates due to the vortex shedding behind the upstream blades and their interaction with the downstream blades and other non-ideal conditions like small fluctuations in the inflow velocity. The power coefficient deviation is much more limited for a turbine operating in a uniform inflow. Upstream cylinders increase the power coefficient deviation. Larger and closer

cylinders impose more fluctuations to the power coefficient diagram. The power coefficient deviation at different cycles is evident for $d/D = 0.25$ and 0.34 at the longitudinal distances of $x/D = 1$, 1.5 and 2.

Figure 6.20 shows the power coefficient comparison between a turbine operating in a uniform inflow and a turbine operating downstream of a $d/D = 0.34$ cylinder located at a longitudinal distance $x/D = 1$ without any lateral distance. The upstream cylinder diminishes the value of the peaks in the power diagram and adds two minor peaks between the two major peaks. The power diagram of the turbine operating in the uniform inflow has some small fluctuations around the minimum power coefficient values. These small fluctuations are extended on the entire rotation cycle while the turbine operates downstream the cylinder.

For a better understanding of the effect of the upstream cylinder on the power coefficient, the power coefficient is studied in the frequency domain. The wavelet and power spectral density methods are employed for frequency analysis of the power coefficient signal.

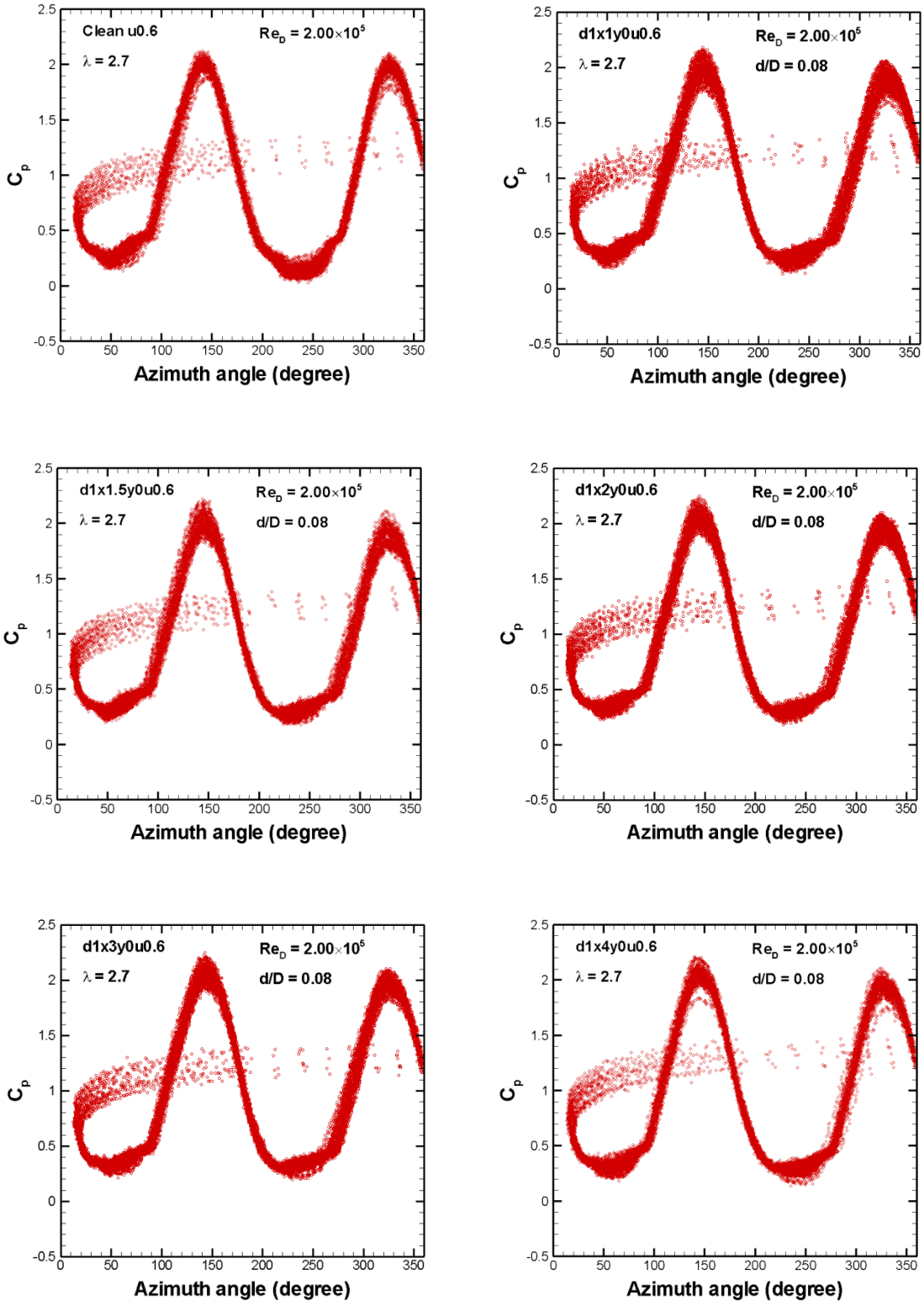

Figure 6.19: Instantaneous power coefficient of the turbine variations versus azimuth angle at the tip speed ratio of 2.7 for sizes and location of upstream cylinders

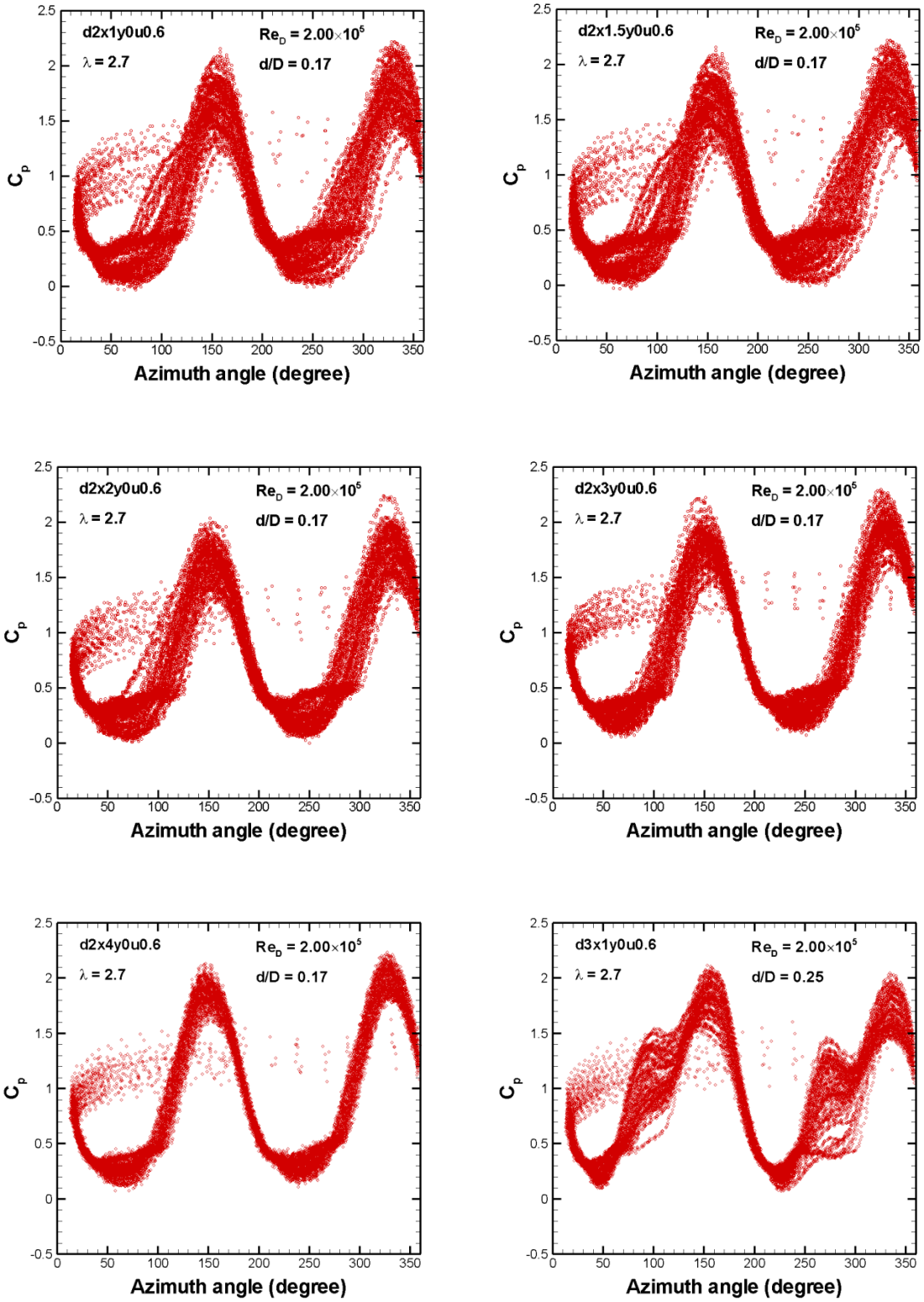

Figure 6.19 (cont.): Instantaneous power coefficient of the turbine variations versus azimuth angle at the tip speed ratio of 2.7 for sizes and location of upstream cylinders

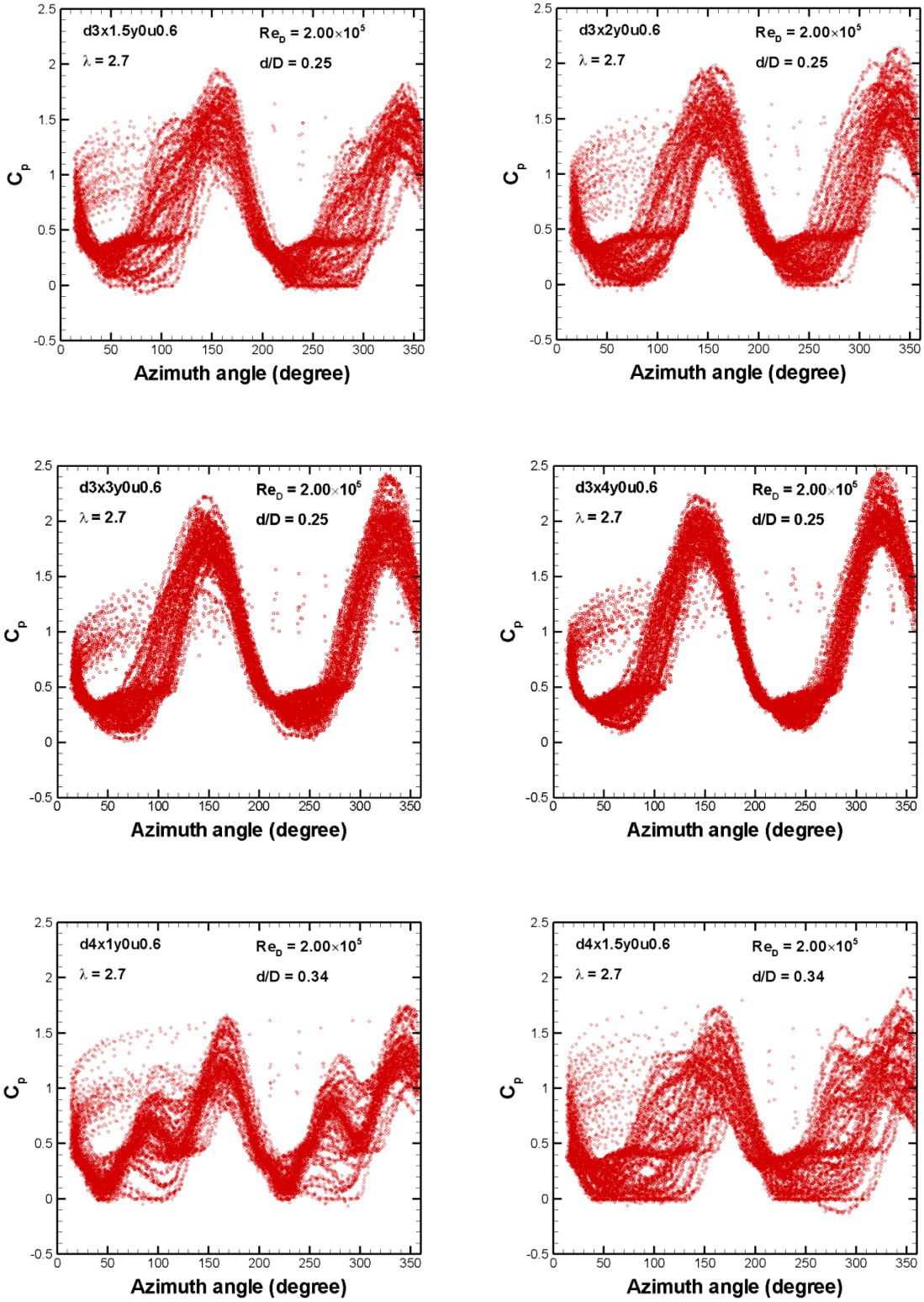

Figure 6.19 (cont.): Instantaneous power coefficient of the turbine variations versus azimuth angle at the tip speed ratio of 2.7 for sizes and location of upstream cylinders

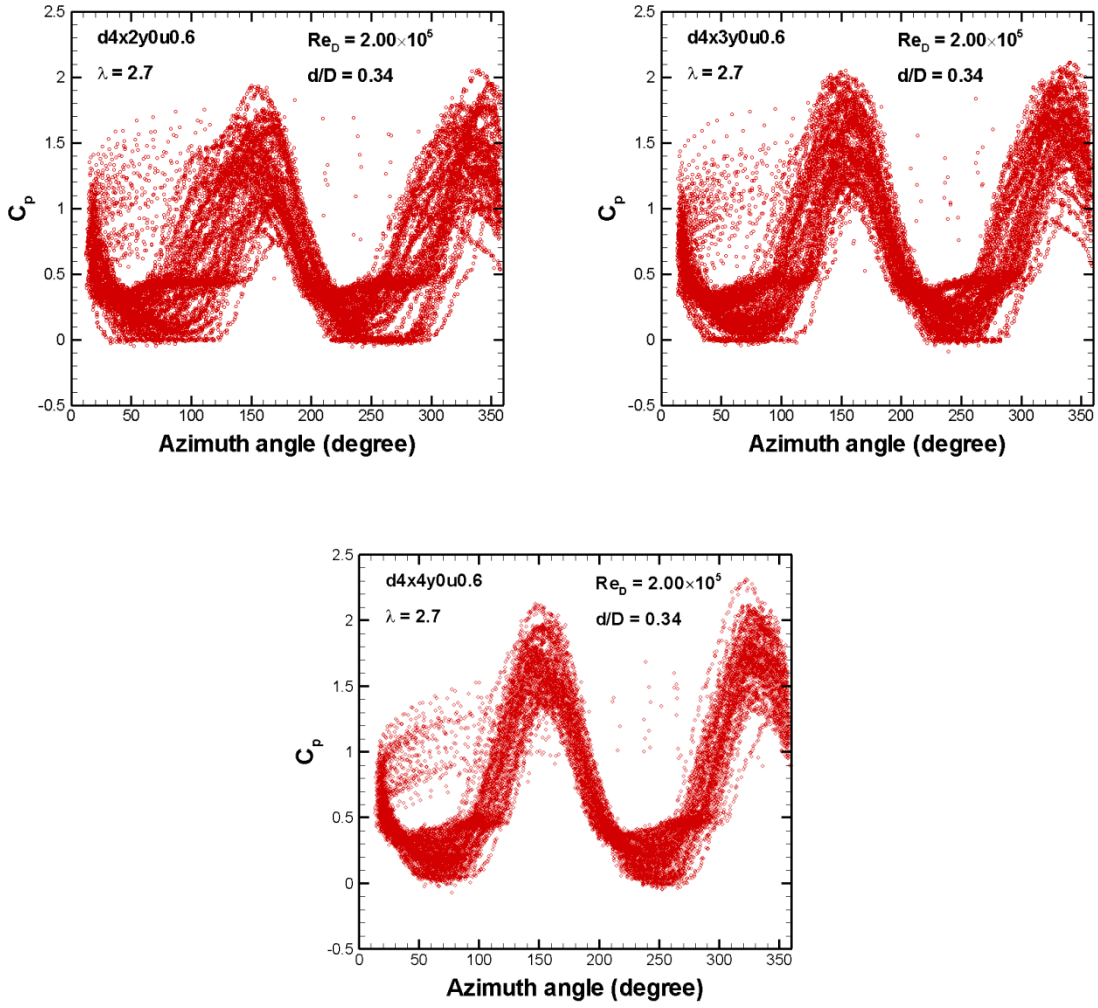

Figure 6.19 (cont.): Instantaneous power coefficient of the turbine variations versus azimuth angle at the tip speed ratio of 2.7 for sizes and location of upstream cylinders

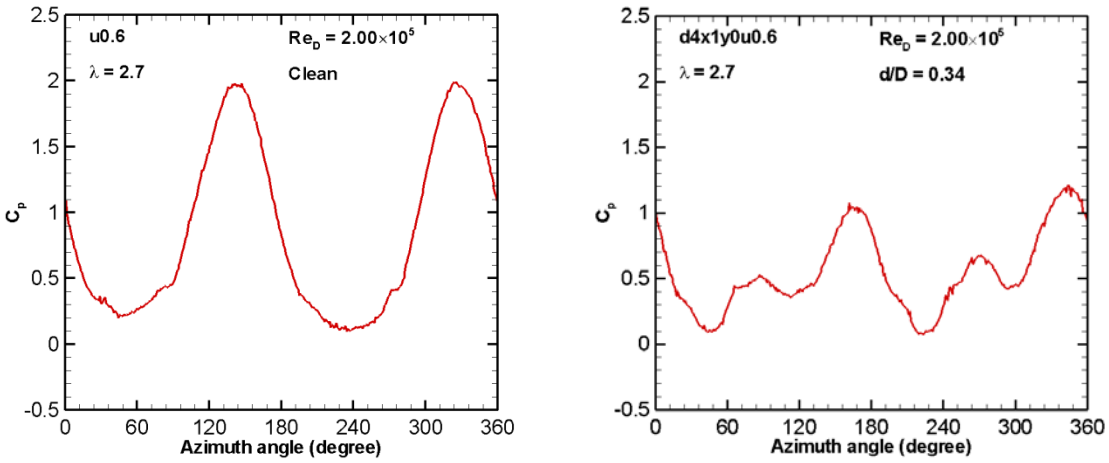

(a) (b)

Figure 6.20: Power coefficient comparison at the tip speed ratio of 2.7 between a turbine operating in (a) a uniform inflow, and (b) a turbine operating downstream a $d/D = 0.34$ cylinder at $x/D = 1$

6.6.1 Power spectral density

The power spectral density (PSD) function transfers the signal from the time domain to the frequency domain and describes the energy distribution of the signal with frequency. In this study, the PSD function is calculated for the power output signal using Welch's method [139]. Welch's method divides the signal into several overlapping segments and fits a specified window to each segment. Thus, a Hann window with 50% overlapping is applied to the power signal.

The rotational speed of the turbine with the radius of 15 cm at a tip speed ratio of 2.7 and the flow speed of 0.6 m/s is 10.8 rad/s, which is equivalent to a rotational frequency of 1.72 Hz. Due to the two-bladed configuration of the turbine, the principal frequency of the power output signal is 1.72×2 = 3.44 Hz. Figure 6.21 shows the energy distribution of the power output signal for the

turbine operating with no cylinder upstream. The highest energy belongs to the principal frequency. PSD also shows other peaks in the power output signal. The next high-energy point has a frequency twice the principal frequency. The frequencies that are the integer factors of the principal frequency are called prime frequencies. Between the first and second prime frequencies, another energy peak occurs in the middle of those two frequencies. This pattern is repeated to the end of the frequency domain. At higher frequencies, the energy difference between these three points is reduced. Before the principal frequency, there is an energy peak at the frequency of 1.75 Hz, which represents the blade rotational frequency. Although the blades of the turbine are similar in their design, in the manufacturing process it is impossible to have two identical blades. Small differences, like surface roughness, would cause different hydrodynamic characteristics for each blade. The difference between two blades is magnified near the stall angle of attack at which the flow separates from the blade surface and the lift coefficient drops suddenly. A small difference in manufacturing can accelerate or postpone the stall phenomenon considerably.

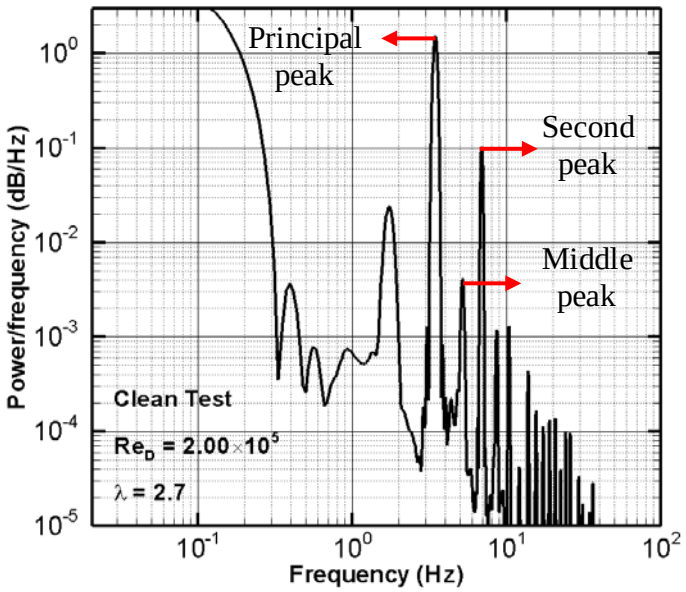

Figure 6.21: PSD of the power coefficient signal for the turbine operating in a uniform inflow

The upstream cylinder changes the pattern of the inflow to the turbine. The local low and high velocity zones disrupt the smooth sinusoidal pattern of the blade angle of attack in one rotation. Figure 6.22 compares the PSD of the turbine operating in a uniform inflow and the turbine downstream a $d/D = 0.34$ cylinder at $x/D = 1.5$. The upstream cylinder diminishes the power at the principal frequency and all integer factors of that. However, between the two consequent prime frequencies there are two power peaks instead of one. From Figure 6.22b, one can see the power of the frequencies between the first and the second prime frequencies is higher for the turbine operating downstream the cylinder compared to the turbine operating in a uniform inflow.

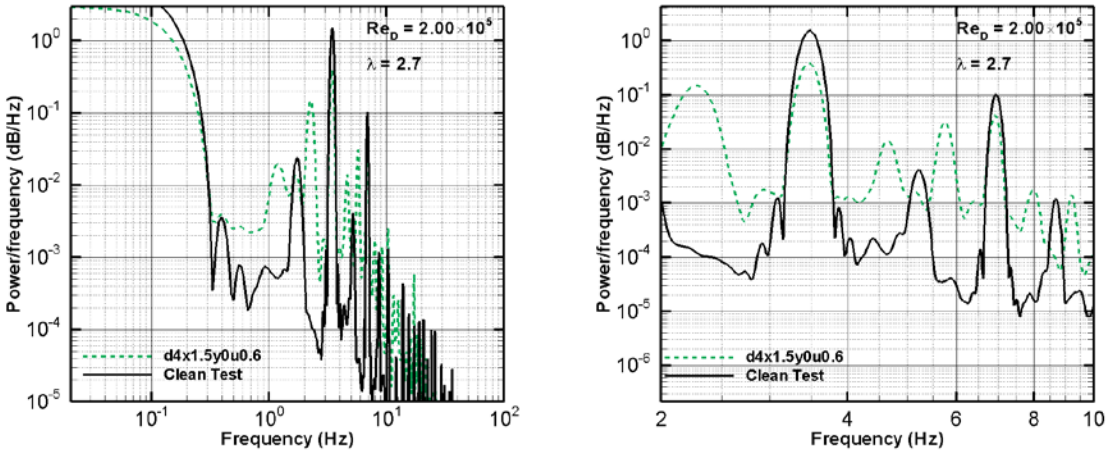

Figure 6.22: Power distribution of the power coefficient signal for the turbine operating in a uniform inflow and downstream a $d/D = 0.34$ cylinder at $x/D = 1.5$, between the frequency of (a) 0.02 and 100, and (b) 2 and 10

In the PSD diagram, events that occur in an integer number for the blade in one rotation of the turbine, like dynamic stall, appear on the prime frequencies. The summation of powers at prime frequencies represents the share of these events in the total power. Events that occur irregularly during rotations of the turbine lie between the two consequent prime frequencies. Compared to the regular events, the irregular events carry a small amount of energy, as shown in Figure 6.22. However, irregular events are important for power output quality and fatigue studies.

Table 6.3 summarizes the amount of power distributed under the PSD diagram for different test conditions. The second column of the table represents the power of the frequencies between the first two prime frequencies and the third column is the power on the total range of the frequencies. Results show that the turbine operating in a uniform inflow has the minimum power level between the two prime frequencies. This power increases when the inflow is disturbed by

upstream cylinders. The larger size of the cylinder causes a higher power between the two prime frequencies. For the small cylinders, $d/D = 0.08$ and 0.17, the maximum power occurs when the cylinder is in the closest distance to the turbine, $x/D = 1$. As the size of the cylinder increases, the maximum power occurs at a farther distance of the cylinder from the turbine. For $d/D = 0.25$ it occurs at $x/D = 1.5$ and for $d/D = 0.34$ it occurs at $x/D = 2$. However, the total power of the PSD is maximized while the turbine operates in a uniform inflow. Upstream cylinders reduce the total PSD power. The larger cylinders and close distances have the highest adverse effects on the total PSD power.

Figure 6.23 compares the spectrogram of the power coefficient for a clean test with uniform flow and a cylinder $d/D = 0.34$ and a longitudinal distance $x/D = 2$. The red colors indicate the high power locations and the blue colors represent the low power areas. Results show that the high power is mainly concentrated around the first and second prime frequencies when the turbine operates in uniform inflow. Irregular events have a negligible power in this case. The upstream cylinder diminishes the power at prime frequencies and increases the power of irregular events. The level of the power between the two prime frequencies considerably increases. The smooth sinusoidal shape of the PSD is disrupted by upstream cylinders.

Table 6.3: Energy distribution under the PSD diagram (dB/Hz)

Test	Between the two first prime frequencies	On the total frequency range
Clean test	0.030	20.701
d1x1y0u0.6	0.049	14.719
d1x1.5y0u0.6	0.042	15.036
d1x2y0u0.6	0.041	16.692
d1x3y0u0.6	0.042	17.613
d1x4y0u0.6	0.046	17.921
d2x1y0u0.6	0.397	8.796
d2x1.5y0u0.6	0.308	8.838
d2x2y0u0.6	0.227	8.898
d2x3y0u0.6	0.089	13.032
d2x4y0u0.6	0.053	14.999
d3x1y0u0.6	0.391	6.883
d3x1.5y0u0.6	0.645	3.787
d3x2y0u0.6	0.612	6.911
d3x3y0u0.6	0.485	13.071
d3x4y0u0.6	0.255	16.703
d4x1y0u0.6	0.385	1.020
d4x1.5y0u0.6	0.702	1.563
d4x2y0u0.6	0.756	3.463
d4x3y0u0.6	0.510	7.248
d4x4y0u0.6	0.337	9.901

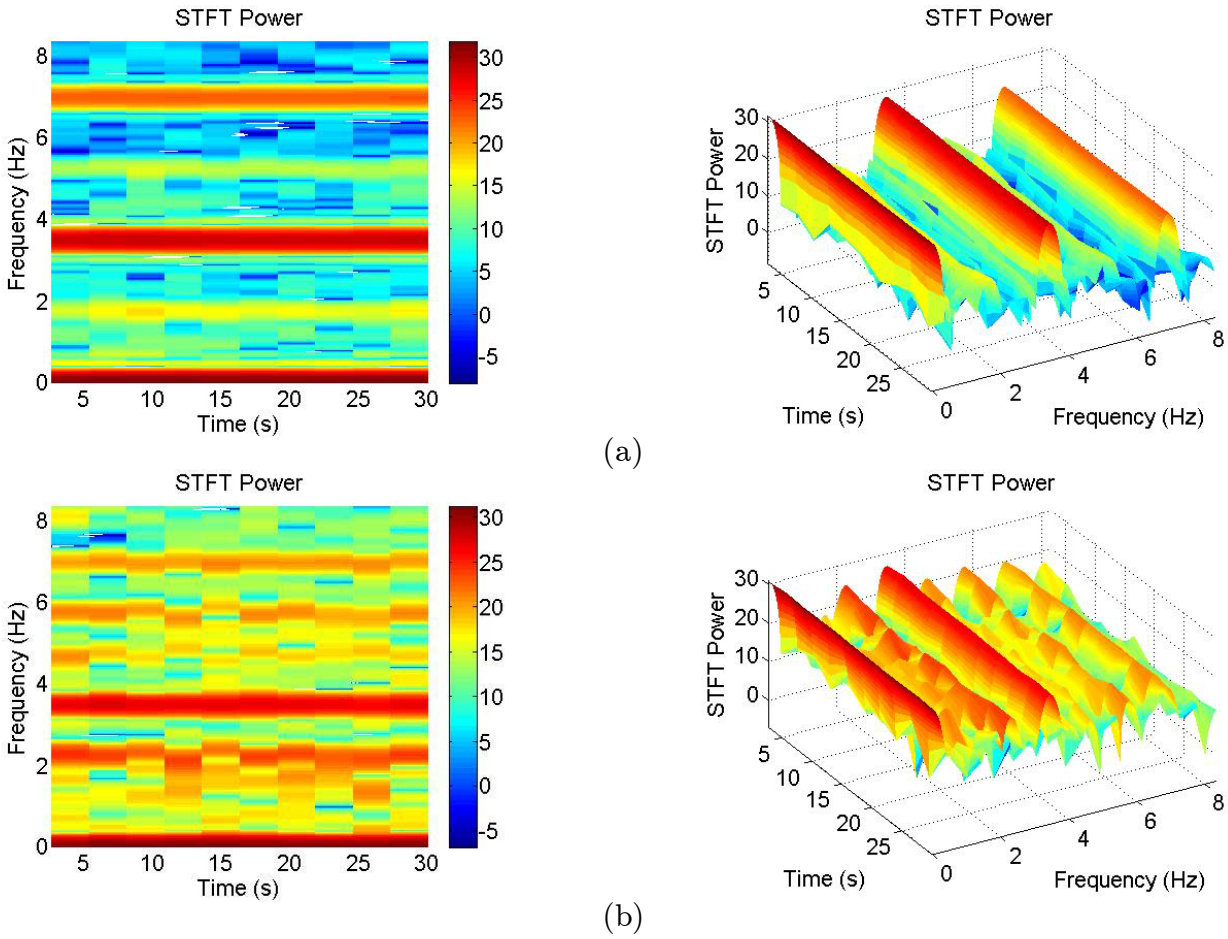

Figure 6.23: Spectrogram of power coefficient signal (a) clean test, and (b) d4x2y0u0.6 test

6.6.2 District wavelet transform

The second method employed to investigate the power coefficient signal in the frequency domain is the Discrete Wavelet Transform (DWT) [140,141]. DWT is a time-frequency method used in many fields of research ranging from signal processing to biometrics with a growing list of applications. DWT can be used as an alternative to Short Time Fourier Transform (STFT) [142] to overcome the time and frequency resolution drawbacks of STFT. DWT provides high time resolution and low frequency resolution for high frequencies. It also provides high

frequency resolution and low time resolution for low frequencies whereas STFT gives a uniform time resolution for all frequencies [143,144].

In wavelet analysis, an orthogonal finite function is defined as the basis function for describing a set of functions or signals. Then, the signal is described in some scales by which the components of the signal in the subspace spanned by the specified basis function.

$$f(t)=\sum_{k=-\infty}^{\infty} c_{j_0,k}\,\phi_{j_0,k}+\sum_{k=-\infty}^{\infty}\sum_{j=j_0}^{\infty} d_j(k)\,\Psi_{j,k}(t), \qquad 6.2$$

where $c_{j0,k}$ and d_j are the approximation and detail coefficients, respectively. $\phi_{j0,k}=2^{j/2}\phi(2^{j/2}t-k)$ and $\Psi_{j,k}=2^{j/2}\Psi(2^{j/2}t\text{-}k)$ are the scaled and shifted versions of the scaling and wavelet functions, respectively. The first term in Equation 6.2 shows the approximate components of the signal, *f(t)*, in the subspace spanned by $\phi_{j,k}(t)$, and the second term represents the detailed components of the signal in higher scales. DWT decomposes the signal into a coarse approximation and detail information. This decomposition is repeated on the coarse approximation at different levels, as shown in Figure 6.24.

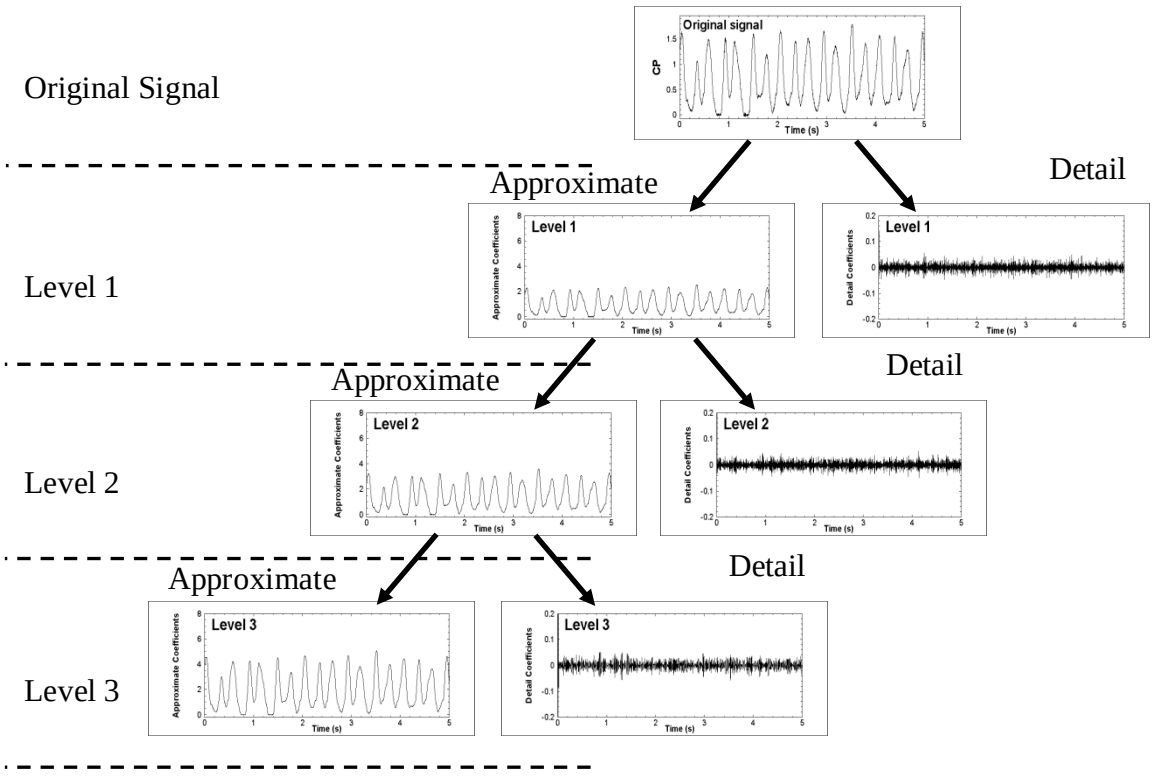

Figure 6.24: Wavelet decomposition in 3 levels

There exist several wavelet families in the literature. In this study, a Symlet basis function of order 8 is employed to discrete wavelet approximation and detail coefficients. First, the signal is decomposed into band-limited components. As mentioned previously, the bandwidth at each level of decomposition gets smaller; therefore, down-sampling can be performed without any loss of information. Reconstruction of the signal from its wavelet components can be accomplished by up-sampling, filtering, and summing all the sub-bands.

In order to compare the effect of upstream cylinder on the quality of the power output, the standard deviation of wavelet detail coefficients at each level in calculated. To simplify the writing process D_n is used for detail coefficients at level n of decomposition and A_n represents the approximate coefficients at level n.

The power coefficient signal is decomposed up to 10 levels. Table 6.4 shows the standard deviation of detail coefficients at 10 levels of wavelet decomposition for all test cases. Detail coefficients of all test cases have the standard deviation with the same order of magnitude until level 6. In level 7 the standard deviation increases in all cases. The clean test has the highest standard deviation of details while the details of the turbine operating at $x/D = 1$ downstream the $d/D = 0.34$ cylinder have the lowest standard deviation in this level. In level 8 details of the turbine operating at $x/D = 1.5$ downstream the $d/D = 0.34$ cylinder have the highest standard deviation. However, the standard deviations of the clean and the turbine with an upstream cylinder have the same order of magnitude. In level 9 the difference between the clean test and the rest of the case is pronounced. The detail coefficients of the turbines operating downstream a cylinder have standard deviations 10 times greater than that of the clean test. Results show that at frequencies lower than the first prime frequency, level 8 and higher, the standard deviation of the power coefficient details for the turbines operating downstream a cylinder is higher than that of the turbine operating in a uniform inflow.

Table 6.4: Standard deviation of detail coefficients at 10 levels of wavelet decomposition

	Standard deviation of detail coefficients									
Test	D1	D2	D3	D4	D5	D6	D7	D8	D9	D10
Clean test	0.017	0.017	0.020	0.051	0.163	1.406	6.873	2.143	0.0894	1.472
d1x1y0u0.6	0.013	0.014	0.019	0.046	0.159	1.341	6.337	1.764	1.022	1.734
d1x1.5y0u0.6	0.012	0.013	0.016	0.040	0.149	1.365	6.353	1.763	0.871	1.621
d1x2y0u0.6	0.014	0.017	0.026	0.060	0.172	1.391	6.500	1.762	0.910	1.507
d1x3y0u0.6	0.012	0.013	0.015	0.041	0.149	1.382	6.611	1.787	0.918	1.560
d1x4y0u0.6	0.012	0.013	0.016	0.044	0.144	1.395	6.631	1.849	0.925	1.650
d2x1y0u0.6	0.016	0.016	0.019	0.044	0.192	1.327	5.587	2.646	2.025	1.516
d2x1.5y0u0.6	0.015	0.015	0.017	0.043	0.171	1.20	5.591	2.063	2.581	1.528
d2x2y0u0.6	0.015	0.015	0.017	0.042	0.173	1.226	5.595	1.882	2.242	1.569
d2x3y0u0.6	0.016	0.017	0.020	0.045	0.157	1.282	6.121	1.884	1.471	1.642
d2x4y0u0.6	0.017	0.017	0.022	0.051	0.163	1.362	6.364	1.837	1.142	1.720
d3x1y0u0.6	0.009	0.011	0.018	0.053	0.271	1.499	5.243	2.190	1.056	1.701
d3x1.5y0u0.6	0.013	0.015	0.021	0.051	0.200	1.232	4.564	3.015	1.137	1.392
d3x2y0u0.6	0.014	0.015	0.019	0.050	0.184	1.201	5.285	2.965	1.116	1.388
d3x3y0u0.6	0.015	0.017	0.028	0.063	0.205	1.412	6.218	2.405	1.05	1.669
d3x4y0u0.6	0.018	0.021	0.032	0.066	0.188	1.348	6.584	2.246	1.118	1.816
d4x1y0u0.6	0.013	0.014	0.018	0.058	0.257	1.621	3.228	2.045	1.012	1.31
d4x1.5y0u0.6	0.013	0.013	0.016	0.048	0.197	1.163	3.725	3.333	1.752	1.441
d4x2y0u0.6	0.013	0.014	0.018	0.048	0.183	1.141	4.525	3.257	1.454	1.929
d4x3y0u0.6	0.013	0.013	0.016	0.048	0.185	1.176	5.401	2.717	1.416	1.856
d4x4y0u0.6	0.017	0.019	0.026	0.061	0.199	1.224	5.800	2.342	1.201	1.724

6.7 Summary

The non-uniform inflow was simulated for the turbine by upstream cylinders with different sizes. The effects of the longitudinal and lateral positions of the cylinder on the power output of the turbine were investigated. Results for the average power output show that the cylinder at the longitudinal distance of $x/D = 1.5$ has the maximum adverse effect on the average power output of the turbine. Compared to the cylinder aligned with the center of the turbine, the off-center cylinder increases the power output of the turbine. This increase is higher for positive lateral positions compared to the negative lateral positions.

The frequency analysis shows that the upstream cylinder diminishes the power of the turbine at prime frequencies while the frequencies between the two prime frequencies gain power. The non-uniform inflow not only increases the power of the frequencies between the two prim frequencies but also it increases the power of the low frequencies, lower than the first prime frequency. The diagram of the power output in one rotation is unrepeatable due to the variations in the inflow condition. The size of these fluctuations increases when the turbine operates downstream a cylinder.

Chapter 7

Conclusions and recommendations

7.1 Conclusion

Field measurements show that the inflow velocity is a time dependant parameter. Large eddies behind upstream obstacles, or river boundaries, introduce velocity variations in the river flow. The velocity measurements one diameter upstream the 25-kW VAHT show that the operating turbine creates a low velocity area around the turbine. Therefore, the negative velocity gradient near the actuating disk breaks the size of the large eddies in the flow. The size of large eddies one diameter upstream of the operating turbine is in the order of magnitude of the blade chord length. This size of eddies causes local high and low velocity areas for the blades and results in high frequency fluctuations in the power output.

A small-scale VAHT was designed, manufactured, and equipped with torque and positions sensors. The model turbine was tested in the University of Manitoba's water tunnel. The results obtained for the small-scale model are extendable to the real size turbine according to the similarity laws extracted for this purpose. Sensitivity studies were conducted in a uniform inflow condition to assess the solidity, preset pitch angle, free-surface and Reynolds number effects on the performance of the turbine.

The performance sensitivity of the turbine to the solidity is pronounced at low Reynolds numbers. Tests and investigations show that the efficiency of a high solidity VAT is higher compared to a low solidity VAT. A turbine with a solidity less than 0.2 is considered low solidity turbine while the turbine operates in a low blockage ratio condition. The sensitivity of the turbine to solidity extends to higher solidities while the blockage ratio increases. The performance of a single VAT in a wide channel or river, low blockage ratio, remains almost unaffected while the solidity increases above 0.2. However, for a turbine in an array or narrow waterway, where the flow is forced to pass through the turbine, higher solidity improves the performance of the turbine. At higher solidities, the maximum power coefficient occurs at lower tip speed ratios.

The performance of VATs is highly sensitive to the preset pitch angle. Toe-in angle has a negative effect on the efficiency of the turbine while toe-out angles between 2° and 7° can help to improve the efficiency of the turbine. The toe-out angle reduces the angle of attack in the upstream pass and increases the absolute value of the blade angle of attack in the downstream pass. Therefore, the toe-out preset pitch angle reduces the intensity of the dynamic stall in the upstream pass and increases the power extraction in the downstream pass of the turbine. By considering results at the solidity section one can conclude that the toe-out preset pitch angle is an essential rule for high solidity turbines. High solidity turbines operate at low tip speed ratios; therefore, the maximum angle of attack in the upstream pass is high above the stall angle of attack. In this condition, the turbine loses efficiency due to the deep dynamic stall conditions. The toe-out preset pitch angle reduces the maximum angle of attack in the upstream pass and moderates the dynamic stall intensity. At the same time, the toe-out angle

enables the turbine to extract more power in the downstream pass. Thus, the toe-out preset pitch angle is highly recommended for VATs, particularly for high solidity models.

The free-surface blockage increases the power coefficient of the vertical kinetic turbine. In this condition, the maximum power coefficient can be higher than the Betz's limit. Results show that the power coefficient decreases with the positive clearance coefficient. The maximum power coefficient occurs around the clearance coefficient of zero. Negative clearance coefficient decreases the power coefficient considerably. The negative clearance coefficient means the turbine is semi-submerged and part of the blade is exposed to air. The suction side of the blade draws air into the water and separates the water from the blade, causing stall. This separation sometimes expands and covers the whole blade length and results in a negative torque and power coefficient. High-speed camera images show that the full water separation starts with an air bubble formation on the blade. This air bubble eventually bursts and forms an air vortex. The air vortex convects on the blade and after it leaves the trailing edge of the blade and the full water separation occurs and causes the stall.

At low free stream Reynolds numbers, the power coefficient of the VAHT is sensitive to the Reynolds number and increases with the Reynolds number. The power coefficient becomes independent of the Reynolds number at high Reynolds numbers. The high Reynolds number region is defined based on the turbine geometry and other operating parameters; however, typically when the blade Reynolds number exceeds 10^6, the operating behavior of the turbine becomes almost independent of the Reynolds number.

Freewheeling vertical turbines have three operating zones based on the free stream Reynolds number. At low Reynolds numbers, the tip speed ratio is lower than unity and the turbine operates in a stall condition. At a threshold value of the Reynolds number, the tip speed ratio increases above unity. Due to the unstable condition of the blades near a tip speed ratio of one, a vertical turbine is unable to operate with stability near this tip speed ratio. When the freewheeling tip speed ratio is less than unity, operating the turbine at these Reynolds numbers is not practical. When the turbine passes the tip speed ratio of unity, the variation of the tip speed ratio with Reynolds number is linear until the maximum angle of attack approaches the stall angle of attack of the blade. The tip speed ratio during freewheeling remains constant.

The non-uniform inflow condition was modeled by upstream cylinders with various sizes. Results for the average power output show that the cylinder at the longitudinal distance of $x/D = 1.5$ has the maximum adverse effect on the average power output of the turbine. Compared to the cylinder aligned with the center of the turbine, the off-center cylinder increases the power output of the turbine. This increase is higher for positive lateral positions compared to the negative lateral positions.

The frequency analysis showed that the upstream cylinder diminishes the power of the turbine at prime frequencies while the frequencies between the two prime frequencies gain power. The non-uniform inflow not only increases the power of the frequencies between the two prime frequencies but also it increases the power of the low frequencies, lower than the first prime frequency. The diagram of the power output in one rotation is not reputable due to the variations in the inflow condition. The size of these fluctuations increases when the turbine operates

downstream a cylinder. The wavelet analysis shows that detail coefficients at the level of the second prime frequency have a high standard deviation for the clean condition, level 7 in the case of this study. At higher levels, the standard deviations of detail coefficients of the power output for non-uniform inflow condition have higher values.

7.2 Recommendations

The following suggestions are recommended for further study of effect of flow and fluid structures on performance of vertical river hydrokinetic turbines:

1. Particle image velocimetry (PIV) of the interaction between upstream large eddies and the blade of the turbine would be helpful to gain a better understanding of the physics of the phenomenon. The PIV measurement is able to visualize the flow structure motions and flow separation on the blades. The Plexiglas endplates enable PIV measurements inside the actuating disk of the turbine.
2. The wake study of the VAHT is recommended. The accurate size of the shed eddies and the pattern of the wake can improve the modeling of the flow structures. In addition, the wake study improves the spacing between the turbines in arrays of turbine for higher power extraction from a specified area.
3. Developing a numerical model to simulate the effect of upstream wakes on the performance of VAHT is useful to simulate various arrangement scenarios of VAHTs. This model would be useful to obtain the optimum arrangement for the highest energy extraction. The numerical model considerably reduces experimental expenses.
4. How VAHT affects the marine life is important for environmental study. For this purpose, it is suggested to secure the inlet and outlet of the water tunnel

test section with screens and release some small fishes in the water tunnel. Then a high-speed camera records the swimming path of fishes through the VAHT. This experiment should be conducted at various tip speed ratios and Reynolds numbers.

5. Developing a structural and vibrational model based on the experimental results obtained in this research helps to improve the structural design and fatigue lifetime estimation of VAHTs. The fatigue lifetime of the turbine is estimated based on the amplitude and frequency of dynamic loads applying on the turbine. Therefore, accurate dynamic loads as an input to the model results in a better fatigue lifetime estimation. In addition, for the design of the supporting structure, the natural frequencies of the supporting structure should be uncoupled with frequencies of dynamic loads imposed by the turbine.
6. Due to the facility limitations, the one-bladed turbine configuration was not tested in this research. The output power of the one-bladed configuration explicitly expresses the loads acting on one blade. This helps the better understanding the dynamic and aerodynamic of the blade.
7. The built VAT is capable of being tested in the wind tunnel. The ice accumulation process on the blades of the operating VAT in the icing tunnel of University of Manitoba can provide a unique source of data for cold climate application of VATs. This study can focus on the ice formation characteristics of the blades at various tip speed ratios and Reynolds numbers and power output variations versus the ice accumulation level.

References

1. Edmonds J. A., Reilly J. M., "A long-term global energy-economic model of carbon dioxide release from fossil fuel use," Energy Economics, vol. 5(2), pp. 74-88, 1983.

2. Population division of the department of economic and social affairs of the United Nations Secretariat, "World population prospects," Report, United Nations, New York, 2008.

3. Energy information administration office of integrated analysis and forecasting U.S. Department of Energy, "International energy outlook," Report, USA, 2009.

4. Manwell J. F., McGowan, J. G., Rogers, A. L., Wind energy explained theory, design and application. John Wiley and Sons, New Yourk, 2002.

5. Templin R. J., Rangi, R. S., "Vertical-axis wind turbine development in Canada," IEE Proceedings A: Physical Science. Measurement and Instrumentation Management and Education Reviews, vol. 130(9), pp. 555-561, 1983.

6. Ocean Renewable Energy Coalition "U.S marine and hydrokinetic renewable energy roadmap", November 2011.

7. The Ocean Renewable Energy Group, "Charting the course, Canada's marine renewable energy technology roadmap," October 2011.

8. Natural Resources Canada, "Marine Energy, What is marine renewable energy?," http://canmetenergy.nrcan.gc.ca/renewables/marine-energy/2475, Accessed January 2011.

9. El-Shamy F. M., "Environmental impacts of hydroelectric power plants," ASCE J Hydraul Div, vol. 103(9), pp. 1007-1020, 1977.

10. Baxter R. M., "Environmental effects of reservoirs," Microbial processes in reservoirs, pp. 1-26, 1985.

11. Darrieus G. J. M., "Turbine having its rotating shaft transverse to the flow of the current," U.S. Patent No. 1.835.018, 1931.

12. Sheng W., Galbraith R. A. M., Coton F. N., "Applications of low-speed dynamic-stall model to the NREL airfoils," Journal of Wind Energy Engineering, 132, pp. 0110061-0110068, 2010.

13. Sutherland H. J., Kelley N. D., "Fatigue damage estimate comparisons for Northern European and U.S. wind farm loading environments," Proceedings of WindPower, AWEA, Washington, DC., U.S.,1995.

14. Hand M. M., Simms D. A., Fingersh L. J., Jager D. W., Cotrell J. R., Schreck S., Larwood S. M., "Unsteady aerodynamics experiment phase VI: wind tunnel test configurations and available data campaigns unsteady aerodynamics experiment," NREL Technical Report, NREL/TP-500-29955, December 2001.

15. Kelley N., Hand M., Larwood S., McKenna E., "The NREL large-scale turbine inflow and response experiment: preliminary results," Proceedings of the Wind Energy Symposium, ASME, Reno, U.S., January 2002.

16. Sheng W., Galbraith R. A. M., Coton F. N., "Applications of low-speed dynamic-stall model to the NREL airfoils," Journal of Solar Energy Engineering, vol. 132, pp. 011006 (8 pages), 2010.

17. Yokosi S., "The structure of river turbulence," Bulletin of the Disaster Prevention Research Institute, Kyoto University, vol. 17, pp. 1-29, 1967.

18. Leishman, J. G., "Challenge in modeling the unsteady aerodynamics of wind turbines," Wind Energy, vol. 5(2-3), pp. 85-132, 2002.

19. Stack J., "Tests in the variable density wind tunnel to investigate the effects of scale and turbulence on airfoil characteristics," NACA Report 364, 1931.

20. Swalwell K. E., Sheridan J., Melbourne W. H., "The effect of turbulence intensity on stall of the NACA 0021 aerofoil," 14th Australasian Fluid Mechanics Conference, Adelaide, Australia, 2001.

21. Jacobs E. N., "The aerodynamic characteristics of eight very thick airfoils from tests in the variable density wind tunnel," NACA report 391, 1932.

22. McCroskey W. J., Mcalister K. W., Carr L. W., Pucci S. L., "An experimental study of dynamic stall on advanced airfoil sections," NASA TM-84245, 1982.

23. McCroskey W. J., Carr L. W., Mcalister K. W., "Dynamic stall experiments on oscillating airfoils," AIAA Journal, vol. 14, pp. 57-63, 1976.

24. Beddoes T. S., "A synthesis of unsteady aerodynamic effects including stall hysteresis," Vertica, vol. 1(2), pp.113-123, 1976.

25. Galbraith R. A. McD., Niven A. J., Seto L. Y., "On the duration of low speed dynamic stall," Congress of the International Council of the Aeronautical Sciences 15th, pp. 522-531, 1986.

26. Carr L. W., Mcalister K. W., McCroskey W. J., "Analysis of the development of dynamic stall based on oscillating airfoil measurements," NASA TN D-8382, 1977.

27. Crata F. O., "An analysis of the stall flutter instability of helicopter rotor blades," Journal of the American Helicopter Society, vol. 12(4), pp. 1-18, 1967.

28. Birjandi A. H., Gaden D., Shahsavarifard M., Bibeau E., "Scaling-up, hydrodynamic similarity laws, and guidelines to design hydrokinetic turbines for vertical hydrokinetic turbines," NRCAN, Ottawa, Technical Report, 2012

29. Templin R., "Aerodynamic performance theory for the NRC vertical-axis wind turbine," National Aeronautical Establishment, National Research Council of Canada, Technical Report, LTR- LA-160, 1974.

30. Wilson R., Lissaman P.,"Applied aerodynamics of wind powered machines," Oregon State University, Technical Report NSF-RA- N-74-113, 1974.

31. Strickland J., "The Darrieus turbine: a performance prediction model using multiple stream tubes," Sandia National Laboratories, Technical Report SAND75-041, 1975.

32. Paraschivoiu I., "Double-multiple streamtube model for Darrieus wind turbines," Second DOE/NASA Wind Turbines Dynamics Workshop, NASA CP-2186, pp. 19–25, Cleveland, OH, February, 1981.

33. Fanucci J. B., Walter R. E., "Innovative wind machines: the theoretical performance of a vertical-axis wind turbine," Vertical-Axis Wind Turbine Technology Workshop, Sandia Laboratories, USA 1976.

34. Strickland J. H., Smith T. G., Sun K., "A vortex model of the Darrieus turbine: an analytical and experimental study," Sandia National Laboratories, SAND81-7107, 1981.

35. Harlow F. H., Nakayama P. I. "Turbulence transport equations," Physics of Fluids, vol. 10(11), pp. 2323-2328, 1967.

36. Saffman P. G., "A model for inhomogeneous turbulent flow," Proceeding of the Royal Society of London, vol. 317, pp. 417-433, 1970.

37. Younis B. A., "Models of Turbulence", City University, 1993.

38. Eastman N. J., "The aerodynamic characteristics of eight very thick airfoils from tests in the variable density wind tunnel," NACA Technical Report, NACA-TR-391, 1932.

39. Soltani M. R, Birjandi A. H., Seddighi M., "Effect of Surface Contamination on the Performance of a Section of a Wind Turbine Blade," Journal of Scientia Iranica, vol.18(3), 349-357, 2011.

40. Sheldahl R. E., Blackwell B. F., "Free-air performance tests of a 5-metre diameter Darrieus turbine," Sandia National Laboratories, SAND77-1063, 1977.

41. Sheldah R. E., Klimas P., Fletz L. V., "Aerodynamic performance of a 5-metre Diameter Darrieus turbine with extruded aluminum NACA0015 blades," Sandia National Laboratories, SAND80-0179, 1980.

42. Sheldahl R. E., "Comparison of field and wind tunnel Dariues wind turbine data," Sandia Laboratories Technical Report, SAND80-2469, 1981.

43. Barthelmie R. J., Frandsen S. T., Nielsen M. N., Pryor S. C., Rethore P. E., Jorgensen H. E., "Modeling and measurement of power losses and turbulence intensity in wind turbine wakes at Middelgrunden offshore wind farm," Wind Energy, vol. 10(6), pp. 517-528, 2007.

44. Veers P. S., "Modeling stochastic wind loads on vertical axis wind turbine," Sandia Laboratories Technical Report, SAND83-1909, 1984.

45. Frost W., Long D. H., Turner R. E., "Engineering handbook on the atmospheric environment guideline for use in wind turbine generator development," NASA Technical Report 1359, December 1979.

46. Strickland J. H., "The Darrieus turbine: a performance prediction model using multiple streamtubes," Sandia Laboratories Technical Report, SAND75-0431, 1975.

47. Mann J., "The spatial structure of neutral atmospheric surface-layer turbulence," Journal of Fluid Mechanics, vol. 273, pp. 141-168, 1994.

48. Mann J., "Wind field simulation," Probabilistic Engineering Mechanics, vol. 13(4), pp.269-289, 1998.

49. Milborrow D. J., "Wake and cluster research: past, present and future," IEE Proceedings A, (Physical Science, Measurement and Instrumentation, Management and Education, Reviews, vol. 130(9), pp. 566-573, 1983.

50. MacLeod A. J., Barnes S., Rados K. G., "Wake effects in tidal current turbine farms," MAREC 2002, International Conference on Marine Renewable Energy - Conference Proceedings, pp. 49-53, 2002.

51. Rados K., Larsen G., Barthelmie R., Schlez W., Lange B., Schepers G., Hegberg T., Magnisson M., "Comparison of wake models with data for offshore wind farms," Wind Engineering, vol. 25(5), pp. 271-280, 2001.

52. Thomsen K., Madsen H. A., Larsen G. C., Larse T. J., "Comparison of methods for load simulation for wind turbines operating in wake," Journal of Physics: Conference Series, vol. 75, 012072 (12 pp.), 2007.

53. Troldborg N., Sorensen J. N., Mikkelsen R., "Actuator line simulation of wake of wind turbine operating in turbulent inflow," Journal of Physics: Conference Series, vol. 70, 012063 (15 pp.), 2007.

54. Michelsen J. A., "Basis3D- a platform for development of multiblock PDE solvers," Technical Report AFM 92-05, Department of Fluid Mechanics, Technical University of Denmark, DTU, 1992.

55. Michelsen J. A., "Block structured multigrid solution of 2D and 3D elliptic PDE's," Technical Report AFM 94-06, Department of Fluid Mechanics, Technical University of Denmark, DTU, 1994.

56. Sorensen, N. N., "General purpose flow solver applied to flow over hills," Ph.D. desertation, Riso-R-827(EN), Riso National Laboratoty, Roskilde, Denmark, 1995.

57. Sorensen J. N., Shen W. Z. "Computation of wind turbine wakes using combined Navier-Stokes/actuator-line methodology," Proceedings of European Wind Energy Conference EWEC '99, Nice, pp. 156-159, 1999.

58. Laesen G. C., Claren I., Schepers G. J., "European Wind Turbine Standards 2," Project Results, Technical Report, ECN-C-99-073, 1999.

59. Madsen H. A. A., "Aerodynamics of wind turbines," Proceeding of IEA Joint Action, 13th Symposium, Stokholm, 1999.

60. Magnusson M., Rados K. G., Voutsinas S. G., "A Study of the flow downstream of a wind turbine using measurements and simulation," Wind Engineering, vol. 20(6), pp. 389-403, 1996.

61. Hassan U., "A wind tunnel investigation of the wake structure within small wind turbine farms," Energy Technology Support Unit (ETSU), Technical Report, ETSU WN 5113, 1993.

62. Ainslie J. F., "Calculating the flowfield in the wake of wind turbines," Journal of Wind Engineering and Industrial Aerodynamics, vol. 27, pp. 213-224 ,1988.

63. Schepers J. G., "Wakefarm, Nabij zog model en ongestoord wind snel heisveld (in Dutch), Technical Report, ECN-C-98-016, 1998.

64. Fujisawa N., Shibuya S., "Observations of dynamic stall on Darrieus wind turbine blades," Journal of Wind Engineering and Industrial Aerodynamics, vol. 89(2), pp. 201-214, 2001.

65. Ferreira C. S., Van Kuik G., Van Bussel G., Scarano F., "Visualization by PIV of dynamic stall on a vertical axis wind turbine," Experiments in Fluids, vol. 46, pp. 97-108, 2009.

66. Ferreira C. S., Van Bussel G., Van Kuik G., "2D CFD simulation of dynamic stall on a vertical axis wind turbine: Verification and validation with PIV measurements," 45th AIAA Aerospace Sciences Meeting, Reno, NV, United states, vol. 23, pp. 16191-16201, 2007.

67. Ferreira C. S., Van Zuijlen A., Bijl H., Van Bussel G., Van Kuik G., "Simulating dynamic stall in a two-dimensional vertical-axis wind turbine: verification and validation with particle image velocimetry data," Wind Energy, vol. 13, pp. 1-17, 2010.

68. Ferreira C. S., Bijl H., Van Bussel G., Van Kuik G., "Simulating dynamic stall in a 2D VAWT: modeling strategy, verification and validation with particle image Velocimetry data," Journal of Physics: Conference Series, vol. 75, pp. 012023-1-13, 2007.

69. Ferreira C. S., Van Bussel G., Van Kuik G., "Wind tunnel hotwire measurements, flow visualization and thrust measurement of a VAWT in skew," Journal of Solar Energy Engineering, vol. 128(4), pp. 487-497, 2006.

70. Birjandi A. H., Woods J., Bibeau E. L., "Investigation of macro-turbulent flow structures interaction with a vertical hydrokinetic river turbine," To be published at Renewable Energy.

71. Yokosi S., "The structure of river turbulence," Bulletin of the Disaster Prevention Research Institute, Kyoto University, vol. 17, pp. 1-29, 1967.

72. Sutherland H. J., Kelley N. D., "Fatigue damage estimate comparisons for northern European and U.S. wind farm loading environments," Proceedings of Wind Power, AWEA, Washington, DC, U.S., 1995.

73. Hand M. M., Simms D. A., Fingersh L. J., Jager D. W., Cotrell J. R., Schreck S., Larwood S. M., "Unsteady aerodynamics experiment phase VI: wind tunnel test configurations and available data campaigns unsteady aerodynamics experiment," NREL Technical Report, NREL/TP-500-29955, December 2001.

74. Kelley N., Hand M., Larwood S., McKenna E., "The NREL large-scale turbine inflow and response experiment: preliminary results," Proceedings of the Wind Energy Symposium, ASME, Reno, U.S., January 2002.

75. Sheng W., Galbraith R. A. M., Coton F. N., "Applications of low-speed dynamic-stall model to the NREL airfoils," Journal of Solar Energy Engineering, 132: 011006, 2010.

76. Ainslie, J. F., Milbrrow, D. J., "Energy yield and turbulence properties of 320-turbine offshore windfarm," Proceedings of the 8th British Wind Energy Association Conference, pp. 121-129, 1986.

77. Frandsen S. T.,"Turbulence and turbulence generated fatigue loading in wind turbine clusters," Risø National Laboratory, Technical Report, Risø-R-1188, 2007.

78. Jørgensen H, Frandsen S, Vølund P., "Analyses of wake effects on Middelgrunden wind farm," Risø National Laboratory, Technical Report, Risø-R-1415, 2003.

79. Medici D., Alfredsson P. H., "Measurements on a wind turbine vortex shedding," Wind Energy, vol. 9, pp. 219-236, 2006.

80. Neopane H. P., "Sediment erosion in hydro turbines," Ph.D. Thesis, Norwegian University of Science and Technology, 2010.

81. Kassam S., "In-situ testing of a Darrieus hydro kinetic turbine," Master's Thesis, University of Manitoba, 2009.

82. Ginter V. J., "Robust gain scheduled control of a hydrokinetic turbine,". Master's Thesis, University of Calgary, 2009.

83. Goring D. G., Nikora V. I., "Despiking acoustic Doppler velocimeter data," Journal of Hydraulic Engineering, vol. 128, pp. 117-126, 2002.

84. Akhtaruzzaman Sarker M. D., "Flow measurement around scoured bridge piers using acoustic-Doppler velocimeter," Flow Measurement and Instrumentation, vol. 9(4), pp. 217-227, 1998.

85. Duraiswami R., Prabhukumar S., Chahine G. L., "Bubble counting using an inverse acoustic scattering method," Journal of the Acoustical Society of America, vol. 104(5), pp. 2699-2717, 1998.

86. Vallé B. L., Pasternack G. B., "Field mapping and digital elevation modeling of submerged and unsubmerged hydraulic jump regions in a bedrock step–pool channel," Earth Surface Processes and Landforms, vol. 31(6), pp. 646-664, 2006.

87. Chanson H., Trevethan M., Aoki S., "Acoustic Doppler velocimetry (ADV) in small estuary: field experience and signal post-processing," Flow Measurement and Instrumentation, vol. 19(5), pp. 307-313, 2008.

88. Trowbridge J., Elgar S., "Turbulence measurements in the surf zone," Journal of Physical Oceanography, vol. 31(8), pp. 2403-2417, 2001.

89. Trevethan M., Chanson H., Takeuchi M., "Continuous high-frequency turbulence and suspended sediment concentration measurements in an upper estuary," Estuarine, Coastal and Shelf Science, vol. 73(1), pp. 341-350, 2007.

90. Vectrino velocimeter user guide. Nortek As., October 2004.

91. Rodriguez A., Sánchez-Arcilla A., Redondo J. M., Mösso C., "Macroturbulence measurements with electromagnetic and ultrasonic sensors: a comparison under high-turbulent flows," Experiments in Fluids, vol. 27(1), pp. 31-42, 1999.

92. Rehmel M., "Application of acoustic Doppler velocimeters for streamflow measurements," Journal of Hydraulic Engineering, vol. 133(12), pp.1433-1438, 2007.

93. Macvicar B. J., Beaulieu E., Champagne V., Roy A. G., "Measuring water velocity in highly turbulent flows: field tests of an electromagnetic current meter (ECM) and an acoustic Doppler velocimeter (ADV)," Earth Surface Processes and Landforms, vol. 32(9), pp. 1412-1432, 2007.

94. Farmer D. M., Deane G. B., Vagle S., "The influence of bubble clouds on acoustic propagation in the surf zone," IEEE Journal of Oceanic Engineering, vol. 26, pp. 113-124, 2001.

95. Mori N., Suzuki T., Kakuno S. "Experimental study of air bubbles and turbulence characteristics in the surf zone," Journal of Geophysical Research, vol. 112, C05014, 2007.

96. Strom K. B., Papanicolaou A.N., "ADV measurements around a cluster microform in a shallow mountain stream," Journal of Hydraulic Engineering, vol. 133(12), pp. 1379-1389, 2007.

97. Wilcox A., Wohl E., "Field measurements of three-dimensional hydraulics in a step-pool channel," Geomorphology, vol. 83, pp. 215-231, 2007.

98. Elgar S., Raubenheimer B., Guza R. T., "Current meter performance in the surf zone," Journal of Atmospheric and Oceanic Technology, vol. 18(10), pp. 1735-1746, 2001.

99. Elgar S., Raubenheimer B., Guza R. T., "Quality control of acoustic Doppler velocimeter data in the surfzone," Measurement Science and Technology, vol. 16(10), pp. 1889-1893, 2005.

100. Birjandi A. H., Bibeau E. L., "Bubble effects on the acoustic Doppler velocimeter (ADV) measurements," Proceedings of the ASME Fluids

Engineering Division Summer Conference, Vail, U.S., vol. 2, pp. 27-32, August 2009.

101. Anderson S., Lohrmann A., "Open water test of the SonTek acoustic Doppler velocimeter," Proceedings of the IEEE Working Conference on Current Measurement, St. Petersburg, U.S., pp. 188-192, February 1995.

102. Birjandi A. H., Bibeau E.L., "Improvement of acoustic Doppler velocimetry in bubbly flow measurements as applied to river characterization for kinetic turbines," International Journal of Multiphase Flow, vol. 37(8), pp. 919-929, 2011.

103. Birjandi A. H., "River ADV measurement and hybrid filter," DOI: 10.5203/ds˙bib˙3, 2010.

104. Bibeau E. L., Kassam S., Woods J., Molinski M., Bear C., "Operating a 5-kW grid-connected hydro kinetic turbine in a river in cold climates," Canadian Journal of Ocean Engineering, vol. 35, pp. 67-79, 2009.

105. Soltani M. R., Birjandi A. H., Seddighi M., "Effect of surface contamination on the performance of a section of a wind turbine blade," Journal of Scientia Iranica, vol. 18(3), pp. 349-357, 2011.

106. Ghorbanian K., Soltani M. R., Dehghan Manshadi M., "Experimental investigation on turbulence intensity reduction in subsonic wind tunnels," Aerospace Science and Technology, vol. 15(2), pp. 137-147, 2011.

107. Strom K. B., Papanicolaou A. N., "ADV measurements around a cluster microform in a shallow mountain stream" Journal of Hydraulic Engineering, vol. 133(12), pp. 1379-1389, 2007.

108. Balcer B. E., "Boundary layer flow control using plasma induced velocity," Master's Thesis, Air Force Institute of Technology, Department of Aeronautics and Astronautics, 2005.

109. George R., Flick R. E., Guza R. T., "Observations of turbulence in the surf zone," Journal of Geophysical Research, vol. 99, pp. 801-810, 1994.

110. Wilcox A. C., Wohl E. E., "Field measurements of three-dimensional hydraulics in a step-pool channel," Geomorphology, vol. 83, pp. 215–231, 2007.

111. Nikora V. I., Smart G. M., "Turbulence characteristics of New Zealand gravel-bed rivers," Journal of Hydraulic Engineering, vol. 123(9), pp. 764-773, 1997.

112. Mathieu J., Scott J., "An introduction to turbulent flow," Cambridge University Press, 2000.

113. Schlichting H., "Boundary-layer theory," Springer 8th edition, 2000.

114. Whelan J. I., Graham J. M. R., Peiró J., "A free-surface and blockage correction for tidal turbines," Journal of Fluid Mechanics, vol. 624, pp. 281-291, 2009.

115. Bahaj A. S., Molland A. F., Chaplin J. R., Batten W. M. J., "Power and thrust measurements of marine current turbines under various hydrodynamic flow conditions in a cavitation tunnel and a towing tank," Renewable Energy, vol. 32, pp. 407-426, 2007.

116. Kirke B. K., "Evaluation of self-starting of vertical axis wind turbines for stand-alone applications," Ph.D. thesis, School of Engineering Griffith University, 1998.

117. Vectrino velocimeter user guide. Nortek As., October 2004.

118. Blackwell B. F., Sheldahl R. E., Feltz L. V., "Wind tunnel performance data for the Darrieus wind turbine with NACA 0012 blades," Sandia National Laboratories, SAND76-0130, 1976.

119. South P., Rangi R. S., "A wind tunnel investigation of a 14ft. Diameter vertical axis windmill," National Aeronautical Establishment, National Research Council of Canada, Technical Report, LTR-LA-105, 1972.

120. Armstrong S., "Power performance, flow behaviour and excitation response of canted blades for a vertical axis wind turbine," M.Sc. thesis, McMaster University, 2009.

121. Klimas P., Worstell M., "Effects of blade preset pitch/offset on curved-blade Darrieus vertical axis wind turbine performance" Sandia National Laboratories, SAND-81-1762, 1981.

122. Bibeau E., Kassam S., Woods J., Molinski T., Bear C., "Operating a 5-kw grid-connected hydrokinetic turbine in a river in cold climates," Journal Of Ocean Technology, vol. 4(4), pp. 71-82, 2009.

123. Thake J., "Development, installation and testing of a large-scale tidal current turbine," UK Department of Trade and Industry, Contract No. T/06/00210/00/REP, Oct. 2005.

124. Douglas C. A., Harrison G. P., Chick J. P., "Life cycle assessment of the Seagen marine current turbine," Proceedings of the Institution of Mechanical Engineers, Part M: Journal of Engineering for the Maritime Environment, vol. 222(1), pp. 1-12, Jan. 2008.

125. Rourke F. O., Boyle F., Reynolds A., "Tidal energy update 2009," Applied Energy, vol. 87, pp. 398-409, Feb. 2010.

126. Foubister L., Penwarden G., "EMEC tidal test facility Fall of Warness Eday, Orkney: environmental statement," AURORA Environmental Ltd, June, 2005.

127. Li Y., Colby J. A., Kelley N., Thresher R., Jonkman B., Hughes S., "Inflow measurement in a tidal strait for deploying tidal current turbines: lessons, opportunities and challenges," ASME Conference Proceedings, vol. 3, pp. 569-576, 2010.

128. Betz A., "Das maximum der theoretisch moglichen ausnuzung des windes durch windmotoren," Zeitschrift fur das Gesamte Turbinenwesen, vol. 17, pp. 307-309, 1920.

129. Garrett C., Cummins P., "The efficiency of a turbine in a tidal channel," Journal of Fluid Mechanics, vol. 588, pp. 243-251, 2007.

130. Whelan J. I., Graham J. M. R., Peiró J., "A free-surface and blockage correction for tidal turbines," Journal of Fluid Mechanics, vol. 624, pp. 281-291, 2009.

131. Bahaj A. S., Molland A. F., Chaplin J. R., Batten W. M. J., "Power and thrust measurements of marine current turbines under various hydrodynamic flow conditions in a cavitation tunnel and a towing tank," Renewable Energy, vol. 32, pp. 407-426, 2007.

132. Anderson J. D., "Fundamental of aerodynamics", Third Edition. New York: Mc Graw Hill, 2001.

133. Beddoes T. S., "Synthesis of unsteady aerodynamic effects including stall hysteresis," Vertica, vol. 1, pp. 113-123, 1976.

134. Galbraith R. A. M., Niven A. J., Seto L. Y., "On the duration of low speed dynamic stall," in Congress of the International Council of the Aeronautical Sciences, vol. 1, pp. 522-531, 1986.

135. Bravo R., Tullis S., Ziada S., "Performance testing of a small vertical-axis wind turbine," Proceedings of the 21st Canadian Congress of Applied Mechanics (CANCAM), pp. 470-471, 2007.

136. Modi V. J., Hein W., "Transducer for study of wake geometry," Journal of Scientific Instruments, vol. 42(7), pp. 497-498, 1965.

137. Taneda S., "Experimental investigation of vortex streets," Physical Society of Japan, vol. 20(9), pp. 1714-1721, 1965.

138. Hanson F. B., Kozak S. H., Richardson P. D., "Velocity spikes in separated flows," Journal of Fluid Mechanics, vol. 25(1), pp. 43-50, 1966.

139. Welch P. D, "The use of fast Fourier transform for the estimation of power spectra: a method based on time averaging over short, modified periodograms," IEEE Transaction Audio Electroacoustics, vol. AU-15, pp.70-73, 1967.

140. Mallat S. G., "A wavelet tour of signal processing," Academic Press, 1999.

141. Mallat S. G., "A theory for multiresolution signal decomposition: the wavelet representation," IEEE Transaction Pattern Anal. Mach. Intell., vol. 11, pp. 674-693, 1989.

142. Proakis J. G., Manolakis D. K., "Digital signal processing," Prentice Hall, 2006.

143. Kronland-Martinet R., "The Wavelet transform for analysis, synthesis, and processing of speech and music sounds," Computer Music Journal, vol. 12, pp. pp. 11-20, 1988.

144. Tzanetakis G., Cook P., "Musical genre classification of audio signals," IEEE Transactions on Speech and Audio Processing, vol. 10(5), pp. 293-302, 2002.

145. Daubechies I., "Orthonormal bases of compactly supported wavelets," Communications on Pure and Applied Mathematics, vol. 41, pp. 909-996, 1988.

146. Birjandi, A. H., "Vertical kinetic turbines operation at low tip speed ratios," New Energy Company, Calgary, Technical Report, 2009.

Appendix A

The power coefficient is defined as:

$$C_p = \frac{P}{0.5\rho A V^3} = \frac{\tau\omega}{0.5\rho(\pi r^2 L)U^3} = \frac{Volt_\tau (0.5\pi Volt_\omega)}{0.5\rho(\pi r^2 L)U^3}$$

Where the $Volt_\tau$ is the output voltage representing the torque and $Volt_\omega$ is the output voltage representing the rotational speed. Therefore the power coefficient error is:

$$\frac{\Delta C_p}{C_p} = \frac{\Delta Volt_\tau}{Volt_\tau} + \frac{\Delta(0.5\pi Volt_\omega)}{0.5\pi Volt_\omega} + \frac{\Delta(0.5\rho(\pi r^2 L)U^3)}{0.5\rho(\pi r^2 L)U^3} = \frac{\Delta Volt_\tau}{Volt_\tau} + \frac{\Delta Volt_\omega}{Volt_\omega} + \frac{\Delta\rho}{\rho} + 2\frac{\Delta r}{r} + \frac{\Delta L}{L} + 3\frac{\Delta U}{U}$$

By replacing the following values:

$$\frac{\Delta Volt_\tau}{Volt_\tau} = 0.0025,\ \frac{\Delta Volt_\omega}{Volt_\omega} = 0.0025,\ \frac{\Delta Volt_\omega}{Volt_\omega} = 0.0025,\ \frac{\Delta\rho}{\rho} = 0.001,\ \frac{\Delta r}{r} = 0.001,\ \frac{\Delta L}{L} = 0.001,$$

$$\frac{\Delta U}{U} = 0.01$$

The value of the power coefficient error is obtained.

$$\frac{\Delta C_p}{C_p} = 0.0025 + 0.0025 + 0.001 + 0.002 + 0.001 + 0.03 = 0.039$$